

https://dspace.org/

# Metal-insulator transition in boron-ion implanted type IIa diamond.

**Tshepe, Tshakane**

**2000**
https://hdl.handle.net/10539/26301

Downloaded from a DSpace repository. https://dspace.org/

# METAL-INSULATOR TRANSITION IN BORON-ION IMPLANTED TYPE II*a* DIAMOND

**Tshakane Tshepe**

A thesis submitted to the Faculty of Science, University of the Witwatersrand, Johannesburg, in fulfillment of the requirements for the degree of Doctor of Philosophy.

Johannesburg, 2000

# Declaration

I declare that this thesis is my own, unaided work. It is being submitted for the degree of Doctor of Philosophy in the University of the Witwatersrand, Johannesburg. It has not been submitted before for any degree or examination in any other University.

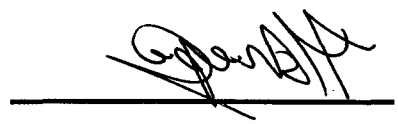

(Signature of Candidate)

$23^{rd}$ *August* 2000

# Abstract

High purity natural type II$a$ diamond specimens were used in this study. Conducting layers in the surfaces of these diamonds were generated using low-ion dose multiple implantation-annealing steps. The implantation energies and the ion-doses were spread evenly to intermix the point-defects, thereby increasing the probability of interstitial-vacancy recombinations and promoting dopant-interstitial-vacancy combination resulting in activated dopant sites in the implanted layers. The process used to prepare our samples is known as cold-implantation-rapid-annealing (CIRA). Carbon-ion and boron-ion implantation was used to prepare the diamond specimens, and dc-conductivity measurements in the temperature range of 1.5-300 K were made following each CIRA sequence.

An electrical conductivity crossover from the Mott variable range hopping (VRH) to the Efros-Shklovskii VRH conduction was observed when the temperature of insulating samples was lowered. The conductivity crossover temperature $T_{cross}$ decreases with increasing concentration of the boron-ion dose in the implanted layers, indicating the narrowing of the Coulomb gap in the single-particle density of states near the Fermi energy. The critical boron-ion concentration $n_c$ for the metal-insulator transition and the critical conductivity exponent $\mu$ have been estimated to be $n_c \simeq 4.0 \times 10^{21}$ cm$^{-2}$ and $\mu \simeq 1.7$. There is, however, a fairly large uncertainty in $n_c$ since it is not absolutely certain that all the boron ions are activated during the high-temperature annealing processes.

The importance of annealing boron-ion implanted diamond samples at high temperatures was demonstrated in this study. A significant rise in electrical conductivity (drop in resistivity) is reported with increasing annealing temperature. Such an increase in conductivity may be linked to the removal of the compensating donor centres and/or the minimization of the lattice disorder.

*Madume le ditebogo ke di lebisa go ba lelapa la me, le botlhe ba ba ineetseng go direla Modimo go ya bukhutlong jwa nako*

# Acknowledgments

This has been a long protracted battle for me. I am therefore tempted to thank everyone I met in the physics department for such is my relief at having completed this thesis. Sanity dictates, though, that I should first thank my supervisor, Prof. Mike Hoch, for his guidance, patience and encouragement throughout this project. I am indeed grateful to have him as my supervisor. I would like to thank Prof. Johan Prins, my second supervisor, for invaluable time and advice he provided during the course of this work.

Many thanks are due to my colleagues in the physics department. In particular, I would like to record my appreciation to Dr. Iain Goudemond for introducing me to the cryogenic system in the Nuclear Magnetic Resonance laboratory. I would like to thank Dr. Graeme Hill (he finished before me) and Charles Kasl for useful suggestions, stimulating discussions during our research activities in the laboratory.

I wish to thank Mrs. Renée Hoch for proof reading this thesis, correcting my grammar, and making sure that what I wrote actually made sense.

I am grateful for the financial assistance I received from the University.

It is with a deep sense of loss and profound sadness that my mother did not see me graduate. Life is such. Ke rata ke leboga botlhe ba ba ileng ba ntshegetsa ka dithapelo le dikeletso. Ammaruri Modimo o mogolo. Ke lo leboga go menagane. E kete kagiso ya Morena, e e fetang ditlhaloganyo tshotle, e ka boloka dipelo le maitlhomo a tsone mo go Keresite Jesu. Go weditswe.

# Contents


**1 General introduction and research overview** **16**

1.1 Scope of this thesis . . . . . 24

**2 The metal-insulator transition in doped semiconductors** **25**

2.1 Introduction . . . . . 25

2.2 Anderson localization and Anderson transition . . . . . 28

2.3 Electron-electron interaction theory . . . . . 29

2.4 Variable-range hopping conduction theory . . . . . 31

2.4.1 Mott VRH conduction theory . . . . . 32

2.4.2 Efros-Shklovskii VRH conduction theory . . . . . 33

2.5 Many-electron transitions in doped systems . . . . . 34

2.6 Transport properties in the metallic regime . . . . . 36

2.7 The derivative method . . . . . 38

2.8 Mott-Hubbard transition . . . . . 40

2.9 Scaling theory of localization . . . . . 43

2.10 Critical conductivity exponent . . . . . 45

2.11 Shlimak method . . . . . 47

2.12 Minimum metallic conductivity . . . . . 49

2.13 Weak localization theory . . . . . 50

**3 Ion implantation** **53**

3.1 Introduction . . . . . 53
3.2 General background . . . . . 54
3.2.1 Stopping processes of ions in a solid . . . . . 54
3.3 Implantation temperature . . . . . 60
3.3.1 Cold-implantation followed by rapid-temperature annealing cycle 60
3.3.2 Selection of the ion energies and doses . . . . . 60
3.3.3 Activation of dopant-interstitials . . . . . 61
3.3.4 Behaviour of self-interstitials in the damaged layers . . . . . 61
3.3.5 Behaviour of vacancies in ion-implanted layers . . . . . 62
3.3.6 High-temperature implantation . . . . . 62
3.4 Annealing studies . . . . . 63
3.4.1 Motivation . . . . . 63
3.4.2 High-temperature anneal ($T \geq 770$ K) . . . . . 63
3.4.3 Low-temperature anneal ($T \leq 770$ K) . . . . . 64
3.5 Lattice swelling . . . . . 64
3.6 Energy-loss simulation program: TRIM92 . . . . . 66
3.7 Secondary ion mass spectroscopy (SIMS) . . . . . 69

**4 Experimental details** **72**
4.1 Introduction . . . . . 72
4.1.1 Sample designation . . . . . 72
4.1.2 Diamond shaping and polishing . . . . . 73
4.1.3 Diamond target holder . . . . . 73
4.2 Ion implantation . . . . . 75
4.3 Annealing furnace . . . . . 76
4.3.1 Cleaning of diamond samples and sample storage . . . . . 76
4.3.2 Implanted boron and carbon ions dose levels . . . . . 78
4.4 Janis cryostat . . . . . 87
4.4.1 Maintenance of the Janis cryostat . . . . . 89

4.4.2 A procedure for the running of the Janis cryostat . . . . . 90
4.4.3 Cryogenic sample probe . . . . . 93
4.4.4 Temperature controller and the Keithley electrometer . . . . . 95
4.4.5 Low-temperature electrical conductivity measurements . . . . . 95
4.5 The dip measuring system . . . . . 97
4.6 High-temperature conductivity measurements . . . . . 98

**5 High-temperature annealing results** **103**
5.0.1 Motivation . . . . . 103
5.1 High-temperature annealing results . . . . . 104
5.2 Theoretical model for the point-defects . . . . . 108
5.3 Discussion . . . . . 109
5.3.1 Multiple CIRA sequences . . . . . 109
5.3.2 Residual damage saturation . . . . . 110
5.3.3 Activation of boron ions in implantation-damaged layers . . . . . 111
5.4 Summary . . . . . 114

**6 Percolative transition in carbon-ion implanted type IIa diamond** **116**
6.0.1 Motivation . . . . . 116
6.1 Introduction and a general overview . . . . . 117
6.2 Percolation theory . . . . . 121
6.3 Experimental results . . . . . 123
6.4 Discussion . . . . . 127
6.5 Insulating samples . . . . . 127
6.5.1 Conduction via the nearest-neighbour hopping sites . . . . . 127
6.5.2 Conduction by variable-range hopping mechanism . . . . . 128
6.5.3 Calculation of the radius of the conducting spheres . . . . . 131
6.5.4 Calculation of Bohr radii of conducting centres. . . . . 132
6.5.5 Minimum metallic conductivity . . . . . 132

6.5.6 Transport in the metallic regime . . . . . 134
6.6 Conclusion . . . . . 134

**7 Electrical conductivity results of boron-ion implanted diamond 136**
7.1 Introduction . . . . . 136
7.2 Insulating samples . . . . . 137
7.2.1 Motivation . . . . . 137
7.3 Metallic Samples . . . . . 143
7.3.1 Motivation . . . . . 143
7.4 Conduction near the M-I transition . . . . . 144
7.4.1 Motivation . . . . . 144
7.5 The derivative method . . . . . 149
7.6 High-temperature measurements . . . . . 149
7.6.1 Motivation . . . . . 149

**8 Discussion of the electrical conductivity results for boron-ion implanted type II*a* diamond 154**
8.1 Introduction . . . . . 154
8.2 Insulating samples . . . . . 155
8.2.1 Activation conduction mechanism . . . . . 156
8.2.2 The derivative method for the insulating materials . . . . . 157
8.2.3 Variable-range hopping conduction . . . . . 162
8.2.4 The optimum hopping distance and tunneling exponent . . . . . 167
8.2.5 A crossover between Mott and ES variable-range hopping . . . . . 169
8.2.6 Coulomb gap and the crossover temperature . . . . . 171
8.2.7 The unperturbed density of states . . . . . 174
8.2.8 Möbius *et al.* scaling model in the VRH regime . . . . . 175
8.2.9 Aharony *et al.* scaling law in the VRH regime . . . . . 176
8.3 Conduction in the metallic regime . . . . . 181

8.3.1 The derivative method for the metallic systems . . . . . 187
8.3.2 Classification of samples due to e-e interactions . . . . . 190
8.3.3 Shlimak *et al.* method near the M-I transition . . . . . 191
8.4 Conduction at the M-I transition . . . . . 193
8.4.1 Mott Criterion and the minimum metallic conductivity . . . . . 193
8.4.2 The derivative method for systems at the M-I transition . . . . . 196
8.5 Compensation of boron-ion impurity centres . . . . . 200

**9 Conclusions** **201**
9.1 Insulating samples . . . . . 201
9.2 Conduction near the metal-insulator transition . . . . . 202
9.3 Conduction in the metallic regime . . . . . 203
9.4 High-temperature annealing . . . . . 203
9.5 Percolation transition . . . . . 204
9.6 Future Directions . . . . . 204
9.7 Published papers . . . . . 205

# List of Figures

1-1 A schematic view of the diamond band gap, which is an indirect band gap system[3], showing locations of impurity bands. . . . . 20

1-2 The critical behaviour of $\sigma(0)$ in uncompensated Si:P and heavily compensated Si:(P,B) systems. The system shows a continuous transition with solid lines being fits to Eq. (1.6). The experimental data have been taken from articles by Palaanen *et al.*[18] and Hirsch *et al.* [19]. . . . . 23

2-1 The figure shows the main theories which describe transport properties for systems near the metal-insulator transition in the presence and absence of a magnetic field. The electron concentration is represented by a horizontal axis. The effects of the electron-electron interactions are divided into three conductivity regimes: insulating, near the metal-insulator transition, and metallic. The y-axis reflects the importance of electron-electron interactions in various theories. This figure has been taken from Uwe Hans Thomanschefsky's PhD thesis[26]. $\sigma_B$ is the Boltzmann conductivity. The other symbols are defined in the text. . . . . 27

2-2 The single-electron DOS is shown when effects due to electron-electron interactions are (a) neglected and (b) included in the variable-range hopping theory. The depletion in the DOS is referred to as the Coulomb gap. . . 30

2-3 A schematic diagram showing the Mott-Hubbard transition brought about by electron-electron interactions. The model used by Mott and Hubbard ignores the effect due to disorder and the magnetic behaviour of the system. The splitting of the top band ($D^{-1}$ band) into lower and upper Hubbard bands is due to Coulomb repulsion by intrasite electrons. At $T = 0$ K, the bottom band ($D$ band) is completely filled with one electron per site, while the upper band is empty. The energy that separates the top band from the lower band is the difference between the Coulomb repulsion energy $U$ and the bandwidth energy $B$, i.e., $\varepsilon_2 = U - B$. A metal-insulator transition will occur when $U = B$. This situation occurs when the interatomic spacing is systematically reduced to allow electron wavefunctions to overlap more strongly. . . . . 42

2-4 Predictions of a one-parameter scaling theory of localization are depicted in this figure, where we have plotted the scaling function $\beta(g)$ as a function of ln $(g(L))$. All states are localized in 1-dimensional and 2-dimensional systems for any amount of disorder. $g_c$ defines the critical conductance for a 3-dimensional system. . . . . 46

2-5 The diagram shows a succession of electron scattering events as the electron moves from point A to point B. An electron can be scattered around a closed loop, as shown at point Z. In this case, phase coherence can be maintained around the loop, resulting in a reduction in the total conductivity of the system, hence the phenomenon of weak localization. The dashed lines show the complimentary (either clockwise or anti-clockwise) paths. These paths are referred to as the time-reversal paths. The weak localization phenomenon can be destroyed when the temperature of the system is increased or a magnetic field is applied to the system. . . . . 52

3-1 A simplified schematic description of the damage cascade introduced during the ion-implantation process. This figure is taken out of ref.[5]. . . . . 58

3-2 A typical figure showing a cold-implantation damage profile of a diamond specimen implanted with boron-ions which were accelerated into the diamond surface at 130 keV. This profile was obtained using the TRIM-92 computer simulation program in which the following parameters were supplied to the program: the displacement energy, $E_d = 35$ eV, and the binding energy, $E_b = 5$ eV. The penetration depth (projected ion range) is given by $R_p$, while straggling (*i.e.* the standard mean deviation from $R_p$) is denoted by $\Delta R_p$. . . . . 68

3-3 SIMS profile for a square boron-ion implanted type II*a* diamond specimen. The actual total dose implanted into this sample was $1.2 \times 10^{16}$ cm$^{-2}$. SIMS measured the same dose as implanted. The sample was annealed at 1200 °C for 30 minutes after each implantation process. . . . . 70

3-4 SIMS profile for a rectangular boron-ion implanted type II*a* diamond specimen. The actual dose implanted into this sample was 7.9 $\times 10^{16}$ cm$^{-2}$ using multiple CIRA steps. The SIMS measured the boron atoms in the implanted layer to be $7.3 \times 10^{16}$ cm$^{-2}$. This sample was annealed at 1200 °C for 5 minutes after each implantation process. . . . . 71

4-1 Shown in this figure is sample A which is one of the four type II*a* diamond specimens used in this thesis. The dimensions of this sample can be read off from the figure. . . . . 74

4-2 A diagram of the annealing furnace used to anneal our diamond specimens after the cold ion-implantation process. Samples were slid down the retractable chute with the implanted face down into a preheated graphite crucible. The annealing was carried out in a pure-argon atmosphere. . . . 77

4-3 Plot of $I(A)$ *vs.* $V(V)$ to demonstrate Ohmic behaviour exhibited by a variety of doses implanted into sample A. . . . . 81

4-4 A cross-sectional view of the Janis cryostat. . . . . 88

4-5 A simplified schematic view of the cryogenic system. The nitrogen bath is not shown in the figure. . . . . 91
4-6 A simplified schematic view of the Janis cryostat. The nitrogen bath is not shown in the figure. . . . . 92
4-7 A schematic view of the cryogenic probe used to mount samples. . . . . 94
4-8 A sample holder used in the study of high-temperature conductivity measurements. . . . . 100
4-9 A block diagram of the conductivity setup for high-temperature conductivity measurements. . . . . 102

5-1 Plots of electrical resistance *vs.* cumulative boron-ion dose. Samples have been annealed at 1200 °C for 5 minutes. . . . . 105
5-2 Plots of $R$ *vs.* $T$ for sample AB81. This sample was annealed over various temperatures shown in the figure. . . . . 106
5-3 Plots of $R$ *vs.* $T$ for sample AB84. This sample was annealed only at 1700 °C after the CIRA routine. . . . . 107
5-4 Plots of $R$ *vs.* $1/T$ for sample DB12 (square sample) annealed at 1300 °C, 1500 °C and 1700 °C. . . . . 113

6-1 The resistivity data of Hauser *et al.* [144] described by the Mott VRH relation over the temperature range 20-300 K. . . . . 120
6-2 Plots of electrical resistance against temperature for various carbon-ion implanted diamond specimens. Symbols and sample designations are given in the figure. . . . . 124
6-3 Plots of $R$ *vs.* $T^{-m}$ ($m = 1/4$ and $1/2$) to determine which of the VRH laws best describe the experimental data. . . . . 125

6-4 The Zabrodskii-Zinov'eva plot to determine $m$. Due to the sensitive dependence of the electrical conductivity on the carbon-ion dose in the narrow percolation regime studied, the results were found not to be reproducible. The carbon-ion doses implanted into the diamond samples are listed in the figure. . . . . 126

6-5 The vacancy-related conducting graphite regions in carbon-ion implanted diamond specimens have been assumed to have a spherical shape[128, 143], but the actual shapes of these graphitic clusters are shown around the spheres. . . . . 133

6-6 The conductivity plots for samples which may be classified as metallic. . 135

7-1 The resistance against temperature for a number of boron-ion implanted type II$a$ diamond specimens. . . . . 139

7-2 Resistance of eleven insulating diamond specimens plotted as a function of $T^{-m}$ ($K^{-m}$) (where $m = 1/4$ and $1/2$) on a semilogarithmic scale. . . . 141

7-3 $\sigma$ *vs.* $T$ for sample AB27. A solid line through the experimental data represents a fit to the conductivity expression: $\sigma(T) = \sigma_o \exp[-(T_o/T)^m]$ where $m \sim 0.5$. . . . . 142

7-4 The electrical conductivity for some of the metallic samples plotted as a function of $T$. Samples have been annealed isochronally (10 minutes) at various temperatures ranging from 1200 °C to 1700 °C. Symbols shown represent: ■-sample AB84 (1700 °C anneal); ▲-AB81 (1700 °C anneal); •-AB78 (1700 °C anneal); △-AB81 (1200 °C anneal) ♦-AB78 (1200 °C anneal). All samples have been annealed for 10 minutes. . . . . 145

7-5 Electrical conductivity *vs.* $T$ for sample AB81. This sample has been annealed at 1700 °C. . . . . 146

7-6 Electrical conductivity *vs.* $T$ for sample AB84. This sample has been annealed at 1700 °C. . . . . 147

7-7 Temperature-dependent electrical conductivity *vs.* $T$ for samples AB78, AB81 and AB84. A closer inspection of the plots reveals that $\sigma(T)$ *vs.* $T^{1/3}$ gives a better fit to the experimental data than $\sigma(T)$ *vs.* $T^{-1/2}$. Plotted here are samples annealed at 1700 °C for 10 minutes. Sample AB84 is shown in Fig. 7-8(b). . . . . 150

7-8 Plots of activation energy $W = \partial \ln \sigma / \ln T$ against $T$. This sample, AB81, is close to the M-I transition. According to the derivative method, sample AB81 is weakly insulating. One of the curves fitted with a solid line has been annealed at 1700 °C, which is the highest temperature at which we can safely anneal our samples. The annealing temperatures for these samples are shown in the figure. The duration of the anneal for all samples was set to 10 minutes. . . . . 151

7-9 Plots of $R(T)$ *vs.* $T^{-m}$ for sample AB84 measured in the temperature range 300-773 K. The insert shows the same experimental data plotted against $T^{-1/4}$ to check whether Mott VRH conduction applies in this temperature range. . . . . 153

8-1 Plots of $R$ *vs.* $1/T$ for a number of insulating samples. Only the data above 400 K may be used for the calculation of the activation energy, $E_A$. 158

8-2 Plots of $R(T)$ *vs.* $T^{-m}$ ($m = 1$; 1/4 and 1/2) for a high insulating sample CB5 measured in the temperature range 300-773 K. . . . . 159

8-3 The derivative method and the White-MacLachlan method were used to generate these plots in an effort to determine the hopping exponent $m$. Samples plotted here lie in the boron-ion concentration range: $1.0 - 1.9 \times 10^{21}$ cm$^{-3}$. The values of the fitted slopes, which are close to the theoretical predicted exponents of 1/2 and 1/4, are shown in the plots. . . . . 163

8-4 The derivative method and the White-MacLachlan method used to generate plots shown in an effort to determine the hopping exponent $m$. Samples lie in the boron-ion concentration range: $2.0 - 3.0 \times 10^{21}$ cm$^{-3}$. The fitted slopes close to the theoretical hopping exponent of 1/2 are shown in the plots. . . . . 164

8-5 The derivative method and the White-MacLachlan method used to determine the hopping exponent $m$. Sample AB78 ($n \simeq 4.0 \times 10^{21}$ cm$^{-3}$) is shown. Solid lines shown in the plots correspond to theoretical slopes of $-1/3$ and $-1/2$. From the plots, a slope of $-1/3$ gives a better fit to the data compared to a slope of $-1/2$. The annealing temperatures for this sample are shown in the table alongside this figure. . . . . 165

8-6 This plot demonstrates the relationship between the Mott and ES characteristic temperatures in the VRH regime. . . . . 173

8-7 Plots of ln $\sigma$ *vs.* $T^{-1/2}$ for boron-ion implanted diamond specimens. The scaling parameter $\sigma_1$ is shown in the figure. . . . . 177

8-8 Plots shown in Fig. 8.7 can be collapsed into a single universal curve using $\sigma_1$ as the scaling parameter. We have plotted data corresponding to doses $3.0 - 4.2 \times 10^{16}$ cm$^{-2}$. Details of the method can be found in papers by Mobius *et al.*[32]. . . . . 178

8-9 Plots of $T_{ES}$ versus $n$ in semilog and linear scales. The $T_{ES}$ values were obtained with the hopping exponent fixed to $m = 1/2$ and $\sigma_1$ read from Fig. 8.7. . . . . 179

8-10 Universal scaling function crossover plot of scaled resistance versus the scaled temperature for some insulating diamond specimens. The method used to generate this plot is given by Aharony *et al.*[200]. . . . . 183

8-11 Electrical conductivity for one of the metallic samples, AB84, which has been annealed at 1700 °C. . . . . 185

8-12 $\sigma(T)$ *vs.* $n$ for samples AB78, AB81 and AB84. These samples have been implanted close to the M-I transition. We obtained $\mu \sim 1.7$ and $\sigma_o = 9736$ $(\Omega-\text{cm})^{-1}$ from the fit of Eq. (1.1). The values of $n$ have been estimated using the SIMS technique with an error of $5-10$ % . . . . . 186

8-13 Following the work of Watanabe *et al.* [178], we can further classify sample AB78 (curve A) as insulating, but AB81 (curve B) may taken as 'weakly' metallic with a finite conductivity at $T = 0$ K. Sample AB84 is represented by curve C. . . . . 192

8-14 Shlimak *et al.*[16] method to determine the critical conductivity exponent $\mu$. We have calculated the $\mu$ value to be $\sim 1.7$. The procedure for the calculation of $\mu$ is outlined in the text. . . . . 195

8-15 Edwards-Sienko plot [79] demonstrating the Mott criterion. The ◇C:B sample that we have studied is shown against other doped semiconductors in this figure. . . . . 197

# List of Tables


4.1 Implantation energies and ion doses used in this study. The accelerating energies and doses were spread into small steps to generate highly conducting boron-ion and carbon-ion layers in the diamond samples. . . . . 79

4.2 Energy, boron-ion dose and carbon-ion fluences used to generate Ohmic contact regions on the diamond surfaces. The electrical contacts are spaced about 5.5 mm apart. . . . . 82

4.3 Summaries of boron-ion and carbon-ion implanted type II*a* diamond samples (insulating samples) used in this study, and their characterizations are given in table 4.3-4.6. . . . . 83

5.1 Ion energies and ion doses used to generate a boron-ion layer in a diamond specimen. The created point-defects are homogeneously distributed in the implanted layer. The vacancies created following each implant have been calculated using the TRIM-92 simulation code in which the displacement energy of 35 eV and the lattice binding energy of 5 eV were assumed. . . 112

6.1 A list of values for some variables determined from the experimental data using the VRH relations. . . . . 130

7.1 The Minuit least squares fitting procedure was used to determine values for the characteristic temperatures in the Mott and the ES VRH regimes. The uncertainty in the characteristic temperatures were estimated by fitting the regression lines over various temperature regions in which the Mott and the ES laws apply. The non-monotonic decrease in $T_M$ and $T_{ES}$ may be an indication of the unreliability of this method . . . . . 140

7.2 Variables of boron-ion implanted diamond obtained from the metallic expression are presented in this table. . . . . 148

8.1 Values of variables determined using electrical conductivity expressions are described in the text. The error estimates for $T_M$ and $T_{ES}$ were given in table 7.1. . . . . 160

8.2 Values for quantities associated with the conductivity theory are listed in this table. Error estimates associated with the characteristic temperatures have been given in table 7.1. The non-consistency in the $T_{Cg} = \Delta_{Cg}/k_B$ (K) values seems to cast some doubts on the reliability of the VRH model over the temperature ranges that we have investigated. . . . . 172

8.3 Quantities extracted using the method of Aharony are summarized in this table. . . . . 182

8.4 Values for $\sigma(0)$ are calculated from one conductivity data point for each different sample using Eq. (8.39). These values are compared to those $\sigma(0)$ values obtained using the extrapolation procedure. . . . . 188

8.5 The $\alpha$ values, shown in the last column, have been calculated using Eq. (8.44) for some samples located close to the metal-insulator transition. The $\alpha$ values were found to increase as annealing temperatures were increased. This is an indication that samples may be driven into the metalic phase by annealing them at high temperatures. . . . . 194

8.6 A comparison of values of parameters obtained from ◇C:B and those of the Si:B semiconductor system. . . . . 198

# Chapter 1

# General introduction and research overview

Diamond is one of the two most common crystalline allotropes of carbon. The other is graphite. Between these two allotropes lie a whole variety of carbon materials, ranging from amorphous $sp^2$ bonded carbon (such as thermally evaporated carbon, and glassy carbon) to amorphous $sp^3$ bonded carbon, which is structurally analogous to amorphous silicon and is formed during low-energy carbon-ion deposition[1]. Diamond is a metastable form of carbon in which the atoms are equidistantly spaced at the corners of a regular tetrahedral lattice structure. The carbon atoms are held together by strong covalent $sp^3$ bonds. The close packing of the carbon atoms in diamond makes it a relatively dense material.

Natural and synthetic diamond single crystals have been the subject of intensive research for decades. The research has been driven by the excellent and often unsurpassed properties that diamond enjoys over other materials. Diamond possesses a unique combination of highly favourable technological properties that puts it in a class of its own. The history and the use of diamond have been documented in a book by Tolansky[2].

Some of the basic properties that put diamond in a class of its own are stated below.

- Diamond is optically transparent to electromagnetic radiation over a wide spectral range, from a 220 nm wavelength in the ultra-violet to the far infra-red.
- Diamond enjoys the highest thermal conductivity at room temperature of all known materials.
- Diamond's thermal conductivity is a factor of five greater than copper and a factor of about ten greater than commonly used thermal conductive insulators.
- At ambient temperatures, diamond has a relatively low specific heat capacity, with a Debye temperature of 2200 K, and therefore diffuses heat efficiently in transient applications in which the speed of heat transfer is important.
- Diamond exhibits one of the lowest coefficients of thermal expansion, which enhances the resistance to thermal shock.
- Diamond remains inert to aggressive acids and bases, and all types of chemical reagents, even at fairly high-temperatures. It therefore offers protection in most severe corrosive environments.
- It is one of the hardest (though brittle) known materials, and has a relatively low coefficient of friction, ensuring a wide range of applications in cutting tools and wear-resistant parts.
- Being a wide-band gap material (with a band-gap energy of $\sim$5.4 eV), diamond can be an electrical insulator. High carrier mobility opens attractive avenues for the application of diamonds in electronic devices and radiation detectors on particle accelerators.

Further articles on diamond properties can be found in a recent book by Field [3] and references cited therein. These properties have been put to use to some extent in the semiconductor and optical industry. See Prins [4] for a recent review article.

The generation of conductive surface layers in diamond, by means of ion implantation, has conclusively been demonstrated and extensively reported in the literature[5]. The study has now matured to the stage that boron-ion layers, which have electrical properties closely matching those that are found in natural semiconducting type II*b* diamond specimens, can selectively and reproducibly be generated in a type II*a* diamond surface. In order to achieve the best results for boron doping, an implantation-annealing scheme was devised and developed by Prins [6, 7]. It is known by the acronym CIRA (cold-implantation-rapid-annealing), and is discussed in chapter 3. The CIRA technique involves implanting samples at low temperatures to inhibit the diffusion of the point defects in the damaged layer, followed by rapid high-temperature annealing to reduce radiation damage and to drive the dopants into the electrically active substitutional sites.

At low temperatures, the electronic properties of doped semiconductors are generally determined by impurities. An impurity can either be a donor or an acceptor, according to its location in the periodic table relative to the host material. Diamond is a covalently bonded group IV insulator. The group III elements are said to be p-type dopants (acceptors) in diamond. Boron, in particular, makes a good dopant since its volume is comparatively close to that of the carbon atom, and boron atoms may occupy substitutional sites after high-temperature annealing.

A characteristic property of an acceptor impurity is its ability to capture an electron from the target material, leaving a hole to conduct electrically. The impurity centre becomes negatively charged by virtue of an electron it has trapped, while a hole appears in the valence band. Since the resulting hole has a positive charge, it is attracted by the

acceptor. An acceptor (donor) is said to be of a shallow type if its energy level lies close to the valence (conduction) band, that is, when the ionization energy (energy required to excite an electron from the top of the valence band to fill the hole) is much smaller than the band-gap energy. A schematic view of the diamond band gap showing locations of impurity bands is given in Fig. 1-1.

Each impurity inserted into a host contributes a discrete local energy level into the forbidden energy band gap. As more and more impurities of a particular type are randomly introduced into the host, their wavefunctions overlap more strongly. The acceptor (donor) energy levels eventually merge and broaden into a band, known as an impurity band. The electrons delocalize and the system transforms into a metallic phase. At low-dopant concentration, the overlap of the electronic wavefunctions of impurities is small, and hopping electrical conduction between spatially distinct localized impurity sites occurs, mediated by phonons.

Insulators are characterized by thermally activated electrical conduction with a vanishing conductivity at absolute zero temperature, while metals exhibit a finite zero temperature conductivity, $\sigma(0)$. In order to distinguish a metal from an insulator, one therefore needs to measure the electrical conductivity as a function of temperature and then extrapolate the results to $T = 0$ K to check for the behaviour of $\sigma(0)$. This procedure involves some optimization of parameters controlling the transition. The exact nature of the M-I transition in doped semiconductors has been the subject of much interest since the 1960's and continues to receive intense experimental and theoretical focus. Some of the well-studied disordered systems include silicon and germanium.

The basic concepts behind the theory of the M-I transition, which extend beyond the band theory, were introduced by Mott[8], who studied the effects of electron-electron interactions, and by Anderson[9], who pointed out the importance of lattice potential

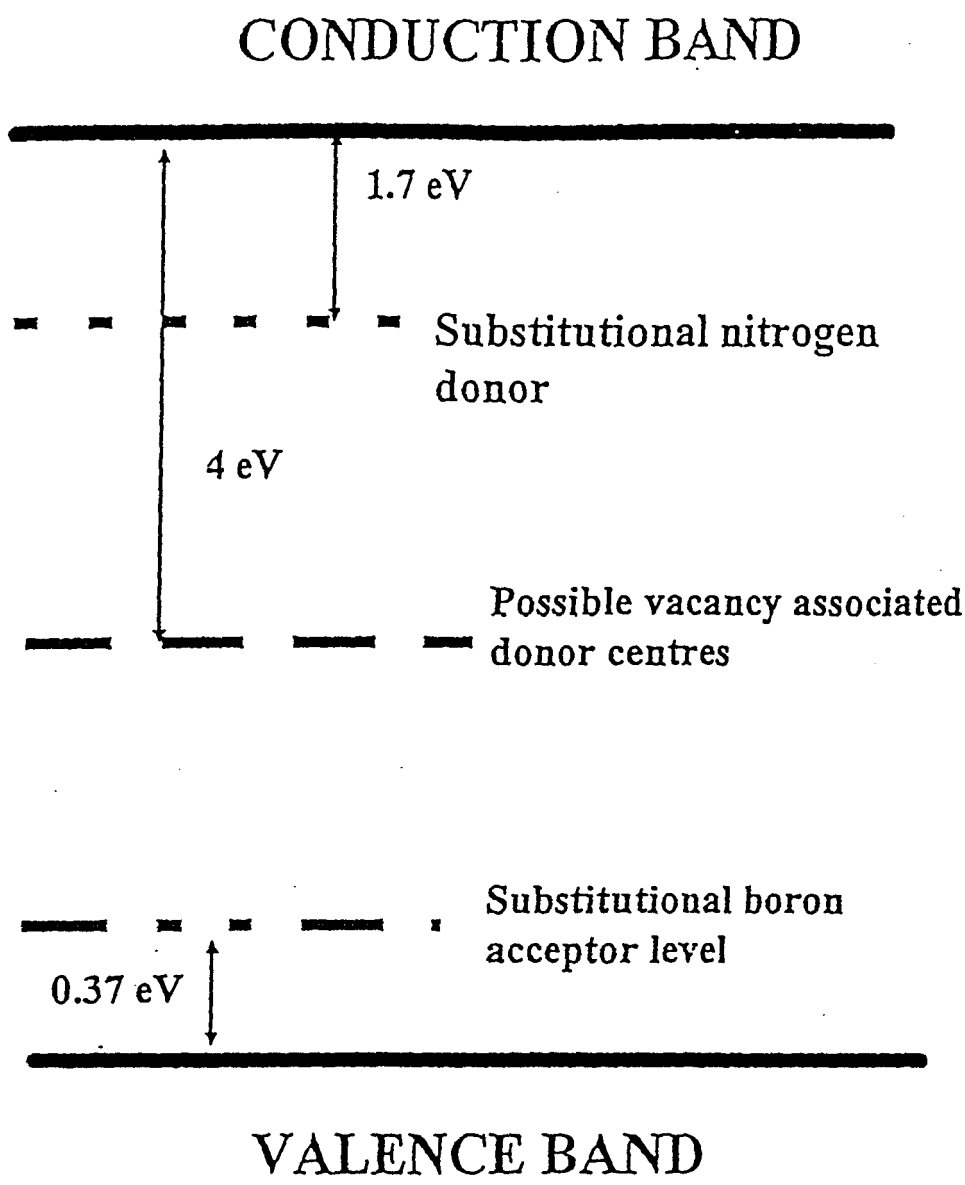


Figure 1-1: A schematic view of the diamond band gap, which is an indirect band gap system[3], showing locations of impurity bands.

disorder in a non-periodic system. Electron-electron (e-e) interactions and disorder are complex phenomena difficult to deal with even when treated separately. Their interplay has complicated what can be perceived as an already complex situation, making transport studies interesting but difficult to explain in detail. It should be pointed out that no complete theory, which incorporates the effects of both electron-electron interactions and disorder on an equal footing, particularly near the M-I transition, is available.

An important question still being debated is whether the electrical conductivity drops abruptly to zero at the critical concentration $n_c$, or is a continuous function of dopant concentration as the M-I transition is approached from either side of the transition, be it metallic or insulating. Mott, using the Ioffe-Regel (IR) criterion[10], argued for the discontinuity in the electrical conductivity at the transition. The IR criterion crudely states that no electrical conductivity will occur when the mean free path between the scattering events is smaller than the interatomic spacing. The scaling theory of localization proposed by Abrahams *et al.* [11] predicts a continuous transition at $n_c$. This debate, though adding some impetus towards the understanding of the transport problem in doped systems, managed for a while to polarize researchers in the field into two opposing camps. One group, championed by Mott, argued for the occurrence of the minimum metallic conductivity $\sigma_{\min}$. Although Mott was later persuaded to accept that $\sigma_{\min}$ does not exist, Möbius *et al.*[12, 13, 14] have come out recently in support of $\sigma_{\min}$. Accepting that the behaviour of $\sigma(0)$ is continuous at the localization threshold, the critical behaviour may be described using a critical exponent $\mu$ as follows[15]:

$$\sigma(0) = \sigma_o \left( \frac{n}{n_c} - 1 \right)^{\mu} \quad , \tag{1.1}$$

with $\sigma_o$ being the parameter which controls the conductivity scale. A wide range of $\mu$ values have been found by a number of authors in various systems which undergo the M-I transition[15]. The reader is referred also to the recent interesting results of Shlimak *et al.*[16] and to contrasting arguments presented by Sarachik and Bogdanovich[17]. Fig.

1-2 shows the critical behaviour of $\sigma(0)$ in the phosphorus doped silicon system, Si:P, measured by Rosenbaum *et al.*[18] and the behaviour of $\sigma(0)$ in Si:(P,B) determined by Hirsch *et al.*[19]. The system shows a continuous transition, with solid lines being fits to Eq. (1.1).

The M-I transition, which occurs as a function of dopant concentration, is the main subject of the present investigation in boron-ion implanted type II*a* diamond. The temperature range of interest is 1.5-300 K. The electrical conductivity measurements were extended up to 773 K.

Electrical conductivity studies have also been carried out in boron-ion doped CVD diamond polycrystalline crystals by a number of authors[20, 21]. A review article which covers the growth, application and electrical conductivity properties has been published recently by Werner and Locher[22]. The conductivity results obtained in CVD diamonds are consistent with those obtained in implanted natural single-crystalline diamonds.

Besides the study of the electronic properties of boron in natural diamond in this thesis, we have also studied the percolative nature of electrical conduction in carbon-ion implanted diamond. The carbon-ion work may be regarded as a preliminary step in the M-I project.

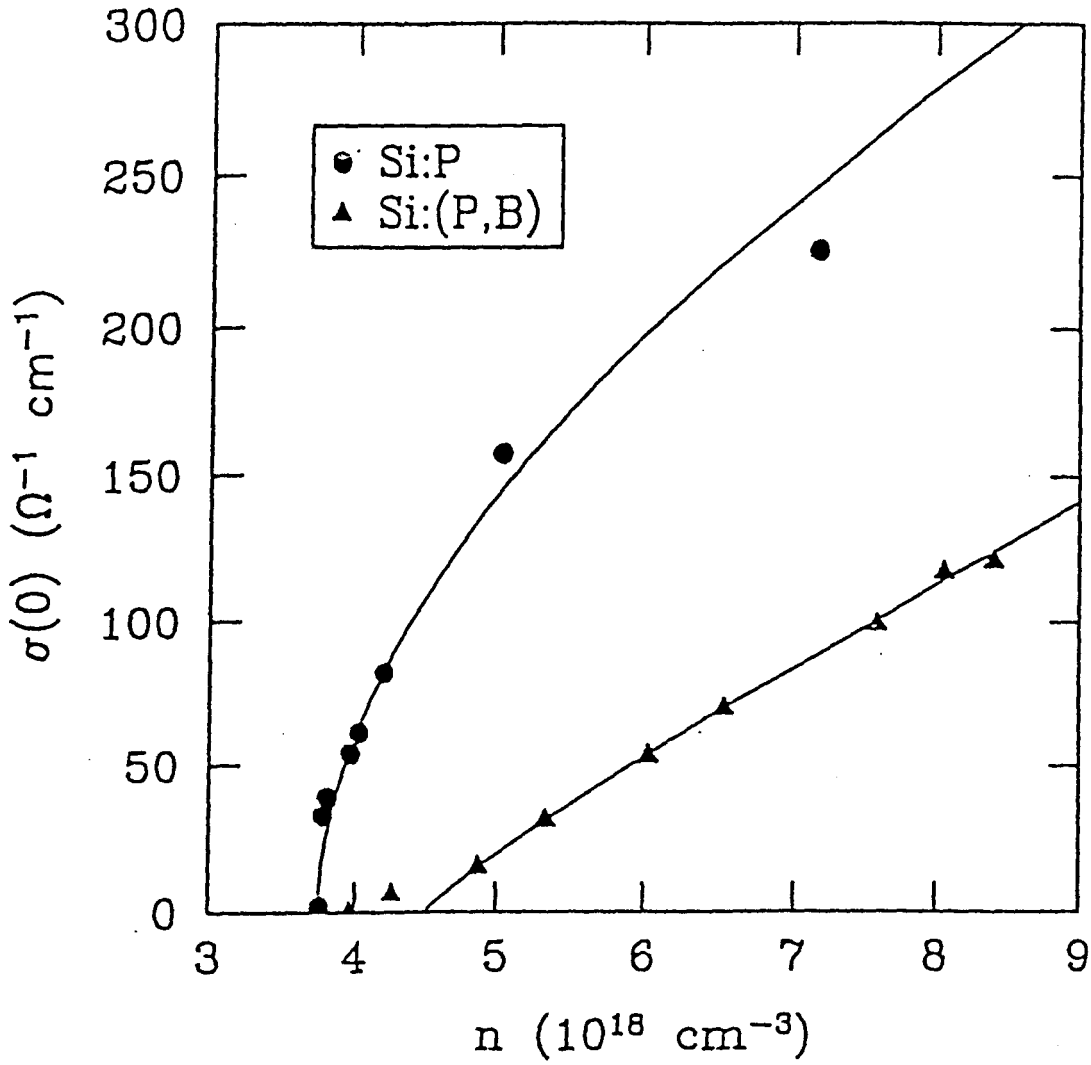


Figure 1-2: The critical behaviour of $\sigma(0)$ in uncompensated Si:P and heavily compensated Si:(P,B) systems. The system shows a continuous transition with solid lines being fits to Eq. (1.6). The experimental data have been taken from articles by Palaanen *et al.*[18] and Hirsch *et al.* [19].

## 1.1 Scope of this thesis

Chapter 2 summarizes the main concepts applied to the study of the metal-insulator transition, reviewing the major approaches to the transport problem and focusing on recent developments. The ion implantation theory is discussed in chapter 3. Chapter 4 describes sample characterizations and the cryogenic apparatus used in the electrical conductivity studies. The work on carbon-ion implanted type II*a* diamond is presented in chapter 5. Chapter 6 is devoted to the results obtained using the CIRA technique. Various annealing cycles were employed in order to achieve substitutionally B-doped diamond with as few other defects present as possible. Chapter 7 presents the conductivity results obtained in the temperature range of 1.5-773 K, while chapter 8 provides an analysis of the results in the light of recent theories. Chapter 9 gives a summary of all the results, offers some comments on the unresolved problems in this field, and suggests some possible areas for future research.

# Chapter 2

# The metal-insulator transition in doped semiconductors

## 2.1 Introduction

In this chapter, a large body of experimental and theoretical work on the study of the metal-insulator (M-I) transition in disordered systems is surveyed. There is an extensive literature on the subject, with an excellent introductory text written by Mott[8]. Other reviews are given by Shklovskii and Efros[23], Bottger and Bryksin[24] and Belitz and Kirkpatrick[25]. The last of these covers the state of the M-I theory on both sides of the transition in depth. Since most of the experimental work in this thesis has been performed on samples located on the insulating side of the transition, only a brief outline of those theories which describe the details of the transport properties in the metallic regime will be given. Some of the models pertinent to the study of the M-I transition are summarized in Fig. 2-1[26]. Not all of these theories are discussed in this chapter, but can be found in references cited above.

The problem of the M-I transition has been addressed theoretically from either of the two conductivity limits: metallic or insulating. The interpretations of the experimental data have been based mainly on extrapolations using the two-parameter power law expression, $\sigma(T \rightarrow 0, x) = a + CT^p$, where $x$ stands for a dopant impurity concentration, and $p = 1/2$ or $1/3$ in the case of metallic samples. On the insulating side of the transition, $a = 0$, and $\sigma \rightarrow 0$ as $T \rightarrow 0$ K. Further work on systems which undergo M-I transitions has been discussed recently by Rosenbaum *et al.*[27, 28, 29, 30]. A power law approximation, however, involves several assumptions and uncertainties, casting some doubt on the reliability of the extrapolated results[12, 31, 32, 33, 34, 35]. Nevertheless, the predictions of some theories, particularly those which incorporate the effects of electron-electron interactions and disorder, have been confirmed near the critical concentration, $n_c$, by a number of authors to a high degree of accuracy[36]. Quite recently, Shlimak and co-workers[16] have proposed a method to determine $n_c$ and the conductivity critical exponent $\mu$ without extrapolating $\sigma(T)$ to zero temperature. The method is based on the assumption that the log $\sigma(T)$ *vs.* $T$ curves are parallel for $n \gtrsim n_c$. This may not be a good assumption. The Shlimak *et al.*[16] method is discussed in a later section in this chapter.

On the insulating side of the transition, a general conductivity relation, $\sigma(T) = \sigma_1 \exp\left[-\left(\frac{T_o}{T}\right)^m\right]$, describes transport behaviour in the variable-range hopping (VRH) conduction regime adequately[8]. An exponent of $m = 1/4$ is associated with negligible electron-electron interaction and non-changing density of states (DOS) near the Fermi energy ($E_F$), while $m = 1/2$ signifies VRH hopping in the strong Coulomb regime[23]. More details on transport properties on the insulating side will be given later in the chapter.

The two main ingredients in the study of M-I transitions are disorder and electron-

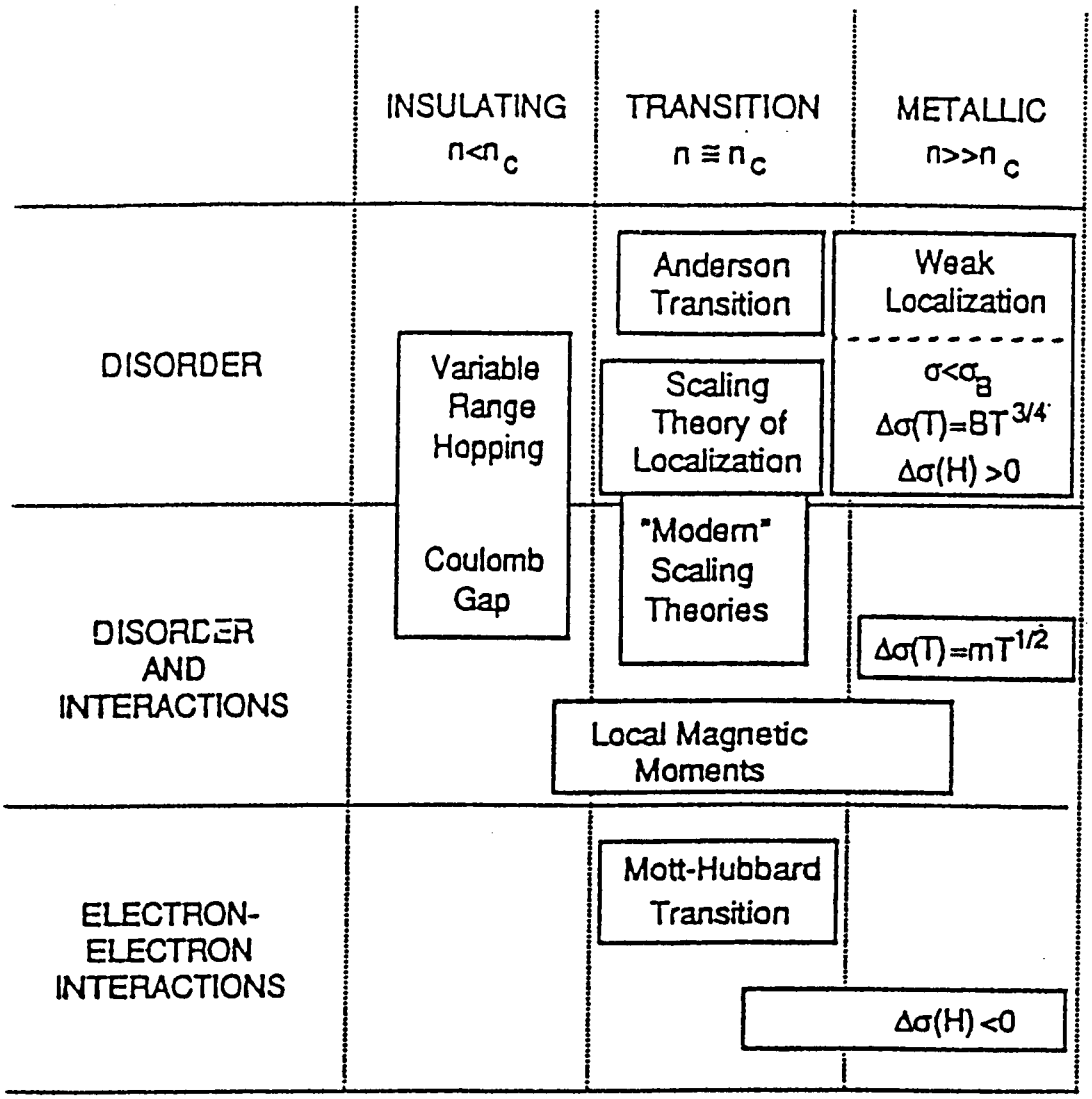


Figure 2-1: The figure shows the main theories which describe transport properties for systems near the metal-insulator transition in the presence and absence of a magnetic field. The electron concentration is represented by a horizontal axis. The effects of the electron-electron interactions are divided into three conductivity regimes: insulating, near the metal-insulator transition, and metallic. The y-axis reflects the importance of electron-electron interactions in various theories. This figure has been taken from Uwe Hans Thomanschefsky's PhD thesis[26]. $\sigma_B$ is the Boltzmann conductivity. The other symbols are defined in the text.

electron (e-e) interactions (also referred to as electron correlations). Both have proven to be very complex phenomena even when treated separately and independently of each other, but their contributions may be of comparable importance and their effects intertwined. As stated in chapter 1, there is no complete theory available which incorporates the two phenomena on equal footing up to this stage. Their influence on systems which undergo the M-I transition are discussed separately.

## 2.2 Anderson localization and Anderson transition

Spin localization, independent of the effects of electronic interactions, was predicted by Anderson in his 1958 classic paper, entitled "Absence of diffusion in certain random lattices", using the tight binding approximation model[9]. He showed that the electronic wavefunctions can become localized in an array of potential wells if sufficient disorder is introduced. The disorder here is introduced by letting the lattice potential due to the randomly incorporated impurity atoms fluctuate from site to site in space. An electron moving through a series of nonidentical potential wells, fluctuating randomly in depth (on-site energies) by a certain amount, can be localized. Taking the size of potential variation to be $\pm W/2$, where $W$ is the energy of disorder, Anderson showed that an electron can stay localized at a particular impurity site when the ratio of $W$ to the bandwidth (electron overlap) $B = 2zV$ exceeds a critical value, $(\frac{W}{B})_{crit}$, where $z$ is the coordination number and $V$ is the potential. This kind of localization, caused solely by disorder, is referred to as Anderson localization.

The transition that takes place as a result of the variation of disorder in a doped semiconducting system is referred to as an Anderson transition. Bottger and Bryksin[24] and Shklovskii and Efros[23] have presented reviews on the Anderson subject in a scholarly

fashion, and this will not be laboured further.

## 2.3 Electron-electron interaction theory

Long-range electron-electron (e-e) interactions have a profound influence on the electronic and thermodynamic properties of disordered systems, particularly in the localized (insulating) regime. In the latter regime, the e-e interactions give rise to a depletion in the single-electron density of states (DOS) near the Fermi energy $E_F$. This depletion region, which may be parabolic in shape, is referred to as a Coulomb gap (Cg)[37]. The Cg is sketched in Fig. 2-2. The theory, manifestation and influence of the Cg on transport properties can be found in standard M-I transition books. The reader is referred here to books by Shklovskii and Efros[23] and Bottger and Bryksin[24].

The first theoretical papers on the pronounced influence of the Coulomb interaction on the DOS near the Fermi energy appeared about three decades ago. Pollak[38] and Srinivasan[39] showed, using analytical studies, that the DOS exhibits a minimum near $E_F$. Such an observation was made when they tried to stabilize the ground state with respect to one-electron transitions. Their observation was later confirmed numerically by Kurosawa and Sugimoto[40, 41]. Efros and Shklovskii[42] pointed out that the long-range tail of the unscreened Coulomb interaction induces a pseudogap in the DOS near $E_F$. The role of the Cg, particularly in transport studies, is still embroiled in controversy up to this date[43], the main source of controversy being the type of the density of states to which the Cg applies. The single-electron density of states can be defined as the number or concentration of localized states, which lie near the chemical potential, per unit energy and unit volume, in which an added electron will increase the energy of the system by $E$ when no other electrons are allowed to move from their original positions[44]. It is

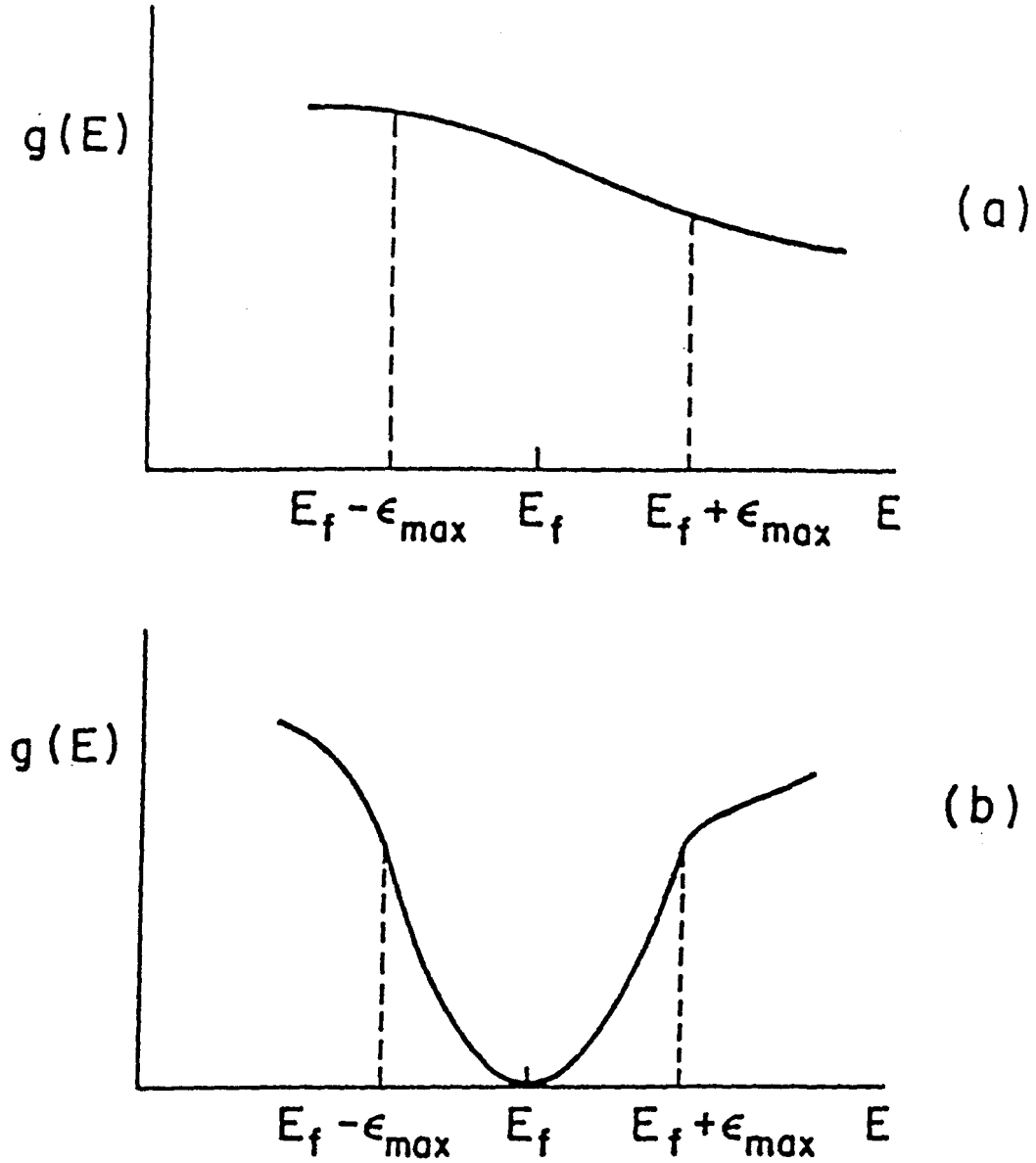


Figure 2-2: The single-electron DOS is shown when effects due to electron-electron interactions are (a) neglected and (b) included in the variable-range hopping theory. The depletion in the DOS is referred to as the Coulomb gap.

worth noting that the Cg does not apply to the many-body thermodynamic density of states which characterizes the density of total system excitations. A detailed review of the e-e interactions in disordered systems can be found in ref.[44]. The reader is referred to chapters 4 and 5 in this book. A great deal of work on the subject has been carried out by a number of authors. Literature on the M-I transition and related transport phenomena is growing at a bewildering rate, making it extremely difficult to keep abreast of the new developments. This could well reflect on the amount of interest this field generates. For an up-to-date review on the subject, the reader is referred to recent articles by Rosenbaum *et al.*[27, 30] and Imada *et al.*[45]. Further references on the subject can be found also in a paper by Massey and Lee[46], and conference proceedings in *Hopping and Related Phenomena* [47] and *Metal-non-Metal Transition in Macroscopic and Microscopic systems*[48].

## 2.4 Variable-range hopping conduction theory

Variable-range hopping (VRH) theory has been quite successful in describing transport properties in disordered systems. Early theoretical ideas were proposed by Mott[49]. Others built on these ideas, with notable contributions made by Ambegaokar *et al.*[50], who used percolative models to arrive at the same results as Mott. Shklovskii and Efros (ES) have given an extensive review of the theory in their book, *Electronic Properties of Doped Semiconductors*[23]. I present a summary of both the Mott VRH and ES VRH models below.

### 2.4.1 Mott VRH conduction theory

Consider a situation in a narrow band semiconductor at sufficiently low temperatures. Hopping conduction will take place between the localized impurity states concentrated near the Fermi level whose energies are comparable. It is advantageous for a carrier to hop to a distant site with equivalent energy to the site it leaves behind rather than to be excited to a higher energy state. In order to minimize the interaction energy of the system, charge carriers will be spread far apart from each other, and the spatial distribution of these carriers in space can be considered uncorrelated, and the electronic DOS at the Fermi energy regarded as constant and nonvanishing.

The distance $R$ within which an electron can hop to all available sites can be obtained from an expression[51],

$$W = \frac{3}{4\pi R^3 N(E_F)} \quad . \tag{2.1}$$

This is the energy difference between the two impurity sites involved. The probability for an electron to hop from one localized site to the next is given by

$$\omega = \upsilon_{ph} \exp\left(-2\alpha R - \frac{W}{k_B T}\right) \quad , \tag{2.2}$$

where $\upsilon_{ph}$ depends on the strength of electron-phonon interaction, and $\alpha$ is the rate of fall-off of the impurity wave-function from the centre of localization. Substituting Eq. (2.1) into Eq. (2.2), and carrying out the minimization process with respect to $R$, yields the most probable hopping distance

$$R = \left(\frac{9}{8\pi\alpha N(E_F)}\right)^{1/4} T^{-1/4} \quad . \tag{2.3}$$

Incorporating Eq. (2.3) into the conductivity expression, $\sigma = e^2\omega/(8\pi WR)$, Mott obtained the result

$$\sigma(T) = \sigma_1 \exp\left[-\left(\frac{T_o}{T}\right)^{1/4}\right] \quad , \tag{2.4}$$

where $T_o \equiv T_M$ is the characteristic temperature in the Mott regime, given by

$$T_M = \frac{18}{k_B N_o(E_F)\xi^3} \quad . \tag{2.5}$$

$k_B$ is Boltzmann constant, $\xi \equiv 1/\alpha$ is taken as a measure of the radius of the localized impurity electron wavefunction, and $N_o(E_F)$ is the number of localized electron energy states per ($cm^3$ eV) at the Fermi energy. A full derivation of the Mott VRH law (Eq. (2.4)) can be found in Hamilton's paper[52].

Let me summarize the main assumptions leading to the derivation of the Mott VRH law:

- The DOS should be taken as a constant or slowly varying function of energy, and must remain nonzero at the Fermi energy.
- Effects due to electron-electron interactions should be ignored.
- The temperature of the system must be sufficiently low enough so that phonon-assisted hopping occurs between impurity sites whose energies are not very different. This holds for well-separated impurity sites.
- A hop from site $i$ to an empty site $j$ should not depend on whether a site close to $j$ in space is occupied or not.

### 2.4.2 Efros-Shklovskii VRH conduction theory

ES incorporated effects due to electron-electron interactions into the Mott scenario, and showed that the DOS should have an analytic form[42],

$$N(E_F) = A\,|E - E_F|^{d-1} \quad , \tag{2.6}$$

where $A$ is a proportional constant and $d$ is the dimensionality of the system. If $E' = E - E_F$, then $N(E') \sim |E'|^2$ in 3-dimensions corresponding to a 'soft' parabolic gap with $N(0) = 0$. The change in the DOS at the Fermi energy has a profound influence on the transport properties of doped and disordered semiconductors, modifying the Mott VRH exponent from 1/4 to 1/2. In the ES case, the temperature-dependent electrical conductivity takes the form:

$$\sigma(T) = \sigma_2 \exp\left[-\left(\frac{T_{ES}}{T}\right)^{1/2}\right] \quad , \tag{2.7}$$

with

$$T_{ES} = \frac{\beta_{ES}\, e^2}{k_B \epsilon \xi} \quad . \tag{2.8}$$

The prefactors, $\sigma_1$ and $\sigma_2$, are marked with different subscripts because they apply to different temperature regimes. Experimental results which exhibit $\sigma(T) \propto \exp(T^{-1/2})$ are common, and are now interpreted in terms of the Cg model [47, 53, 54, 55].

## 2.5 Many-electron transitions in doped systems

There are other forms of excitations of the charge-carriers that can also take place when the temperature of the system is sufficiently low. These excitations are generally referred to as many-electron transitions. In most cases, the system should be in the millikelvin-temperature range for one to observe these excitations. The motion of electrons are described as correlated since

- the hopping probability of the electron depends on the previous hops of other electrons in the neighbourhood. This type of hopping has been referred to as successive or sequential correlated hopping[56], process A[57] or adiabatic hopping[58].

- Correlation in motion of electrons may be inherent in the many-electron impurity system. This effect is referred to as quantum correlation. Details of quantum correlations can be found in a review article by Pollak and Ortuno[44].

- In some situations, several electrons participate in a single-hopping transition. What happens here is that electrons hop to other localized impurity sites when, for example, electron $a$ moves from site $i$ to site $j$ which are far apart. The distance that each electron covers is small compared to the distance travelled by electron $a$. Such a process is referred to as correlated multi-electron hopping. This process is more important in our case than the first two, and is further described below.

At very low temperatures (below which Mott and ES VRH are not observed), electrons behave as polarons or quasi-particles because they are considered to be "dressed-up". The dressing consists of a polarization cloud that an electron drags along as it moves from one site to the next. Due to this dressing, the energy of the system is much less in comparison to the same system where excitations are effected by unscreened electrons[59].

Studies have revealed that at sufficiently low temperatures, the low-energy polaron excitations, following the long-range electron hopping process, cause a complete vanishing of the DOS within a Cg. The result is a hard gap (hg) where the DOS is effectively zero over a finite range of energy within a Cg[60, 61, 62, 63, 64]. Transitions across the hg lead to the conduction mechanism of the form

$$\sigma(T) \propto \exp\left(-T_{hg}/T\right) \quad , \tag{2.9}$$

where $T_{hg}$ is the "hg" characteristic temperature. An hg is always much narrower in variation than $\mid E - E_F \mid^2$of the soft Cg, irrespective of the system disorder. Two types of hard gaps are known to occur in disordered systems at low temperatures. These are magnetic hard gaps and electrical hard gaps. The manifestations of magnetic hard gaps

are due to the interactions of the magnetic moments of the spins[65, 66], and have been found to be temperature- and magnetic field- dependent. It has been observed in several materials, such as CdMnTe:In[66], that the magnetic hard gap transforms into a soft gap under strong magnetic fields, with the exponent of unity changing to a 1/2. The temperature range in which the hg phenomenon has been observed is 300 mK-2 K. In contrast to the origin of the magnetic hard gaps, electrical hard gaps have been found to be insensitive to an external magnetic field. Typical examples which have been well studied include In/$InO_x$ composite films, which retain the hopping conductivity exponent of unity up to 8 T over the temperature range 7-35 K, exhibiting hard gap phenomena[53].

## 2.6 Transport properties in the metallic regime

Effects of electron-electron interactions in dirty (or disordered) metals have traditionally been treated within the framework of Fermi liquid theory. A dirty metal is described as one in which the scattering mechanisms of the conduction electrons by static local impurities are strong, but not sufficient to localize the electronic eigenstates. In the Fermi liquid theory, no anomaly in the behaviour of the DOS is expected. Al'tshuler and Aronov[67], using diagrammatic techniques, have shown that the effects of electron-electron interactions in dirty metals give rise to a dip (sometimes referred to as a pseudogap) in the single-electron DOS at the Fermi energy. This dip deepens as the M-I transition is approached from the metallic side, and is expected to become a true gap right at the transition, with $N_o(E_F) = 0$. Near the Fermi energy, the DOS can be written as

$$N(E) = N_o(E_F) + A|E - E_F|^{1/2} \quad , \tag{2.10}$$

where $N_o(E_F)$ is the DOS calculated in the absence of electron-electron interactions at

the Fermi energy, and $A$ is a constant greater than zero. The work of Al'tshuler and Aronov only describes systems well in the metallic regime but does not treat the problem of transport and other transport-related activities right at the transition.

In the case of the barely metallic phase, Thomas *et al.*[68] have shown that the temperature-dependent conductivity can be expressed in the form,

$$\sigma(T) = \sigma(0) + CT^{1/2} \ , \tag{2.11}$$

where $\sigma(0)$ is the extrapolated conductivity to zero temperature and $C$ is a constant which depends on the carrier concentration of the system in particular, and can have either sign. The constant $C$ is elusive to pin down and it is difficult to understand its physical meaning. It has acquired different formulations over the years, and Al'tshuler and Aronov[69] give the form

$$C = \frac{\gamma\, e^2}{4\pi^2\hbar}\left(\frac{k}{D\hbar}\right)^{1/2}\left[\frac{4}{3}+\frac{16}{F}\left(1-\frac{3F}{4}-\left(1-\frac{F}{2}\right)^{3/2}\right)\right] \ . \tag{2.12}$$

Here, $\gamma$ is a constant of order unity, $D$ is the diffusion constant and $F$ is the Hartree screening factor. The details about the derivation of Eq. (2.12), which are not very important in this thesis, can be found in refs. [70, 71].

There is an additional term that may be included in Eq. (2.11). This term is $ST^{p/2}$, and it is referred to as the inelastic term. The exponent $p$ takes on various values, depending on which of the scattering mechanisms listed below are dominant. In the case of electron-phonon scattering, which is expected at higher temperatures, $p \geq 3$. In the regime where e-e interaction is dominant in doped semiconductors, $p = 2$, predicted from the Fermi liquid theory. In our boron-ion implanted diamond system, the strength of e-e interactions becomes more evident below 100 K. In other doped semiconductors, such as silicon, e-e interaction is stronger at temperatures below 4 K. In the presence of disorder,

$p = 3/2$[72], while at the M-I transition, $p = 1$[73].

We decided to ignore the term $ZT^{p/2}$ since we could not measure conductivity of our doped diamond specimens down into the milli-kelvin regime. Effects associated with $ZT^{p/2}$ are known to be important at temperatures below 1.5 K.

## 2.7 The derivative method

The derivative method has proved to be a very sensitive tool for probing transport properties in disordered systems[35]. Below I give a general overview of the derivative method. Further reading on this theory can be found in Rosenbaum *et al.* papers[28, 29, 30] and references therein.

I have, for convenience, combined expressions for the electrical conductivity at low temperatures into the form represented by Eq. (2.13):

$$\sigma(T) = A\left(\sigma(0) + CT^Z \exp\left[-\left(\frac{T_o}{T}\right)^m\right]\right) \quad . \tag{2.13}$$

According to Hill[74] and Jonscher[75], and Zabrodskii and Zinov'eva[76], a comparison of the experimental data with Eq. (2.13) can be carried out in terms of the local activation energy, $W$, defined as the gradient of an Arrhenius plot of the conductivity. *i.e.*,

$$W = \frac{\partial \ln \sigma}{\partial \ln T} = T\frac{\partial \ln \sigma}{\partial T} \quad . \tag{2.14}$$

Substituting Eq. (2.13) into Eq. (2.14) gives,

$$W(T) = \begin{cases} Z + m\,T_o^m T^{-m} \simeq m\,T_o^m T^{-m} & \text{(strongly insulating)} \\ Z & \text{(weakly insulating)} \\ ZCT^Z/\left(\sigma(0) + CT^Z\right) & \text{(metallic)} \end{cases} \quad . \tag{2.15}$$

From Eq. (2.15), we see that in the case of strongly insulating samples, $W \to \infty$ as $T \to 0$. For weakly insulating materials, $W = Z$ as $T \to 0$, where $Z$ is a positive finite value. For convenience in handling the experimental data of strong insulating samples, Eq. (2.15) is usually transformed into a straight line graph of the form,

$$\log W = -m \log T + \log\left(mT_o^m\right) \quad . \tag{2.16}$$

In the case of metallic samples, we have $W(T) \to 0$ as $T \to 0$, provided the term $\sigma(0)$ is non-zero. By allowing $\sigma(0) = 0$ (according to the scaling theory of localization[11]), we get $W = Z$. This means that $W$ is independent of the temperature of the sample at the transition. $\sigma(0)$ can be obtained by writing the metallic equation (7.1) as

$$\sigma(0) = CT^Z\left(\frac{Z}{W} - 1\right) \quad , \tag{2.17}$$

where constants $Z$ and $B$, from Eq. (2.15), were obtained from a straight line graph of the form

$$\log\left(W(T)\,\sigma(T)\right) = Z \log T + \log\left(Z\,C\right) \quad . \tag{2.18}$$

The $\sigma(0)$ values can therefore be extracted from the experimental data without having to extrapolate the conductivity results to zero temperature.

## 2.8 Mott-Hubbard transition

Mott has shown that effects of e-e correlation in a narrow band semiconductor can induce an M-I transition. This type of transition has come to be known as a Mott-Hubbard transition[77] (or simply Mott transition). Mott has envisaged the problem from a particular point of view of screening. When the screening of the impurity potential by electrons is sufficiently large to prevent the formation of bound states, electrons will delocalize, otherwise Coulomb repulsion will localize them on their atomic sites. Mott based his hypothesis on a simple hydrogenic model[8, 78]. Using the Thomas-Fermi model, he argued that the transition from localized to delocalized electronic impurity states will take place when the Thomas-Fermi screening length $\lambda$ equals the effective impurity centre Bohr radius, $a_H^*$. The Thomas-Fermi screening length is given by

$$\frac{1}{\lambda^2} = \frac{4\pi e^2}{\epsilon}\frac{dn}{dE_F} \quad , \tag{2.19}$$

and $a_H^*$ is given by

$$a_H^* = \frac{\hbar^2 \epsilon}{m^* e^2} \quad . \tag{2.20}$$

Setting $\lambda = a_H^*$, and using the free electron density of states( $dn/dE_F = 3n/2E_F$) [8], we obtain, for systems which undergo the M-I transition,

$$n^{\frac{1}{3}} a_H^* \simeq 0.26 \quad . \tag{2.21}$$

This result is known as the Mott criterion. The famous Edwards and Sienko [79] plot shows the observed $n^{1/3}$ *vs.* $a_H^*$ for a wide range of systems which undergo M-I transitions, with the critical electron density varying over eight orders of magnitude. Further work, as well as the Edwards-Sienko plot, is presented in chapter 8.

A more rigorous picture on the study of the M-I transition driven by e-e interactions has been presented by Hubbard[77, 80]. Hubbard introduced a Hamiltonian for a system of electrons that interact in a particular way. He considered a situation where two electrons can interact only when they occupy the same site (intra-site interaction), and ignored the long-range electron interactions (inter-site interactions). Using the tight-binding approximation, Hubbard suggested a Hamiltonian that can be expressed in the form

$$\varkappa = -t \sum c_{is}^{+} c_{i's} + U \sum n_{i\uparrow}^{+} n_{i\downarrow} \quad , \tag{2.22}$$

where $c_{is}^{+}$ ($c_{i's}$) are the creation (annihilation) operators which create (annihilate) an electron of spin $s$ ( $=\uparrow, \downarrow$) on a site $i$, and $n_{is}^{+} = c_{is}^{+} c_{is}$ is an electron number operator which counts the number of electrons of spin $s$ on site $i$. The second term in Eq. (2.22) is the on-site Coulomb repulsion between two electrons occupying the same site. On the insulating side of the transition, an energy gap opens up in the DOS at the Fermi level. This gap, of width $(U-B)$, separates the lower band from the upper Hubbard band. In an uncompensated semiconductor at zero temperature, the states in the lower band are all filled with one electron per site and the upper band is empty. When the lattice constant is reduced or the electron concentration is increased, the bands broaden and eventually merge. An M-I transition will occur when the bandwidth $B$ for the non-interacting electrons becomes equal to the intra-site repulsion energy $U$. A Mott-Hubbard transition is shown in Fig. 2-3.

Both the Mott and the Hubbard treatments of the M-I transition completely ignore the effects due to disorder and the magnetic behaviour of the system. In these models, a regular array of donor sites is assumed. In real systems, there is always an element of disorder which is evident in doped systems in which the dopants are randomly incorporated into the system.

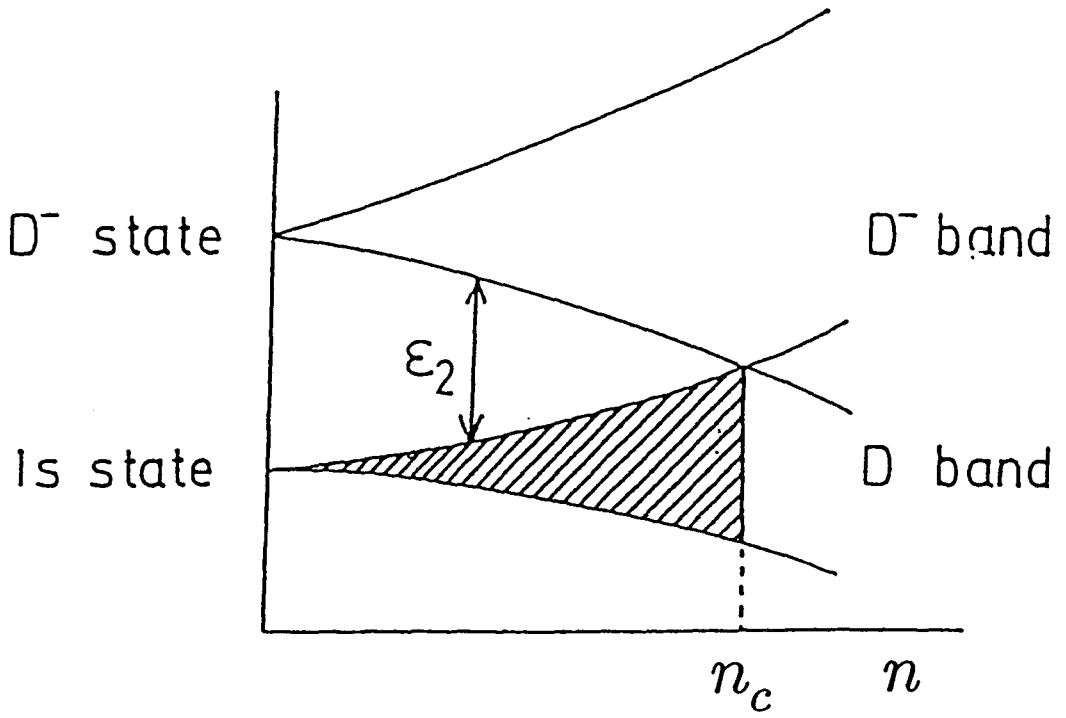


Figure 2-3: A schematic diagram showing the Mott-Hubbard transition brought about by electron-electron interactions. The model used by Mott and Hubbard ignores the effect due to disorder and the magnetic behaviour of the system. The splitting of the top band ($D^{-1}$ band) into lower and upper Hubbard bands is due to Coulomb repulsion by intrasite electrons. At $T = 0$ K, the bottom band ($D$ band) is completely filled with one electron per site, while the upper band is empty. The energy that separates the top band from the lower band is the difference between the Coulomb repulsion energy $U$ and the bandwidth energy $B$, i.e., $\varepsilon_2 = U - B$. A metal-insulator transition will occur when $U = B$. This situation occurs when the interatomic spacing is systematically reduced to allow electron wavefunctions to overlap more strongly.

## 2.9 Scaling theory of localization

Early theoretical formulations of the scaling theory were presented by Thouless[81] and Wegner[82]. Their work culminated in the 1979 paper of Abrahams *et al.*[11] which has had great impact on this field and increased our understanding of the physics of M-I transitions.

The scaling theory has made some interesting and very intriguing predictions. For example, a thin long wire and a thin film are effectively 1- and 2- dimensional systems, respectively, and their eigenstates are always localized in space irrespective of the amount of disorder one introduces to these systems. These systems should be insulating at sufficiently low temperatures. Many experiments have been carried out in trying to observe these effects[83, 84].

In 3-dimensional systems, in which we are interested, the scaling theory predicts a continuous M-I transition. The theory further suggests that the electrical properties of a macroscopic system can be understood, based on information extracted from microscopic properties of this system. We study this situation below.

Abrahams *et al.*[11] using the Kubo-Greenwood formulation, showed that the conductance of a system with a linear size $L$ depends on perturbations to the boundary conditions in the following way:

$$g(L) = \frac{e^2}{2\hbar} \frac{\Delta E(L)}{dE(L)/dN} \quad , \tag{2.23}$$

where $dE/dN$ is the mean spacing of the electron energy levels. The system for which Abrahams *et al.* [11] derived this result is a hypercube of size $L^d$. ($d$ is for dimensions.) $\Delta E$ represents the geometric mean of the fluctuation in energy eigenvalues which is produced when the boundary conditions are changed from periodic to antiperiodic on oppo-

site edges of a square. Thouless[81] had previously derived a dimensionless conductance of the system as

$$g(L) = \frac{e^2}{2\hbar}\left(\frac{W(L)}{B(L)}\right)^{-1} \quad , \tag{2.24}$$

where the ratio $W(L)/B(L)$ may be taken as the localization criterion. The reader may recall that, in the Anderson localization problem, $W/B$ was the main factor which described the localization transition. Thus, a direct connection can be made between the Anderson localization and the scaling theory. We now define the scaling function, in a differential form, as

$$\beta(g(L)) = \frac{d\ln g(L)}{d\ln L} \quad , \tag{2.25}$$

where $\beta$ depends only on $g$. Hence, this theory is referred to as a one-parameter scaling theory. We consider situations in the asymptotic limits, $g \to \infty$ and $g \to 0$. In the limit $g \to \infty$, the system obeys Ohm's law, where $g(L)$ is expressed as $g(L) \sim L^{d-2}$. Taking the limit on $\beta(g)$ gives $\lim \beta(g \to \infty) \sim d-2$. As $g \to 0$, all states are exponentially localized, and $g(L)$ can be given as $g(L) \sim \exp(-\lambda L)$. In this limit, $\beta(g(L) \to 0) \sim \ln g$. Fig. 2-4 shows the expected behaviour of $\beta(g(L))$ as a function of $\ln g$. $\beta(g) = 0$ defines the critical conductance, $g = g_c$. This means that any sample with the critical conductance will have the same conductance for any value of length $L$. That is, $g(nL) = g(L)$, where $n$ is a positive integer. For $g < g_c$, the conductance scales to zero at macroscopic length scale, while, for $g > g_c$, the conductance scales to a large value[70]. $g_c$ is a fixed point which locates the mobility edge (*i.e.*, energy separating the extended states from the localized states) of the system. No minimum metallic conductivity is predicted by the scaling theory. The minimum metallic conductivity is discussed later in the chapter. The transformation of $g$ to $n$ (sample concentration) is valid as long as the relation between the two is smooth and monotonic. The end result, in which we are interested, is given by Eq. (2.28) in section 2.10.

## 2.10 Critical conductivity exponent

A great deal of experimental and theoretical work has been carried out over many years to determine the critical conductivity exponent $\mu$[16, 17, 18, 85, 86, 87, 88, 89, 90]. In spite of these years of intense effort, the critical behaviour of the electrical conductivity $\sigma(0)$ in the vicinity of the M-I transition remains unresolved[91, 92]. Most of the theoretical work done to date estimates $\mu$ to be unity[93, 94], while some theories predict $\mu = 1/2$[95, 96]. $\mu$ values close to unity have been found experimentally in most amorphous M-I alloys, such as Ge:As[97] and Si:Nb[98], crystalline compensated semiconductors such as Ge:Sb[99] and Si:(P,B)[19, 100], and in certain semiconductor systems when measured in the presence of a magnetic field[87, 101]. Values of $\mu$ close to 1/2 have been found in all uncompensated silicon-based semiconductors[88, 102, 103, 104] and in some neutron-transmutation doped systems[65, 105].

The classification of disordered systems by their conductivity exponent $\mu \approx 1/2$ and $\mu \approx 1$ without a clear physical distinction constitutes what is known as an "exponent puzzle". In other words, systems are assigned to universality classes based on their estimated conductivity exponents, and not on the behaviour of $\sigma(0)$ in the critical regime. In our case, we have determined $\mu \approx 1.7$, which lies outside the two universal classes. It has been suggested that systems which exhibit $\mu \approx 2$ may have percolation characteristics[107]. There is still an on-going debate on the methodology leading to the determination of $\mu$. Some of the main concerns are the following:

(i) the extrapolation to zero temperature of the measured temperature-dependent conductivity,

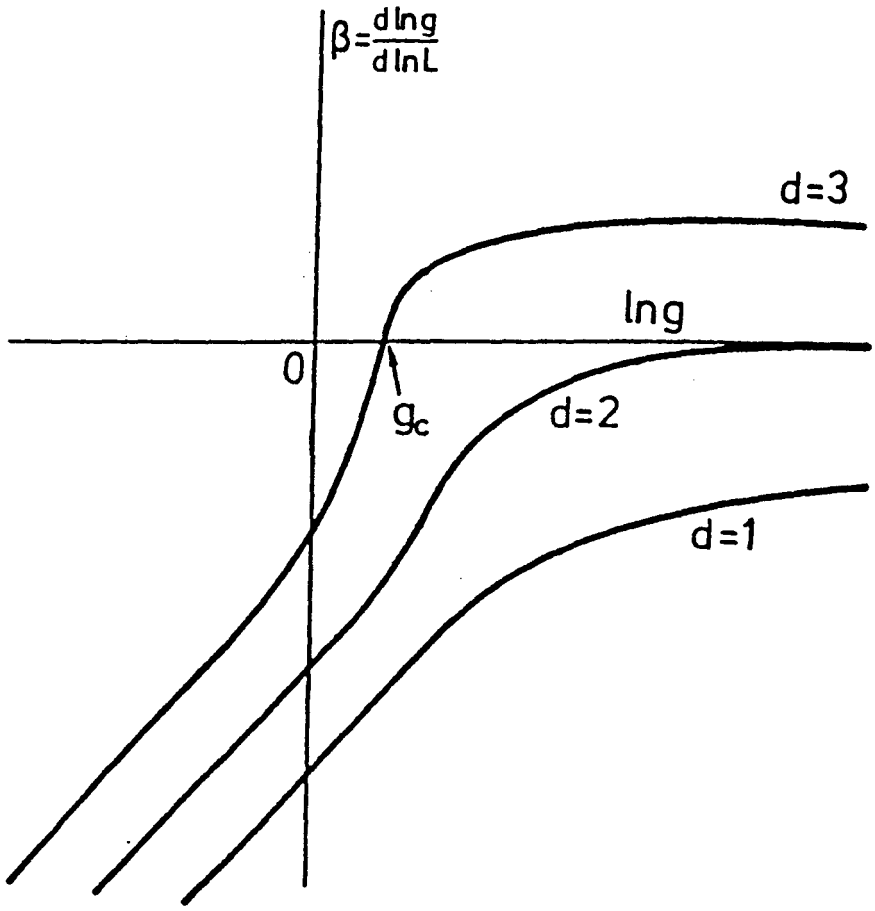


Figure 2-4: Predictions of a one-parameter scaling theory of localization are depicted in this figure, where we have plotted the scaling function $\beta(g)$ as a function of ln $(g(L))$. All states are localized in 1-dimensional and 2-dimensional systems for any amount of disorder. $g_c$ defines the critical conductance for a 3-dimensional system.

Figure 2-4: Predictions of a one-parameter scaling theory of localization are depicted in this figure, where we have plotted the scaling function $\beta(g)$ as a function of ln $(g(L))$. All states are localized in 1-dimensional and 2-dimensional systems for any amount of disorder. $g_c$ defines the critical conductance for a 3-dimensional system.

(ii) the determination of $n_c$, in the doped systems,

(iii) the determination of the actual dopant concentration in these samples,

(iv) possible sample inhomogeneity, and

(v) the range of the experimental data used to determine $n_c$.

The method presented below suggests ways of circumventing some of the problems listed above.

## 2.11 Shlimak method

Near the M-I transition, Maliepaard *et al.*[108] have shown theoretically that $\sigma(T)$ should obey the form,

$$\sigma(T) = \sigma(0) + CT^{1/3} \quad . \tag{2.26}$$

At the transition, $\sigma(0)$ is zero[67]. The applicability of the $\sigma(T) \propto CT^{1/3}$ law has been demonstrated recently by Shlimak *et al.*[16] on two sets of Ge:As and Ge:Sb samples. A new approach to analyze the conductivity measurements has been suggested in ref.[16], in which $\mu$ and $n_c$ of the M-I transition can be determined without extrapolating the temperature-dependent electrical conductivity results to zero temperature. The principal point of this method is to replace $\sigma(0)$ with $\Delta\sigma(T^*) = \sigma_n(T^*) - \sigma_{n_c}(T^*)$, calculated at any temperature $T^*$ at which the conductivity obeys the general approximation, $\sigma(T) = a + CT^p$ ($p = 1/2$ or $p = 1/3$). It follows therefore that

$$\Delta\sigma(T^*) = \begin{cases} (\sigma_2(0) + CT^{*1/3}) - (\sigma(0) + CT^{*1/3}) \\ \sigma_2(0) - \sigma(0) \\ \sigma_2(0) \quad , \text{ since } \sigma(0) = 0 \text{ at the M-I transition.} \end{cases} \tag{2.27}$$

According to the scaling theory of localization[11], $\sigma(0)$, when plotted against the impu-

rity concentration $n$, is equal to zero on the insulating side of the M-I transition, and is finite for $n > n_c$. In the vicinity of the M-I transition, $\sigma(0)$ is governed by the relation

$$\sigma(0) = \sigma_o \left( \frac{n}{n_c} - 1 \right)^{\mu} \quad . \tag{2.28}$$

We can also write Eq. (2.28), following Eq. (2.27), as

$$\Delta\sigma(T^*) = \sigma_o \left( \frac{n}{n_c} - 1 \right)^{\mu} \quad . \tag{2.29}$$

Eq. (2.29) can be transformed into a straight line form by taking logs on both sides to give

$$\log \left( \frac{\Delta\sigma(T^*)}{\sigma_o} \right) = \mu \log \left( \frac{n}{n_c} - 1 \right) \quad , \tag{2.30}$$

where $\mu$ is determined from the slope of a straight line graph using a least squares fitting procedure.

In order to characterize the M-I transition, Shlimak *et al.* introduced a dimensionless parameter, $\alpha$, given by

$$\alpha = \frac{R(T_1)}{R(T_2)} \left( \frac{T_1}{T_2} \right)^{1/3} = \begin{cases} > 1 & \text{(metallic conductivity} \\ 1 & \text{(metal-insulator transition)} \\ < 1 & \text{(insulating)} \quad , \end{cases} \tag{2.31}$$

where temperatures $R(T_1)$ and $R(T_2)$ are resistances of a given sample measured at any two temperatures in a regime where the power law, $\sigma(T) = a + CT^{1/3}$, is observed. Results obtained using the method of Shlimak *et al.* are reported in chapter 8.

## 2.12 Minimum metallic conductivity

IR[10] have observed that no ordinary (macroscopic) metallic conduction will take place when the electron mean free path $l$ is shorter than the distance between the impurity centres $a$. According to the IR criterion, there should be a lower limit in the Boltzmann conductivity, and this limit is reached when $l = a$. At this point, the conductivity takes the form:

$$\sigma(0) \equiv \sigma_{IR} \sim \frac{e^2}{3\hbar l} = \frac{8 \times 10^{-5}\Omega^{-1}}{l} \quad . \tag{2.32}$$

The idea of a lower conductivity limit was formalized into the concept of a minimum metallic conductivity $\sigma_{\min}$ by Mott in 1972 [109]. In a series of papers, Mott argued that as the M-I transition was approached from above (metallic side), $\sigma(0)$ decreased with $l$ until $l = a$, and then the system became insulating, with an abrupt drop in $\sigma(0)$ from a minimum value $\sigma_{\min}$ to zero. $\sigma_{\min}$ can be expressed in a general form:

$$\sigma_{\min} = C_1 \frac{e^2}{\hbar a} = \frac{C_1}{l}\left(2.4 \times 10^{-4}\right) \quad \Omega^{-1} \quad , \tag{2.33}$$

where $C_1$ is a numerical constant in the range 0.025 to 0.1. $\sigma_{\min}$ is always smaller than $\sigma_{IR}$ due to the reduction in the density of states at the Fermi energy by electron correlations[8]. Theoretical arguments, based on experimental results of Rosenbaum *et al.*[27], have been presented by Möbius's group in support of $\sigma_{\min}$[13]. Most experiments on standard doped semiconductors, carried out by leading researchers in the field, have, however, failed to observe $\sigma_{\min}$ of the predicted magnitude but have measured conductivities far below $\sigma_{\min}$[110] and their results are consistent with the scaling theory, proposed by Abrahams *et al.*[11], which predicts a continuous M-I transition as $T \rightarrow 0$ K.

For completeness and for reference purposes, I have added an outline of the weak localization theory in this chapter.

## 2.13 Weak localization theory

The weak localization theory does not necessarily address the question of localization, but computes corrections to the Boltzmann conductivity due to a special set of elastic scattering events known as coherent backscattering. The term "weak localization" is somewhat a misnomer and may be misleading. The theory obtains results from the weak scattering regime, where the product of the Fermi wavevector and the elastic mean free path is far greater than unity, *i.e.* $k_F l \gg 1$. Such a situation can only occur deep in the metallic phase, far away from the transition in 3-dimensions. All states are computed to be localized in a 1-dimensional system and a 2-dimensional system. The theory acquired its name from the latter context.

The basic ideas behind this theory were presented by Langer[111] and Neal[112] in the 1960s, using Feynmann's diagrammatic techniques. Bergmann[113] has translated these diagrammatic perturbation calculations into a very lucid physical picture. I present a brief description of the central ideas of Bergmann below.

Consider an electron moving from point A to point B, as shown in Fig. 2-5. A Feynmann diagram can be constructed with many possible scattering paths, depending on the scattering that occurs, and each path has an associated amplitude. Ignoring the interference effects due to multiple scattering, these accumulated amplitudes can be summed and squared individually to give the total electron transmission probability from A to B. Closed loops may occur, such as at point Z, shown in Fig. 2-5. In closed loops only elastic collisions occur. In this case, phase coherence can be maintained around the loop. This effect is called coherent backscattering. The loop provides two alternative

(complementary) paths, clockwise and anti clockwise, and these paths are time-reversal pairs. Let the amplitudes of these transmission paths be $s_1$ and $s_2$. Then the probability of an electron to return to its starting position is given by

$$P = \sum_{i=1}^{2} |s_i^2| = |s_1|^2 + |s_2|^2 + |s_1 s_2| + |s_2 s_1| \quad . \tag{2.34}$$

There are three possibilities from Eq. (2.34). When the paths are in phase at Z with $s_1 = s_2$, we have

$$P = 4\,|s_1|^2 \quad . \tag{2.35}$$

In the case of phase incoherence, $|s_1 s_2| = |s_2 s_1| = 0$, and we get

$$P = 2\,|s_1|^2 \quad . \tag{2.36}$$

When the paths are out of phase at Z, $s_1$ = -$s_2$ and $s_2$ = -$s_1$, and we obtain

$$P = |s_1|^2 + |s_2|^2 - |s_1|^2 - |s_2|^2 = 0 \quad . \tag{2.37}$$

The higher the probability of an electron being in the closed loop, the less likely it will conduct current leading to an overall reduction in conductivity. This effect is called weak localization. This phenomenon can easily be destroyed by the application of a magnetic field which destroys time reversal symmetry[113, 70], by an increase in temperature (inelastic collisions are known to destroy weak localization at finite temperatures), etc.[114]. If $T^{1/2}$ is the temperature dependence of the inelastic scattering process, then at high temperature it will dominate the total scattering. A complete description of the theory can be found in the review articles by Lee and Ramakrishnan [70] and Al'tshuler and Aronov[115].

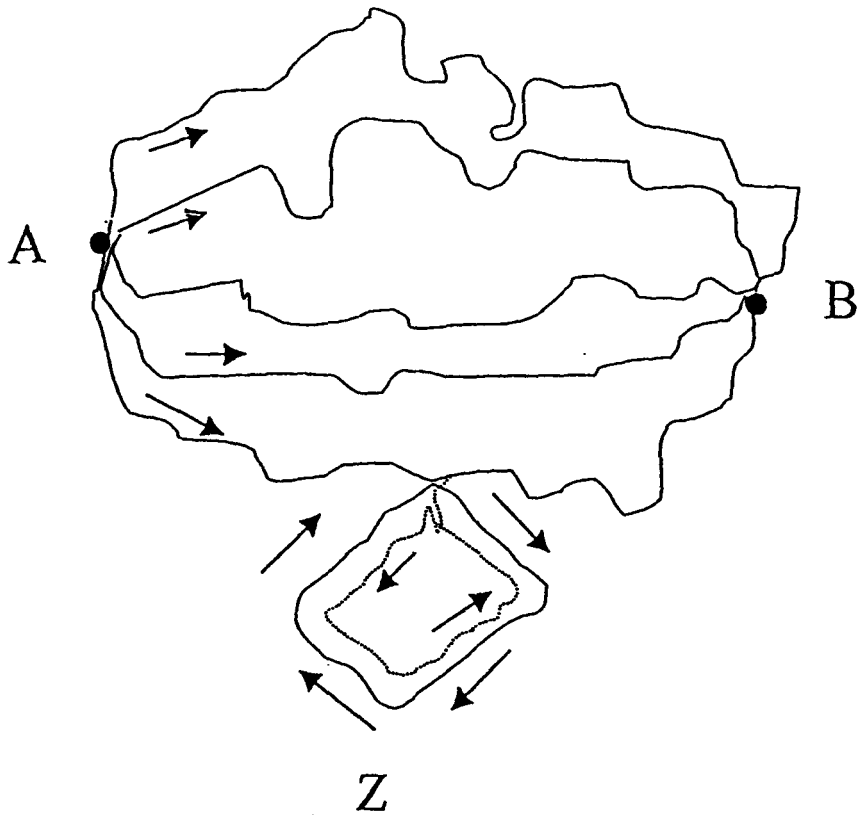


Figure 2-5: The diagram shows a succession of electron scattering events as the electron moves from point A to point B. An electron can be scattered around a closed loop, as shown at point Z. In this case, phase coherence can be maintained around the loop, resulting in a reduction in the total conductivity of the system, hence the phenomenon of weak localization. The dashed lines show the complimentary (either clockwise or anti-clockwise) paths. These paths are referred to as the time-reversal paths. The weak localization phenomenon can be destroyed when the temperature of the system is increased or a magnetic field is applied to the system.

# Chapter 3

# Ion implantation

## 3.1 Introduction

Ion implantation is a process by which a flux of energetic atomic particles is introduced by bombardment into the near surface region of any solid material. It is a process which allows one to insert almost any impurity ion into any desirable target material regardless of the phase diagram, solubility and thermodynamic metastability of the target. It is a technique which permits the near surface properties, electrical, chemical and structural, of any material to be modified as desired.

Since ion implantation is a high-energy process, with dopant atoms accelerated at energies far exceeding the typical binding and displacement energies of atoms in the target material, it is usually accompanied by severe radiation damage to the target. It is the control or engineering of this radiation damage in producing well-characterized implanted materials which is of interest in obtaining sample materials used in the present experiments.

Doping of diamond by means of ion implantation has been attempted since the early 1960's but with limited success[116] until fairly recently [5]. The introduction and the annealing of the resultant radiation damage, as well as the concomitant modifications caused by these processes, is now fairly well understood, but, presently, only substitutional boron-ion doped layers can be selectively and reproducibly generated in single-crystal diamond surfaces. Some attempts at implanting other species into diamond have been undertaken[117]. Progress in this field has recently been reviewed by several authors[5, 118].

In this chapter, the general processes which accompany the slowing down of ions as they enter the target material are reviewed. The annealing and the possible graphitization of the implanted surface layers during the high-temperature annealing are described. The lattice expansion due to high ion implantation into diamond is briefly discussed. The reaction-rate theory of point-defect interactions in diamond during the annealing stage is outlined. I discuss the energy-loss simulation program Transport of Ions in Matter (TRIM) applied to the implantation processes of interest, and the Secondary-Ion Mass Spectroscopy (SIMS) profiles performed on boron-ion implanted diamond specimens.

## 3.2 General background

### 3.2.1 Stopping processes of ions in a solid

When an implanted ion enters into a substrate, it gradually transfers its kinetic energy to the host atoms through two main scattering events: electronic and nuclear scatterings. The first scattering mechanism, which is predominant at the beginning of the ion's path through the substrate, is known as 'electronic stopping'. Here the kinetic energy of the moving ion is lost through the excitation and ionization of the electrons of the substrate

atoms. It is, therefore, an inelastic scattering process. By this approach, the electrons in a solid can be viewed as a free electron gas which is affected by a traversing positive ion of the projectile. The inhomogeneity in the electron plasma introduced by the projectile ion induces a retardation force on the ion, and hence a loss in the projectile energy.

As the ion penetrates deeper into the substrate, it encounters more violent scattering collisions with the host atoms, displacing some of them from their lattice sites. Towards the end of the ion range in the substrate, the remainder of the kinetic energy is lost through ballistic displacement collisions with atoms. This is the nuclear stopping process.

Despite having the same incident energy when entering the substrate, ions have different random impact parameters with the surface atoms. This results in a different number of collisions and path lengths for each ion before coming to rest. Since the slowing down of ions is a statistical process, the ion distribution in the host should be expressed using statistical variables. The distribution of the implants in the host can be approximated by a (symmetric) Gaussian curve[119]. The density of the implanted species as a function of the distance $x$ (measured along the beam direction) is given by

$$n(x) = n_p \exp\left[-\frac{1}{2}\frac{(x - R_p)^2}{\Delta R_p^2}\right] \quad , \tag{3.1}$$

where $n_p$ is the peak ion density at $R_p$. The parameter, $R_p$, is the projectile range which gives the mean penetration depth of the ion relative to the surface, while $\Delta R_p$ is the standard deviation in the projectile range (also referred to as the ion range straggling). This Gaussian approximation paints a simple physical picture of the implant profile. It ignores the substrate temperature, which is particularly important when interstitial diffusion and higher order effects occur. The theoretical details can be found in an article by Prins[119].

When the imparted kinetic energy from the incident ion to the substrate is greater

than the displacement energy, a Frenkel defect (a closely separated vacancy and interstitial) is formed. The displacement energy of diamond has been estimated by a number of authors. Prins[120] has used a value of 55 eV in his work, but the present consensus favours a value of $\simeq$ 35 eV[121]. If the interstitial and the vacancy that are created do not recombine spontaneously, and the interstitial still possesses some kinetic energy greater than the displacement energy after collision, it will move away from the vacancy and continue to collide with stationary target atoms, whereupon more Frenkel pairs may be created. In addition to this process, the recoiling interstitial may transfer its kinetic energy along a close-packed row of atoms in a sequence of replacement collisions. The resultant interstitial from this replacement collision will be located far away from the original vacancy, preventing any interstitial-vacancy (Frenkel pair) recombination. Also, secondary cascade collisions occur when the substrate atoms absorb energies far greater than the displacement energy, and thus in turn continue to knock off other atoms from their lattice positions, creating more vacancies and interstitials.

When the implanted ion reaches its final range in the host, it dissipates all its remaining energy to the surrounding substrate atoms. This results in an isolated (localized) region of high vacancy density (depleted zone). As the fluence is further increased, these damaged isolated regions may overlap and coalesce to form new vacancy-related phases. Unless controlled, the agglomeration of the vacancy defects could lower the material density, and eventually produce surface graphitization.

The reason why more vacancies are created when the ion reaches its final projectile energy range has to do with elastic momentum transfer of the incident ion to the substrate atoms. As the momentum of the implanted ion continues to decrease, its cross section for elastic scattering off the host atoms increases. The slower the ion traversing thorough the substrate, the longer is the period of time over which momentum transfer to another ion occurs. Slower ions are more capable of displacing the substrate atoms from their

lattice positions by ballistic collisions than faster moving ions, which require a more direct "head on" collision to effect the same displacement. When the energy of the incident ion drops below the displacement energy, no more vacancies are created. The ion eventually comes to rest in a depletion zone, either in an interstitial or substitutional site. The model described above is captured in Fig. 3-1. It does not, however, present a stable picture. It is only applicable at temperatures below which the points defects are immobile. When the substrate temperature is high enough for interstitials to diffuse, more Frenkel pairs are annihilated thus reducing the lattice damage. At these elevated temperatures, some of the interstitials can escape from the damaged layer, while the residual vacancies remaining behind may agglomerate into more complex defect structures[122].

Owing to the fact that diamond is a metastable form of carbon, there exists a critical threshold determining how much damage an implanted layer can suffer before an irreversible structural change (graphitization) occurs. The critical dose at which graphitization can be initiated depends on a number of factors, most of which are discussed in a fairly recent book by Dresselhaus and Kalish[5]. Some of these factors are:

- The target ions used for implantation - massive ions generally lead to more damage than lighter ones owing to their larger stopping powers.
- The dose rate (beam current) - slow implantation is characterized by a slow arrival rate of ions at the target surface, and this may allow the system to partially recover from the radiation damage before further implantation-induced damage is produced in the same volume in the target. Fast implantation may cause overlap of the damage cascades, resulting in a different kind of damage profile. The implantation rate is expressed in terms of the beam current density in units of $\mu A/cm^2$. Values in the range of 1-1.6 $\mu A/cm^2$, corresponding to slow implantation, were used in our case. Typical values for fast implantation are in the range of 100 $\mu A/cm^2$ or more.

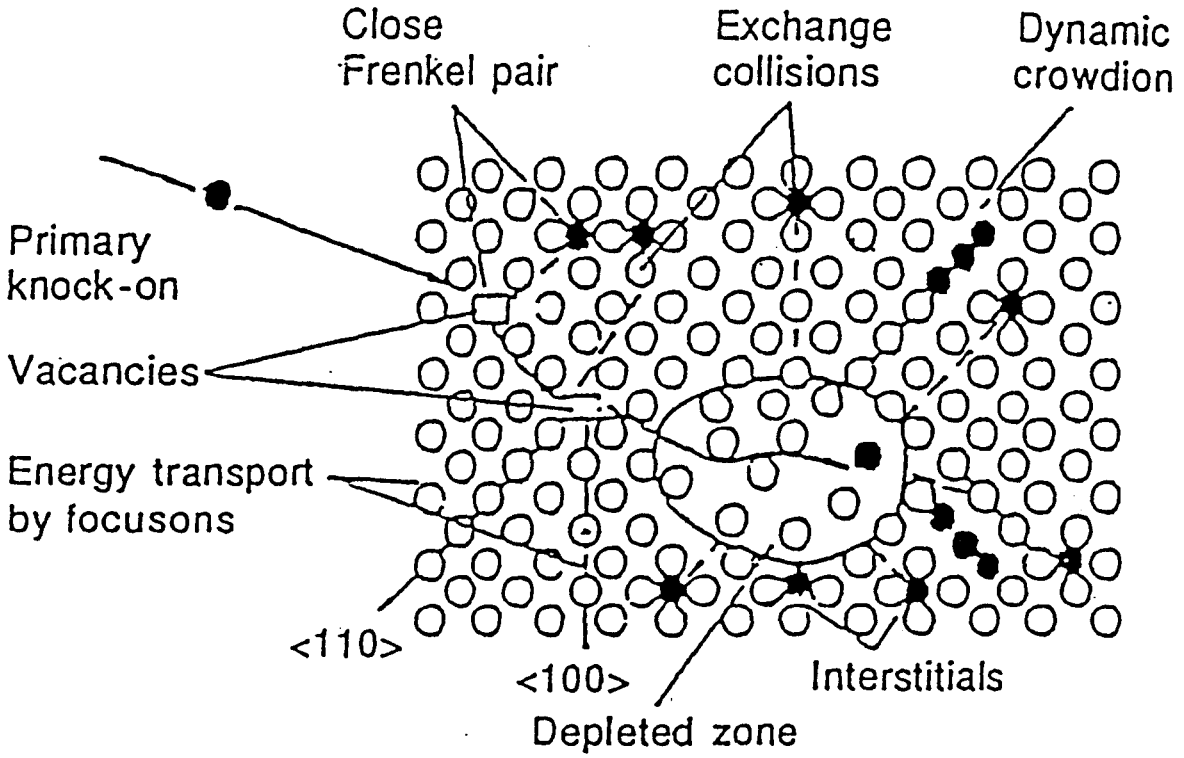


Figure 3-1: A simplified schematic description of the damage cascade introduced during the ion-implantation process. This figure is taken out of ref.[5].

- Orientation of the target material to the beam of implanted ions - different levels of radiation damage are generated when a target is oriented in a random direction than when the implanted ions channel through the substrate materials.

- Ion dose - whether ions are implanted into a target material in a single step or distributed in multiple steps.

- Implantation temperature - different types of damage are created when the target temperature is varied. Increasing the implantation temperature substantially increases the mobility rate of both the implants and the created defects, and thus increases the probability of interstitial-vacancy recombinations. The damage profile will spread out when the substrate is implanted at elevated temperatures, while implantation at a low temperature is desirable for maintaining a sharp impurity distribution profile.

- Type of annealing used - the type of point defects that are formed and their density depend on the annealing cycle employed. The duration of anneal does not appear to alter the electronic properties of the diamond specimens in a very significant way.

The last two factors, *i.e.* the implantation temperature and the annealing cycles used, are important in this thesis and are further described below. Chapter 6 is devoted to the results obtained using various annealing routines employed in this work. The first four factors mentioned above are described in the experimental chapter (chapter 4).

## 3.3 Implantation temperature

### 3.3.1 Cold-implantation followed by rapid-temperature annealing cycle

The most successful scheme for reliable doping of diamond samples involves cold implantation followed by rapid thermal annealing. The basic idea behind the CIRA technique is that the diamond substrate is implanted while held at liquid nitrogen temperature to impede the diffusion of the point defects, followed by rapid annealing to high-temperatures to allow the diffusion of both vacancies and interstitials. This encourages interstitial-vacancy recombination and dopant atom-vacancy combination in the damaged layer, thus minimizing the radiation damage[123, 124].

I wish to make the reader aware of some inherent complications associated with the CIRA routine. I have broken these 'complications' into small sub-topics below to highlight their importance or influence on the CIRA scheme.

### 3.3.2 Selection of the ion energies and doses

The ion-implantation energies and the doses that one selects to implant into the diamond substrate should be kept low enough so as not to exceed the amorphization threshold. As mentioned in section 3.2, ion-implantation by more massive ions than the target atoms can give rise to huge radiation damage and this may lead to immediate amorphization (or graphitization) of the implanted layer during annealing. Less massive ions or ions with masses close to that of the target atoms yield reproducible results provided certain procedures are used[125]. The implantation energies and the doses must be spread evenly to intermix the point-defects and to ensure their proximity within the ion-implantation

damaged layer. This is to increase the probability of the point-defects interacting with each other during the annealing stage. Failure to follow a multi-step small dose implantation sequence can lead to results not being reproducible.

### 3.3.3 Activation of dopant-interstitials

Studies reveal that some boron interstitials, which do not become activated, diffuse out of the implanted layer during the high-temperature annealing, leaving behind an excess of vacancies[118]. A large concentration of vacancy-defects are known to lower the material density and this can lead to the amorphization or graphitization of implanted surface layers in diamond. In order to avoid this process from taking place, one needs to optimize the implantation-annealing parameters. The manipulation, or choice, of the implantation-annealing parameters leading to the distribution of the dopant atoms in the surface layer are crucial in this study, and have been examined.

### 3.3.4 Behaviour of self-interstitials in the damaged layers

Carbon self-interstitials and boron-interstitials do not behave in the same manner during the annealing processes. Recent studies show that self-interstitial-vacancy recombinations increase with increasing annealing temperature, while boron-interstitial-vacancy combinations decrease as most of the boron diffuse away from the implanted layer[126, 127]. This behaviour of can be modelled in terms of two activation energies for each interstitial type: an energy for activation (interstitial-vacancy recombination) and an energy for self-interstitial diffusion[120]. A two-stage high-temperature annealing process, following the cold-implantation, has been the route to follow in an effort to encourage boron-interstitial-vacancy combinations.

### 3.3.5 Behaviour of vacancies in ion-implanted layers

Vacancies prefer to interact with each other to form more complex structures rather than to combine with other point-defects[118]. The presence of these complex defect structures in the damage cascade is a serious drawback in our efforts to effectively remove the radiation damage introduced during ion-implantation. Moreover, these complex-vacancy defect structures are known to be optically and electronically active, and act as deep-lying donors which can compensate the activated boron acceptors. They have been found to lie about 4 eV below the conduction band[6, 7].

### 3.3.6 High-temperature implantation

This section has been included for completeness as no attempt has been made to implant our diamond specimens at elevated temperatures. All our implants have been carried out at liquid nitrogen temperature.

To avoid any permanent damage (apart from the formation of extended defects which are very difficult to remove) such as surface graphitization and to greatly reduce the levels of radiation damage in the implanted layer, most workers have chosen to implant their diamond specimens at temperatures above 570 K[128, 129, 130]. Such an approach has been based on the knowledge that the closely separated carbon self-interstitials and vacancies which occur in the implantation process induce damage cascades, but will readily recombine if given sufficient thermal excitation. This reduces the need to carry out post-implantation annealing. If dopant interstitials are introduced in a vacancy rich region during the high-temperature implantation, their activation probability will be enhanced accordingly. It should be pointed out that such an approach has some shortcomings, as was later discovered in a depth-profiling study on the distribution of the carbon ions in diamond by Spitz *et al.*[131]. This study has revealed that the implanted ions are, on average, located deeper than the vacancies in the damaged surface layer. It

follows, therefore, that by the time the implanted ions have diffused into the vacancy-rich regime, the majority of the vacancies would have been annihilated by the carbon self-interstitials, leaving only a few vacancies for dopant activation. Another disadvantage of the high-temperature annealing procedure is that the presence of these extended defect phases degrades the electrical performance of the doped layer[132].

## 3.4 Annealing studies

### 3.4.1 Motivation

The two main purposes of annealing are to reduce the levels of radiation damage inflicted on the diamond surface during the implantation process, and to drive the implants into the desirable lattice sites (usually substitutional sites), where they act as donors or acceptors. Both these processes can be realized when sufficient energy is imparted to the point defects in the damaged region.

Annealing can be classified into two categories: high-temperature anneal and low-temperature anneal. I briefly describe these annealing procedures below.

### 3.4.2 High-temperature anneal ($T \geq 770$ K)

Above 700 K, both the interstitials and vacancies diffuse in the damaged diamond layer. This increases the probability of interstitial-vacancy recombination. Those point defects that do not recombine with each other either diffuse away from the damaged layer or agglomerate to plate out as dislocations and other complex, extended defect phases. Recent studies indicate that the major fraction of the vacancies agglomerate rather than

diffuse out of the implanted layer[118]. These vacancy-related defects have been found to act as deep lying donors and are situated about 4 eV below the conduction band[133]. When annealing vacancies in the implanted layer over the temperature range of 870 to $\sim$ 2000 K, compensating donors with large degeneracy weighting factors $g_D$ form. It is postulated that these vacancies are formed by single vacancies diffusing towards each other and in the process generating regions in which their wavefunctions overlap into extended structures[133]. They occupy positions separated by fewer carbon atoms. These proposed 'vacancy-crystallites', it is argued, have the electronic properties of a single vacancy, but with an apparently large degeneracy factor[120]. In a boron-doped layer, the vacancy defects will partially compensate some of the boron acceptors[134].

### 3.4.3 Low-temperature anneal ($T \leq 770$ K)

Only the interstitials can diffuse in this temperature region while the vacancies are still immobile. Some fraction of the interstitials will annihilate with stationary vacancies, while others will diffuse out of the damaged layer without recombining with vacancies, leaving behind an excess of vacancies. The latter region, which is manifested by the volume expansion of the damaged layer, has been measured by Maby *et al.*[135] and Prins *et al.*[136] in boron-ion doped diamond specimens that were implanted at different temperatures. Maby *et al.*[135] implanted their samples at room temperature, while Prins *et al.* [136] used the CIRA process. The concept of volume expansion is discussed in the next section.

## 3.5 Lattice swelling

I wish to discuss another phenomenon which may not be related to simple graphitiza-

tion of the implanted layers in diamond as discussed above. This phenomenon is known as the lattice swelling, *i.e.* volume expansion as a result of high ion-dose implantation into diamond. The expansion is reflected in the swelling of the implanted region when the difference between the implanted region and the non-implanted region is taken (noticeable as step heights). This swelling has been found to depend on the implantation temperature.

Three factors may be attributed to increases in lattice volume as a result of ion-implantation. These factors are

- the addition of extra atoms, introduced into the lattice by ion implantation,
- the creation of point-defect (interstitials and vacancies) in the collision cascade during implantation, and
- the possible thermodynamic phase transformation from compact diamond into a graphite structure which is less dense than diamond.

Lattice expansion has been observed by various authors in diamond, but different interpretations for its onset have been given. Early observation of the lattice swelling was presented by Maby *et al.*[135] after implanting a diamond specimen with 200 keV B-ions at room temperature. They explained the swelling of the implanted region as due to the creation of an amorphous region, which has graphite density. Maby *et al.*[135] established a critical boron-ion threshold of $5 \times 10^{15}$ cm$^{-2}$ beyond which the onset of irreversible volume expansion occurs. Below this critical threshold, they did not find any measurable volume expansion.

A different approach to the processes that determine the electrical and structural properties of diamond subject to ion implantation has been given by Prins *et al.*[136,

137]. According to Prins *et al.* [136, 137], volume expansion and the high electrical conductivity observed in ion-implanted diamond specimens are due to the difference in the spatial distribution of the point-defects (interstitials and vacancies) created in the damage cascade and the difference in their diffusivities. Since self-interstitials are mobile at $T \sim 330$ K and vacancies start to diffuse at $T \sim 750$ K, Prins *et al.*[136, 137] have observed that a higher degree of lattice swelling will occur in samples which have been implanted at elevated temperatures than at low temperatures ($T < 330$ K). The escape of some self-interstitials from the damaged layer at high-temperatures (330 K$< T < 750$ K), with vacancies still locked in, should exhibit volume expansion. They demonstrated the lattice swelling by implanting a diamond specimen with 170 keV fluorine ions at $T \sim$100 °C, and found that the lattice expansion increased linearly with a fluorine dose up to $4 \times 10^{16}$ cm$^{-2}$. Contrary to claims made by Maby *et al.*[135] on graphite density-induced swelling, Prins *et al.*[136, 137] have presented arguments as to why graphitization is an unlikely process to explain the swelling in heavily implanted diamond.

## 3.6 Energy-loss simulation program: TRIM92

The most commonly used energy loss simulation code for ion-solid interactions is the TRIM program. It was developed by Ziegler *et al.* [138]. The TRIM program incorporates the best known semi-empirical values as well as the statistical nature of interaction of the point-defects in the damaged layer. The program calculates the kinematics of incident ions individually as soon as they collide with the substrate atoms. It then follows the trajectory of recoiling target atoms which undergo further collisions that may initiate new target atoms in motion, thus creating a branch of recoiling target atoms. The program returns and continues to follow the motion of the original implanted ion once all the recoiling atoms have attained energies below a certain cutoff energy. The program repeats the above procedure until the primary ion comes to rest or is no longer

able to displace target atoms from their lattice sites. The program now stores the collision history of the primary ion and all secondary scatterings and proceeds to follow the next implanted ion. Fig. 3-2 shows some of the cold damage profiles generated using TRIM92 computer code. The target here is diamond implanted with boron ions at 130 keV. The displacement energy (this is the minimum energy required to knock a target atom into the target lattice) and the lattice binding energy (this is the energy that binds an atom to the lattice. A recoiling lattice atom loses this energy when it leaves its lattice site and recoils in the target before it encounters any other target atom[138]) used in the TRIM92 simulation code were 35 eV and 5 eV, respectively. The penetration depth, $R_p$, and its standard deviation, $\Delta R_p$, were calculated by TRIM92 to be 0.21 $\mu$m and 310 $\mu$m, respectively. If the boron-ion dose energies shown in table 4.2 (chapter 4) were all simulated in the TRIM-92 code, the energy distribution will follow a roughly rectangular implanted profile.

Even though the TRIM simulation code gives a deeper insight into the radiation damage process inflicted during implantation, the program has some notable disadvantages. It assumes a homogeneous distribution of host atoms, according to the average density of the substrate, and is incapable of computing anisotropic materials, such as graphite. Orientation of the substrate is not considered in this program. This means that effects which could arise due to the periodicity of the single crystal lattice, such as channeling, are ignored. The program does not allow for the recombination of the point defects. So, no vacancy-interstitial annihilation process is included in the program. It follows therefore that TRIM will always overestimate the absolute magnitude of the radiation damage. The temperature at which the target is kept is zero and the user of the TRIM program cannot adjust it as desired. The TRIM code does not allow for the rearrangement of point defects in the damaged region to form extended defects, which could lead to the transformation of diamond to graphite. The number of vacancies and interstitials created during implantation is uncertain and only an estimate is provided due to the uncertainty in the input values of important parameters, such as the displacement energy

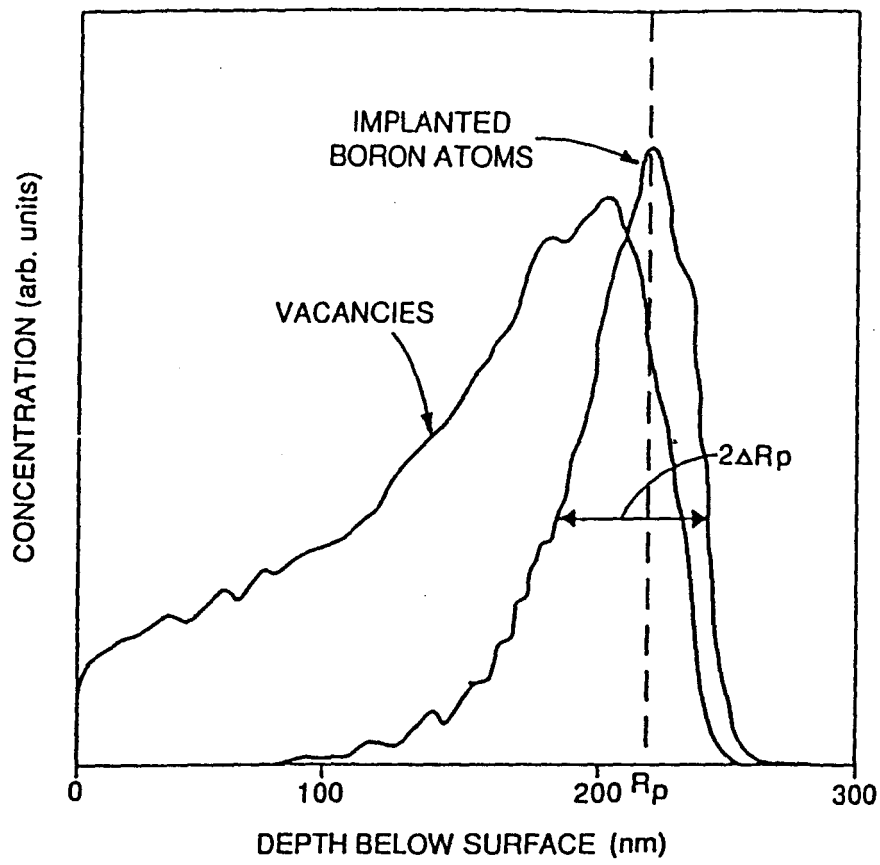


Figure 3-2: A typical figure showing a cold-implantation damage profile of a diamond specimen implanted with boron-ions which were accelerated into the diamond surface at 130 keV. This profile was obtained using the TRIM-92 computer simulation program in which the following parameters were supplied to the program: the displacement energy, $E_d = 35$ eV, and the binding energy, $E_b = 5$ eV. The penetration depth (projected ion range) is given by $R_p$, while straggling (*i.e.* the standard mean deviation from $R_p$) is denoted by $\Delta R_p$.

and ionization energy.

## 3.7 Secondary ion mass spectroscopy (SIMS)

SIMS is an ion beam probing technique in which target atoms are selectively removed from the surface by sputtering. Sputtering is achieved by using low-energy (1-10 keV) heavy ions, and the sputtered particles are analyzed in extremely sensitive high resolution mass spectrometers. The typical resolution of $\Delta M/M$ is of the order of 1:10 000, and the method can resolve isotopes and other species ejected from the target material. In the case of our diamond specimens, the SIMS analyses were performed using a CAMECA IMS-4f double focusing, magnetic sector ion microanalyzer. The primary ion beam and the beam energy used were $O_2^+$ and 8.0 keV, respectively. To avoid surface heating, the beam current was adjusted to 0.16 and 0.312 $\mu$A.

The SIMS analyses on our two diamond specimens were carried out by Charles Evans and Associates in the United States. The actual doses implanted in these samples were $1.2 \times 10^{16}$ cm$^{-2}$ and $7.9 \times 10^{16}$ cm$^{-2}$. SIMS measured these doses to be $1.2 \times 10^{16}$ cm$^{-2}$ and $7.3 \times 10^{16}$ cm$^{-2}$, respectively. The thickness of the implanted conducting surface boron-ion layers was estimated to be 0.25 $\mu$m. Fig. 3-3 and Fig. 3-4 show plots of SIMS depth profiles for these two diamond specimens. There are some obvious disadvantages associated with the SIMS technique. It is destructive to the very surface layers it is intended to probe. In the case of diamond, heavy-ion sputtering could lead to surface graphitization, thus causing very basic alterations to the diamond specimen during the process of analysis. SIMS is incapable of resolving the crystallographic location of the desired ions, i.e. whether they occupy interstitial or substitutional lattice sites. This means it is insensitive to the crystallinity of the specimen under investigation.

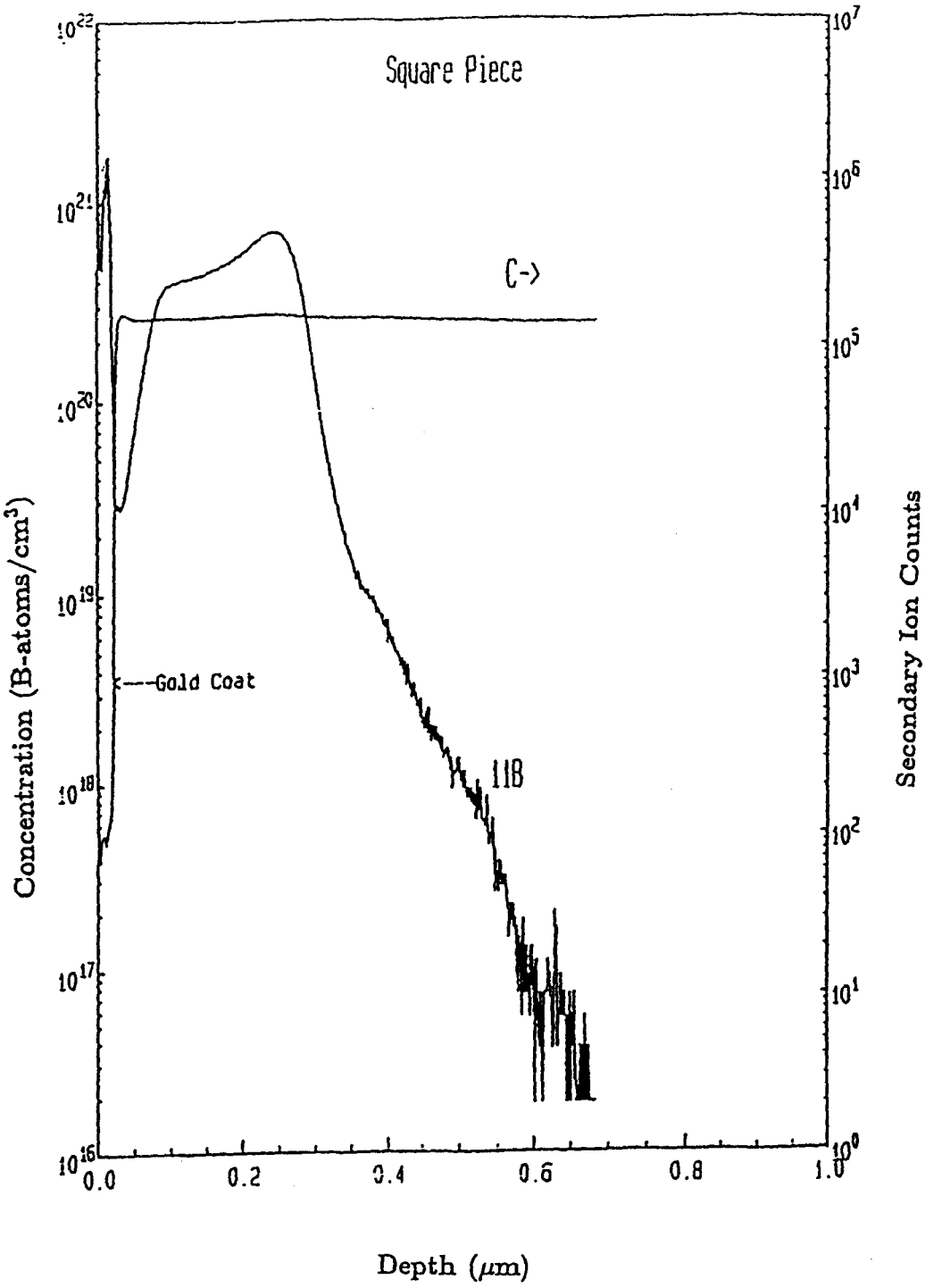


Figure 3-3: SIMS profile for a square boron-ion implanted type II*a* diamond specimen. The actual total dose implanted into this sample was $1.2 \times 10^{16}$ cm$^{-2}$. SIMS measured the same dose as implanted. The sample was annealed at 1200 °C for 30 minutes after each implantation process.

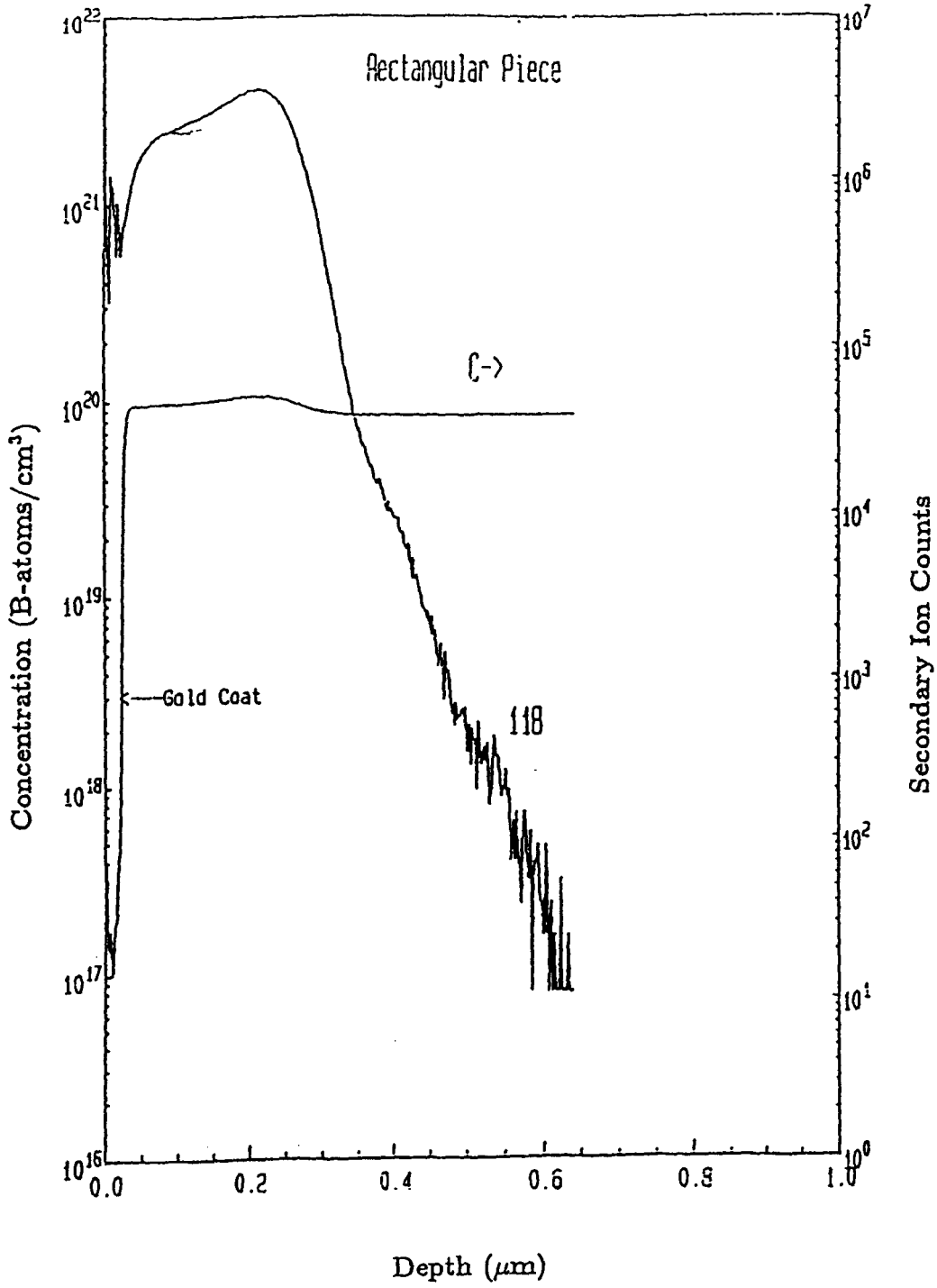


Figure 3-4: SIMS profile for a rectangular boron-ion implanted type II*a* diamond specimen. The actual dose implanted into this sample was 7.9 $\times 10^{16}$ cm$^{-2}$ using multiple CIRA steps. The SIMS measured the boron atoms in the implanted layer to be $7.3 \times 10^{16}$ cm$^{-2}$. This sample was annealed at 1200 °C for 5 minutes after each implantation process.

# Chapter 4

# Experimental details

## 4.1 Introduction

Sample preparation, procedures, experimental techniques and apparatus used in the study are described in this chapter. The first section focuses on the electrical conductivity measurements carried out between $1.5 \leq T \leq 300$ K, while the second section focuses on transport measurements performed in the range of temperature $300 \leq T \leq 773$ K. We have used a Janis cryostat and a "dip" measuring system to carry out the electrical conductivity measurements in the temperature range $1.5 - 300$ K.

### 4.1.1 Sample designation

Fig. 4-1 shows one of the type II$a$ diamond specimens used in this study. The samples have distinctive features by which we can recognize them, as is evident in Fig 4-1. Sample A, which is the main sample, has a dot near the centre. Sample B has two rings at the middle, while sample C has a clear, unmarked surface. Sample D was shaped into a

square after it broke off from a rectangular piece while we were trying to mount contacts under pressure.

Alphabet symbols A to D denote samples. The next letter indicates the implanted ion species. In this case, B stands for boron ions. A number following the alphabet symbol represents a dose fluence implanted into that sample.

### 4.1.2 Diamond shaping and polishing

Two of our type II*a* diamond specimens were sawn off from one parent stone, while the other two were cut from different stones. Three of the diamonds were shaped into rectangular slabs of dimensions $8 \times 3.5 \times 2$ mm$^3$ using a diamond saw covered with a diamond powder and oil. One sample, which broke off from one of the rectangular pieces, was transformed into a square shape of dimensions $4.74 \times 3.6 \times 3$ mm$^3$. Samples were then polished on a cast iron polishing wheel of about 60 cm in diameter, called a scaife. To avoid channeling during ion implantation, samples were oriented 12° off the (110) direction. Information on the preparation of diamond specimens is now commonplace, and the reader is referred to chapter 8 of a fairly recent book on *Ion Implantation in Diamond, Graphite and Related Materials* by Dresselhaus and Kalish[5].

### 4.1.3 Diamond target holder

Special masks, made out of a graphite disc and supported on a stainless steel backing plate, were used to clamp diamonds to the target mounts. Stacks of mica rings were used to provide circumferential support surrounding the diamonds inside the target mounts. Mica, a material which is easily machinable, was sliced into discs of uniform thicknesses. Implantations were carried out through graphite masks defining rectangular areas of $7 \times 3$ mm$^2$ on the highly polished diamond surfaces. A new design was recently put into use,

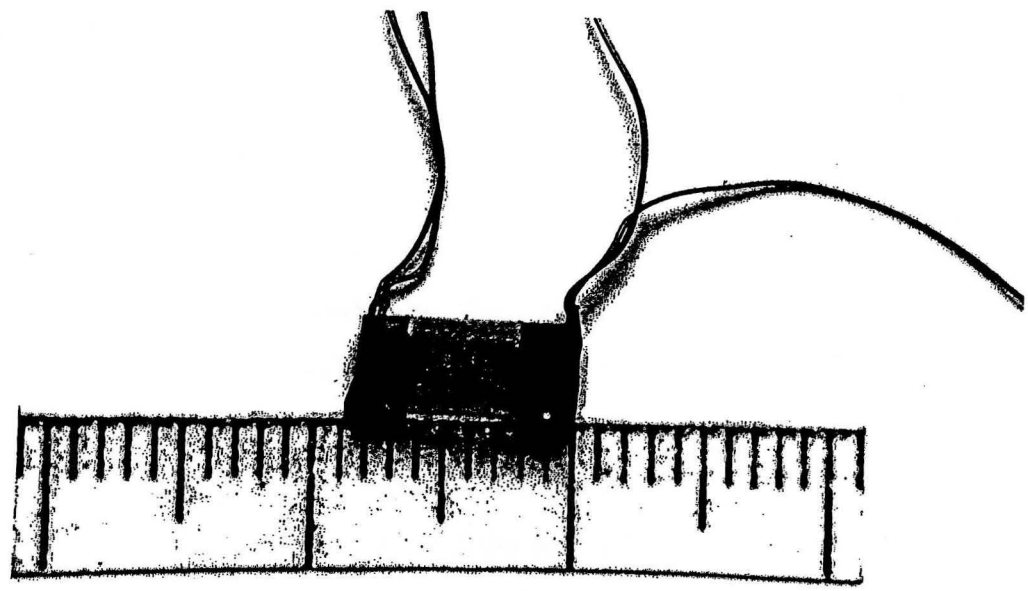

Figure 4-1: Shown in this figure is sample A which is one of the four type II$a$ diamond specimens used in this thesis. The dimensions of this sample can be read off from the figure.

which allowed us to clamp samples by the sides directly to the target holder without the use of graphite disc masks. Using the new set up, a whole diamond surface can be implanted. Previously, we could only mount one sample per side on the target holder. The new design allows us to mount all four samples on one face of the target holder, provided the same dose is to be administered into all the samples.

A target holder was made up of a stainless steel block supported by a hollow tube. The latter was used as a liquid nitrogen reservoir, since we carried out all our implants at liquid nitrogen temperature. A stainless steel holder was used due to its poor thermal conductivity, since the samples had to be transferred from the implanter's end station, after the implantation process, into a liquid nitrogen bath.

## 4.2 Ion implantation

Ion implantations were performed using the Varian Extrion Model 200-20A2F ion implanter stationed at the Schonland Research Centre. The end station of this implanter has been specially modified to allow one to use a variety of target holders. The substrate temperature was monitored with the aid of a chromel-alumel thermocouple which was mounted at the back of the sample holder. In order to avoid condensation on the diamond surfaces, liquid nitrogen was only poured into the reservoir once a vacuum of about $3 \times 10^{-6}$ torr was established at the end station. After the implantation process was completed, the end station was vented with a dry nitrogen gas before dismounting the target holder and transferring it, as quickly as possible, into a styrofoam bath filled with liquid nitrogen.

While samples were still immersed under liquid nitrogen, the annealing furnace was

preset to a desired temperature, and allowed to stabilize for about 30 minutes. The diamond was then dismounted from the target holder whilst under liquid nitrogen, and transferred into a liquid nitrogen-containing styrofoam cup that was cut to size, with a small groove made to accommodate and lock the diamond sample in a stationary position. The sample was then slid down, with no time delay, into a high-temperature preset annealing crucible.

## 4.3 Annealing furnace

The annealing furnace used for this study is shown in Fig. 4-2. It consists of a quartz glass tube with a chimney[6, 7, 139]. Inside the quartz tube is a graphite crucible which is heated by a water-cooled rf (radio frequency) coil. Rapid annealing is achieved by allowing the diamond to slide, implanted face down, along the inclined quartz tube, guided by a retractable quartz chute, into a preheated graphite crucible. Temperatures ranging from 773 K to 2000 K were used in annealing the implanted diamond specimens. The temperature settings in the annealing furnace were achieved by the use of a tungsten/rhenium thermocouple. Throughout the anneals, the furnace was flushed out continuously with inert ultra-pure argon gas to inhibit graphitization on the implanted diamond surface. As a precaution after each anneal, the diamond sample was left in the furnace to cool down to close to room temperature before dismounting from the annealing device. The sample was then placed on top of a metal substrate and allowed to cool down to room temperature before cleaning.

### 4.3.1 Cleaning of diamond samples and sample storage

Samples were cleaned by boiling them in an acidic solution of sulphuric, nitric and perchloric acids mixed in the ratio 3:4:1. They were boiled in a small beaker covered by a

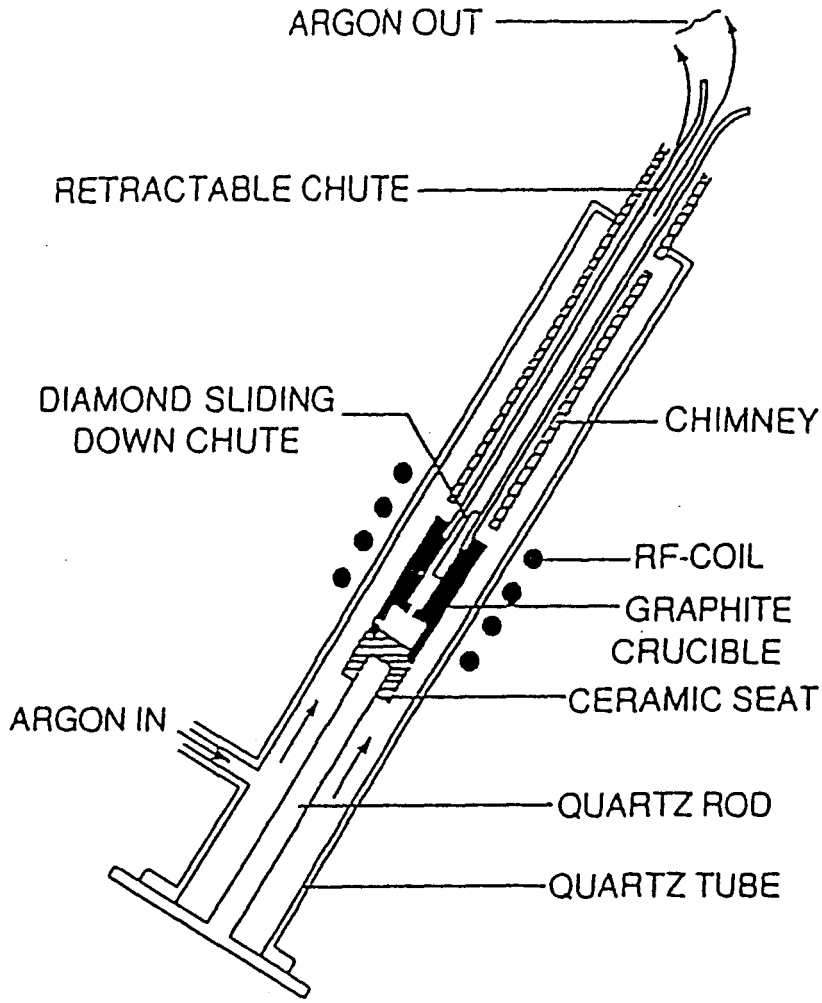


Figure 4-2: A diagram of the annealing furnace used to anneal our diamond specimens after the cold ion-implantation process. Samples were slid down the retractable chute with the implanted face down into a preheated graphite crucible. The annealing was carried out in a pure-argon atmosphere.

watch glass until the acidic solution developed a dark yellow colour, and were allowed to simmer in this solution for about 60 minutes to dissolve graphite and amorphous carbon on their surfaces while leaving diamond specimens intact. Boiling of samples for more than 60 minutes is sometimes necessary, particularly after we have carried out a 2000 K anneal. Afterwards, samples were rinsed thoroughly in distilled water and dried. Cleaning of samples was performed pre and post implantation-annealing cycles.

After cleaning, samples were wrapped with a tissue paper, sealed in a transparent plastic case, and stored at room temperature until needed for further measurements.

### 4.3.2 Implanted boron and carbon ions dose levels

Boron ions were implanted into the diamond targets at different energies in order to create a highly conductive boron-ion surface layer in which the dopant ions and the other point defects would be fairly evenly distributed. For the most reliable and reproducible results, small implantation steps have to be followed using the CIRA method. Table 4.1 shows the accelerating energies, boron-ion and carbon-ion dose fluences administered into the diamond samples. The same boron-ion dose level has been used throughout to build-up a highly conductive layer into the diamond samples. Because of the rapid change in electrical conductivity with carbon-ion dose, the ion dose range which has been used is rather narrow. Samples with the total carbon-ion dose that lie in the interval, $5.60 \times 10^{15}$ cm$^{-2}$ to $5.95 \times 10^{15}$ cm$^{-2}$, were prepared. The only difference in the procedure followed in preparing our samples was that the carbon-ion doped samples were repolished after each CIRA and electrical conductivity measurements.

Ohmic contacts were achieved by evaporating gold strips at the ends of the diamond specimens. A standard spacing of 5.5 mm between the gold strips was kept in the case

| Ion | Energy (keV) | Dose ($cm^{-2}$) $\times 10^{14}$ | Dose ($cm^{-2}$) $\times 10^{14}$ |
|---|---|---|---|
| B | 130 | 11.25 | 18.75 |
| | 110 | 3.75 | 6.25 |
| | 90 | 1.875 | 3.125 |
| | 80 | 1.875 | 3.125 |
| | 70 | 1.875 | 3.125 |
| | 60 | 1.875 | 3.125 |
| | 50 | 1.875 | 3.125 |
| | 40 | 1.875 | 3.125 |
| | 30 | 1.875 | 3.125 |
| Total B-ion dose | → | $3.0 \times 10^{15}$ $cm^{-2}$ | $5.0 \times 10^{15}$ $cm^{-2}$ |

| Ion | Energy (KeV) | Dose ($cm^{-2}$) $\times 10^{15}$ | Dose ($cm^{-2}$) $\times 10^{15}$ | Dose ($cm^{-2}$) $\times 10^{15}$ |
|---|---|---|---|---|
| C | 150 | 2.24 | 2.30 | 2.38 |
| | 120 | 1.456 | 1.495 | 1.547 |
| | 80 | 1.232 | 1.265 | 1.309 |
| | 50 | 0.672 | 0.690 | 0.714 |
| Total C-ion dose | → | $5.60 \times 10^{15}(cm^{-2})$ | $5.75 \times 10^{15}(cm^{-2})$ | $5.95 \times 10^{15}(cm^{-2})$ |

Table 4.1: Implantation energies and ion doses used in this study. The accelerating energies and doses were spread into small steps to generate highly conducting boron-ion and carbon-ion layers in the diamond samples.

of three samples (A, B and C), and a spacing of 1.5 mm was left as a measurable region for sample D. Evaporation of gold onto the samples were carried out at the Electron Microscope Unit, and a thickness of about 100 nm was deposited. Fig. 4-3 shows plots of $I$ (A) *vs.* $V$ (V) to demonstrate ohmic behaviour exhibited by sample A for a variety of doses implanted onto the surface.

An alternative way of achieving good ohmic contacts was by means of heavy ion implantation. In this case, we covered the regions where the electrical conductivity measurements were to be made with an aluminium foil or a copper slab and only exposed those regions on which we wanted to create contacts. As described above, a spacing of 5.5 mm was covered with a foil prior to contact implantation. A total dose of 6.1 $\times 10^{15}$ B-cm$^{-2}$ was then implanted, broken up into small steps at different energies. Table 4.2 summarizes the ion dose and various energies used to generate these contact regions. Linear ohmic contacts were achieved by applying silver paint onto the contact regions and then baking the diamonds in an oven at 70-80 °C for over 2 hours[118]. Table 4.3 gives a summary of sample characterizations. The rectangular diamond samples used in this study have dimensions 8 $\times$ 3.5 $\times$ 2 mm$^3$. The thickness, $t$, of the implanted layer has been estimated by the SIMS technique to be 2200 . The square resistances in table 4.3 were obtained using the procedure: $R_{\square} = t\,(W/L)\,R_i$ , where $W$ is the width of the sample, $L$ is the distance between the electrical contacts and $R(\Omega)$ is the sample resistance at any measured temperature. $\sigma = 1/\ R_{\square}$ in units of $(\Omega -\ \mathrm{cm})^{-1}$.

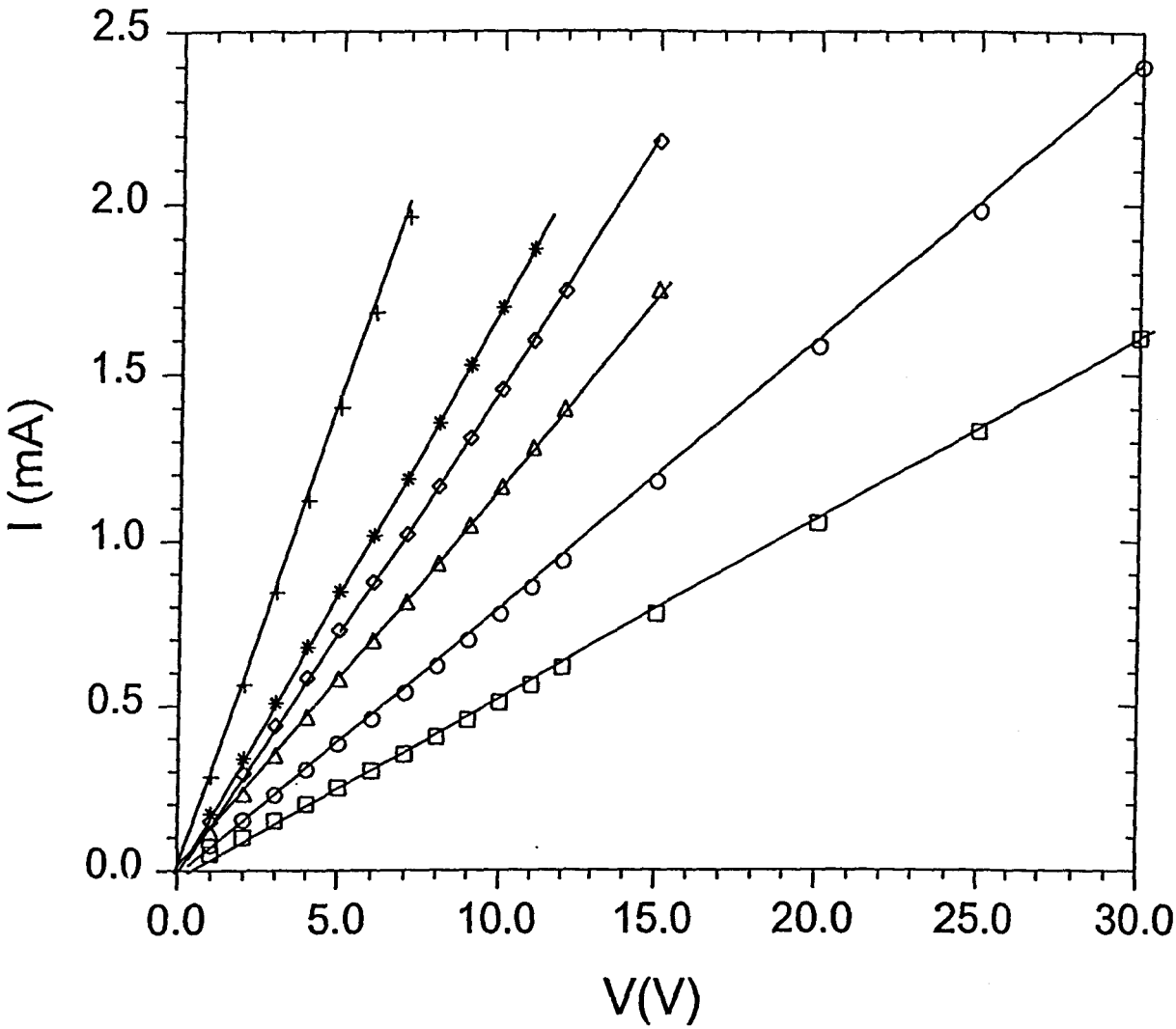


Figure 4-3: Plot of $I(A)$ *vs.* $V(V)$ to demonstrate Ohmic behaviour exhibited by a variety of doses implanted into sample A.

| Ion | Energy (keV) | Dose ($cm^{-2}$) $\times 10^{14}$ |
|---|---|---|
| B | 130 | 22.50 |
| | 110 | 7.50 |
| | 90 | 3.75 |
| | 80 | 3.75 |
| | 70 | 3.75 |
| | 60 | 3.75 |
| | 50 | 3.75 |
| | 40 | 3.75 |
| | 30 | 3.75 |
| Total B-ion dose | $\rightarrow$ | $6.0 \times 10^{15}$ $cm^{-2}$ |

| Ion | Energy (keV) | Dose ($cm^{-2}$) $\times 10^{15}$ |
|---|---|---|
| C | 150 | 2.44 |
| | 120 | 1.586 |
| | 80 | 1.342 |
| | 50 | 0.732 |
| Total C-ion dose | $\rightarrow$ | $6.10 \times 10^{15}$ $cm^{-2}$ |

Table 4.2: Energy, boron-ion dose and carbon-ion fluences used to generate Ohmic contact regions on the diamond surfaces. The electrical contacts are spaced about 5.5 mm apart.

Table 4.3: A summary of insulating boron-ion implanted type IIa diamond samples used in this study, and their characterizations. Samples dimensions are $8 \times 3.5 \times 2$ mm$^3$.

**Boron-ion implanted type IIa diamond samples (RECTANGULAR SAMPLES)**

**Insulating samples**

| Sample designation | Implanted ion-dose | Implanted- ion concentration, *n*, estimated by TRIM-92 simulation program | *n* estimated from SIMS results | Relative % error in *n* | Annealing temperature | Annealing period | R (T=300 K) | $R_{\square}$ (T=300 K) | σ (T=300 K) |
|---|---|---|---|---|---|---|---|---|---|
| | $\times 10^{15}$ (cm$^{-2}$) | $\times 10^{21}$ (cm$^{-3}$) | $\times 10^{21}$ (cm$^{-3}$) | | (°C) | (minutes) | (kΩ) | (Ω-cm) | (Ω -cm)$^{-1}$ |
| AB21 | 21 | 1.0 | 1.02 | 1.48 | 1200 | 5 | 373 | 5.09 | 0.196 |
| AB24 | 24 | 1.14 | 1.16 | 1.72 | 1200 | 5 | 119 | 1.63 | 0.61 |
| AB27 | 27 | 1.29 | 1.31 | 1.15 | 1200 | 5 | 65.7 | 0.89 | 1.12 |
| AB30 | 30 | 1.43 | 1.45 | 1.38 | 1200 | 5 | 31.5 | 0.43 | 2.33 |
| AB33 | 33 | 1.57 | 1.60 | 1.57 | 1200 | 5 | 20 | 0.27 | 3.66 |
| AB36 | 36 | 1.71 | 1.74 | 1.72 | 1200 | 5 | 13.1 | 0.18 | 5.57 |
| AB39 | 39 | 1.86 | 1.89 | 1.33 | 1200 | 5 | 8.49 | 0.12 | 8.62 |
| AB42 | 42 | 2.0 | 2.03 | 1.48 | 1200 | 5 | 6.89 | $9.4 \times 10^{-2}$ | 10.63 |
| AB45 | 45 | 2.14 | 2.18 | 1.61 | 1200 | 5 | 5.92 | $8.1 \times 10^{-2}$ | 12.37 |
| AB48 | 48 | 2.29 | 2.41 | 5.07 | 1200 | 5 | 4.37 | $6.0 \times 10^{-2}$ | 16.76 |
| AB51 | 51 | 2.43 | 2.56 | 5.19 | 1200 | 5 | 3.57 | $4.9 \times 10^{-2}$ | 20.51 |
| AB54 | 54 | 2.57 | 2.71 | 5.30 | 1200 | 5 | 3.49 | $4.7 \times 10^{-2}$ | 20.98 |
| AB57 | 57 | 2.71 | 2.87 | 5.40 | 1200 | 5 | 2.60 | $3.6 \times 10^{-2}$ | 28.16 |
| AB60 | 60 | 2.86 | 3.02 | 5.15 | 1200 | 5 | 2.32 | $3.12 \times 10^{-2}$ | 31.56 |
| AB63 | 63 | 3.0 | 3.17 | 5.25 | 1200 | 5 | 1.81 | $2.5 \times 10^{-2}$ | 40.54 |
| AB66 | 66 | 3.14 | 3.32 | 5.33 | 1200 | 5 | 1.77 | $2.4 \times 10^{-2}$ | 43.30 |
| AB69 | 69 | 3.29 | 3.47 | 5.12 | 1200 | 5 | 1.51 | $2.1 \times 10^{-2}$ | 48.46 |

Table 4.4: A summary of boron-ion implanted type IIa diamond samples (samples in the vicinity of the M-I transition) and their characterizations. Samples dimensions are $8 \times 3.5 \times 2$ mm$^3$.

**Samples in the vicinity of the M-I Transition (RECTANGULAR SAMPLES)**

| Sample designation | Implanted ion-dose | Implanted- ion concentration, *n*, estimated by TRIM-92 simulation program | *n* estimated from SIMS results | Relative % error in *n* | Annealing temperature | Annealing period | R (T=50 K) | σ (T=50 K) | σ (T=1.56K) |
|---|---|---|---|---|---|---|---|---|---|
| | $\times 10^{15}$ (cm$^{-2}$) | $\times 10^{21}$ (cm$^{-3}$) | $\times 10^{21}$ (cm$^{-3}$) | | (°C) | (minutes) | (Ω) | (Ω-cm)$^{-1}$ | (Ω -cm)$^{-1}$ |
| AB72 | 72 | 3.43 | 3.62 | 5.21 | 1200 | 5 | 5476 | 13.37 | 0.14 |
| AB75 | 75 | 3.57 | 3.77 | 5.29 | 1200 | 5 | 4353 | 16.82 | 2.30 |
| AB78anl | 78 | 3.71 | 3.92 | 5.36 | 1200 | 5 | 4427 | 16.7 | 1.17 |
| AB78anl2 | 78 | 3.71 | 3.92 | 5.36 | 1200 | 30 | 4599 | 15.9 | 1.49 |
| AB78anl3 | 78 | 3.71 | 3.92 | 5.36 | 1200 | 120 | 3211 | 22.8 | 2.50 |
| AB78anl4 | 78 | 3.71 | 3.92 | 5.36 | 500 | 30 | 2720 | 26.9 | 3.68 |
| AB78anl5 | 78 | 3.71 | 3.92 | 5.36 | 500 | 120 | 3044 | 24.1 | 3.54 |
| AB78 | 78 | 3.71 | 3.92 | 5.36 | 1700 | 10 | 5307 | 13.8 | 4.17 |
| AB81anl1 | 81 | 3.86 | 4.07 | 5.18 | 1200 | 5 | 3602 | 20.3 | 0.98 |
| AB81anl2 | 81 | 3.86 | 4.07 | 5.18 | 1300 | 30 | 4621 | 15.8 | 3.7 |
| AB81anl3 | 81 | 3.86 | 4.07 | 5.18 | 1400 | 60 | 4557 | 16.1 | 4.7 |
| AB81anl4 | 81 | 3.86 | 4.07 | 5.18 | 500 | 30 | 4244 | 17.3 | 3.7 |
| AB81anl5 | 81 | 3.86 | 4.07 | 5.18 | 500 | 60 | 5122 | 14.3 | 3.4 |
| AB81anl6 | 81 | 3.86 | 4.07 | 5.18 | 500 | 120 | 5306 | 13.8 | 4.2 |
| AB81anl7 | 81 | 3.86 | 4.07 | 5.18 | 1300 | 10 | 2882 | 25.4 | 10.4 |
| AB81anl8 | 81 | 3.86 | 4.07 | 5.18 | 1400 | 10 | 2317 | 31.6 | 23.6 |
| AB81anl9 | 81 | 3.86 | 4.07 | 5.18 | 1600 | 10 | 1099 | 66.6 | 26.7 |
| AB81 | 81 | 3.86 | 4.07 | 5.18 | 1700 | 10 | 505 | 145 | 29.4 |
| AB84 | 84 | 4.0 | 4.21 | 5.25 | 1700 | 10 | 711 | 103 | 73.8 |

*5.5 (mm) is the distance between the two-point electrical contacts

Table 4.5: A summary of insulating boron-ion implanted type IIa diamond samples (square samples) and their characterizations. Samples dimensions are 4.75 ×3.5 × 3 $mm^3$.

**Boron-ion implanted type II*a* diamond samples (SQUARE SAMPLE)**

**Insulating samples**

| Sample designation | Implanted ion-dose | Implanted- ion concentration, *n*, estimated by TRIM-92 simulation program | *n* estimated from SIMS results | Relative % error in *n* | Annealing temperature | Annealing period | R (T=300K) | $R_{\square}$ (T=300 K) | σ (T=300 K) |
|---|---|---|---|---|---|---|---|---|---|
| | $\times 10^{15}$ ($cm^{-2}$) | $\times 10^{21}$ ($cm^{-3}$) | $\times 10^{21}$ ($cm^{-3}$) | | (°C) | (minutes) | (kΩ) | (Ω-cm) | (Ω -cm)$^{-1}$ |
| SQ5 | 5 | 0.23 | 0.24 | 4.17 | 1200 | 10 | 856 | 42.86 | 0.023 |
| SQ10 | 10 | 0.47 | 0.48 | 2.08 | 1200 | 10 | 761 | 38.11 | 0.026 |
| SQ15 | 15 | 0.70 | 0.73 | 4.11 | 1200 | 10 | 650 | 32.55 | 0.031 |
| SB12a900 | 12 | 0.56 | 0.58 | 3.45 | 900 | 5 | 415 | 20.66 | 0.05 |
| SB12a900 | 12 | 0.56 | 0.58 | 3.45 | 900 | 10 | 182 | 9.12 | 0.11 |
| SB12a900 | 12 | 0.56 | 0.58 | 3.45 | 900 | 120 | 119 | 5.97 | 0.17 |
| SB12a900 | 12 | 0.56 | 0.58 | 3.45 | 900 | 150 | 92.5 | 4.63 | 0.22 |
| SB12a12 | 12 | 0.56 | 0.58 | 3.45 | 1200 | 30 | 26.6 | 1.33 | 0.75 |
| SB12a13 | 12 | 0.56 | 0.58 | 3.45 | 1300 | 10 | 19.6 | 0.98 | 1.02 |
| SB12a14 | 12 | 0.56 | 0.58 | 3.45 | 1400 | 10 | 18.3 | 0.92 | 1.09 |
| SB12a15 | 12 | 0.56 | 0.58 | 3.45 | 1500 | 10 | 9.7 | 0.48 | 2.06 |
| SB12a16 | 12 | 0.56 | 0.58 | 3.45 | 1600 | 10 | 5.46 | 0.27 | 3.66 |
| SB12a17 | 12 | 0.56 | 0.58 | 3.45 | 1700 | 10 | 5.18 | 0.26 | 3.86 |

*1.5 (mm) is the distance between the two-point electrical contacts

Table 4.6: A summary of carbon-ion implanted type IIa diamond samples (insulating and metallic samples) used in this study and their characterizations. Samples dimensions are $8 \times 3.5 \times 3$ mm$^3$.

**Carbon-ion implanted type II*a* diamond samples (RECTANGULAR SAMPLES)**

**Insulating samples**

| Sample designation | Implanted ion-dose | Implanted- ion concentration, *n*, estimated by TRIM-92 simulation program | Annealing temperature | Annealing period | R (T=300 K) | $R_{\square}$ (T=300 K) | σ (T=300 K) | σ (T=4 K) |
|---|---|---|---|---|---|---|---|---|
| | $\times 10^{15}$ (cm$^{-2}$) | $\times 10^{20}$ (cm$^{-3}$) | (°C) | (minutes) | (kΩ) | (Ω-cm) | (Ω -cm)$^{-1}$ | (Ω -cm)$^{-1}$ |
| C560 | 5.6 | 2.61 | 1200 | 30 | 11.81 | 0.16 | 6.19 | 0.69 |
| R2C560 (repeated) | 5.6 | 2.61 | 1200 | 30 | 5.394 | $7.38 \times 10^{-2}$ | 13.55 | 5.08 |
| C565 | 5.65 | 2.63 | 1200 | 30 | 24.28 | 0.33 | 3.01 | $2.2 \times 10^{-2}$ |
| R2C565 (repeated) | 5.65 | 2.63 | 1200 | 30 | 10.65 | 0.15 | 6.86 | 0.39 |
| C570 | 5.70 | 2.65 | 1200 | 30 | 14.21 | 0.19 | 5.14 | $1.64 \times 10^{-3}$ |
| R2C570 (repeated) | 5.70 | 2.65 | 1200 | 30 | 8.94 | 0.12 | 8.17 | 0.924 |
| **Metallic Samples** | | | | | | | | |
| C575 | 5.75 | 2.67 | 1200 | 30 | 4.69 | $6.41 \times 10^{-2}$ | 15.58 | 7.9 |
| R2C575 (repeated) | 5.75 | 2.67 | 1200 | 30 | 5.11 | $6.99 \times 10^{-2}$ | 14.3 | - |
| R3C575 (repeated) | 5.75 | 2.67 | 1200 | 30 | 2.04 | $2.8 \times 10^{-2}$ | 35.88 | 20.45 |
| C580 | 5.80 | 2.70 | 1200 | 30 | 3.31 | $4.5 \times 10^{-2}$ | 22.09 | 12.6 |
| C590 | 5.90 | 2.74 | 1200 | 30 | 2.11 | $2.88 \times 10^{-2}$ | 34.71 | 22.0 |
| C595 | 5.95 | 2.77 | 1200 | 30 | 0.68 | $9.28 \times 10^{-3}$ | 107.71 | 88.25 |
| C1425 | 14.25 | 6.63 | 1200 | 30 | 0.45 | $6.20 \times 10^{-3}$ | 161.24 | 139.71 |

## 4.4 Janis cryostat

The main components that make up the Janis cryostat are the $8l$ liquid nitrogen and $5l$ liquid helium reservoirs, both of which are contained in a vacuum jacket. In close contact to the helium bath is the sample chamber, where the cryogenic probe (sample holder) freely hangs. The link between the liquid helium bath and the sample chamber is provided by a needle valve. A cross sectional view of the Janis cryostat is shown in Fig. 4-4.

Before the initiation of the low-temperature experiment, the vacuum jackets on the Janis cryostat were first pumped out through the vacuum pumping port, which is attached to a diffusion pump, until a vacuum of $10^{-6} - 10^{-7}$ torr was registered on the Edwards Penning gauge (model 8). Such a vacuum was achieved after continuously pumping the cryostat for about two days using the two-stage oil diffusion pump backed by a rotary vacuum pump. The cryostat was then purged with helium and back-filled with pure helium exchange gas. The purging process was repeated several times even when the experiment was in progress. This was to safeguard against blockage of the needle valve by frozen air.

Samples were first cooled down using liquid nitrogen to about 110 K, while maintaining the sample chamber and the helium bath pressured to $\sim 1$ atmosphere with helium gas. When a temperature close to 110 K was reached, liquid helium was transferred into its $5l$ main reservoir. The procedure for such a transfer is described later in the text to serve as a guide towards an efficient running of the cryostat. The liquid helium was drawn out of the helium bath via the needle valve, through the capillary tube, into the base of the sample chamber at which a vaporizer was mounted. The vaporizer was connected to an external power supply, of which a maximum of 2 V could be used for a

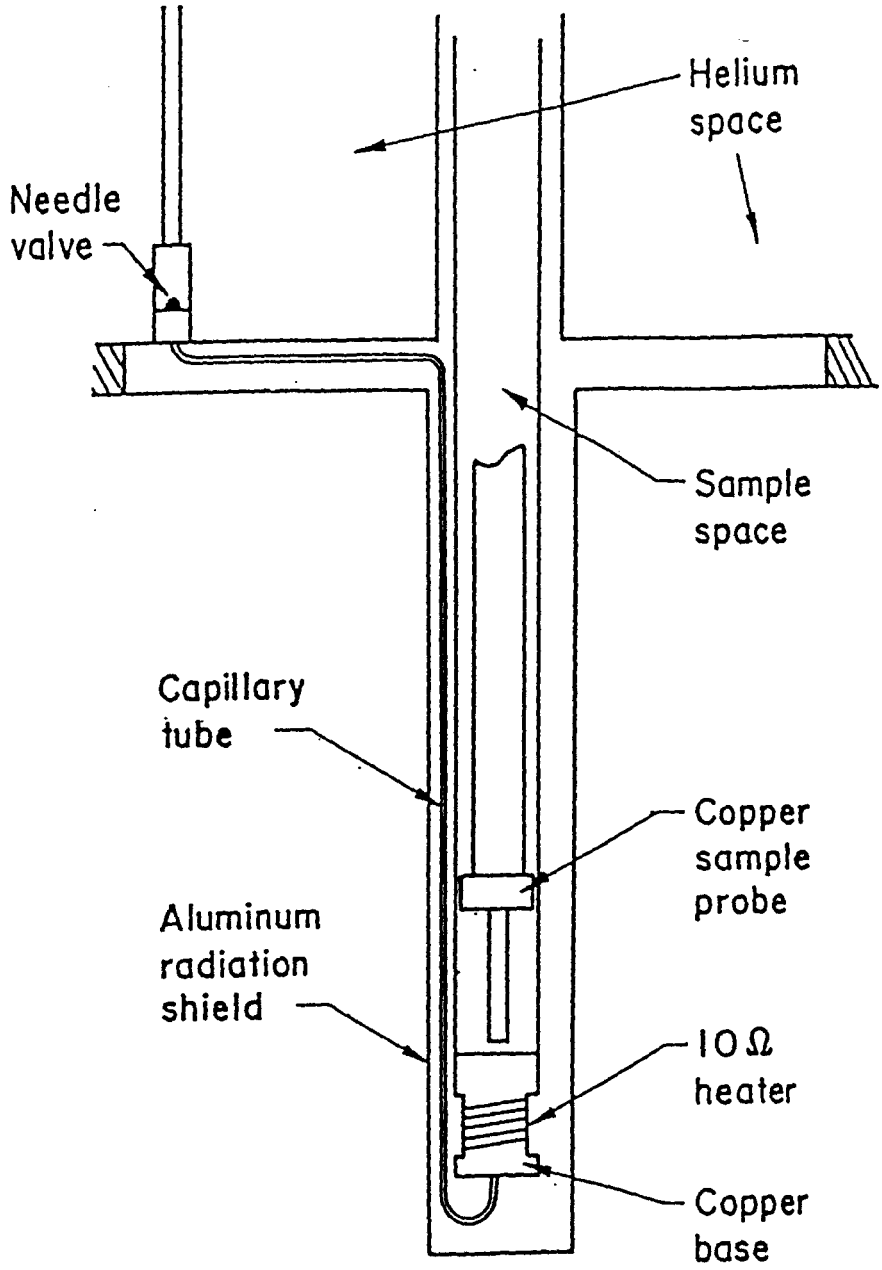


Figure 4-4: A cross-sectional view of the Janis cryostat.

safe operation.

The rate of cooling of samples, which is achieved by an upward evaporation of helium vapour, is determined by three factors:

1. 
   - The amount by which the needle valve is opened. A quarter of a full turn is recommended for measurements at $T > 50$ K, or can be adjusted as desired.
   - The energy supplied to the vaporizer by the power supply. This energy should be reduced systematically by decreasing the voltage on the power supply from 2 V to 0 V for the conductivity measurements at $T \leq 50$ K.
   - The energy supplied by the mounted heater on the sample probe. The heater range is selected on the Lakeshore temperature controller. A 100 $\Omega$ heater used in this work provided a maximum power output of 25 Watts, as the compliance voltage of the temperature controller is 50 V and the maximum current that one can use is 1 A.

Keeping the needle valve free to turn about and the capillary tube unblocked are the main concerns before the liquid helium precooling procedure. By following the procedure as described in the point-form below, I managed to achieve a success rate of over 95%.

### 4.4.1 Maintenance of the Janis cryostat

Before the cryostat was used, a check was made to detect any collection of water or ice in the nitrogen reservoir from the previous run. If any was found, it was sucked out using a sponge mounted at the end of a long thin rod. This involved dismounting one metal seal that covered the top of the cryostat. When all the water had been cleared out, a latex transfer line was connected to a nitrogen gas cylinder and one end inserted to the

base of the nitrogen bath. A small nitrogen gas flow was used to dry out any remaining water droplets.

### 4.4.2 A procedure for the running of the Janis cryostat

Fig. 4-5 and Fig. 4-6 show different views of the cryogenic system where all the components are labelled for the description below. The procedure to run the Janis cryostat includes the following steps:

All the nitrogen cold-traps connected to the Janis cryostat have to be filled prior to the running of the Janis to avoid hot oil vapour back-streaming into the vacuum jackets and the liquid helium space, with the latter leading into the sample chamber.

- Open the exhaust valve (glass valve) (A) and close the main valve (B) leading to the recovery line. This is to avoid transmitting an exhaust gas down the recovery line to the helium plant, or sucking in dirt from the recovery line into the cryostat.
- Isolate the liquid helium bath and the sample chamber by closing the needle valve (C) and the 'main regulator' valve (D). Both the sample chamber (E) and the helium reservoir (F) will now be under vacuum.
- Backfill the cryostat with pure helium gas, while keeping either the sample chamber or the helium reservoir under vacuum.
- Open the needle valve and monitor the pressure gauge mounted on one of the valves (G). If the pressure variation is observed on the pressure gauge, it means that the needle valve and the capillary are free and unblocked.
- Liquid helium can then be transferred into its main reservoir.

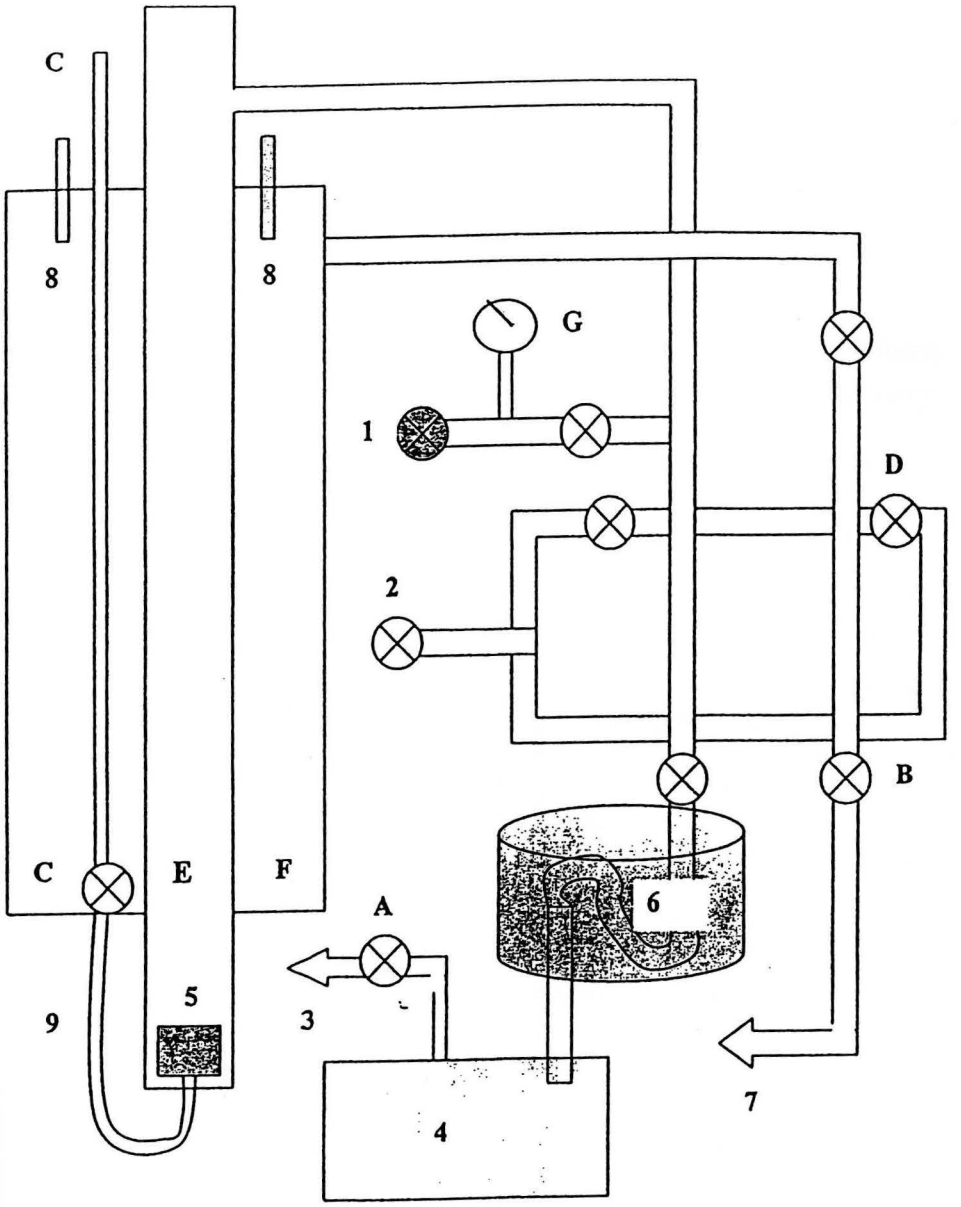


A——exhaust valve

B——valve leading to the recovery line

C——needle valve

D——valve used to isolate helium reservoir and sample chamber

E——sample chamber

F——helium reservoir

G——pressure gauge meter

1——valve behind the pressure gauge meter is always closed

2——helium gas inlet valve

3——valve transmitting exhaust gas to the outside of the building

4——rotary pump

5——vaporizer

6——liquid nitrogen cold trap

7——recovery line

8——liquid helium inlet ports

9——capillary tube

Figure 4-5: A simplified schematic view of the cryogenic system. The nitrogen bath is not shown in the figure.

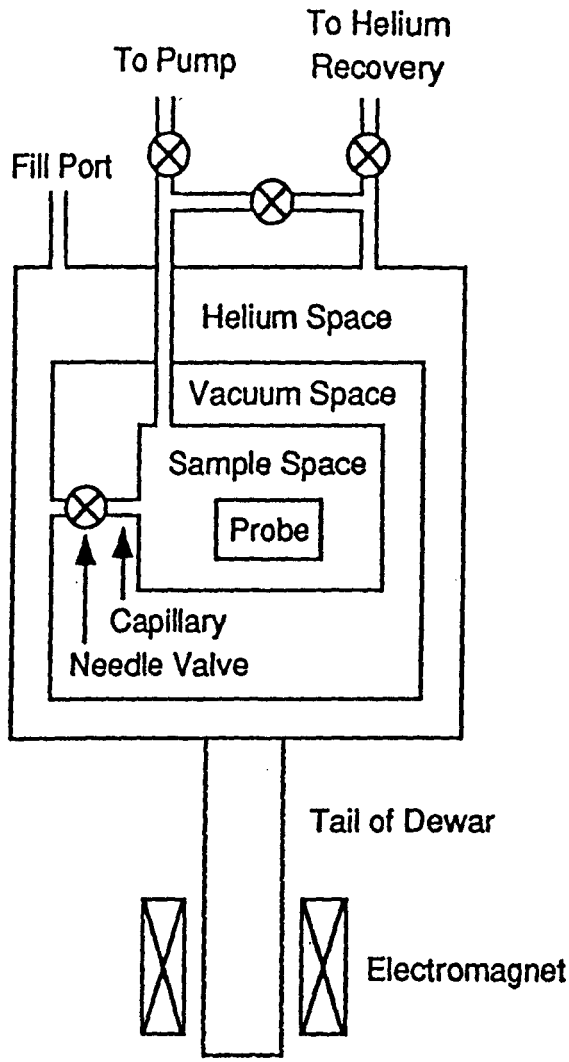


Figure 4-6: A simplified schematic view of the Janis cryostat. The nitrogen bath is not shown in the figure.

### 4.4.3 Cryogenic sample probe

A schematic view of the cryogenic sample probe is shown in Fig. 4-7. Mounted on the cryogenic probe is a carbon glass thermometer (model CGR-1-500) which has been calibrated by Lakeshore in the temperature range 300-1.56 K. An Alan Bradley resistor has been mounted just above the sample in order to monitor the level of liquid helium in the sample chamber. This is necessary when we have to carry out transport measurements below 4 K. In this case, we have to pump on the liquid helium to reduce its pressure. Wound at the base of the probe is a 100 $\Omega$ heater to help us fine tune the cooling rate. A number of breathing holes were made through the copper block to allow liquid helium into the sample can, and to let electrical leads run out of these holes to the ten pin connectors situated at the top of the cryogenic probe.

Thermal anchoring of samples to a copper substrate is provided by a low-temperature vacuum grease. To do this, I applied a thin layer of Apiezon vacuum grease or Dow Corning vacuum grease on a cigarette paper and placed a sample on top until it dried. Baking in an oven set at 60 °C for some time can also help in solidifying the vacuum grease. The sample was wrapped with a teflon tape to avoid contamination on the surface. The sample holder was then screwed on to the same copper block to which the carbon glass thermometer was mounted. Anchoring of the thermometer to the copper block is achieved by means of the leads. Initially, the leads were wound round a copper slab specifically designed for this and then covered with a thick varnish layer. Recently, the electrical leads of the carbon glass resistor were sandwiched between the gold plate metal slabs and anchored to the copper block. This was to avoid having to unwind the thermometer leads every time we exchanged the cryogenic probes with other workers.

Some nylon spacers were placed around the probe to help keep the probe in a clearly vertical position. Orientation of the sample is important when conductivity measurements are to be made in the presence of a magnetic field. In this case, samples were

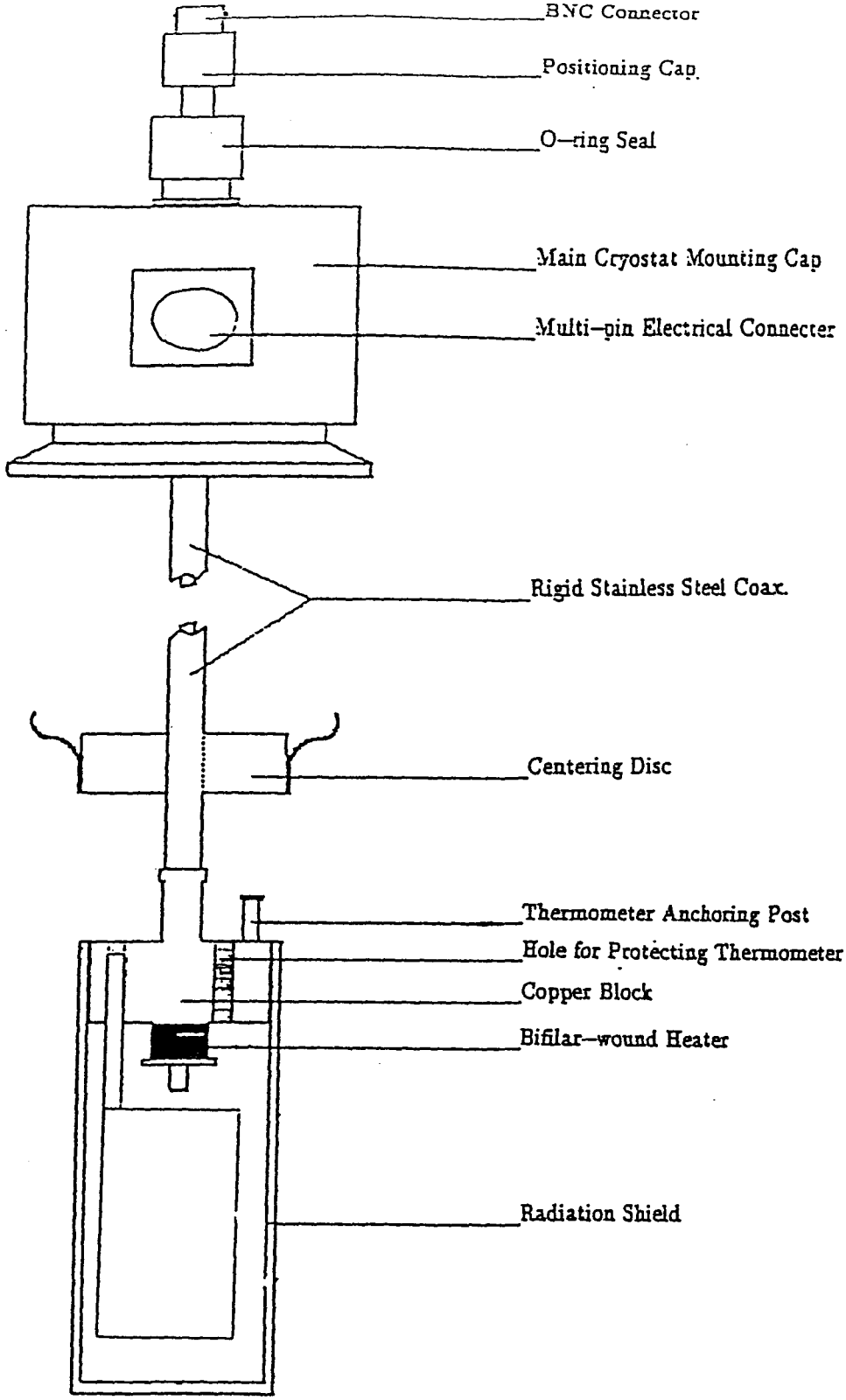


Figure 4-7: A schematic view of the cryogenic probe used to mount samples.

oriented perpendicular (*i.e.* transverse) to the field.

### 4.4.4 Temperature controller and the Keithley electrometer

The sample temperature is monitored and controlled with the use of a Lakeshore temperature controller, model DRC-93A. The controller monitors temperatures by comparing the actual sensor voltage or signal with an analog voltage created by the unit which corresponds to the user's desired temperature or set-point. The controller is able to stabilize temperature to within 1 mK.

Highly resistive samples were measured using a Keithley electrometer, model 617. The Keithley electrometer affords us the means to measure samples up $10^{16}$ $\Omega$, but, due to huge fluctuations in the resistance of our samples, we decided to analyze only the $R-T$ data measured up to $10^{11}$ $\Omega$. We tried screening the current and voltage leads as well as the measuring instruments but it did not help us much. The maximum current that one can use is 2 mA, while the measuring range of voltage is $\pm$102.40 V. The voltages that I used for carrying out conductivity measurements were in the range 2-10 V. A Fluke digital multimeter (model 8840 A) was used for some samples which showed metallic-type conduction.

### 4.4.5 Low-temperature electrical conductivity measurements

The low-temperature electrical conductivity measurements were carried out using the Janis cryostat and the dip measuring system. Since we started with highly insulating samples, only two-point conductivity measurements were carried out using the Janis cryostat. As the samples became more and more metallic, subject to further implantations, we switched over to the four-point electrical contact measurement technique, and the dip system was then used.

I briefly describe the experimental process involved in measuring transport in samples using these techniques. I describe first the Janis cryostat procedure.

A typical low-temperature run proceeds as follows. The sample probe is first connected to the data capturing system, the temperature controller and the Keithley, or the multimeter electrometer devices, via the IEEE interchange bus. The cryostat is first purged, as described under the maintenance section, and the nitrogen pot filled. The dewar is then left to cool overnight. The needle valve is kept closed so that no liquid that can have found its way into the helium space can enter the capillary tube and the sample chamber. Such a possibility is remote except when liquid nitrogen has been transferred into the helium bath (and then removed) to achieve a faster cooling rate. After about 10 hours, the temperature of the cryogenic system will have reached 110 K. At this point the helium reservoir and the sample space are both purged and backfilled with pure helium gas. The needle valve and the capillary tube have to be clear of any blockage. If any blockage is detected, the experiment has to be aborted by warming the cryostat to room temperature for maintenance. With the needle valve still closed, a transfer of liquid helium into the helium bath is carried out. The rate of liquid helium transfer is monitored by a helium meter gauge mounted on the helium recovery line. On average, two litres of liquid helium are lost to the recovery line by boil off during a fill. After the transfer, the needle valve is opened as desired to allow liquid helium to gather at the base of the sample space. Because of the location of the sample chamber in relation to the helium can, the flow of helium from the main helium bath into the sample chamber is mediated by gravity. A faster transfer can be induced if a pressure differential between the helium bath and the sample chamber is maintained. This can be achieved by evacuating the sample space with the needle valve kept wide open, while maintaining the helium reservoir at atmospheric pressure.

After collecting about a litre of liquid helium into the sample space, a process that can last about an hour, the needle valve was closed and the sample space isolated. The sample chamber was then pumped with a rotary pump connected directly to the sample chamber. The cooling rate depends on the pumping speed and the input heat by the vaporizer or heater mounted on the probe. Much practice is needed to control the temperature efficiently with sufficient accuracy. To cover the temperature range 1.56 to 4.02 K, it usually took over an hour to obtain reliable data, which in most cases were reproducible.

In order to measure samples on the way up, the pumping speed was systematically reduced and vaporizer turned on to fine tune the temperature. In this case, cooling of samples is achieved via the helium vapour. The needle valve was kept closed until a temperature of 4 K was reached, and then opened to about a 1/8 of a full turn to allow a steady inflow of liquid helium into the sample chamber. After a successful run, samples can be replaced with new ones by pulling out the sample probe without having to warm the cryostat to room temperature. With the probe taken out, the sample chamber is over-pressurized with helium gas and the chamber closed by a rubber stopper.

## 4.5 The dip measuring system

Before running the dip system, the cryogenic probe, which is sealed with a stainless steel tube, is evacuated using a single stage rotary pump and backfilled with a pure helium exchange gas. This is to avoid condensation on the surfaces of the mounted samples even though precautionary measures of wrapping samples fully with teflon tape are applied. The typical temperature range over which the electrical conductivity measurements can be made is 4.5 to 300 K. On average, a complete run takes about 5 hours when a cooling rate of one degree per minute is maintained.

Four-point resistivity measurements on our samples were performed by slowly lowering the cryogenic probe in a liquid helium dewar. The rate of insertion of the probe to the helium reservoir is controlled by a home-built motor-lowering device. In the case of highly insulating samples, a two-point configuration Keithley electrometer (model 617) is used to measure the voltage across the sample with a known constant current flowing through the sample. The sample temperature is obtained with the use of a Rh/Fe resistance thermometer connected to the Prema digital voltmeter, model 5000. The resistance of low resistive samples is determined by measuring the voltage across the sample, also employing the Prema digital voltmeter, but the current is determined using two standard resistors (each of resistance of 98 $\Omega$). In some cases, an external buffer resistor has to be added to obtain the desired current through the sample. The cryogenic probe is similar to the one used in a Janis cryostat but with some modification.

The details of the dip system can be found in a number of standard cryogenic books on low-temperature cryogenics. The following books, written by Richardson[140], Betts[141] and Kent[142], have been found useful in introducing the writer to this field.

## 4.6 High-temperature conductivity measurements

The two-point electrical conductivity measurements were extended to temperatures up to 773 K. These measurements were sufficiently accurate for the purpose of our study in trying to measure the activation energies at high temperatures. We could not carry out the 4-point electrical measurements due to the experimental difficulties encountered with our measuring system. Platinum wires were used as measuring leads, by running them through the ceramic tube which has two open-ended separate holes. A sample

holder was made up of a stainless steel plate punctured with four holes to accommodate stainless steel screws. Platinum wires were put on the baked contacts and supported in place by a piezoid quartz plate, which had been cut to dimensions $12 \times 12 \times 3$ mm$^3$. Fig. 4-8 shows a schematic view of the sample holder.

After a sample was mounted, it was sealed inside a stainless steel tube. Before the initiation of the experiment, this 'mini cryostat' was purged and backfilled with inert ultra pure argon gas. During measurements, the sample was continuously flushed with argon gas to inhibit surface graphitization. The inflow of argon into the cryostat was monitored by dropping one end of the latex transfer line into a beaker filled with water. A home-built oven, made up of asbestos and covered by a metal shield, was used in this study. A RKC (model Rex P9) 8 step programmable temperature sensor was used to control the system's temperature, with a J-type iron and constantan thermocouple connected to an oven. As a form of precaution, this oven was rested squarely on ceramic blocks.

The sample resistivity was measured with the use of a Keithley electrometer. Fig. 4-9 shows a block diagram of the measuring system employed in this study. Electrical contacts have been prepared using two different procedures. The first procedure involved implanting the ends of the diamond specimens with boron ions, as described in earlier sections, and then evaporating a layer of gold onto the implanted electrodes. Another method involved the use of silver paint covering the same region as the implanted contacts, so that the same sample geometry is maintained. The silver paint was then annealed to 70 °C for at least two hours. This method was put into use after we encountered numerous problems with the first one. We have observed that, at $T > 773$ K, the implanted contacts were etched out of the diamond layer, taking with them some of the implanted boron-ion conducting layer. We measured this sample again at low temperatures and recorded a slight increase in its resistivity. Since we were uncertain

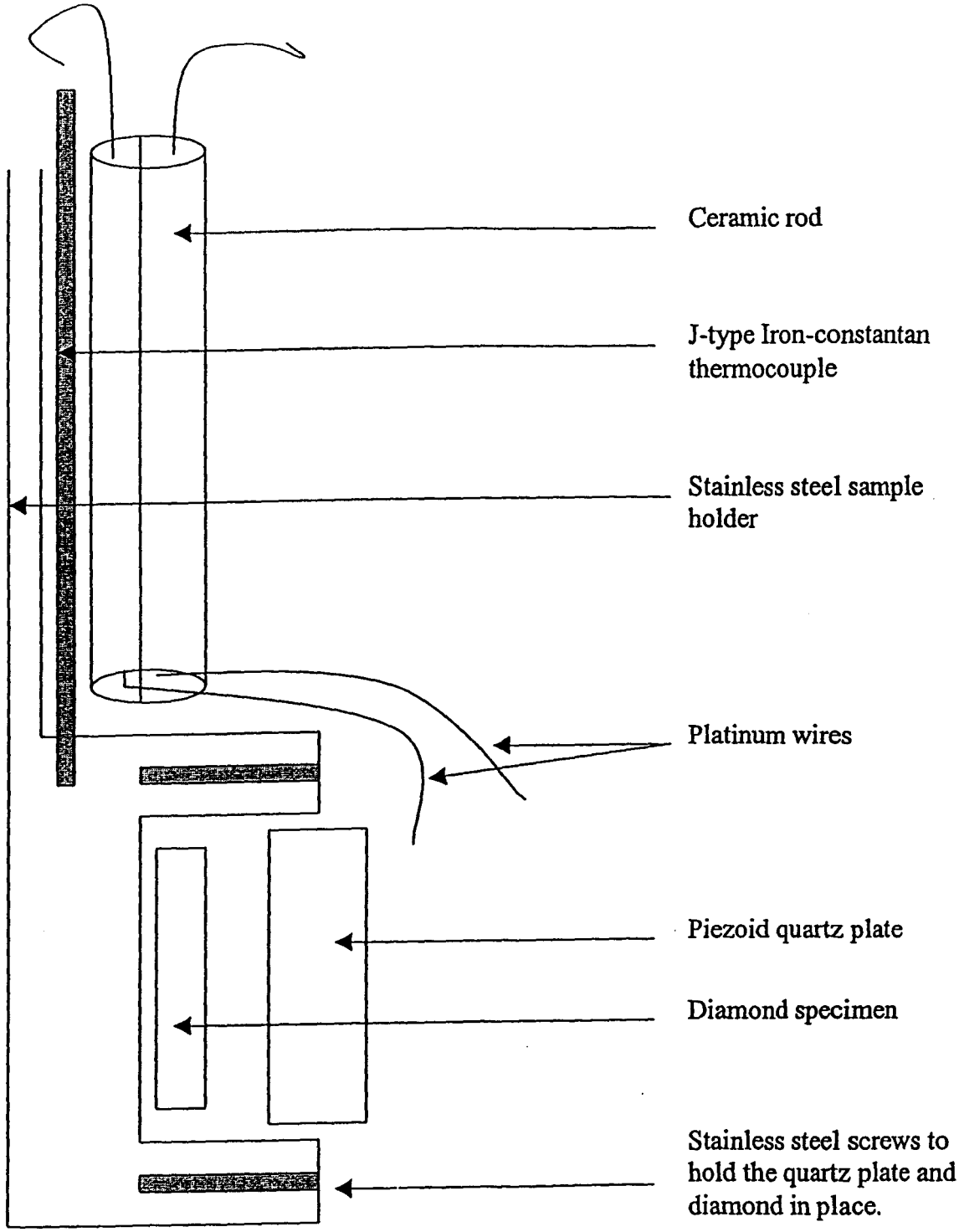


Figure 4-8: A sample holder used in the study of high-temperature conductivity measurements.

about the actual boron concentration in these samples, it was decided that they had to be repolished. An alternative way would have been to carry out the SIMS analysis-a procedure we could not follow due to time constraints. Besides this setback, the evaporated gold strips were completely burned out at $T$ around 773 K. Occurring concomitantly with these incidents was the recorded stray conductance of ceramic, shorting the circuit of our system. Due to these multiple problems, we decided to limit our conductivity measurements to 773 K.

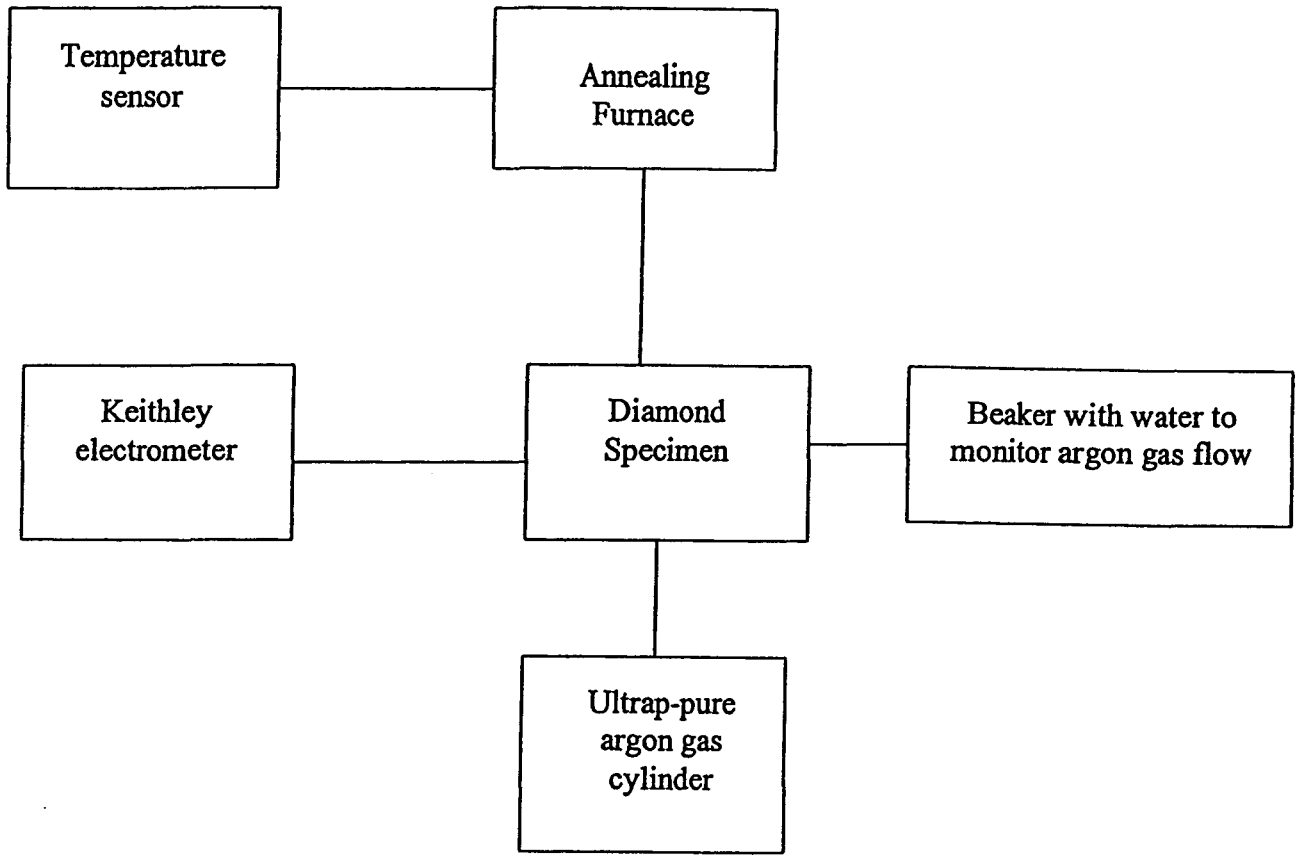


Figure 4-9: A block diagram of the conductivity setup for high-temperature conductivity measurements.

# Chapter 5

# High-temperature annealing results

### 5.0.1 Motivation

A major objective of the present work is to find ways in which we can optimize the implantation-annealing parameters so that we can activate as many of the implanted boron ions into substitutional sites as possible. Our approach is based on the experimental observations made by various authors [5, 120] about the behavior of boron atoms in ion-implanted damaged layers in diamond. It has been found that more and more of the implanted boron-interstitials diffuse out of the damaged cascade when the annealing temperature is increased[120]. This is in clear contrast to the behaviour of carbon self-interstitials[131]. Our expectation is that the probability of self-interstitials recombining with vacancies should grow as the annealing temperature is raised.

We have studied effects of high-temperature annealing on boron-ion doped layers in diamond. This study was carried out by monitoring the electrical resistance as a function of dose and annealing temperature. A wide range of samples implanted progressively from the insulating regime to the vicinity of the metal-insulator transition, using the multiple-step CIRA technique, were used in this study.

## 5.1 High-temperature annealing results

Fig. 5-1 shows plots of electrical resistance *vs.* cumulative boron-ion doses following annealing at 1200 °C. The results were taken at three temperatures, shown in the figure, to demonstrate saturation effects of the point-defects within the ion-implantation damaged layer in diamond. It is apparent in the figure that as the boron-ion dose is increased in the damage cascade, the resistance-dose curves tend to saturation (asymptotic) limit with $R \sim 1$ K$\Omega$.

Fig. 5-2 and Fig. 5-3 show plots of resistance *vs.* temperature for samples AB81 and AB84. These samples have been subjected to anneals at temperatures above 1200 °C. As seen in the figures, the resistance of the samples decreases with increasing annealing temperature. Several reasons which can account for a decrease in the sample resistivity have been suggested. Some of these reasons include the following: the removal or diminishing effects of compensating donors including vacancies and/or a decrease in Anderson disorder (see chapter 2) in this system. We report further on this issue in the discussion section below. As a point of caution, we could not anneal our samples beyond 1700 °C due to the possible graphitization of the implanted layer, particularly for samples which were implanted quite close to the metal-insulator transition. Actually, some of the samples developed a milky colour on the implanted region even when annealed below 1700 °C. In these samples some of the boron-ion doped layers were partly etched out. So we had to repolish the doped layer and start all over again.

The resistance against annealing temperature plots for samples AB81 show a steady drop in resistance with increasing annealing temperature. A drop is expected as long

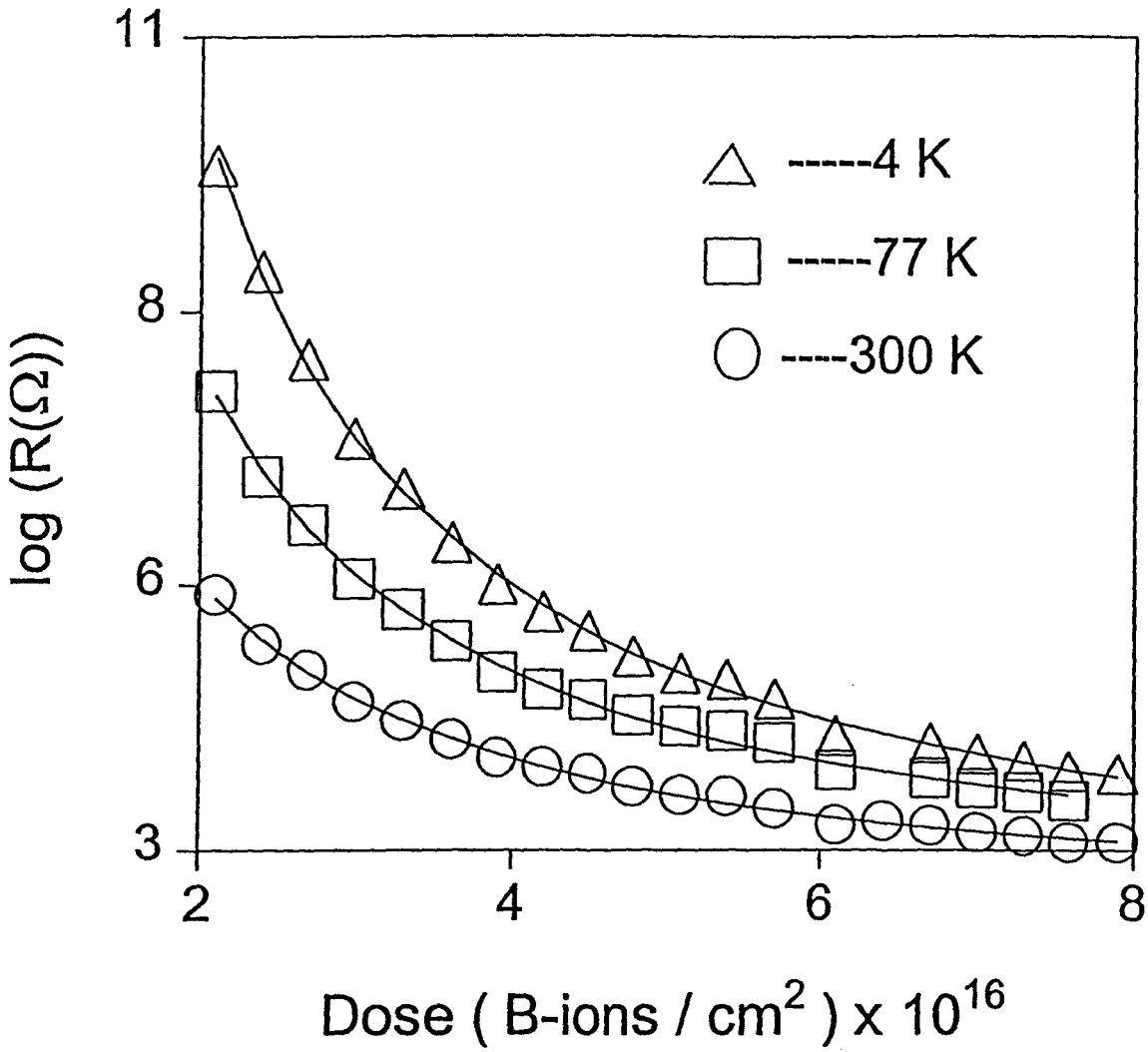


Figure 5-1: Plots of electrical resistance *vs.* cumulative boron-ion dose. Samples have been annealed at 1200 °C for 5 minutes.

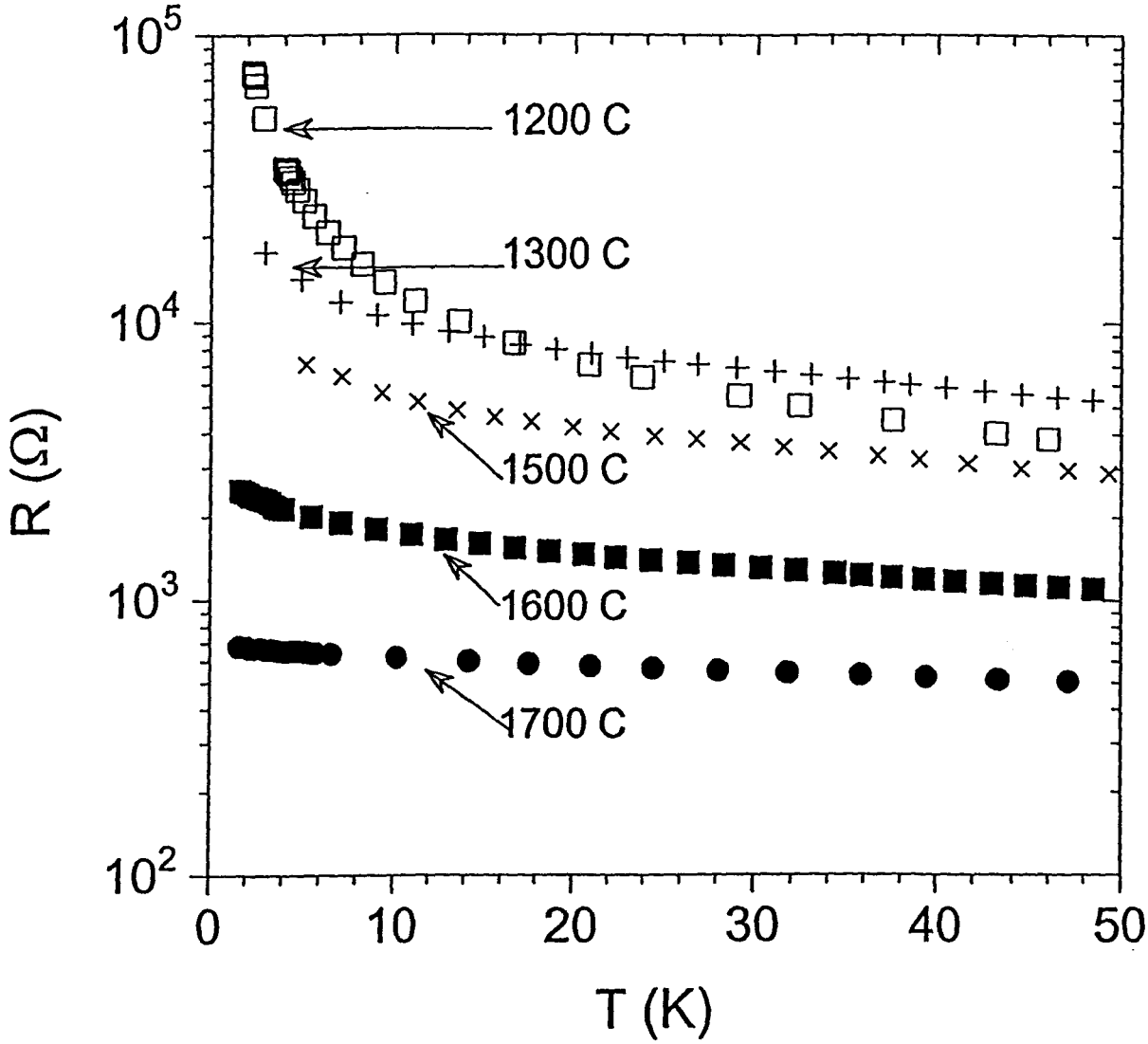


Figure 5-2: Plots of $R$ *vs.* $T$ for sample AB81. This sample was annealed over various temperatures shown in the figure.

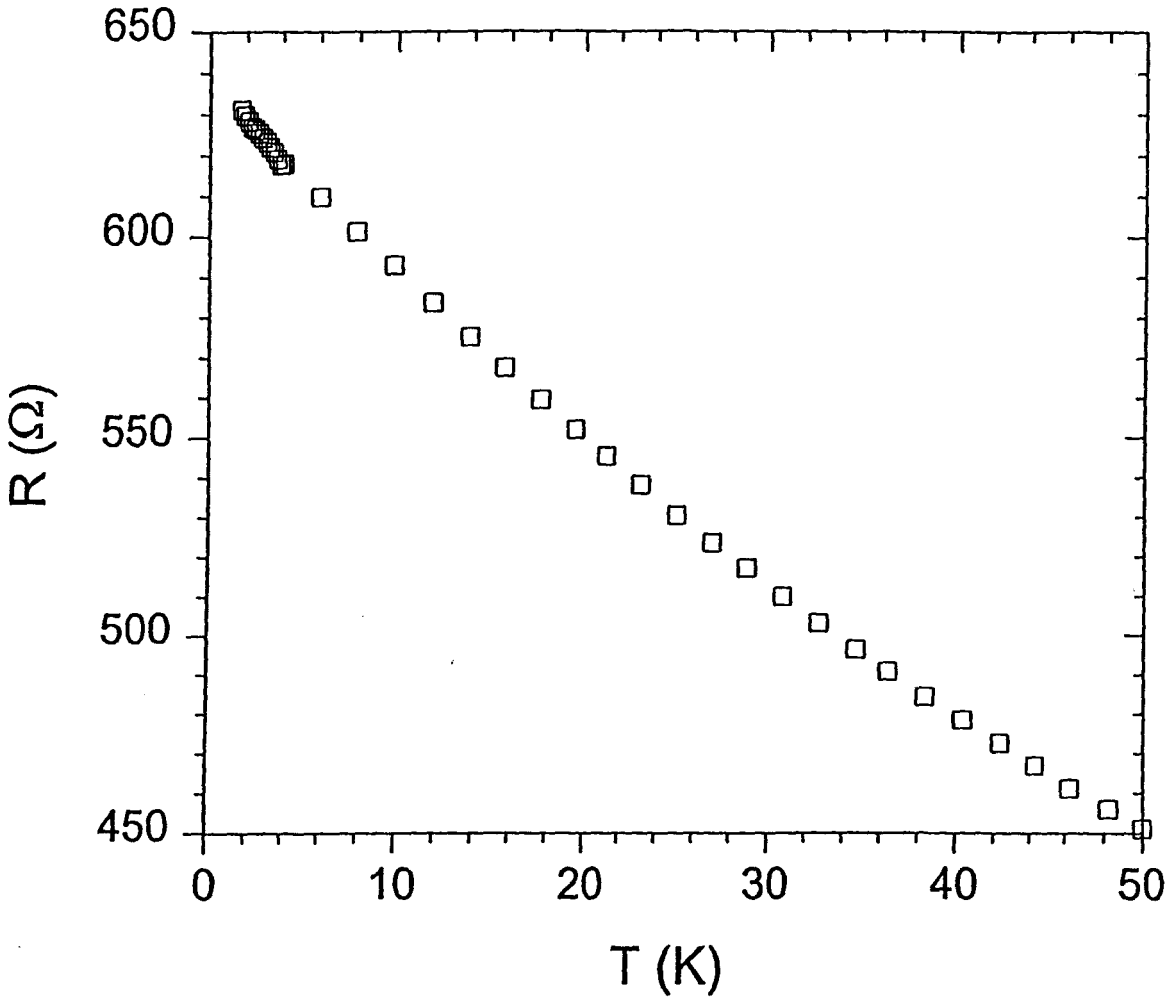


Figure 5-3: Plots of $R$ *vs.* $T$ for sample AB84. This sample was annealed only at 1700 °C after the CIRA routine.

as compensating centres (and/or lattice disorder) are not completely eliminated in this system. Such a possibility (of effectively removing the compensating centres) seems remote in our case owing to the constraints related to annealing under which we have to work. This is also compounded by the fact that diamond is thermodynamically unstable, and can transform permanently to graphite at high-temperatures.

As a fore-runner to the discussion of the experimental results, I give a review of pertinent models which apply in the case of doped diamond.

## 5.2 Theoretical model for the point-defects

Prins[120] has outlined a theoretical model to describe the interstitial-vacancy recombination in an implanted surface layer in diamond during the annealing process. The main purpose of this model is to demonstrate the importance of multiple ion-implantation steps in order to circumvent graphitization of the implanted layer on the diamond surface.

During a high-temperature annealing cycle (on a diamond specimen that was implanted at liquid nitrogen temperature), there will be a continuous dynamic recombination of the point-defects, with self-interstitials recombining with vacancies and dopant interstitials combining with some vacancies. Some of the dopant-interstitials may diffuse out of the implanted layer before recombining with vacancies.

Let the number of interstitials and vacancies created per implantation dose, step $J$, of ions per unit area, be $\alpha J$, where $\alpha$ is the average number of atoms displaced from their lattice positions by a projectile ion. From previous anneals, we would have some residual vacancies, $n_{vr}$, remaining in the damage cascade. Prins showed that the residual

vacancies $n_{vf}$ remaining after the next annealing step can be given by[120],

$$n_{vf} = (n_{vr} + \alpha J) \exp\left[-\frac{\alpha J \kappa \tau_i}{\omega^2}\right] \quad , \tag{5.1}$$

where $\tau_i$ is given by

$$\tau_i = \frac{\omega^2}{\varphi} (\Psi + 1)^{-1} \quad , \tag{5.2}$$

with $\Psi = \frac{\alpha J}{n_{vf} - n_{vr}} - 1$. In the case of dopant ions, it can be shown that[123]

$$\tau_d = \frac{\omega^2}{\varphi_d} \left(1 + \frac{\Psi}{\Gamma}\right) \quad , \tag{5.3}$$

where $\Gamma$ is a constant. The ratios for the self-interstitial-vacancy recombination and dopant-interstitial-vacancy combination have been derived by Prins[120], respectively as

$$R_c = \left(1 + \frac{1}{\Psi}\right)^{-1} \tag{5.4}$$

and

$$R_a = \left(1 + \frac{\Gamma}{\Psi}\right)^{-1} \quad . \tag{5.5}$$

Analysis of Eqs. (5.4) and (5.5) will help us gain some insight into the damage cascade. This is discussed in section 5.6.

## 5.3 Discussion

### 5.3.1 Multiple CIRA sequences

It has been established recently that effective control over the distribution and interactions of point-defects in the ion-damaged layer can be gained by multiple-implantation

sequences[120, 123]. We consider this claim from a theoretical point of view. The main important theoretical predictions derived from the point-defect interaction model are,

$$R_c = \left(1 + \frac{1}{\Psi}\right)^{-1} \quad , \qquad R_a = \left(1 + \frac{\Gamma}{\Psi}\right)^{-1} \quad , \tag{5.6}$$

where $\Psi \equiv \frac{\alpha J}{n_{vf} - n_{vr}} - 1$. If the factor $n_{vf} - n_{vr}$ is kept small, ideally zero, for small implantation steps, then the activation energy increases and more of the implanted boron ions combine with vacancies (residual and newly created) during the follow-up annealing cycle. This means that $\Psi$ will be large and $R_c$ and $R_a$ will approach unity. For the latter to be close to unity, the term $\Gamma$ must be small. This procedure justifies the use of small dose steps, which introduce small numbers of vacancies into the damaged layer and keep $n_{vf}$ just slightly bigger than $n_{vr}$. In other words, multiple implantation steps introduce the implanted ions into an area which already contains vacancies, increasing the probability of vacancy-interstitial recombinations. By following this procedure, the vacancy threshold beyond which the implanted diamond surface layers will be transformed to graphite can be avoided.

### 5.3.2 Residual damage saturation

The TRIM-92 computer simulation program has been used to further probe the generation of residual damage for multiple implantation-annealing sequences. For a boron-ion implantation into diamond, TRIM-92 indicates that the average number of vacancies produced per ion is 183 for an ion accelerated into the target at 120 keV. For diamond, the displacement energy is 35 eV and the binding energy 5 eV. Since a large number of vacancies are generated, they would outstrip the activated dopant-interstitial atoms in the damaged region. The difference becomes even larger following the next implantation-annealing cycle. As more boron ions are implanted into the damaged cascade, the residual damage starts to saturate. We expect the probability for boron activation to increase in

the already saturated layer. Table 5.1 shows the energies, ion dose and the generated vacancies in diamond.

### 5.3.3 Activation of boron ions in implantation-damaged layers

Fig. 5-4 shows plots of the electrical resistivity vs. inverse temperature for sample DB12 (square sample) annealed at 1300 °C, 1500 °C and 1700 °C. The sample has been implanted to a total dose of $1.2 \times 10^{16}$ cm$^{-2}$ ($\sim 4.8 \times 10^{21}$ cm$^{-3}$). It is difficult from Fig. 5-4 to fit straight lines to determine slopes and hence determine the activation energy over the entire temperature range measured. This means that transport in this system is not activated but occurs via non-nearest-neighbour hopping sites. It has been argued that these hopping centres may be associated with excess vacancy clusters (agglomerates) which have been dispersed randomly in the ion-damaged layer[128, 143, 144].

Our experimental results do not indicate that more of the subsequent implanted boron atoms escape the damaged layer during high-temperature annealings, as reported recently by Prins[120] on similar systems. This may indicate that boron atoms become even more 'severely' compensated upon further ion implantations.

| Ion | Energy (keV) | Dose ($cm^{-2}$) $\times 10^{14}$ | vacancies ($cm^{-2}$) $\times 10^{16}$ |
|---|---|---|---|
| B | 130 | 11.25 | 20.6 |
| | 110 | 3.75 | 6.49 |
| | 90 | 1.875 | 3.13 |
| | 80 | 1.875 | 3.02 |
| | 70 | 1.875 | 2.74 |
| | 60 | 1.875 | 2.57 |
| | 50 | 1.875 | 2.34 |
| | 40 | 1.875 | 2.08 |
| | 30 | 1.875 | 1.78 |
| Total | $\rightarrow$ | $3.0 \times 10^{15}$ $cm^{-2}$ | $4.17 \times 10^{17}$ $cm^{-2}$ |

Table 5.1: Ion energies and ion doses used to generate a boron-ion layer in a diamond specimen. The created point-defects are homogeneously distributed in the implanted layer. The vacancies created following each implant have been calculated using the TRIM-92 simulation code in which the displacement energy of 35 eV and the lattice binding energy of 5 eV were assumed.

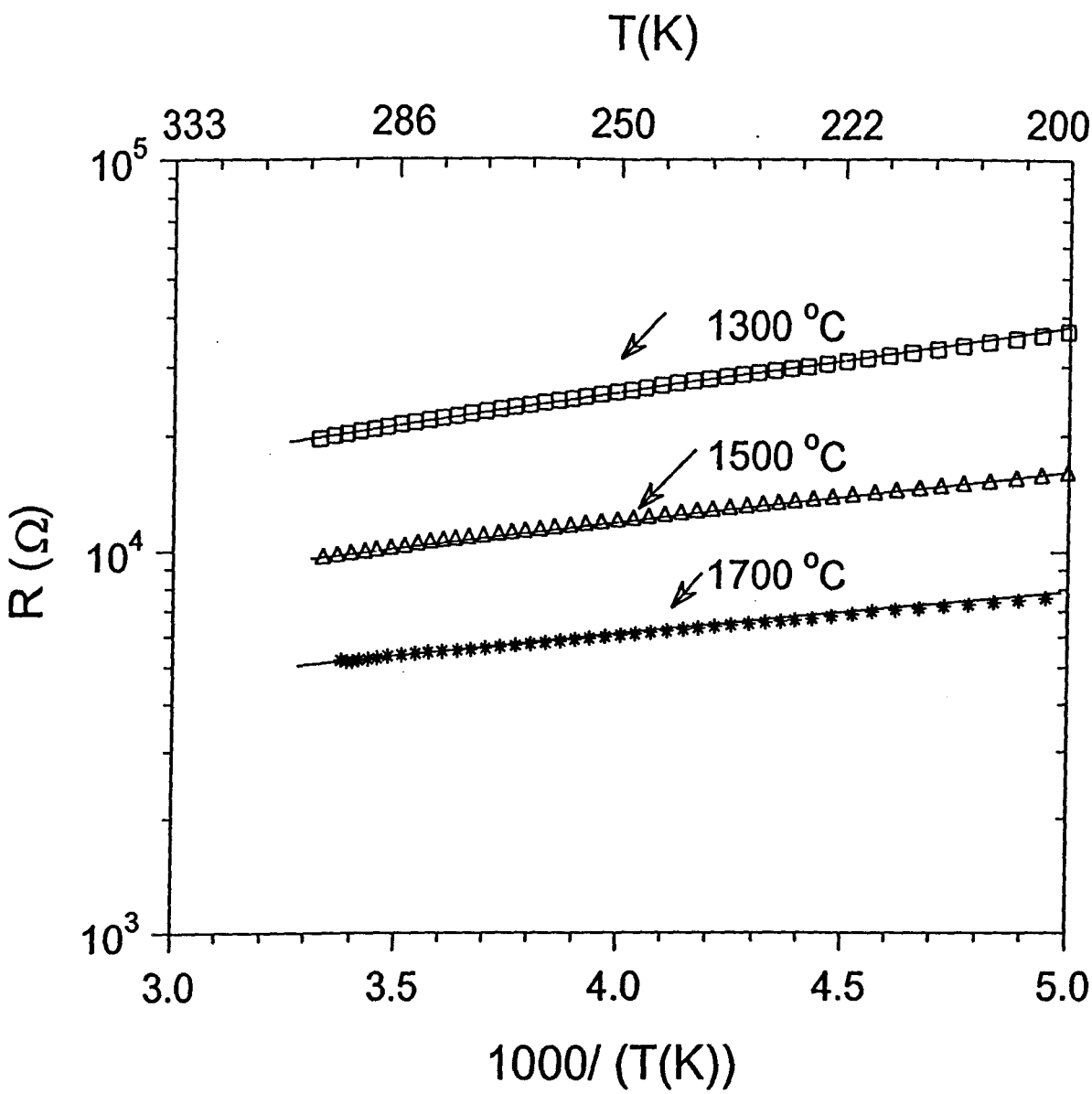


Figure 5-4: Plots of $R$ *vs.* $1/T$ for sample DB12 (square sample) annealed at 1300 °C, 1500 °C and 1700 °C.

## 5.4 Summary

Optimization of different parameters to get high quality and reproducible boron-ion doped layers in diamond is the key in this study. This involves carrying out multiple post annealing cycles at high-temperatures following the CIRA steps. We have done this to a number of samples which have been implanted with low boron-ion doses, and to some samples implanted closer to the amorphization threshold value. Both experimental observations and theoretical predictions render a consistent picture on the nature and behaviour of residual point-defects in ion-implantation radiation damaged layers.

We started annealing our boron-ion implanted diamond ($\diamond$C:B ) samples at 1200 C until a total boron-ion dose of $7.8 \times 10^{16}$ cm$^{-2}$ was reached. To reach this dose level, a multiple CIRA routine was used and the dose spread out in small energies. The total dose administered to the sample per CIRA treatment was $0.3 \times 10^{16}$ cm$^{-2}$. The annealing cycle was limited throughout to 5 minutes. Annealing over extended periods had an insignificant impact on the experimental results. We carried out a SIMS analysis on this sample to determine the concentration of boron atoms in the surface layers. SIMS measurements estimated the concentration to be $\sim 3.6 \times 10^{21}$ cm$^{-3}$, which corresponds to the dose level of $7.3 \times 10^{16}$ cm$^{-2}$. This means about 94% of the implanted boron atoms were "locked-in" the implanted layer. We managed to trap almost all the implanted boron-ions in samples that have been implanted deep in the insulating side of the transition.

After reaching a residual damage saturation in some samples which have been heavily implanted, we carried out some post rapid temperature anneals. Samples were annealed from 1200 °C to 1700 °C for ten minutes at each temperature in incremental steps of 100 $^0$C. The results are shown in Fig. 5-2. It can be seen from the plots that the resistance of these samples decreases with increasing annealing temperature. A decrease in resistance

indicates two phenomena: an efficient activation of boron interstitials accompanied by a self-interstitial-vacancy recombination to further reduce the lattice damage, and, secondly, a reduction in the electrical activity of excess vacancy agglomerates. At 1700 °C, a major fraction, if not all, of the boron atoms would have combined with vacancies. Some samples, particularly the insulating ones, were annealed at 1200 °C followed by a 1700 °C anneal, and a significant drop in resistance was observed.

In brief, high-temperature anneals following the cold-implantation process has provided further insight into the nature, interaction and behaviour of point-defects within the damaged cascade. The complexities associated with these point-defects are still being studied.

# Chapter 6

# Percolative transition in carbon-ion implanted type II$a$ diamond

Electrical conductivity studies on diamond single crystals, implanted with carbon ions using the CIRA technique, have been carried out as precursors to the study of electronic properties of boron ions in diamond. The objectives of the work presented in this chapter are to demonstrate the importance of multiple implantation steps in the characterization of diamond samples, and the sensitive dependence of the conductivity on the type of ion one uses in the implantation process.

### 6.0.1 Motivation

Implanted layers created with carbon ions using the CIRA routine for ion doses exceeding the critical threshold dose are the subject of the present investigation in type II$a$ diamond. This work also explores transport phenomena in the vicinity of the M-I transition, and deep into the insulating phase in which a low-temperature conductivity crossover between the Mott VRH and Efros-Shklovskii VRH is demonstrated.

## 6.1 Introduction and a general overview

The transformation that a natural diamond crystal undergoes, from a purely insulating state into a highly conducting form of carbon, as a result of ion-implantation, has been studied for many years. Early pioneering work on ion implantation has been carried out by Vavilov *et al.*[116] , who implanted their diamond specimens with a variety of ion species and monitored the changes in the electrical conductivity, $\Delta\sigma$, as functions of dose and temperature. General surveys which include in-depth discussions, figures and models which offer insight into the processes involved in the implantation and annealing can be found in a recent book by Dresselhaus and Kalish[5], and in comprehensive review articles by Prins[118] and Kalish[145, 146, 147].

Studies reveal that the transformation of diamond, subject to ion implantation, is not a sudden process. The diamond structure undergoes a transitional state in which it is first transformed to an amorphous phase ($a$-$sp^3$) and then collapses into an amorphous $sp^2$ graphite phase ($a$-$sp^2$). The difference between these amorphous carbon states is that the $a$-$sp^3$ state is highly insulating and still has characteristic properties similar to those of amorphous diamond[146], whereas the $a$-$sp^2$ graphitic state is a highly conductive form of carbon. The conversion from $a$-$sp^3$ to $a$-$sp^2$ occurs at doses far exceeding those required for $a$-$sp^3$ amorphization. Kalish[146] has listed a number of factors which inhibit the immediate graphitization of diamond during ion implantation. These factors include the following:

- The transformation of a diamond crystal into a graphitic form is governed by an increase in density of defects[143]. The density of defects is determined by the amount of energy transferred during nuclear collisions to each target atom, and the implantation temperature. The volume density of point defects is cumulative, since each ion, irrespective of its energy, cannot by itself induce surface graphitization[146]. This means that the implanted volume has to be hit several times by a number of

projectile ions. It is then on further implantations, and the breakage of more $a$-$sp^3$ diamond bonds, that the affected volume spreads out to form a 'sea' of $sp^2$ graphite bonds.

- There should be a threshold damage level (*i.e.* a critical ion dose) in implanted diamond beyond which the diamond structure cannot be recovered any further even by high-temperature annealing, but will instead transform to the graphite phase[145].

Some notable changes occur as the diamond transforms into a graphitic form. These changes include the following:

(i) a large increase in the electrical conductivity,

(ii) a decrease in material density,

(iii) a mechanical weakening of the diamond,

(iv) the appearance of new optical absorption lines and

(v) changes in chemical properties. (Graphite is etchable while diamond is chemically inert to aggressive acids.)

All these changes that diamond undergoes as a result of implantation have been discussed by a number of authors in the book on diamond properties edited by Field[3].

Early work, similar in some respects to that reported in this chapter, has been carried out by Hauser *et al.*[128], in which they measured the electrical conductivity in carbon-ion implanted diamond specimens over the temperature range 20-300 K. Their work on diamond is reviewed below.

Hauser and co-workers[128, 144] have implanted diamond specimens at $\sim$ 295 K (room temperature) using carbon-ions. They selected doses ranging from $3 \times 10^{15}$ to $6 \times 10^{16}$ cm$^{-2}$, spread over energies 70, 40 and 20 keV to create a fairly homogenous

carbon implant profile in their specimens. The thickness of the implanted layer was estimated to be $\sim$ 100 nm. They measured the temperature-dependent resistivity $\rho(T)$ from room temperature down to 20 K. The results from their second publication[144] are shown in Fig. 6-1. Their data follow the phonon-assisted variable-range hopping (VRH) conduction process[8] over the measured temperature range. (See chapters 2 and 8 for discussions on VRH conduction mechanisms.) A departure from this transport process occurs for the lowest dose near room temperature, in which case the resistivity follows a thermally activated process with an activation energy, extracted from the data, of 1.7 eV. For the highest implanted carbon-ion doses, the authors have observed metallic-type conduction close to that of graphite. It was concluded from these measurements that a large increase in the electrical conductivity may be related to the formation of $sp^2$-bonded microcrystallite graphitic islands (regions or clusters)[148] in diamond, and that these graphitic islands act as the hopping centres. However, from the hardness measurements, Hauser *et al.* found the implanted layers to be still diamond-like in mechanical properties.

Prins[119] has shown that for carbon-ion implanted diamonds, there is a critical implantation threshold beyond which the properties of the implanted layer change in a dramatic fashion. The CIRA layers take on a dark colour and the electrical conductivity increases very rapidly in the interval $5 \times 10^{15}$ cm$^{-2}$ to $6 \times 10^{15}$ cm$^{-2}$ for $C^+$-ions. The properties of layers generated in this way are highly reproducible with ion dose[149, 150].

A different approach to the onset of conductivity in carbon-ion implanted diamond specimens was proposed by Kalish *et al.*[143]. Their recent work in this direction has been published in refs.[129, 145]. Kalish *et al.* implanted a number of species into diamond crystals held at various temperatures. They found that the electrical conductivity changes dramatically with increasing dose in the vicinity of the critical dose, $D_c$, and that $\sigma(T, D)$ follows a sharp percolation transition for samples implanted at elevated temperatures. In the case of carbon implants, they found that $\sigma$ *vs.* $D$ was not sharp

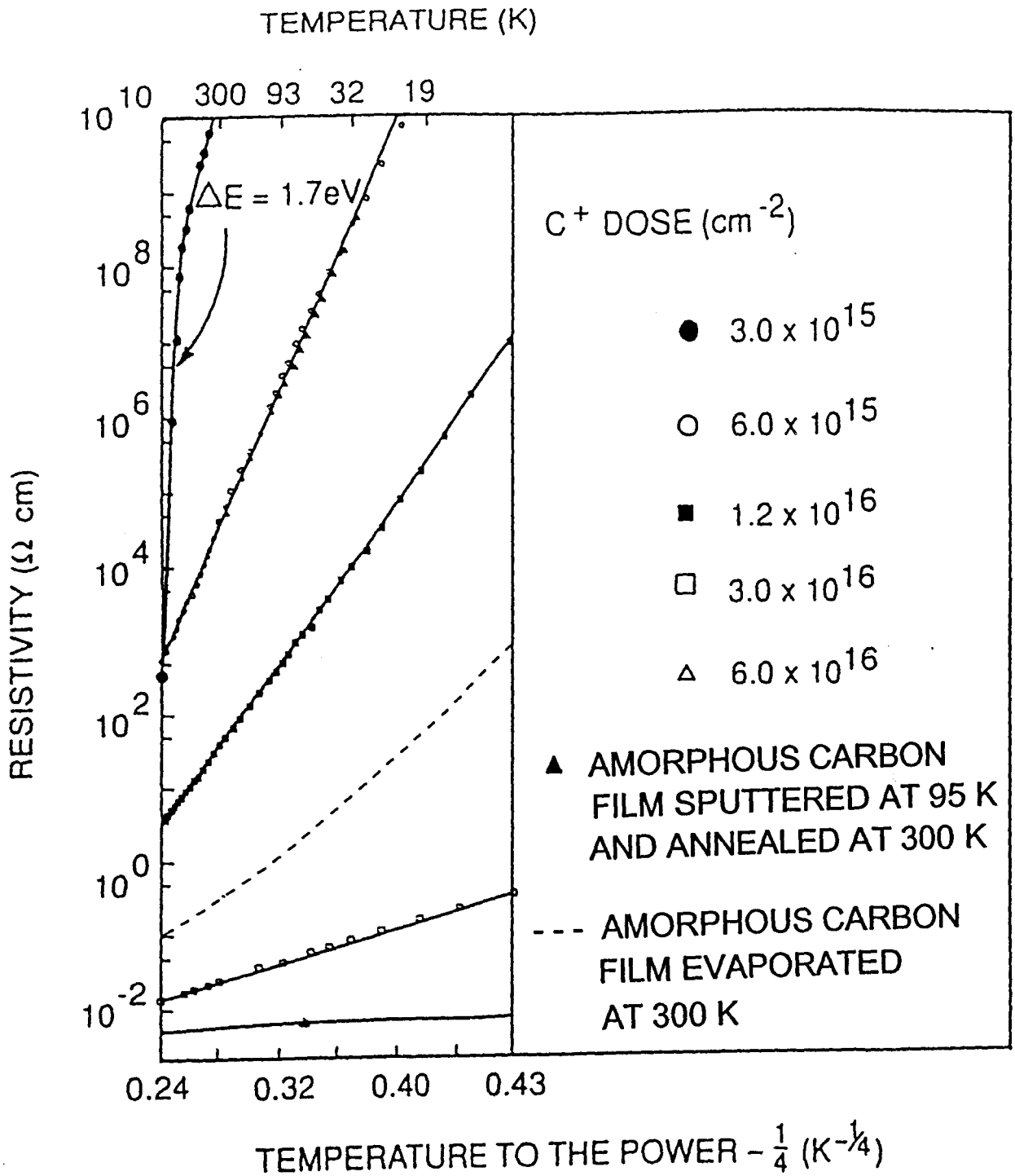


Figure 6-1: The resistivity data of Hauser *et al.* [141] described by the Mott VRH relation over the temperature range 20-300 K.

enough to be accounted for by either a sharp percolation transition or a critical energy density amorphization model for the transition.

## 6.2 Percolation theory

Percolation theory is one of the mathematical techniques widely used to analyze transport phenomena in spatially random systems. The origin of percolation theory is attributed to Broadbent and Hammersley[151] who introduced lattice models for the flow of a fluid through a random medium and argued, using probabilistic and geometric concepts, that no fluid will flow if the concentration of active medium (pores) is smaller than some nonzero percolation threshold value. A percolation threshold is a point of the transition between states of short-range connectivity and long-range connectivity in which properties of a percolation system suddenly change when a concentration of conducting sites is continuously increased. General applications of the percolation theory, in a variety of systems, can be found in review papers[152, 153, 154, 155] and a recent book by Stauffer and Aharony[156].

According to the percolation theory, two distinctive electronic conduction regimes can be identified depending on the concentration (volume fraction) of the conducting bonds or sites $\Phi$. When $\Phi$ is large, conducting centres form a connected metallic network so that electrons can percolate directly through the metallic connected pathways. In this metallic regime, the microgeometry (*i.e.* size, shape and orientation)[157, 158, 159, 160, 161, 162] of metallic channels plays an important role in the actual sample conductivity. When $\Phi$ is small, the metallic conducting centres are randomly distributed in an insulating matrix. Transport of charge carriers between the localized metallic clusters, dispersed in this dielectric regime, is mediated by phonons. The two conduction regimes (metallic and

insulating) are characterized by a percolation threshold at which the conducting metallic backbone first becomes disconnected. Kalish *et al.*[143] have presented the above scenario in a very interesting and elementary fashion.

In the vicinity of the percolative metal-insulator (M-I) transition, the dc-conductivity between any nearest neighbour conduction sites is described by the relation

$$\sigma = \sigma_o (\Phi - \Phi_c)^v \quad \text{for } \Phi > \Phi_c \quad , \tag{6.1}$$

where $\sigma_o$ is a proportionality constant, $\Phi_c$ is the critical metallic volume fraction of the dopant carbon ions and $v$ is the critical exponent which depends on the sample dimensionality. This exponent indicates whether the M-I transition is driven by disorder with $0.5 < v < 1$, or is forced by geometrical constraints leading to a classical percolation threshold at $\Phi_c$ with $1.5 < v < 2$[163, 164]. The $v$ values have been found to be system-dependent[165, 166].

According to Kalish *et al.*[143], the percolation conductivity within the framework of the effective medium theory can be expressed as

$$\sigma(T) = \sigma_o \left(1 - B^{\frac{D}{D_c}-1}\right) \quad , \tag{6.2}$$

where $\sigma_o$ is the conductivity of the amorphous regions, B = 1/2 in 2-dimensions (2-D) and B = 2/3 in 3-D, while $D_c$ is the critical dose level for the onset of metallic conductivity. Equation (6.2) is only valid at $D > D_c$ (*i.e.*, above $\Phi_c$), and can also be written as[129]

$$R = R_s \left(1 - B^{D/D_c - 1}\right)^{-1} \quad , \tag{6.3}$$

where $R_s$ is the saturation resistance at high doses. We have used Eq. (6.3) to analyze our experimental data.

## 6.3 Experimental results

Fig. 6-2 shows plots of electrical resistance against temperature for various carbon-ion implanted diamond specimens. The carbon dose level that we have studied spans the range $5.60 - 5.95 \times 10^{16}$ cm$^{-2}$. In spite of the narrow range of the dose level measured, Fig. 6-2 shows a dramatic drop in the electrical resistance of five orders of magnitude at low temperatures.

It is now an established practice to plot $R$ *vs.* $T^{-m}$ (where $m = 1/4$ and $1/2$) to determine which of the VRH laws best describes the experimental data. Though the method is not very reliable due to its applicability over a small experimental $R - T$ data region, it nonetheless remains a useful tool to probe the nature of the VRH behaviour in doped semiconductors. Plots generated using this procedure are shown in Fig. 6-3. It is evident in Fig. 6-3(a) that the Mott VRH law is applicable at high-temperatures (~100-300 K), and that this changes to ES VRH relation at lower temperatures (4-100 K) (6-3(b)).

To determine $m$,which characterizes the nature of the VRH behaviour as either of Mott of ES VRH type, we have used the Hill and Jonscher[75] and Zabrodskii and Zinov'eva [76] approach (The details can be found in chapter 2). A Zabrodskii-Zinov'eva type plot is shown in Fig. 6-4 for a wide range of carbon-ion implanted diamond specimens.

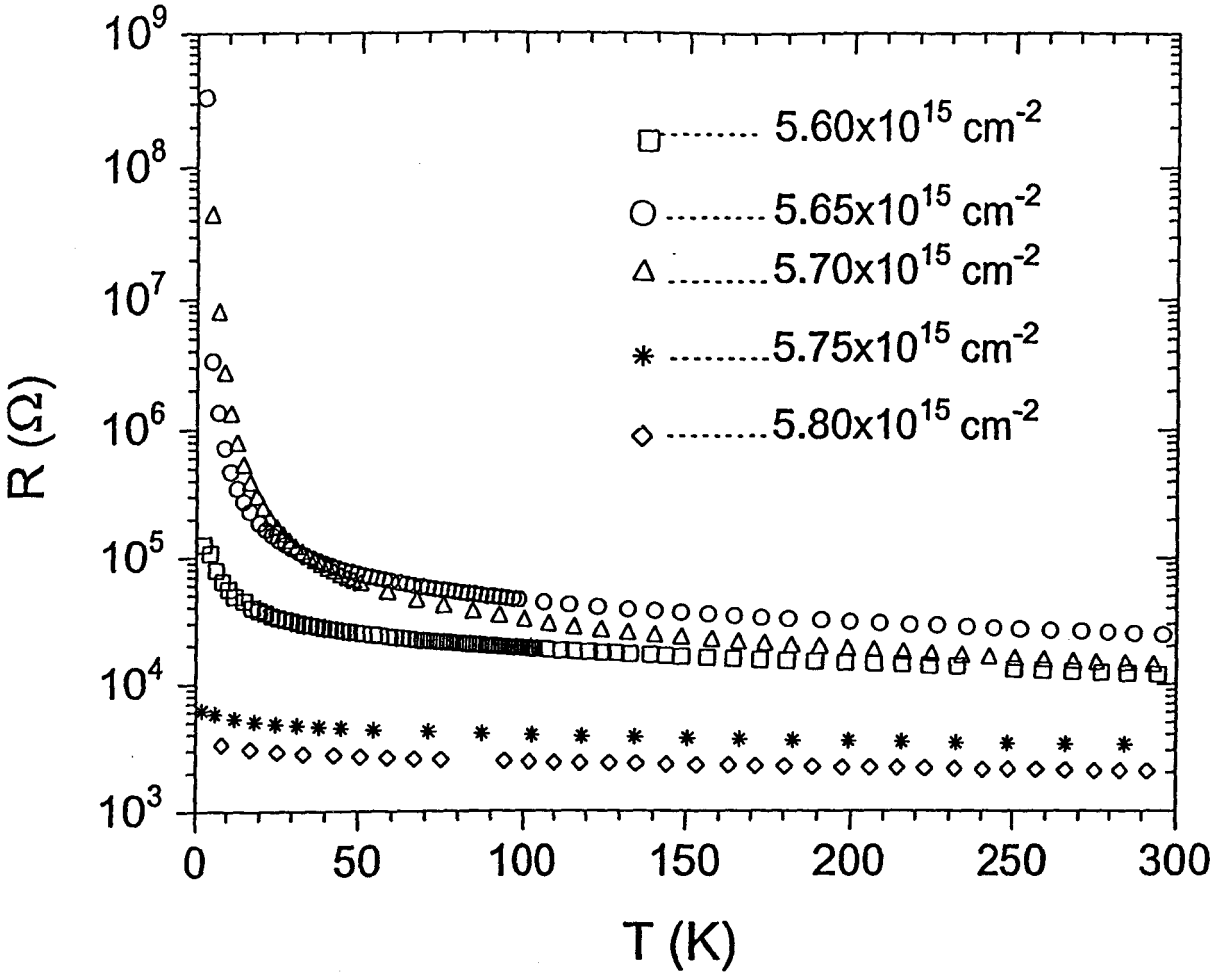


Figure 6-2: Plots of electrical resistance against temperature for various carbon-ion implanted diamond specimens. Symbols and sample designations are given in the figure.

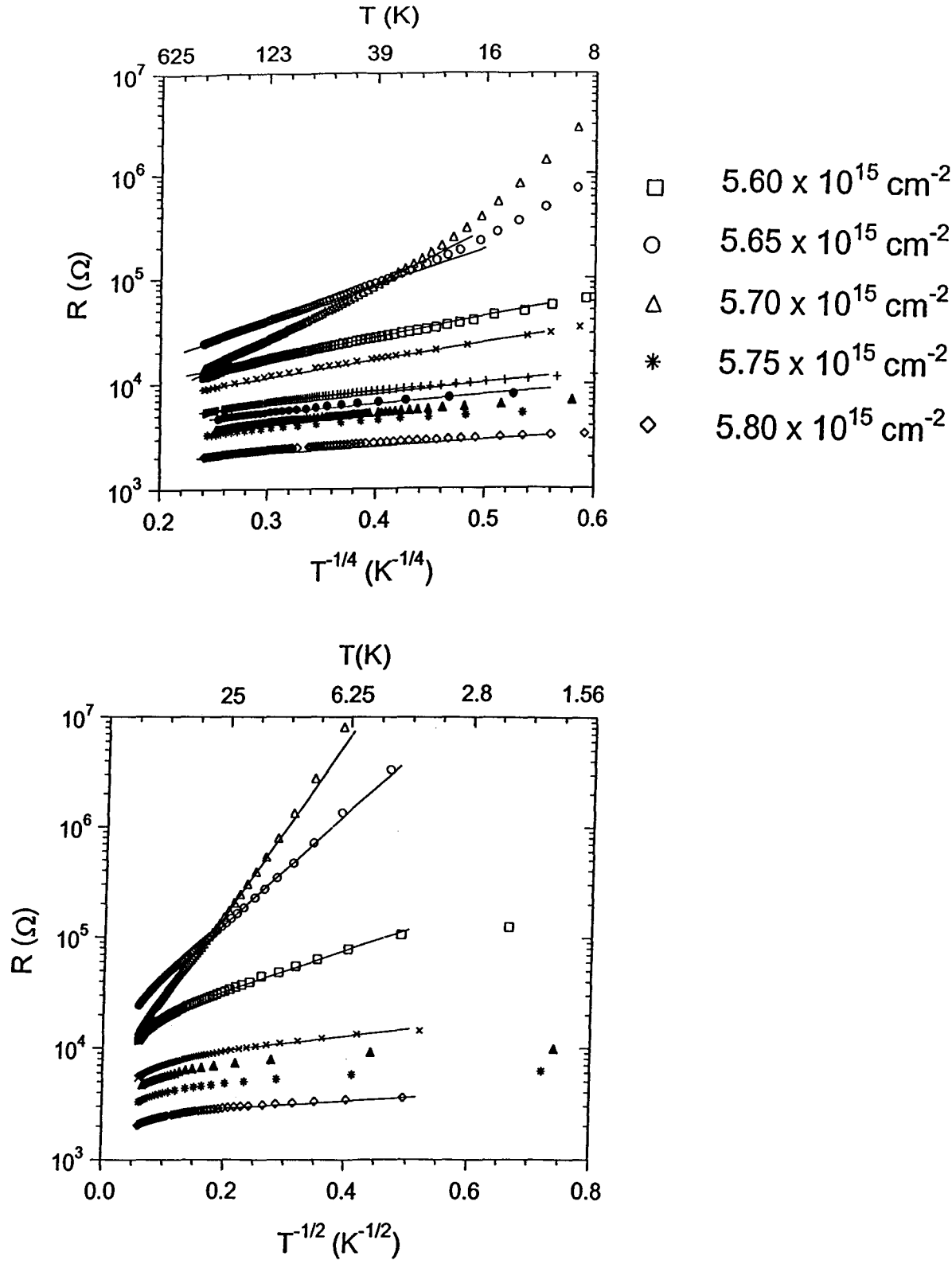


Figure 6-3: Plots of $R$ *vs.* $T^{-m}$ ($m = 1/4$ and $1/2$) to determine which of the VRH laws best describe the experimental data.

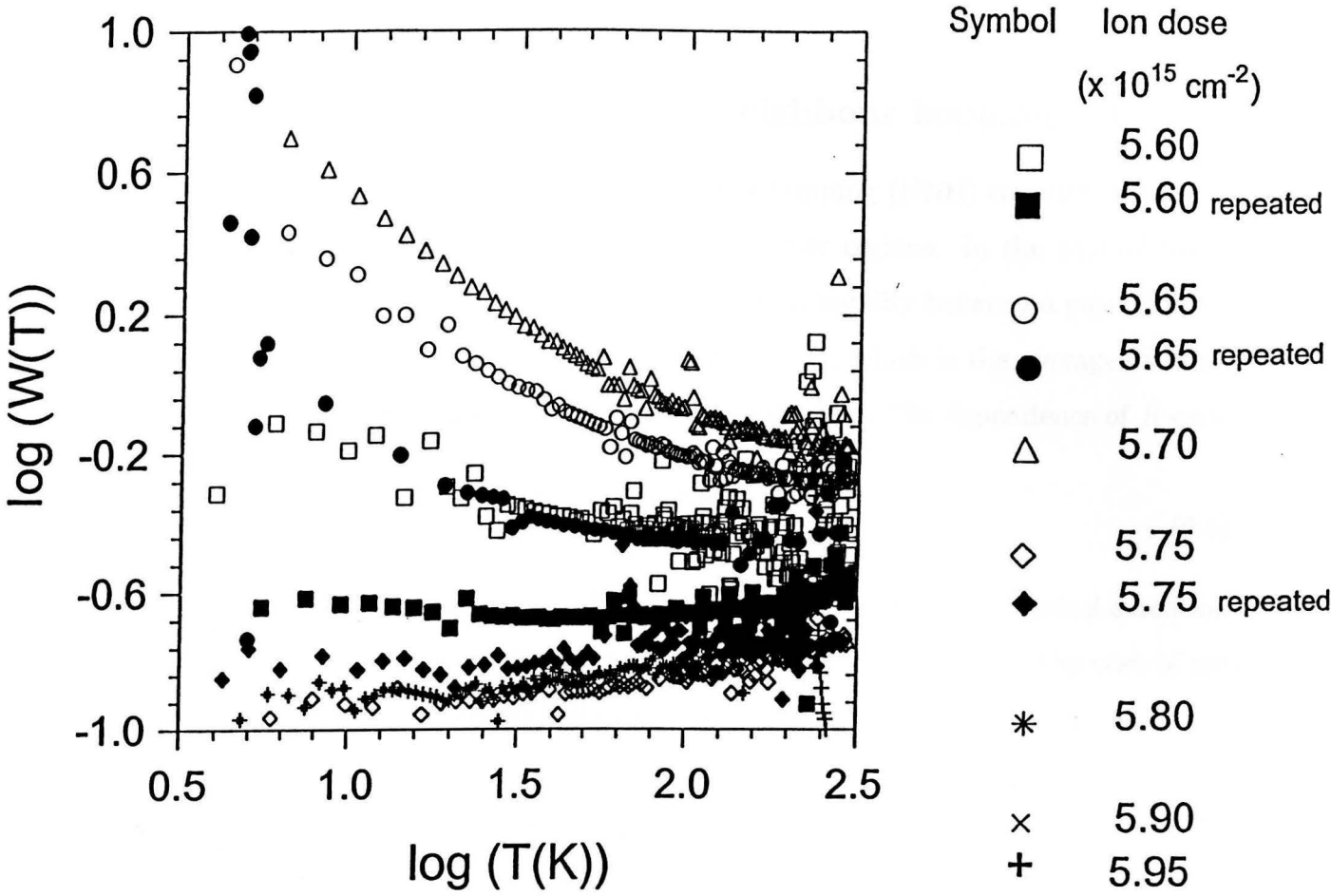


Figure 6-4: The Zabrodskii-Zinov'eva plot to determine $m$. Due to the sensitive dependence of the electrical conductivity on the carbon-ion dose in the narrow percolation regime studied, the results were found not to be reproducible. The carbon-ion doses implanted into the diamond samples are listed in the figure.

## 6.4 Discussion

## 6.5 Insulating samples

### 6.5.1 Conduction via the nearest-neighbour hopping sites

For ion doses well below $D_c$, the nearest-neighbour hopping (NNH) conduction mechanism is expected to occur between the graphitic cluster regions. In the case of NNH, the electrical resistance is governed by the tunneling probability between a pair of defect states separated by a distance of a typical order of $n^{-1/3}$, which is the average distance between graphitic clusters whose volume concentration is $n$. The dependence of $R$ on $n$ is given by[143],

$$R \propto \exp\left(\frac{\gamma n^{-1/3}}{\alpha}\right) \quad , \tag{6.4}$$

where $\gamma$ is a numerical factor of the order of unity. and $\alpha$ describes the spatial extension of the localized electronic wave function. It has been suggested that in the case of ion implantation $n$ should be proportional to the ion-dose $D$ (in ions/cm$^2$)[143],

$$n = \vartheta \frac{D}{R_p + \Delta R_p} \quad . \tag{6.5}$$

Here $\vartheta$ is a numerical coefficient equal to the number of hopping centres created by each incident ion. $R_p$ and $\Delta R_p$ are the projectile range and straggling, respectively. Substituting Eq. (6.5) into Eq. (6.4) gives the expression[167]

$$R \propto \exp\left[\frac{\gamma}{\alpha}\left(\frac{\vartheta}{R_p + \Delta R_p}\right)^{-1/3} D^{-1/3}\right] \quad . \tag{6.6}$$

A plot of log $(R)$ against $D^{-1/3}$ should yield a straight line. Our experimental data do not follow this behaviour. I also tried plotting $R$ *vs.* $1/T$ to see if the activated transport mechanism occurs in this system at high temperatures. It is difficult from these plots to isolate linear regions unless a small segment of the experimental data is selected for

analysis. The NNH mechanisms could not be observed due to the fact that the density of the least doped samples was insufficient for this process to occur.

### 6.5.2 Conduction by variable-range hopping mechanism

The failure of the NNH mechanism obviously suggests that transport in this system is by VRH. This is indeed so, since plots shown in Fig. 6-3(a,b) yield some linear regions. An electrical conductivity crossover between an exponent of 1/4 and an exponent of 1/2 as the temperature of the system is lowered is clearly evident from Fig. 6-4. The empirical crossover temperature, $T_{cross}$, between the Mott ($m = 1/4$) and the electron-electron interaction ( $m = 1/2$) VRH regimes can be defined where the slopes of $-1/4$ and $-1/2$ intersect. We observe from Fig. 6-4 that $T_{cross}$ decreases with increasing dose, which is indicative of the narrowing of the Coulomb gap[168]. Because of the sharp percolative transitional nature of our system, one needs to be cautious with the classification of samples as either insulating or metallic. According to Thomas *et al.*[99, 169], positive slopes are taken to be indicative of insulating behaviour of samples and negative slopes are associated with metallic conductivity. Recently, Möbius *et al.*[13, 14] have argued that one needs to extrapolate the $W - T$ curves to absolute zero temperature before any information on the behaviour of $\sigma(0)$ can be obtained.

To examine whether the carbon-ion doped system undergoes a dimensional crossover, we need to calculate the temperature-dependent hopping length, $R_{opt}(T)$ and compare it to the thickness, $t$, of the implanted layer. If $R_{opt} > t$, then the system is 2-D and if $R_{opt} < t$, it is 3-D.

Adkins[170, 171] has presented a model for systems which percolate near the M-I transition. He describes, in the case of 3-D, a parabolic density of localized electronic states at the Fermi energy using an expression,

$$g(E_F) = \left(\frac{3^8\pi^2\epsilon_o^3}{2^5e^6}\right)\epsilon_r^3\,E^2 = \left(1.55\times10^{85}\ \mathrm{J^{-3}m^{-3}}\right)E^2 \quad , \tag{6.7}$$

taking the dielectric permittivity of diamond, $\epsilon_r = 5.7$. Some doubts have been raised recently about the reliability of this dielectric permittivity, $\epsilon_r$[171]. This is due to the fact that $\epsilon_r$ increases rapidly as the M-I transition is approached from the insulator side, and diverges right at the transition. The temperature-dependent tunneling exponent, $\alpha$, in the ES VRH regime is given by [171, 172, 173]

$$\alpha = \frac{1}{10.5}k_BT_{ES}\,(\pi g_{ES})^{1/3} \simeq 4.8\times10^4\,T_{ES}(\mathrm{K})\ (\mathrm{m^{-1}}) \quad . \tag{6.8}$$

The maximum hopping distance in the ES VRH regime, according to Adkins[172], is given by

$$R_{opt} = \frac{1}{4\alpha}\left(\frac{T_{ES}}{T}\right)^{1/2} = 5.208\times10^{-6}\,(T\,T_{ES})^{-1/2} \quad . \tag{6.9}$$

At $T = 100$ K and 4 K, $R_{opt} = 46$ nm and 232 nm, respectively. The latter value is close to the estimated penetration depth of 215 nm determined using the TRIM92 computer simulation program. This may suggest that our carbon-ion doped diamond samples are in the borderline of between 2-D and 3-D. Further measurements on a wide range of samples, in relation to the implantation energies and doses, are needed to confirm whether our samples are indeed 2-D. Table 6.1 lists some variables extracted from the VRH equations.

Let us consider, for example, the dose fluence $5.60\times10^{15}$ cm$^{-2}$. We have calculated the characteristic temperatures for this dose to be $T_M = 2263$ K and $T_{ES} = 149$ K. According to Eq. (2.5), *viz*, $T_M = 18\alpha^3/(k_BN_o(E_F))$, we can calculate the localized electronic DOS at the Fermi energy $N_o(E_F) = 2\times10^{41}$ J$^{-1}$m$^{-3}$ $= 3.4\times10^{16}$ states (eV$^{-1}$ cm$^{-3}$). This value is two orders of magnitude less than that calculated by Prawer and Kalish on diamond which had been irradiated with a total carbon-ion dose of $8\times10^{16}$ cm$^{-2}$[129],

**Insulating samples ↓**

| Sample | Dose | Symbol | Temperature | $R_o(\Omega)$ | $T_o$ (K) | $m$ |
|---|---|---|---|---|---|---|
| Name | ($\times 10^{15}$ cm$^{-2}$) | | range (K) | | | |
| C560 | 560 | □ | 300 – 100 | 239 | 2263 | 0.20 |
| | | | 100 – 4 | 52 | 149 | 0.48 |
| C565 | 5.65 | ○ | 300 – 100 | 655 | 5203 | 0.22 |
| | | | 100 – 4 | 47 | 127 | 0.51 |
| | | | 50 – 4 | 20284 | 75 | 0.65 |
| C570 | 5.70 | △ | 160 – 100 | 1286 | 9656 | 0.25 |
| | | | 100 – 4 | 10796 | 118 | 0.66 |
| | | | 50 – 4 | 11650 | 109 | 0.67 |

| Sample | Dose | Symbol | $R_{hop,M}/\xi$ | $R_{hop,ES}/\xi$ | $\alpha$ (m$^{-1}$) | $\xi$(nm) |
|---|---|---|---|---|---|---|
| Name | ($\times 10^{15}$ cm$^{-2}$) | | | | $\times 10^6$ | |
| C560 | 5.60 | □ | $2.59/T^{1/4}$ | $3.05/T^{1/2}$ | 7.15 | 140 |
| C565 | 5.65 | ○ | $3.19/T^{1/4}$ | $2.82/T^{1/2}$ | 6.10 | 164 |
| C570 | 5.70 | △ | $3.72/T^{1/4}$ | $2.72/T^{1/2}$ | 5.66 | 177 |

**Metallic samples ↓**

| Sample | Dose | Symbol | Temperature | $\sigma(0)$ | $C$ | $Z$ |
|---|---|---|---|---|---|---|
| Name | ($\times 10^{15}$ cm$^{-2}$) | | range (K) | | | |
| C575 | 5.75 | ◇ | 50 – 0 | 8.9 | 8.81 | 0.2 |
| C580 | 5.80 | * | 50 – 1.92 | 9.5 | 1.75 | 0.4 |
| C590 | 5.90 | × | 47 – 7.4 | 6.6 | 12.14 | 0.14 |

Table 6.1: A list of values for some variables determined from the experimental data using the VRH relations.

and is too low when compared to the atomic density of diamond but is consistent with the results obtained by Hauser *et al.*[144]. In ref. [144] it is explained why diamond still retain its hardness despite the very large increase in its conductivity even though a low concentration of conducting centres was introduced in the diamond surface by ion-implantation. The main finding of Hauser *et al.*[144], which is consistent with our results, is that transport, via the vacancy-related graphitic clusters, is by VRH process.

Dawson and Adkins[173] have studied carbon composites materials which have some similarities to carbon-ion implanted diamond systems. The $N_o(E_F)$ values they have calculated are three orders of magnitude more than we calculated.

### 6.5.3 Calculation of the radius of the conducting spheres

Kalish *et al.*[143] have proposed that the conducting centres in systems of this kind may be approximately spherical. This leads them to derive an expression that relates the average radius of the conducting spheres in 3-D to the critical ion dose. This expression can be written as

$$\overline{r} \simeq \left[\frac{0.425}{\pi}\left(\frac{R_p + \Delta R_p}{D_c}\right)\right]^{1/3} \quad . \tag{6.10}$$

From the TRIM-92 simulation program, developed by Ziegler *et al.*[138], we have estimated $R_p = 215$ nm and $\Delta R_p = 25$ nm for a diamond crystal implanted with a carbon-ion dose which had been accelerated at an energy of 150 keV. If we take the critical carbon ion-dose to be $5.68 \times 10^{15}$ cm$^{-2}$, then Eq. (6.10) yields $\overline{r} \simeq 1.08$ nm. This value is close to the one recently obtained by Prawer and Kalish[129], *viz*, $\overline{r} \simeq 1.01$ nm on high-temperature carbon-ion implanted type II*a* diamond specimens.

### 6.5.4 Calculation of Bohr radii of conducting centres.

The critical carbon-ion concentration and the critical dose can be related by $n_c \simeq D_c/(\Delta R_p + R_p)$[143]. This gives $n_c = 2.4 \times 10^{20}$ cm$^{-3}$ for values of $R_p$ and $\Delta R_p$ given in the section above. We wish to adapt the Mott criterion, $n_c^{1/3} a_H^* \simeq 0.26$, described in chapter 2, to graphitic islands. Using $n_c = 2.4 \times 10^{20}$ cm$^{-3}$, we obtain $a_H^* = 0.4$ nm which is a factor of 2.6 greater than the diamond lattice spacing (The diamond lattice spacing is 0.154 nm). Values for $R_{opt}$, calculated from Eq. (6.9), *viz*, 4.6 nm (at 100 K) and 232 nm (at 4 K), are a factor of 10 to 100 greater than $a_H^*$. We may conclude that transport may be described by VRH relations in this system. Fig. 6-5 shows the graphitic clusters randomly distributed in a dielectric matrix. The conducting graphite regions are assumed to be spherical[143]. The likely shapes of the graphitic regions are shown around the spheres in Fig. 6-5.

### 6.5.5 Minimum metallic conductivity

The determination of $n_c$ prompts one to try and establish the nature of the transition, *i.e.* whether it is of the first order (discontinuous) [109] or follows a continuous monotonic function[11]. Mott, using the concept of IR[10], proposed that the electrical conductivity of the system should follow a temperature-dependent expression at $n_c$,

$$\sigma_{\min}(T) = C\frac{e^2}{\hbar\hbar l} \simeq \frac{0.03}{l}(2.4 \times 10^{-4}\ (\Omega^{-1}\ \text{cm}^{-1}) \quad . \tag{6.11}$$

If we assume $l \simeq R_{opt}(T = 4\ \text{K})$, then $\sigma_{\min} \simeq 0.3\ (\Omega^{-1}\ \text{cm}^{-1})$. It remains a difficult process to clearly determine whether the system shows a discontinuous transition at $n_c$ or not, since such a claim is based on the extrapolation of the temperature-dependent conductivity $\sigma(T)$ to zero temperature. In the case being studied, the limiting factor has been the cryogenic system with which all our electrical conductivity measurements were made. In particular, the carbon glass resistor that we have used to monitor the sample temperatures was calibrated down to 1.5 K. It should be mentioned here that there is,

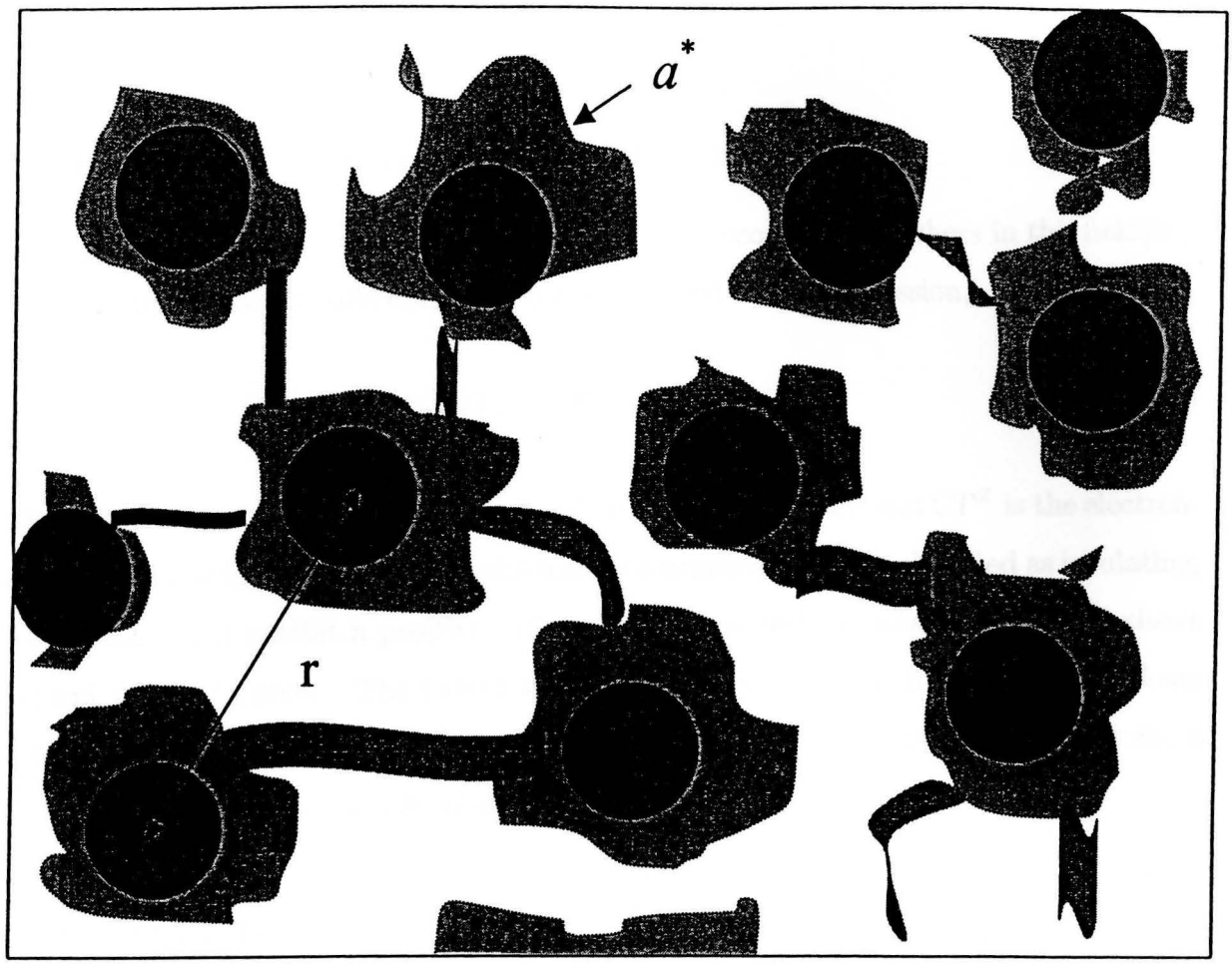


Figure 6-5: The vacancy-related conducting graphite regions in carbon-ion implanted diamond specimens have been assumed to have a spherical shape[125, 140], but the actual shapes of these graphitic clusters are shown around the spheres.

however, a growing consensus that no minimum metallic conductivity occurs in doped semiconductors despite the recent efforts by Möbius *et al.*[13, 14] in support of $\sigma_{\min}$. The arguments of Möbius *et al.*[13, 14] for the occurrence of $\sigma_{\min}$ in doped semiconductors are presented in chapter 8.

### 6.5.6 Transport in the metallic regime

Some samples show a metallic behavioural pattern. According to authors in this field[99], conductivity in the metallic domain can be described by an expression,

$$\sigma(T) = \sigma(0) + CT^Z \quad , \tag{6.12}$$

where $\sigma(0)$ is the conductivity extrapolated to zero temperature and $CT^Z$ is the electron-electron interaction term. Samples which show a negative $\sigma(0)$ are classified as insulating, and those which exhibit a positive $\sigma(0)$ may be regarded as metallic. Fig. 6-6 shows typical metallic curves. The curves were obtained for samples implanted with doses $5.80 \times 10$ cm$^{-2}$, $5.90 \times 10$ cm$^{-2}$ and $5.95 \times 10$ cm$^{-2}$. To avoid repetition of details, a discussion on transport properties of metallic samples is given in chapter 8.

## 6.6 Conclusion

In this chapter we have demonstrated the importance of preparing samples using multiple implantation steps. Samples have been prepared using the CIRA technique. This work on carbon-ion implanted diamond has been carried out to serve as a precursor to the study of the electrical properties of boron atoms in diamond, which is our principal investigation. The VRH mechanism has been found to apply in the case of samples which are located on the insulating side of the metal-insulator transition. The Zabrodskii-Zinov'eva method together with a metallic expression have been used to characterize and classify samples as either insulating or metallic.

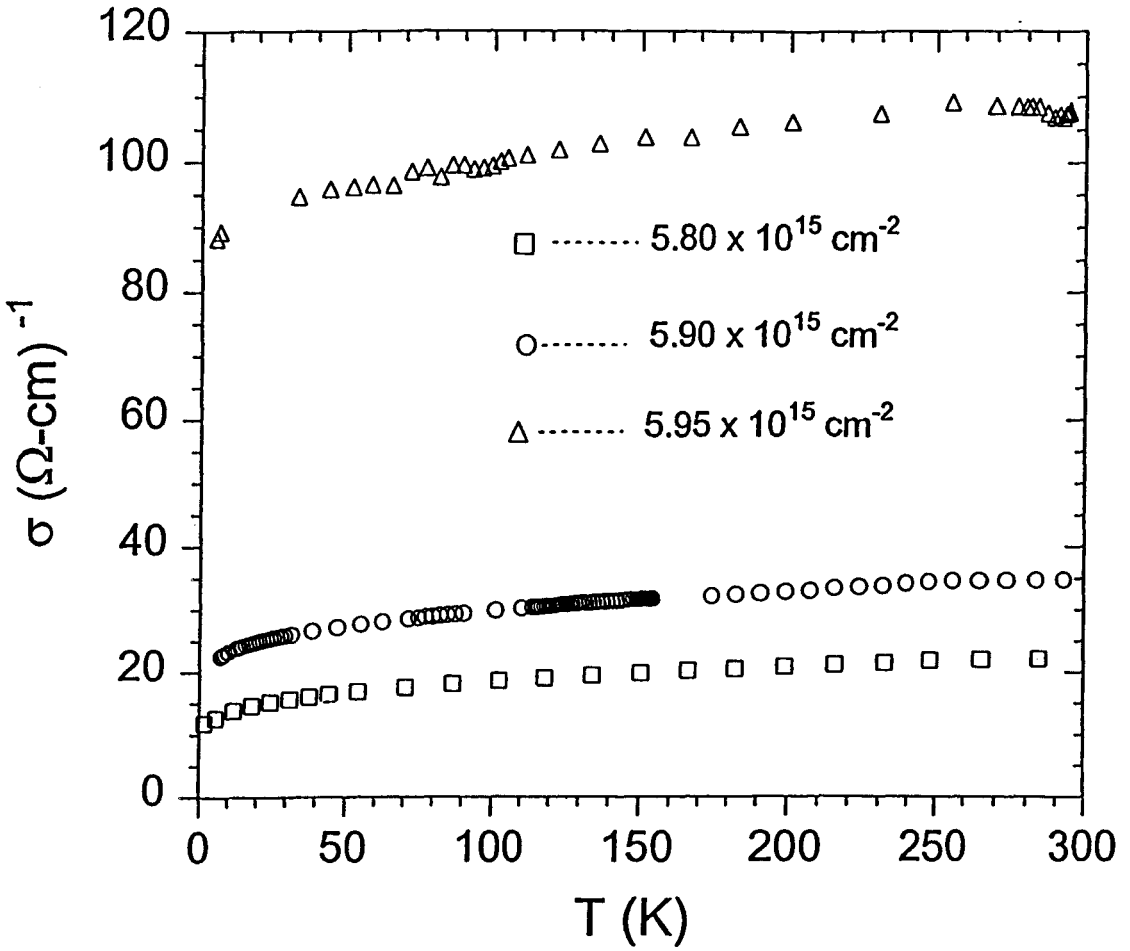


Figure 6-6: The conductivity plots for samples which may be classified as metallic.

# Chapter 7

# Electrical conductivity results of boron-ion implanted diamond

## 7.1 Introduction

The electrical conductivity results, measured in the temperature range 1.5-773 K, are presented in this chapter. In order to gain a better understanding of the transport phenomena in this system, I have employed a number of theoretical procedures to manipulate and interpret the experimental data. This chapter has been divided into four main sections. Section 7.2 presents the electrical conductivity results on the insulating side of the transition. Section 7.3 summarizes the results in the metallic regime, while section 7.4 describes the conductivity data for samples located close to the M-I transition. Section 7.5 reports on the high-temperature (300-773 K) results carried out on both insulating and metallic samples.

## 7.2 Insulating samples

### 7.2.1 Motivation

The electrical conductivity measurements on the insulating side of the transition have been motivated by three objectives. The first objective is to determine the highest value of the boron concentration at which samples still show a characteristic behaviour of insulating materials. We expect that beyond this limit the relation $\sigma \rightarrow 0$ as $T \rightarrow 0$ will be invalid when the transition is approached from below.

The second objective is to identify clearly the transport mechanisms in the boron-ion implanted conducting surface layers as the temperature of the samples is lowered. This involves a careful determination of the hopping exponent $m$ in the VRH relation, $\sigma(T) = \sigma_o \exp\left[-(T_o/T)^m\right]$. As reported in chapter 2, the theoretically determined values for $m$ are 1/4 (Mott VRH law with a constant and non-vanishing DOS), and 1/2 (ES VRH law with parabolic-shaped DOS at the Fermi energy). From these transport properties, the behaviour of the single-particle DOS near the Fermi energy can be established. Another phenomenon that we have probed in this system is the occurrence of the electrical conductivity crossover from Mott to ES VRH behaviour. This phenomenon has widely been studied but observed in only a few doped semiconductors[168, 174, 175].

The third objective is to determine whether the system undergoes a dimensionality crossover as the temperature of the samples is decreased. To do this, we compare the ratio of $R_{hop}$ to $t$, the thickness of the implanted layer, which is obtained from the SIMS profile, and is also estimated from the TRIM92 computer simulation program. An average thickness of the boron-ion implanted layer according to TRIM92 is 0.21 $\mu$m, while the SIMS profile measures this thickness to be 0.25 $\mu$m.

Fig. 7-1 shows plots of resistance against temperature for a number of insulating

boron-ion implanted diamond specimens measured in the range of temperature 1.5-300 K. The plots follow a general resistance (resistivity) relation, $R(T) = R_o \exp[(T_o/T)^m]$. The parameters $R_o$, $T_o$ and $m$ have been determined using several methods. One of the methods used is the Minuit software package least squares fitting procedure. In this program, parameters were allowed to vary within specified bounds or were fixed to theoretically predicted values. The characteristic temperature values, including error estimates, obtained using the Minuit program are listed in table 7.1.

The standard procedure widely used by various researchers in this field[176] to distinguish between the Mott and the ES VRH relations is to plot $\rho(T)$ (or $\sigma(T)$) versus $T^{-1/4}$ and $T^{-1/2}$, respectively. These plots are shown in Fig. 7-2(a,b), covering a wide range of insulating samples. From these plots curves which show some linearity with the experimental data are selected and the least squares regression lines fitted to them. Fig. 7-3 shows a plot of the least-squares fit for one of the insulating samples (AB27) together with the experimental points. The fit is excellent over the range shown, with $m \sim 0.5$. We have, however, noted that, as the M-I transition is approached, the least squares fitting method yields poor values for the fitting variables. Hill[74] and other authors[104] have noted that quantities extracted using this fitting procedure are unreliable, because fittings are usually confined to a small segment of $R-T$ experimental data. If one slightly increases the previous $R-T$ data range for fitting, one always obtains different values for the fitting variables. The procedure used by Hill[74] and Hill and Jonscher[75], and later Zabrodskii and Zinov'eva[76], will be presented in the discussion chapter (chapter 8).

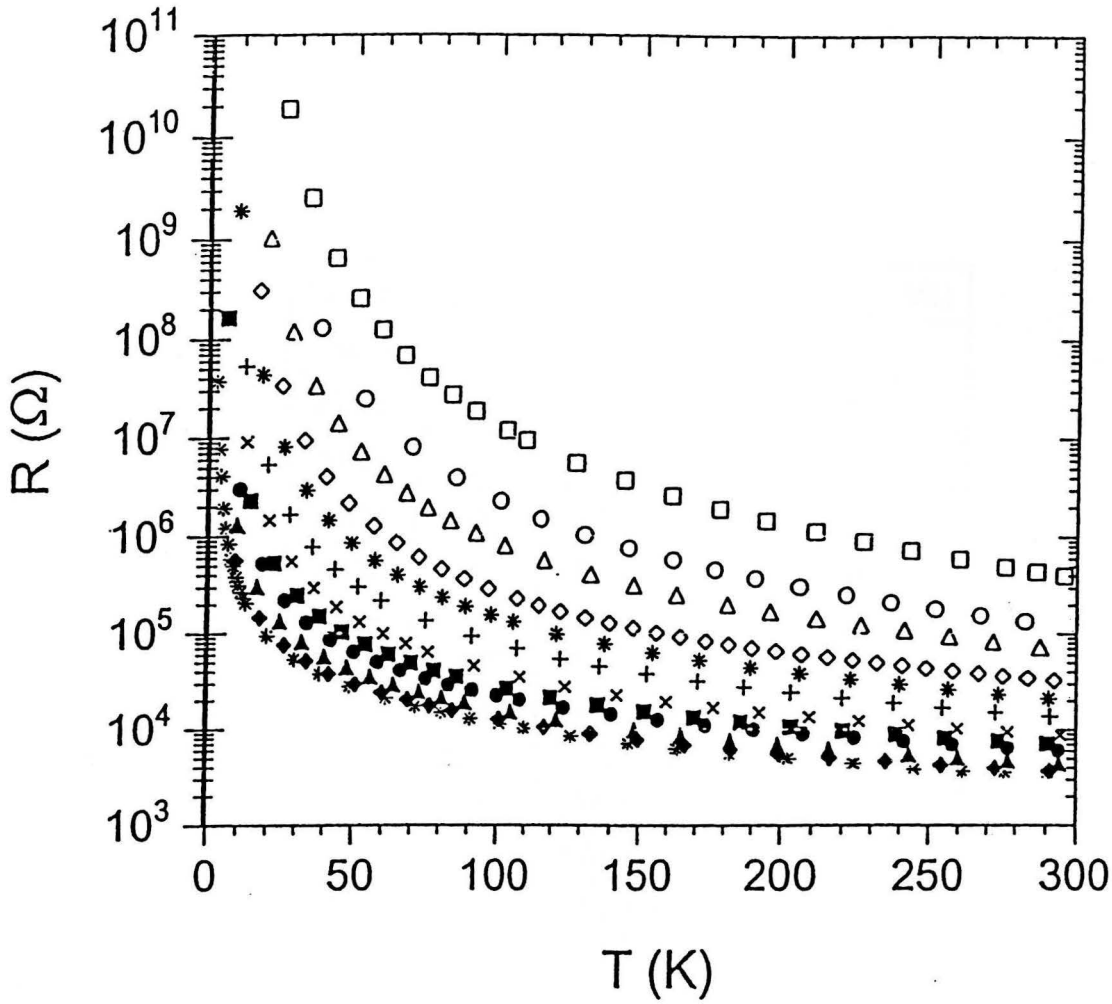


Figure 7-1: The resistance against temperature for a number of boron-ion implanted type II$a$ diamond specimens.

| Sample | Symbol | $T_M$ (K) | $T_{ES}$ (K)±(~ 5%) |
|---|---|---|---|
| Name | | $\times 10^4$ | |
| AB21 | □ | $274 \pm 5.5$ | 6291 |
| AB24 | ○ | $320 \pm 48$ | 7183 |
| AB27 | △ | $49 \pm 5.8$ | 2238 |
| AB30 | ◇ | $65 \pm 5.2$ | 1738 |
| AB33 | * | $1.28 \pm 0.12$ | 2020 |
| AB36 | + | $10.5 \pm 0.9$ | 1043 |
| AB39 | × | $1.03 \pm 0.07$ | 1020 |
| AB42 | ■ | $0.92 \pm 0.10$ | 185 |
| AB45 | • | $8.34 \pm 1.2$ | 262 |
| AB48 | ▲ | $2.05 \pm 0.2$ | 102 |

Table 7.1: The Minuit least squares fitting procedure was used to determine values for the characteristic temperatures in the Mott and the ES VRH regimes. The uncertainty in the characteristic temperatures were estimated by fitting the regression lines over various temperature regions in which the Mott and the ES laws apply. The non-monotonic decrease in $T_M$ and $T_{ES}$ may be an indication of the unreliability of this method

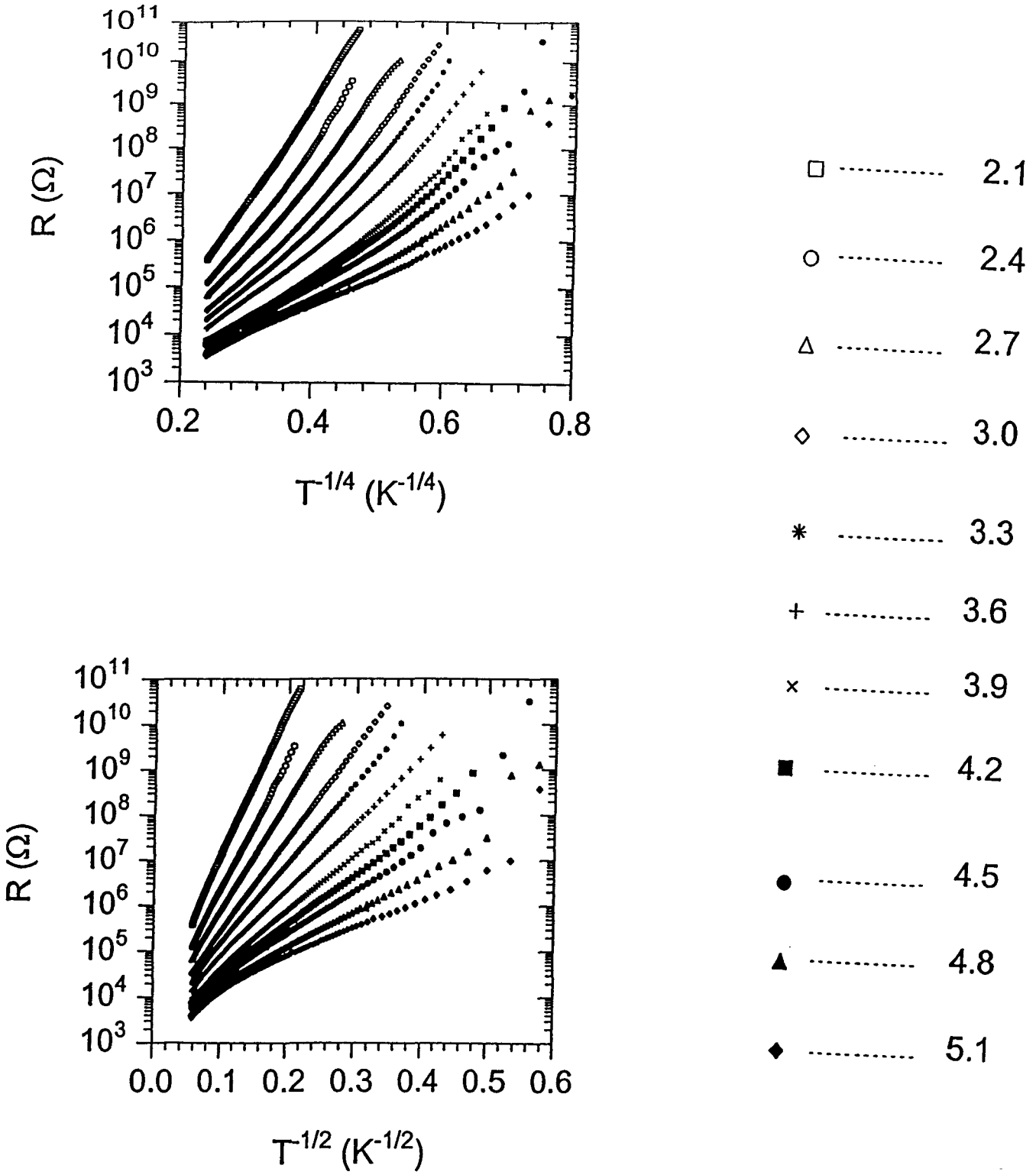


Figure 7-2: Resistance of eleven insulating diamond specimens plotted as a function of $T^{-m}$ ($K^{-m}$) (where $m = 1/4$ and $1/2$) on a semilogarithmic scale.

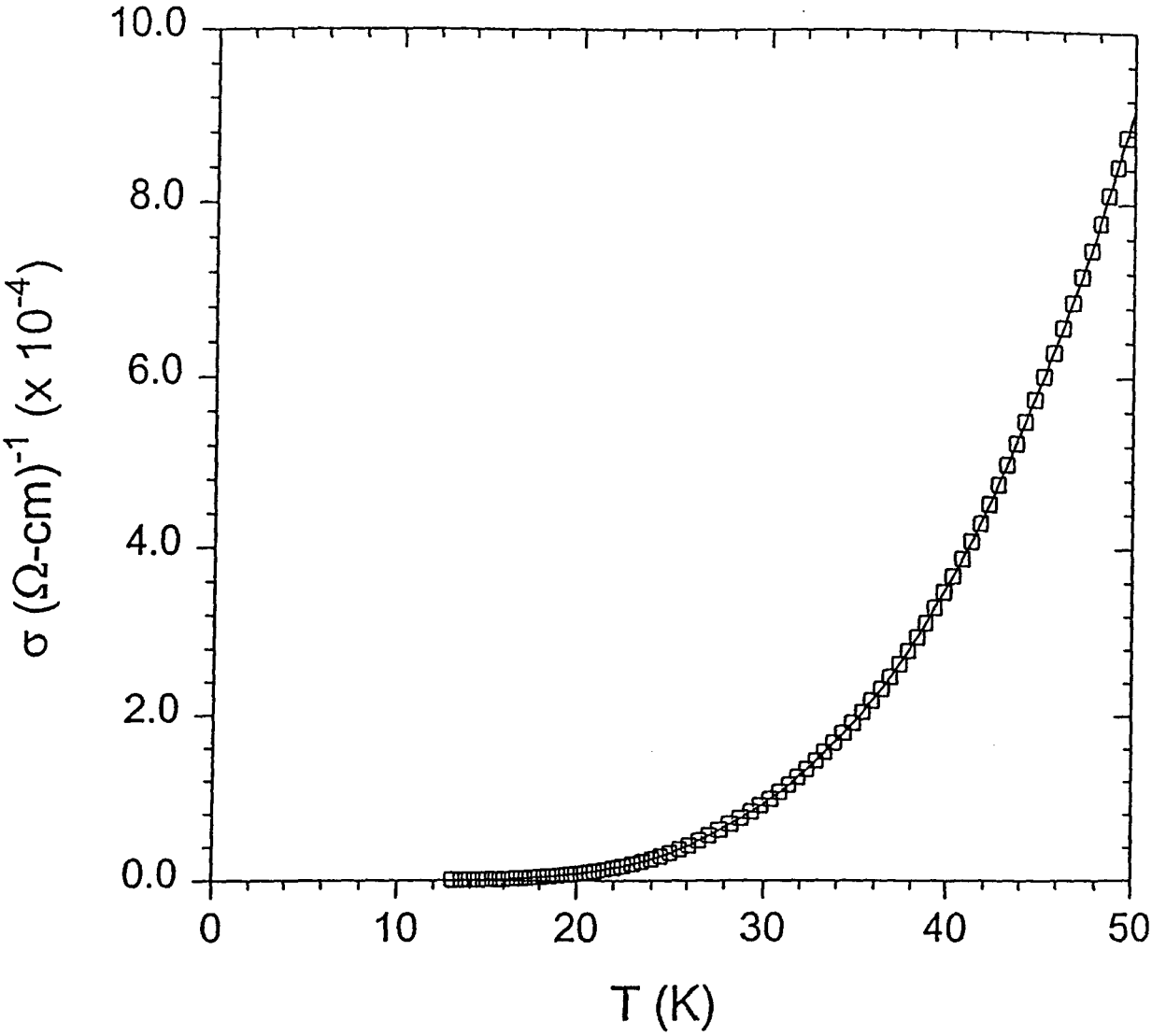


Figure 7-3: $\sigma$ *vs.* $T$ for sample AB27. A solid line through the experimental data represents a fit to the conductivity expression: $\sigma(T) = \sigma_o \exp\left[-\left(T_o/T\right)^m\right]$ where $m \sim 0.5$.

## 7.3 Metallic Samples

### 7.3.1 Motivation

The objective of our investigation has been two-fold. Firstly, to determine a lower conductivity value on the $\sigma - T$ experimental data below which the condition, $\sigma(0) \rightarrow A$ as $T \rightarrow 0$, where $A$ is a finite positive value, is invalid.

The second objective is to study the dominant transport mechanisms in this system, particularly at low temperatures. This means fitting our experimental data, collected in the vicinity of the transition, to the conductivity expression given later by Eq. (7.1) to determine $\sigma(0)$ and $Z$. Therefore, obtaining a correct expression of $\sigma(T)$ is important for a reliable determination for $\sigma(0)$ since $\sigma(0)$ defines the position of the M-I transition. Recall from chapter 2 that samples with $\sigma(0) = 0$ are classified as insulating, while samples with $\sigma(0) > 0$ are metallic.

Fig. 7-4 shows plots of $\sigma(T)$ as a function of $T$(K) for some metallic samples. We have carried out the conductivity measurements in the absence and in the presence of a magnetic field on some metallic samples. The results for samples AB81 and AB84, annealed at 1873 K (1600 °C) and 1973 K( 1700 °C), are shown in Fig. 7-5 and Fig. 7-6, respectively. It is difficult to clearly resolve the curves for conductivities measured with and without a B-field. I therefore decided to ignore the weak inelastic scattering term, $ST^{p/2}$, in the fitting function,

$$\sigma(T) = \sigma(0) + CT^{Z} \quad , \tag{7.1}$$

for two reasons: (i) the contribution of a B-field, which was set to a maximum of B = 1 T, is insignificant, and (ii) we could not reach temperatures below 1.5 K due to the constraints of our cryogenic system. This means that we extrapolated our conductivity results from 1.5 K to 0 K to determine $\sigma(0)$. The dropped inelastic term would have

otherwise served as just another fitting parameter which would have improved the fit, but would have been of questionable physical significance for our system. Recently, Aronzon[177] suggested that I try measuring our samples in the presence of a weak field of strength 0.1-0.5 T to see if I could pick up effects due to weak localization. The preliminary results obtained here did not yield the desired effect, but this study may be followed up after the completion of this thesis. The prefactor $C$ in Eq. (7.1) forms part of the electron-electron interaction term (second term) and may change sign when the M-I transition is crossed, with the conductivity exponent $Z$ expected to take values between 0.5 to 1.0. It has been noted that a sign change of $C$ can also occur for weakly insulating systems which are located close to the M-I transition[106, 107].

Parameters obtained from Eq. (7.1) are presented in table 7.2. The focus is on the electrical conductivity carried out below 50 K. Fig. 7-5 shows a plot of $\sigma(T)$ against $T$ for a sample close to the M-I transition.

## 7.4 Conduction near the M-I transition

### 7.4.1 Motivation

The main objective is to locate precisely where the M-I transition in boron-ion implanted surface layers in single crystal type II$a$ diamond occurs.

A secondary motive is to test the applicability of several theories or models which attempt to describe the transport properties at and quite near the transition.

For a system very close to the transition, an exponent of 1/3 in the electron-electron interaction term gives a better fit than 1/2. This is shown in Fig. 7-7 for a temperature range of 1.5-30 K. The theoretical justification for an exponent of 1/3 is given by

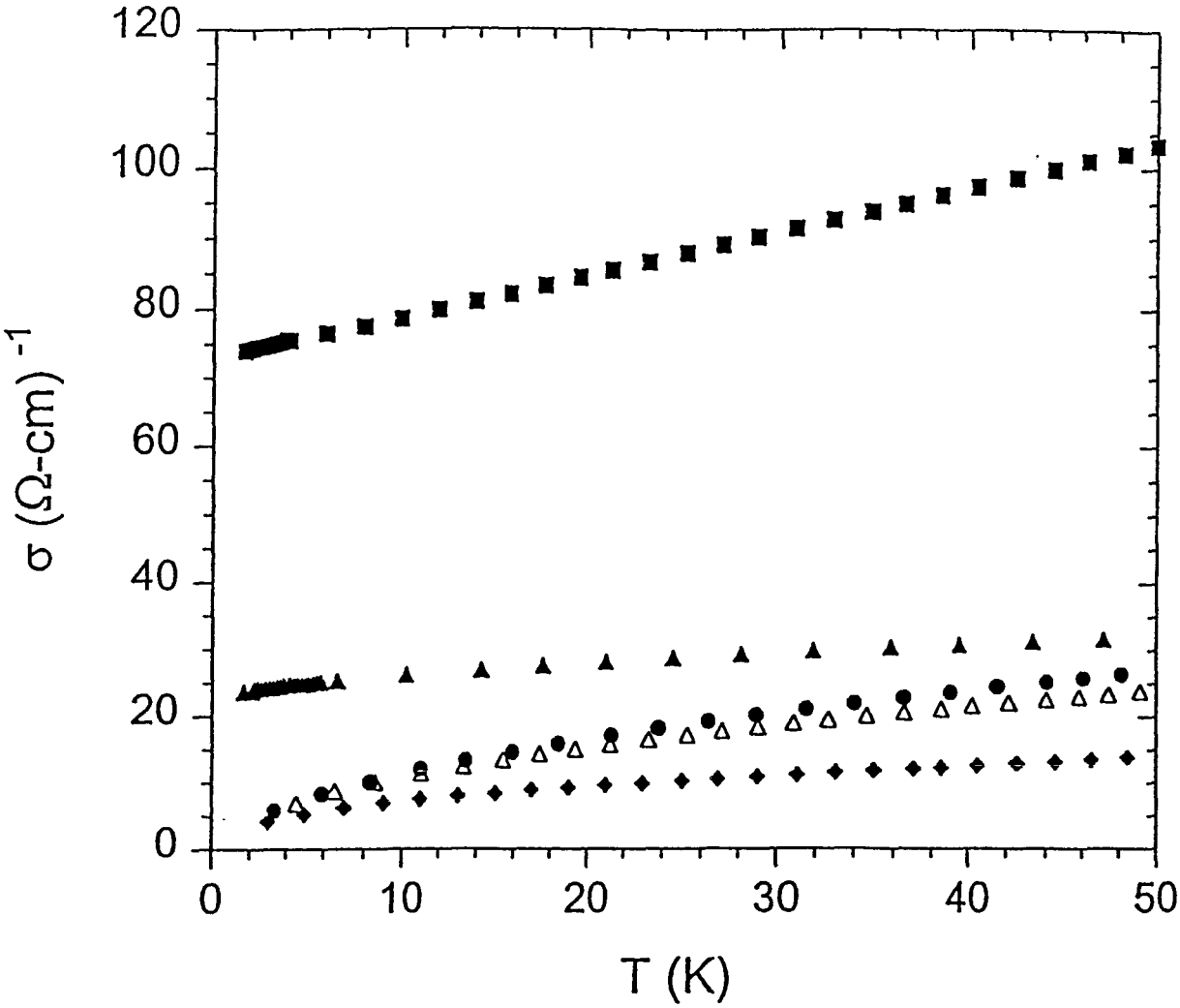


Figure 7-4: The electrical conductivity for some of the metallic samples plotted as a function of $T$. Samples have been annealed isochronally (10 minutes) at various temperatures ranging from 1200 °C to 1700 °C. Symbols shown represent: ■-sample AB84 (1700 °C anneal); ▲-AB81 (1700 °C anneal); •-AB78 (1700 °C anneal); △-AB81 (1200 °C anneal) ♦-AB78 (1200 °C anneal). All samples have been annealed for 10 minutes.

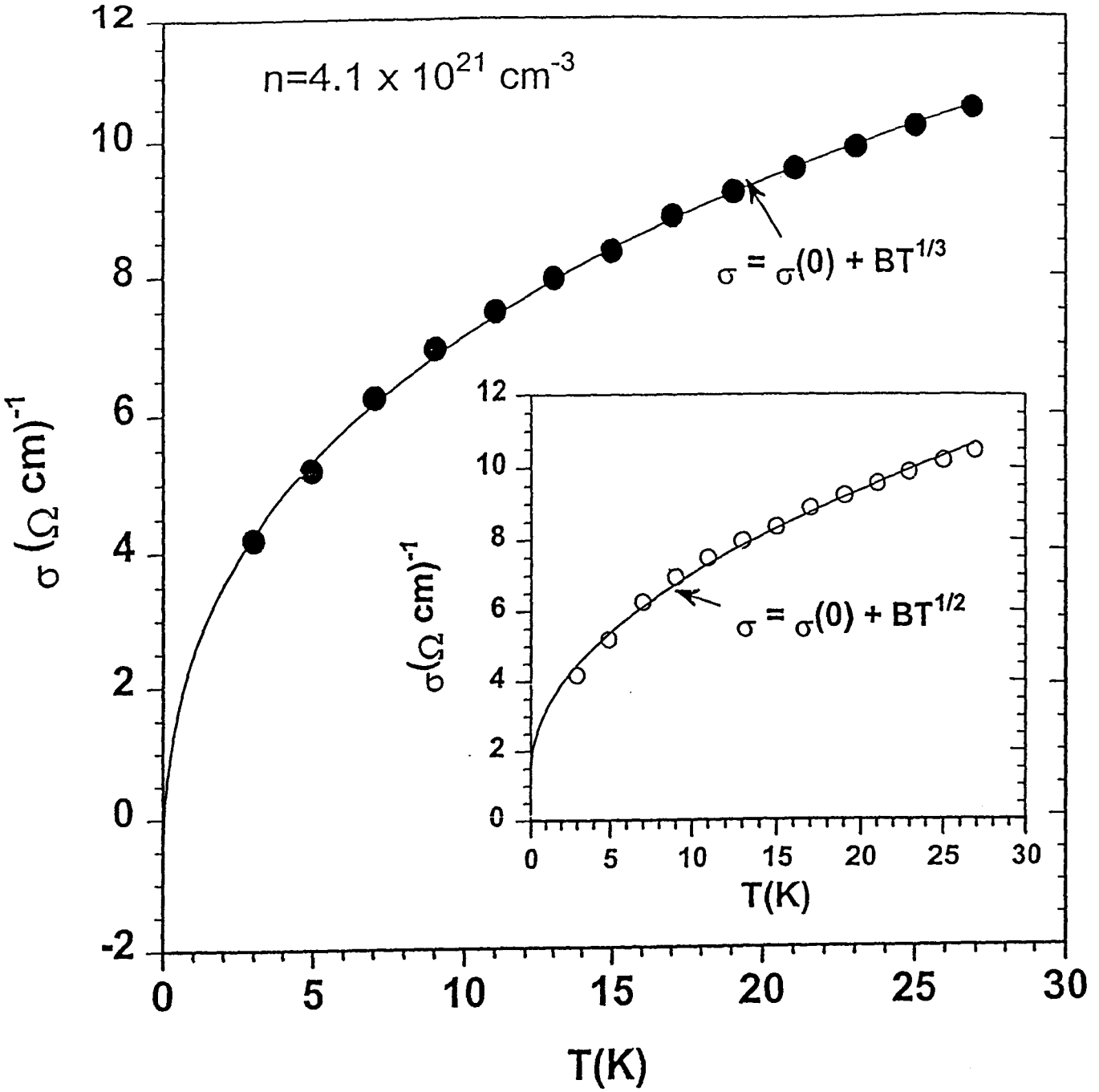


Figure 7-5: Electrical conductivity *vs.* $T$ for sample AB81. This sample has been annealed at 1700 °C.

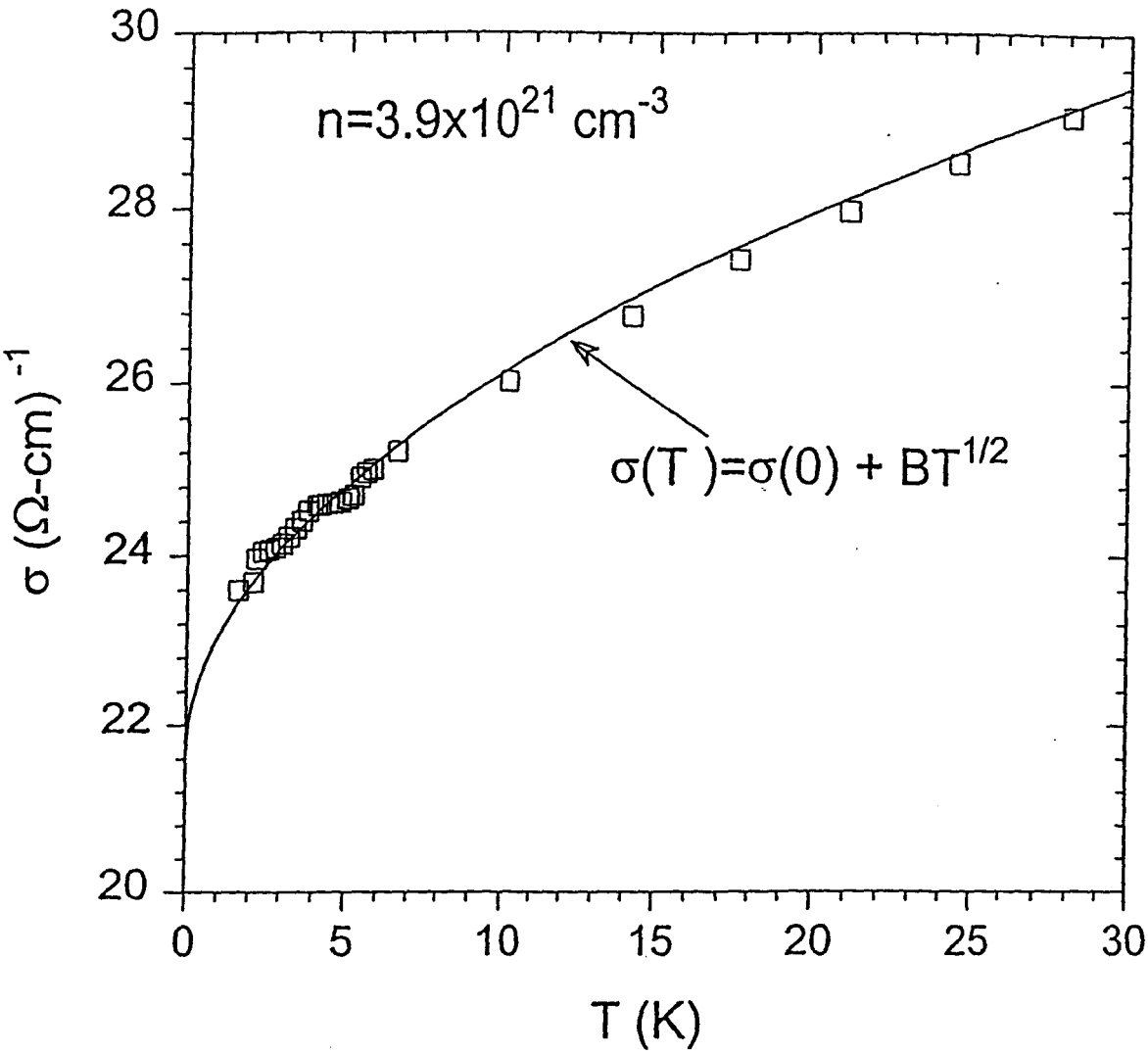


Figure 7-6: Electrical conductivity *vs.* $T$ for sample AB84. This sample has been annealed at 1700 °C.

| Sample | Anneal T(°C) | σ(0) | $C$ | $Z$ |
|---|---|---|---|---|
| AB78 | 1200 | 0.44 | .95 | .72 |
| | 1200 | 3.18 | .33 | .94 |
| | 1200 | 6.25 | .04 | 1.34 |
| | 500 | 3.58 | 1.59 | .66 |
| | 500 | 1.32 | 0.90 | .72 |
| | 500 | 1.53 | 1.74 | 0.5 |
| | 1700 | 0.44 | 2.43 | 0.43 |
| | | | | |
| AB81 | 1200 | 3.81 | .20 | 1.02 |
| | 500 | 3.66 | .35 | .95 |
| | 500 | 3.52 | .32 | .93 |
| | 1300 | 5.62 | 2.06 | .64 |
| | 1400 | 11.07 | .24 | 1.05 |
| | 1600 | 15.56 | 0.08 | .74 |
| | 1700 | 22.61 | 0.77 | 0.64 |
| | | | | |
| AB84 | 1700 | 73.12 | 0.52 | 1.04 |

Conductivity exponent $Z$ fixed to a 0.5 ↓

| Sample | Anneal T(°C) | σ(0) | $C$ | $Z$ |
|---|---|---|---|---|
| AB78anl6 | 1700 | 5.62 | 2.06 | 0.5 |
| | | | | |
| AB81anl1 | 1200 | 0.53 | 2.14 | 0.5 |
| AB81anl8 | 1300 | 1.85 | 4.04 | 0.5 |
| AB81anl9 | 1400 | 9.07 | 1.95 | 0.5 |

Table 7.2: Variables of boron-ion implanted diamond obtained from the metallic expression are presented in this table.

Maliepaard *et al.*[108] and by a number of authors using different approaches[115]. This exponent has recently been found in other neutron doped systems[16, 105, 178]. Recent studies by Castner[92] re-emphasize the 'universality class' of $Z = 1/2$ for systems close to the M-I transition.

## 7.5 The derivative method

The derivative method has been used to characterize the transport properties of our samples. The basic tenets of this method and its application to disordered systems are presented in chapters 2 and 8. Fig. 7-8 shows a typical trend of some $W - T$ plots for one of the samples (AB81) in the vicinity of the M-I transition. The sample has been annealed at various temperatures (from 1200 °C to 1700 °C) for ten minutes.

## 7.6 High-temperature measurements

### 7.6.1 Motivation

The principal objectives are (i) to extend transport studies to systems which show VRH behaviour at low temperatures, and (ii) to measure activation energies and compare them with activation energies which were obtained at low temperatures.

Electrical conductivity measurements on two samples, one highly insulating and the other just metallic, have been carried out in the temperature range 300-773 K. Fig. 7-9 shows $R$ plotted against $1/T$ for sample B84. The insert shows the same experimental data plotted against $T^{-1/4}$ to determine whether the Mott VRH behaviour applies in this sample at high-temperatures. We show only the results for insulating samples after encountering electrical contact problems at high temperatures in the case of metallic

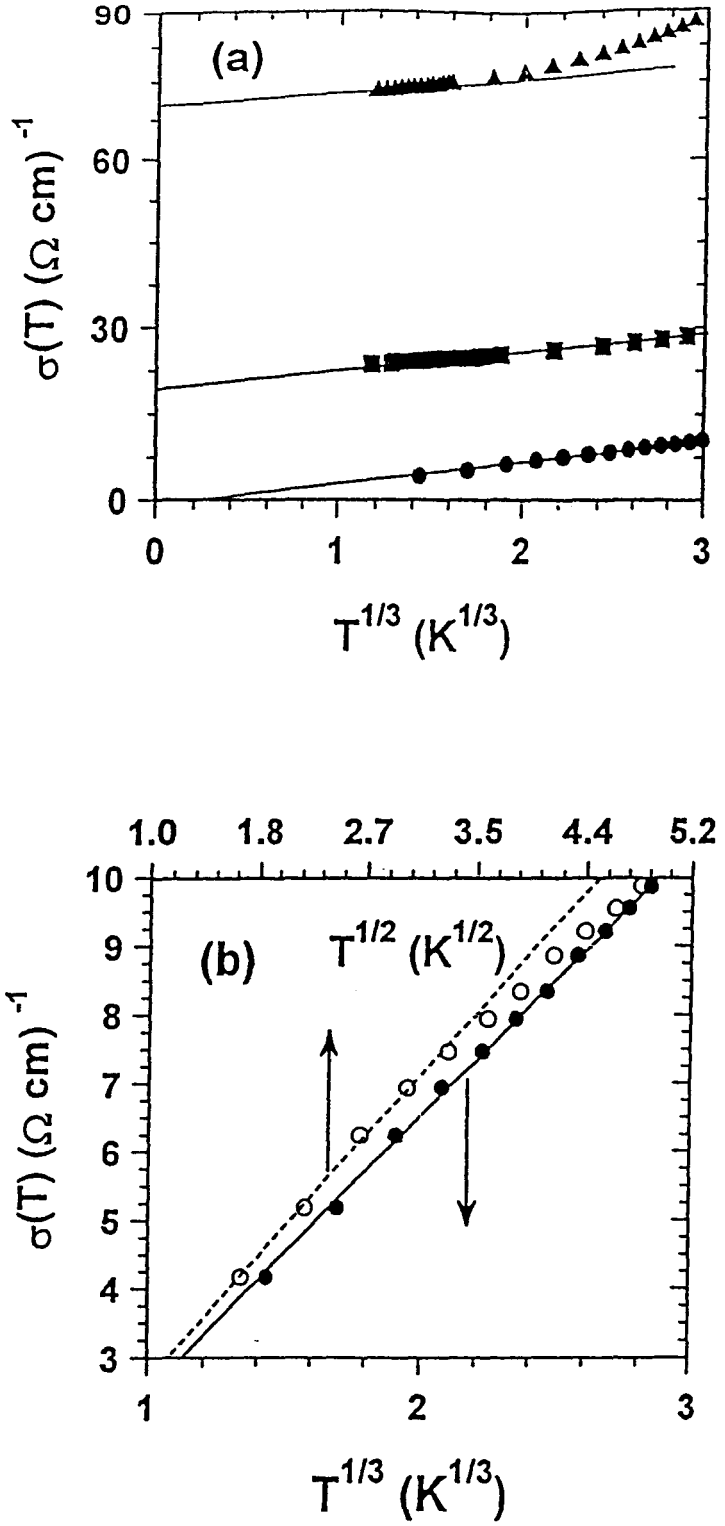


Figure 7-8: Temperature-dependent electrical conductivity *vs.* $T$ for samples AB78, AB81 and AB84. A closer inspection of the plots reveals that $\sigma(T)$ *vs.* $T^{1/3}$ gives a better fit to the experimental data than $\sigma(T)$ *vs.* $T^{-1/2}$. Plotted here are samples annealed at 1700 °C for 10 minutes. Sample AB84 is shown in Fig. 7-8(b).

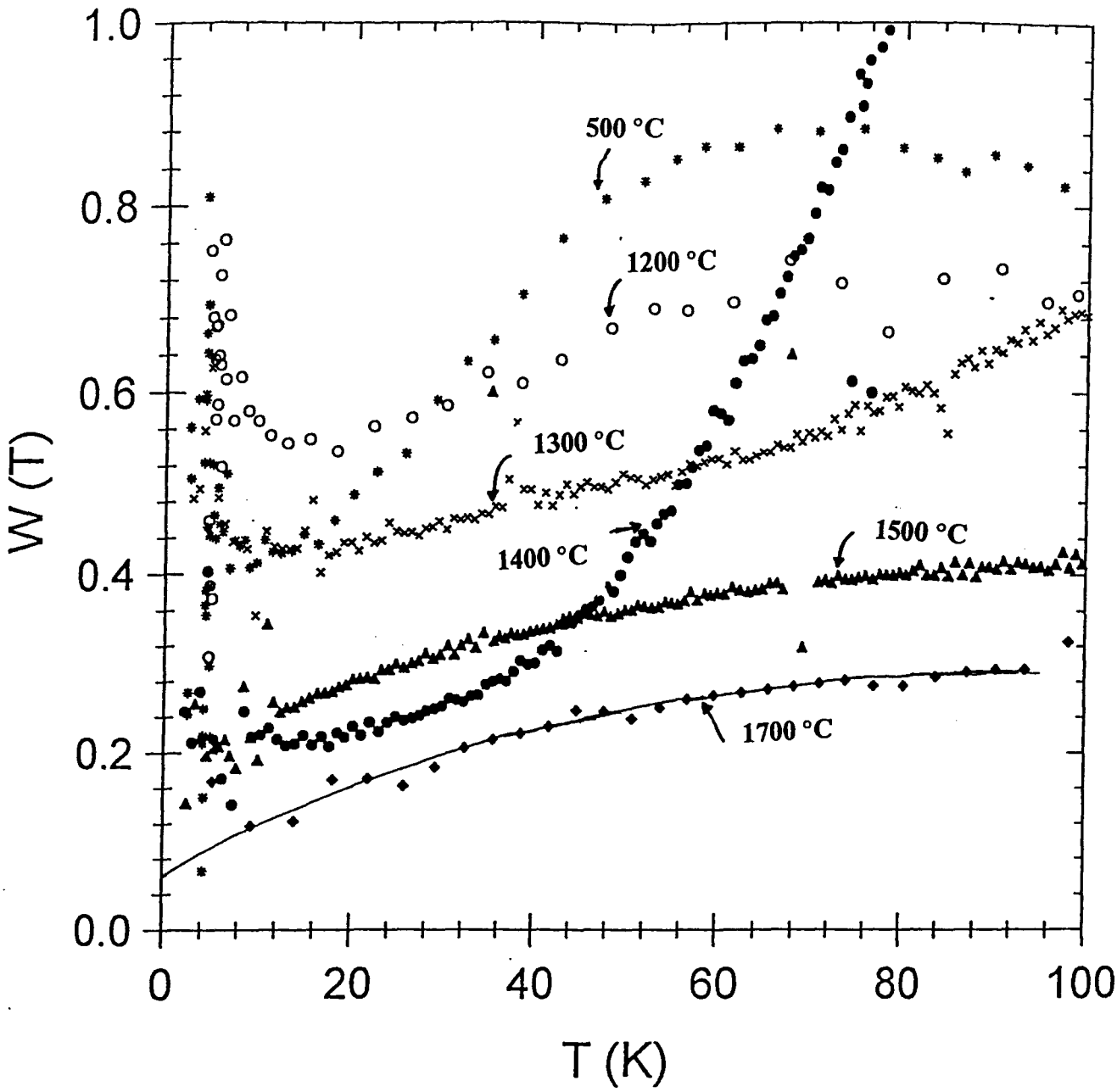


Figure 7-9: Plots of activation energy $W = \partial \ln \sigma / \ln T$ against $T$. This sample, AB81, is close to the M-I transition. According to the derivative method, sample AB81 is weakly insulating. One of the curves fitted with a solid line has been annealed at 1700 °C, which is the highest temperature at which we can safely anneal our samples. The annealing temperatures for these samples are shown in the figure. The duration of the anneal for all samples was set to 10 minutes.

samples. Above $\sim$ 400 K the behaviour changes from hopping conduction to activated carrier transport involving holes in the valence band.

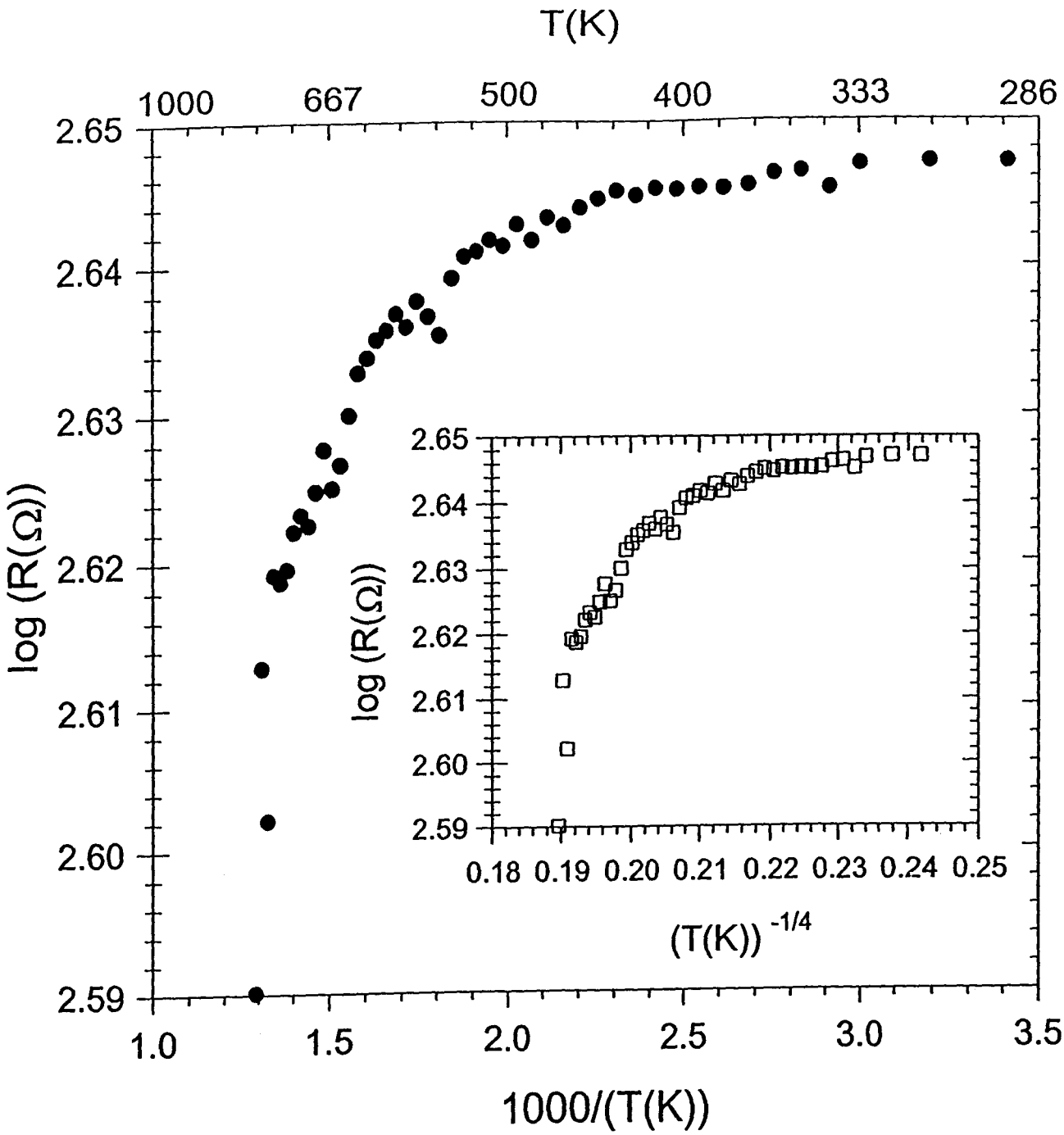


Figure 7-10: Plots of $R(T)$ *vs.* $T^{-m}$ for sample AB84 measured in the temperature range 300-773 K. The insert shows the same experimental data plotted against $T^{-1/4}$ to check whether Mott VRH conduction applies in this temperature range.

# Chapter 8

# Discussion of the electrical conductivity results for boron-ion implanted type II$a$ diamond

## 8.1 Introduction

This chapter discusses the experimental results presented in chapter 7. The chapter has been broken up into three main sections, each focusing on broader aspects of the data analysis. In section 8.2 I discuss the electrical conductivity results on the insulating side of the transition using the current variable-range hopping theories. Section 8.3 is devoted to results obtained on samples located in the metallic domain. The range and validity of the fitting functions used to analyze the data are discussed. Section 8.4 interprets the results in the vicinity of the metal-insulator (M-I) transition in the framework of the scaling theory of localization. Compensation of boron impurity centres by vacancy-related defects is discussed in section 8.5.

## 8.2 Insulating samples

This is the regime where most of the experimental work has been done. It will therefore be the most elaborate section. When this study was initiated, I had four virgin, optically transparent and well polished samples with which to work. As described in chapter 4, the letter A denotes the sample, B stands for the dopant ion (in this case boron), and the number represents the implanted dose ($\times 10^{15}$ cm$^{-2}$). For example, if sample A is implanted with a dose fluence, or to a total dose fluence, of $5 \times 10^{15}$ cm$^{-2}$, it will be designated as AB5.

For convenience, I have converted the boron-ion dose levels to concentrations in some tables where the electrical conductivity quantities are presented. I decided to stick to one nomenclature in referring to my samples, and this involves the use of dose levels. Where necessary I have written down the concentration in brackets, particularly in later sections where I discuss the transport properties in the vicinity of the M-I transition.

I began monitoring the electrical conductivity behaviour for sample A after it had been implanted progressively, using an incremental dose of $3.0 \times 10^{15}$ cm$^{-2}$, for the seventh time. This means that the experimental data for conductivity as a function of temperature were first collected when the implanted dose had reached a level of $21 \times 10^{15}$ cm$^{-2}$ (sample labelled as AB21). Samples B, C and D have been implanted slightly differently to sample A, and annealed differently. We implanted these samples with a total dose of $5.0 \times 10^{15}$ cm$^{-2}$, which is just below the critical threshold beyond which the implanted layer would undergo irreversible structural changes with the appearance of graphitic regions. Unlike sample A which has been annealed initially at 1200 °C for

a standard duration of 10 minutes until a total dose of $78 \times 10^{15}$ cm$^{-2}$ was implanted, samples B to D have been annealed at 500 °C (for at least 120 minutes), 700 °C (30 minutes), 900 °C (30 minutes), 1200 °C (10-30 minutes) and up to 1700 °C (10 minutes). After every implantation-annealing cycle, these samples were repolished immediately after I had measured their electrical conductivities as a function of temperature. It was not until the initial stage of the project had been completed that we decided not to repolish them, but to carry on implanting them incrementally with the same boron-ion dose of $5.0 \times 10^{15}$ cm$^{-2}$, and to anneal them at 1200 °C (for 30 minutes) and 1700 °C (for 10 minutes). Conductivity measurements were performed in between the anneals. A list of the implants for these samples is given in chapter 4.

### 8.2.1 Activation conduction mechanism

An alternative way of presenting the data shown in Fig. 7-1, is to plot $R$ *vs.* $1/T$. This representation is motivated by the expectation that the data would be described by an activated conduction mechanism. The activation energy for such a transport process would then be given by the slope of the straight line on the graph. Typical studies of the M-I transition have examined $R(T)$ in samples that are approaching the transition from the insulating side and determined the value of $n_c$ by the disappearance of a low temperature activation energy $\varepsilon_3$[179, 180, 181]. In the regime where activated conduction takes place

$$R = R_o \exp\left(\frac{E_A}{k_B T}\right) \quad , \tag{8.1}$$

where $\rho_o$ is the temperature-independent prefactor, $E_A$ is the activation energy and $k_B$ is Boltzmann's constant. Taking natural logs on both sides of Eq. (8.1) yields

$$\ln R = \ln R_o + \left(\frac{E_A}{k_B T}\right) \quad , \tag{8.2}$$

and $E_A$ can be obtained from the slope using Eq. (8.2), as

$$E_A = 8.614 \times 10^{-5} \times \left(\frac{\Delta \ln R}{\Delta 1/T}\right) \text{ eV} \quad . \tag{8.3}$$

Figs. 8-1 and 8-2 show plots of $R$ against $1/T$ for a number of samples measured in the temperature range 1.5-300 K and 300-773 K. It is difficult to see from these figures whether our system shows transport properties associated with the activated conduction process or not, unless one selects a small segment of $R - T$ data for analysis. Table 8.1 lists values for some important quantities related to electrical conductivity.

### 8.2.2 The derivative method for the insulating materials

Before discussing the experimental results pertinent to this section, I wish to make the reader aware that the plots made in Figs. 8-3-8-5 have been generated using two different methods. I have put the figures together for the reader to note the consistency of the two methods. These methods will, however, be discussed separately. We begin with the "$w$-derivative" method.

Recall from chapter 2 that the temperature dependence of the electrical conductivity of an Anderson-disordered insulator at low temperatures, follows the general variable range hopping (VRH) law,

$$\sigma = \sigma_o \exp\left[-\left(\frac{T_o}{T}\right)^m\right] \quad . \tag{8.4}$$

Substituting Eq. (8.4) into Eq. (8.5) shown below (defined in chapter 2) gives

$$W = \frac{\partial \ln \sigma}{\partial \ln T} = T\frac{\partial \ln \sigma}{\partial T} \tag{8.5}$$

$$= (mT_o^m)\, T^{-m} \quad . \tag{8.6}$$

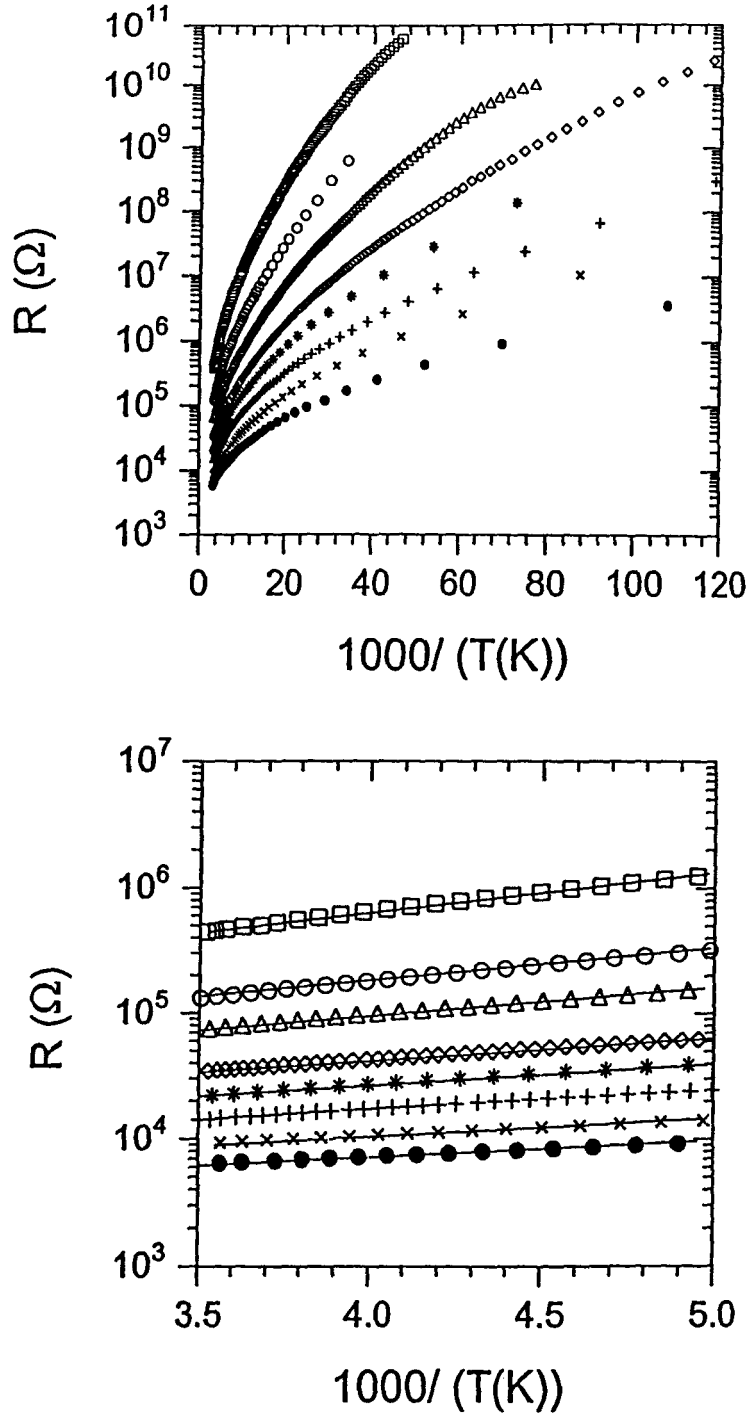


Figure 8-1: Plots of $R$ *vs.* $1/T$ for a number of insulating samples. Only the data above 400 K may be used for the calculation of the activation energy, $E_A$.

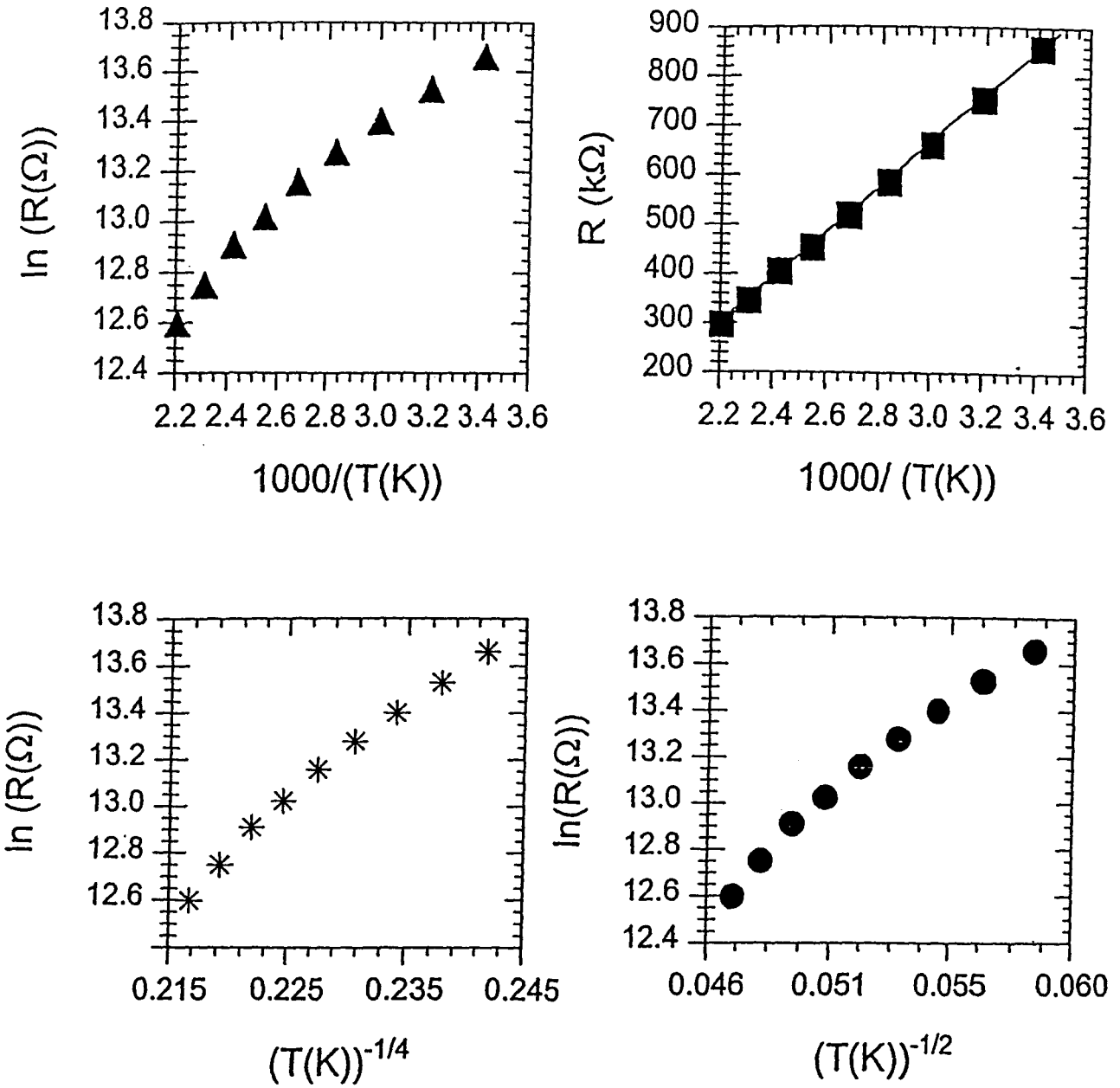


Figure 8-2: Plots of $R(T)$ *vs.* $T^{-m}$ ($m = 1$; 1/4 and 1/2) for a high insulating sample CB5 measured in the temperature range 300-773 K.

| | | | High T Data | | Low T data | | | |
|---|---|---|---|---|---|---|---|---|
| Sample | Dose | Symbol | $T_M$ (K) | $R_{hop,M}/\xi$ | $T_{ES}$ (K) | $R_{hop,ES}/\xi$ | $\alpha$ ($10^8$ m$^{-1}$) | $\xi$ (nm) |
| Name | ($\times 10^{15}$ cm$^{-2}$) | | $\times 10^4$ | | | | | |
| AB21 | 21 . | □ | 274 | $15.3/T^{1/4}$ | 6291 | $6.34/T^{1/2}$ | 3.02 | 4 |
| AB24 | 24 | ○ | 320 | $15.9/T^{1/4}$ | 7183 | $21.19/T^{1/2}$ | 3.45 | 3 |
| AB27 | 27 | △ | 49 | $9.92/T^{1/4}$ | 2238 | $11.83/T^{1/2}$ | 1.07 | 9 |
| AB30 | 30 | ◇ | 65 | $10.65/T^{1/4}$ | 1738 | $10.42/T^{1/2}$ | 0.83 | 12 |
| AB33 | 33 | * | 1.28 | $4.03/T^{1/4}$ | 2020 | $11.24/T^{1/2}$ | 0.97 | 10 |
| AB36 | 36 | + | 10.5 | $6.75/T^{1/4}$ | 1043 | $8.07/T^{1/2}$ | 0.50 | 20 |
| AB39 | 39 | × | 1.03 | $3.78/T^{1/4}$ | 1020 | $7.98/T^{1/2}$ | 0.49 | 20 |
| AB42 | 42 | ■ | 0.92 | $3.67/T^{1/4}$ | 185 | $3.40/T^{1/2}$ | 0.089 | 113 |
| AB45 | 45 | • | 8.34 | $6.37/T^{1/4}$ | 262 | $4.05/T^{1/2}$ | 0.013 | 80 |
| AB48 | 48 | ▲ | 2.05 | $4.49/T^{1/4}$ | 102 | $2.53/T^{1/2}$ | 0.049 | 204 |

Table 8.1: Values of variables determined using electrical conductivity expressions are described in the text. The error estimates for $T_M$ and $T_{ES}$ were given in table 7.1.

Taking the logarithm on both sides transforms Eq. (8.5) into a straight line graph of the form,

$$\log W = -m \log T + \log (m T_o^m) \quad . \tag{8.7}$$

Consider Eq.(8.5). For insulating samples, $W$ is always positive and it diverges as $T \rightarrow 0$. This behaviour is supported by plots shown in Fig. 8-3 and Fig. 8-4, and has been observed widely by various authors[174]. The applicability and validity of the derivative method have been extended even to samples that exhibit finite conductivities at $T = 0$ K, as shown by plots in Fig. 8-5. Samples shown in Fig. 8-5 cannot be interpreted using Eq. (8.4) even though they are classified as insulating by the derivative method. It is interesting to note that a finite $\sigma(0)$, according to the derivative method, does not necessarily mean the exhibition of metallic behaviour[13]. Later in the chapter it is shown that the derivative method does not work well for $n \simeq n_c$.

The advantage of the "$w$-derivative" method is that one does not have to assume any parameter dependence beforehand because the linear region of log $W$ versus log $T$, defines the region where VRH occurs. The hopping exponent $m$ can be obtained directly from the slope, using the least-squares fitting procedure. Once $m$ is known, then the characteristic temperature $T_o$ can be calculated from Eq. (8.7) as

$$T_o = \left( \frac{10^{y_{int}}}{m} \right)^{1/m} \quad , \tag{8.8}$$

where $y_{int}$ is an intercept read from the $W$ ordinate. Variables obtained using the derivative method are summarized in table 8.1. Further details of the derivative method can be found in recent articles by Rosenbaum *et al.*[28, 29, 106, 174].

There is, however, a disadvantage associated with the "$w$-derivative" method. It is very sensitive to any variation of the experimental data, and even small local fluctuations

in the data become amplified. To overcome this draw-back two methods have been suggested. One method involves fitting a fifth-order polynomial through the experimental data points and then extracting pertinent information from the fitted curve. This method was used by Buraschi *et al.*[184]. Another method, which I have used throughout[174, 185], is to group the adjacent data points into small units and then calculate the averages of $R$ and $T$ per group. A unit may be made up of 4 data consecutive points or more, depending on the magnitude of the scatter in the experimental data set[174, 186]. Our data did not show much scatter, so only two consecutive data points were used to work out the averages.

A method analogous to that used by Hill[74] above has been suggested by White and McLachlan[187], following the earlier work of Davies *et al.*[188], in which they showed[187] that

$$\frac{\partial \ln g}{\partial \ln T} = -m \ln(g) - m \ln(R_o) \quad \left(g = \frac{1}{R}\right) \quad , \tag{8.9}$$

in the regime where the VRH relation is valid. This method has been included for completeness, and has been captured in Figs. 8-3(b)-8-5(b) which show a series of samples located in the insulating regime. The scatter in the experimental data becomes pronounced when the M-I transition is approached from below. In order to control this scatter, some shape-preserving cubic splines such as AKIMA[189] have been used. I have found this method not any better than that of Hill[74] and Zabrodskii-Zinov'eva[76], particularly for samples that are in the vicinity of the M-I transition.

### 8.2.3 Variable-range hopping conduction

Although hopping conduction in heavily doped and Anderson disordered semiconduc-

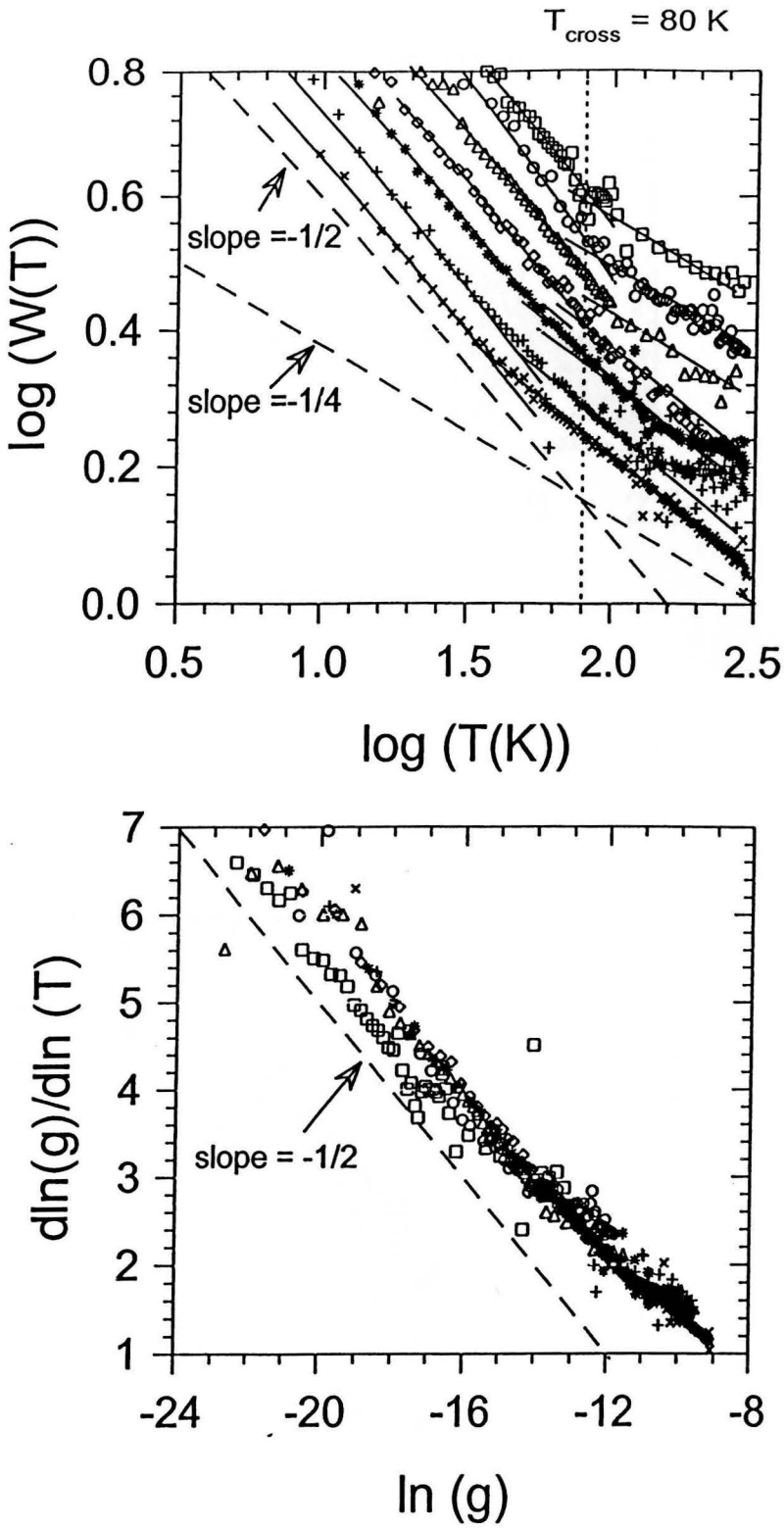


Figure 8-3: The derivative method and the White-MacLachlan method were used to generate these plots in an effort to determine the hopping exponent $m$. Samples plotted here lie in the boron-ion concentration range: $1.0 - 1.9 \times 10^{21}$ cm$^{-3}$.

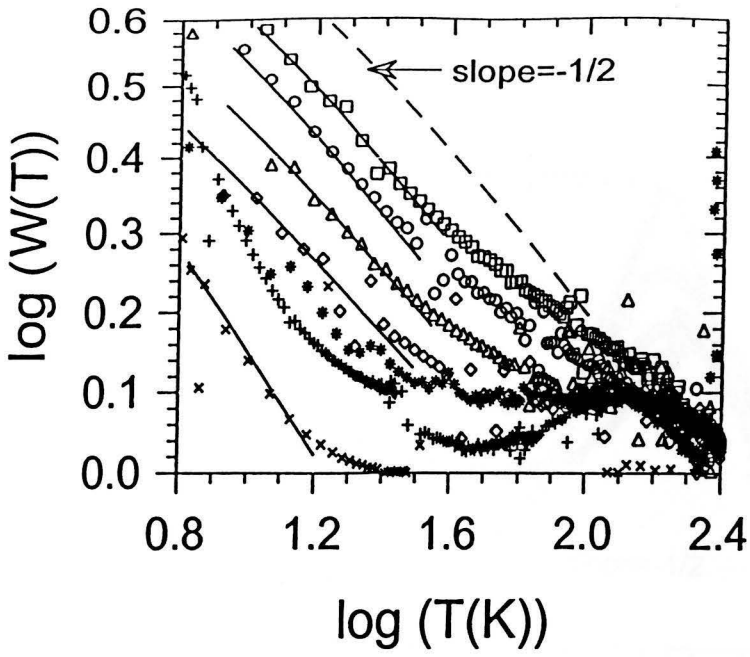


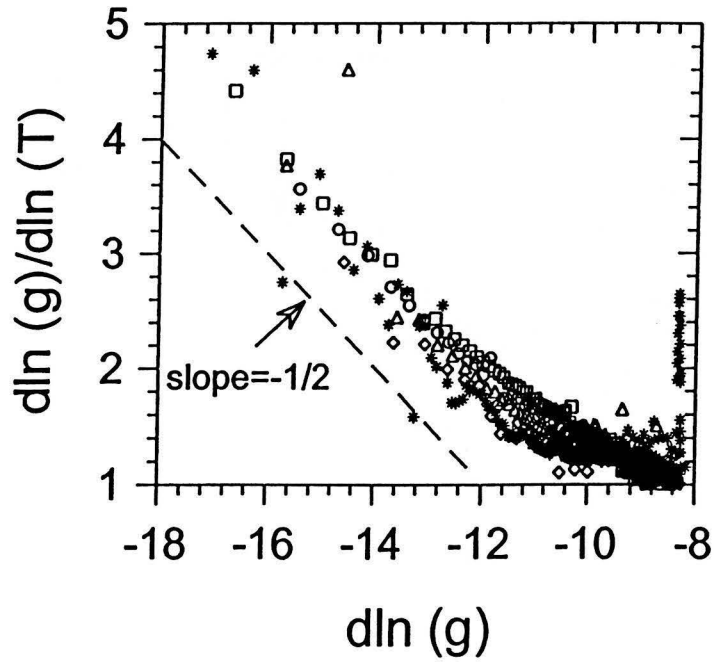


Figure 8-4: The derivative method and the White-MacLachlan method used to generate plots shown in an effort to determine the hopping exponent $m$. Samples lie in the boron-ion concentration range: $2.0 - 3.0 \times 10^{21}$ cm$^{-3}$. The fitted slopes close to the theoretical hopping exponent of $1/2$ are shown in the plots.

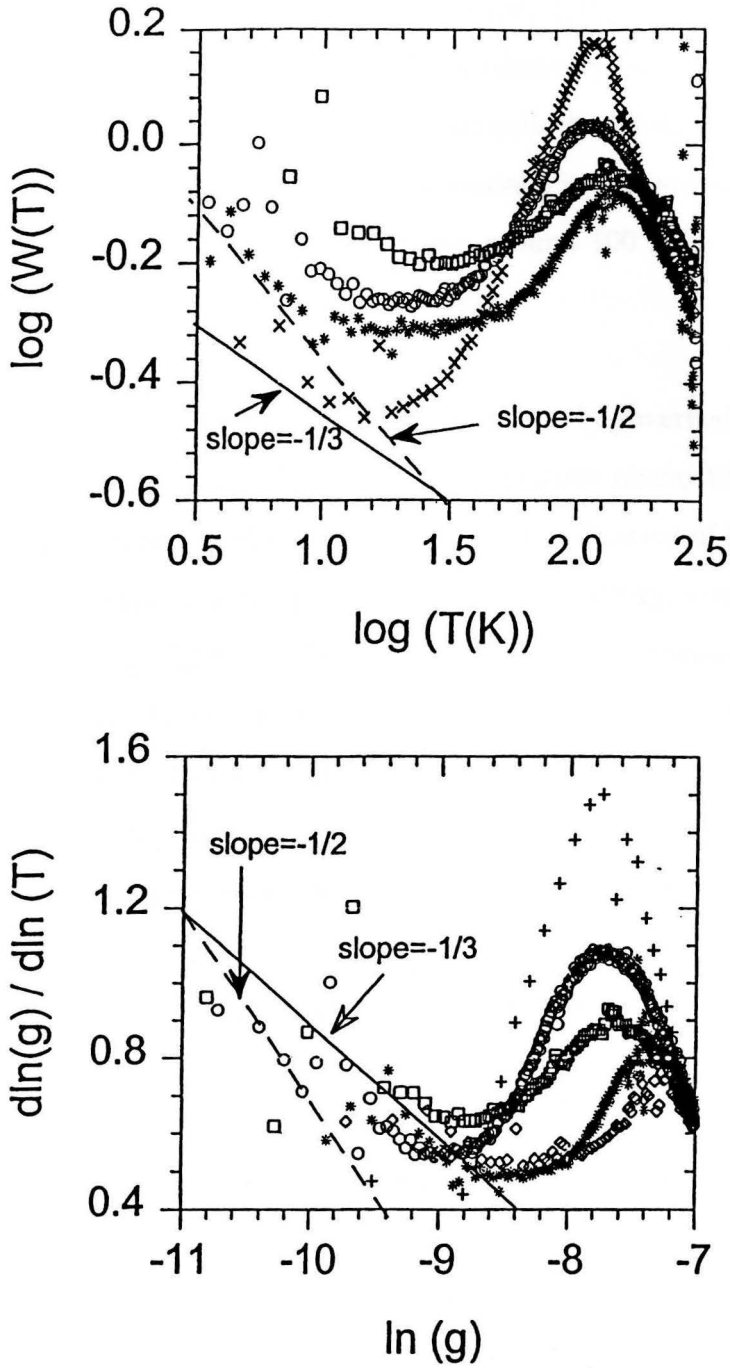


Figure 8-5: The derivative method and the White-MacLachlan method used to determine the hopping exponent $m$. Sample AB78 ($n \simeq 4.0 \times 10^{21}$ cm$^{-3}$) is shown. Solid lines shown in the plots correspond to theoretical slopes of $-1/3$ and $-1/2$. From the plots, a slope of $-1/3$ gives a better fit to the data compared to a slope of $-1/2$. The annealing temperatures for this sample are shown in the table alongside this figure.

tors has been studied intensively over many years[104, 190], a transition from Mott to ES VRH has been observed experimentally only in relatively few cases[27, 168, 174, 191, 192, 193]. In most of these cases, the electrical conductivity crossover occurs at very low temperatures, in some at $T \leq 5$ K[194]. The advantage in our system is that the VRH conductivity crossover is observed at temperatures around 100 K and depends on $n$ (see Fig. 8-3(a)), where $n$ is the boron-ion concentration.

The conductivity data shown in Fig. 8-3(a,b) are clearly governed by the Mott VRH relation[8], $\sigma(T) = \sigma_o \exp\left[-(T_M/T)^{1/4}\right]$, at temperatures above 100 K. The linearity expressed by the data shown in Fig. 7-2 is taken to be indicative of long-range hopping conduction with a constant density of states at the Fermi energy, with the effective temperature $T_M = \beta_M/\left(k_B \xi^3 N_o(E_F)\right)$. There exists, however, a considerable discrepancy as regards the values of the coefficient $\beta_M$, which, in turn, has a sensitive bearing on $T_M$. Mott has provided the following values for $\beta_M$ : 1.5[195] and $24/\pi = 7.6$[196], while Castner has used 18.1[104]. Skal and Skhlovskii[197] estimated $\beta_M$ to be 21.1, which is smaller than a value suggested by Ortuno and Pollak[198] of $\beta_M = 27$. The controversy surrounding the $\beta_M$ value remains unresolved, but many authors have settled for Castner's value of 18. Further reading on the controversy concerning $\beta_M$ can be found in a recent article by Rosenbaum *et al.*[27].

As the temperature of the disordered insulator system is lowered (below 100 K), effects due to long-range electron-electron interactions start to dominate, giving rise to a depletion in the density of states at the Fermi energy. Electrical conductivity for samples which obey the relation $\sigma(T) = \sigma_o \exp\left[-(T_{ES}/T)^{1/2}\right]$, where the characteristic temperature $T_{ES} = e^2 \beta_{ES}/\left(k_B \epsilon \xi\right)$, with $\beta_{ES}$ taking values of 2.8[23], 0.57[170], or 7.27[27], is interpreted in terms of the ES VRH mechanism within the Coulomb gap (Cg). The theory of the Cg is presented in chapter 2.

It is apparent from the derivative method plots shown in Figs. 8-3-8-5 that no single value for the hopping exponent can adequately describe the type of VRH conduction taking place over a wide temperature interval. There exists a conductivity crossover between the Mott VRH ($m = 1/4$) and the ES VRH ($m = 1/2$) as the temperatures of the samples are lowered. The conductivity crossover (see Fig.8-3), is around 100 K. It is difficult though to determine precisely by means of this method the $R - T$ cutoff point beyond which either of the two VRH conduction mechanisms ceases to apply.

We have found, by comparison with other methods such as the White and MacLachlan method[187], the derivative method to be the most sensitive and reliable in probing the transport nature of doped materials.

### 8.2.4 The optimum hopping distance and tunneling exponent

The amount of disorder and the material temperature determine the distance over which a carrier will hop[44]. In this section, we examine the transport properties of ◇C:B (boron-ion implanted diamond) in the VRH conduction regime further. We also calculate some values for model parameters which are important in the VRH regime, and study conditions to which the current VRH theories apply in our system.

Important parameters in the VRH conduction theory are the ratio of the mean hopping distance to the localization length (radius), $\overline{R}_{hop}/\xi$, and the mean hopping energy difference between the localized impurity sites, $\overline{\Delta}_{hop}$. Expressions for these quantities in the Mott VRH conduction regime (with $\beta_M$ chosen to be 18) are [104, 174]

$$\frac{\overline{R}_{hop,M}(T)}{\xi} = \frac{3}{8}\left(\frac{T_M}{T}\right)^{1/4} \tag{8.10}$$

and

$$\overline{\Delta}_{hop,M}(T) = \frac{1}{4} k_B T \left(\frac{T_M}{T}\right)^{1/4} \quad . \tag{8.11}$$

In the ES VRH regime (with $\beta_{ES} = 7.27$), we have

$$\frac{\overline{R}_{hop,ES}(T)}{\xi} = \frac{1}{4}\left(\frac{T_{ES}}{T}\right)^{1/2} \tag{8.12}$$

and

$$\overline{\Delta}_{hop,ES}(T) = \frac{1}{2} k_B T \left(\frac{T_{ES}}{T}\right)^{1/2} \quad . \tag{8.13}$$

The validity of both the Mott and ES VRH models depends on the condition, $\overline{R}_{hop}(T)/\xi > 1$. Re-examining the sample parameters listed in tables 8.1-8.3, the condition, $\overline{R}_{hop}(T)/\xi > 1$, may well be satisfied at lowest temperatures, say at temperatures below 5 K. This condition holds for both the Mott VRH and the ES VRH theories.

We consider the situation in the ES VRH conduction regime. In addition to the condition that $\overline{R}_{hop}(T)/\xi > 1$, there is another important condition which has to be met. The temperature-dependent optimum hop energy of the variable-range hopping process $\overline{\Delta}_{hop,ES}$ must satisfy $\overline{\Delta}_{hop,ES} > k_B T$ for hopping to take place within the Cg. In other words, $T_{ES}$ must always be greater than the measured sample temperature for one to invoke the ES VRH law.

The temperature-dependent tunneling exponent in the ES regime is given by [170]

$$\alpha = \frac{k_B T_{ES}}{10.5} \left(\pi g_{ES}\right)^{1/3} \quad , \tag{8.14}$$

where $g_{ES} = \left(3^8 \pi^2 \epsilon_r^3 \epsilon_o^3\right) / \left(2^5 e^6\right) = 1.55 \times 10^{85}$ J$^{-1}$m$^{-3}$ for $\epsilon_r = 5.7$ (diamond). Substituting values for the standard constants in Eq. (8.14) yields (in the case of diamond) a simpler expression with which to work, *viz.*

$$\alpha = 4.8 \times 10^4 \, T_{ES} \ \ (\mathrm{m}^{-1}) \quad . \tag{8.15}$$

We can then express the maximum hopping distance in terms of $T_{ES}$ (cf. Eq.(8.14)) as

$$\overline{R}_{hop,ES} = 5.2 \times 10^{-6} \, (T \, T_{ES})^{-1/2} \ \ (\mathrm{m}) \quad . \tag{8.16}$$

The tunneling exponent decreases with increasing concentration as $n_c$ is approached from the insulating side. Table 8.1 shows entries for $\overline{R}_{hop}(T)/\xi$ as a function of temperature, and some other related quantities.

We can now determine how $\overline{R}_{hop}(T)$ compares to $t$ by using variables obtained for sample AB21. We calculated $T_{ES} = 6291$ K for sample AB21. At $T = 5$ K, $\overline{R}_{hop,ES} \simeq 29$ nm. According to SIMS profile (see chapter 4), $t$ is measured to be 250 nm. This means that $\overline{R}_{hop}(T) < t$ and hence our system is 3-dimensional. We expect $\overline{R}_{hop}(T)$ to grow as the sample temperature is lowered, and for doses close to the transition (with $T_{ES}$ very small) we may have $\overline{R}_{hop}(T) \simeq t$. A dimensional crossover in systems of this sort has been observed before[173].

We have much confidence in quantities extracted from the ES VRH regime, compared to those obtained in the Mott VRH regime due to the scatter in the $W - T$ data sets for $T \geq 100$ K. I have estimated the uncertainty values for $T_M$ and $T_{ES}$ in table 7.1.

### 8.2.5 A crossover between Mott and ES variable-range hopping

Castner[104] has recently made some interesting theoretical predictions for insulating samples located not too far away from the M-I transition, but which still show a conductivity crossover from the Mott to ES VRH laws as the temperature is lowered. Castner's predictions involve the ratios,

$$\frac{T_M}{T_{ES}} = \frac{18\,(4\pi)}{\beta_{ES}} \quad , \tag{8.17}$$

$$\frac{T_M}{T_{Cg}} = 18\,(4\pi)^{3/2} \quad , \tag{8.18}$$

and

$$\frac{T_{ES}}{T_{Cg}} = \beta_{ES}\,(4\pi)^{1/2} \quad . \tag{8.19}$$

The quantity $T_{Cg}$ is referred to as the 'Coulomb gap' temperature. It is the temperature below which the effect of a Cg on the hopping process is evident. Just beyond $T_{Cg}$, the Mott VRH becomes a dominant transport process. Eq. (8.18) does not depend on $\beta_{ES}$, rendering this equation very useful for estimating $T_{Cg}$ without having to adjust any parameters. The disadvantage though, in my case, and for other authors as well[174], is that $T_M$ cannot be determined to a high degree of accuracy, compared to $T_{ES}$, due to scatter in the experimental data. Eqs. (8.17) and (8.19) contain the coefficient $\beta_{ES}$, which depends upon the compensation ratio $k = N_A/N_D$, where $N_A$ and $N_D$ are the acceptor and the donor concentrations, respectively. It is difficult to determine the value for $\beta_{ES}$ in ◇C:B system since it was not compensated by any extrinsic defect atoms. The only compensation effect we have is due to vacancy-related intrinsic defects.

A number of theoretical values for $\beta_{ES}$ (*viz.* $\beta_{ES} = 7.27$, 2.8 and 0.57) have been reported in the literature as I mentioned earlier. We have used these values in Eqs.(8.17)-(8.19) to estimate $T_{Cg}$ for the ◇C:B system. Such a procedure also affords one the ability to probe the consistency in the VRH laws. The $T_{Cg}$ values are summarized in table 8.2. By using values of $T_M$, $T_{ES}$ and $T_{Cg}$, shown in tables 8.1 to 8.2, respectively, we can estimate $\beta_{ES}$ in ◇C:B system to be $\simeq 0.57$. This value was predicted by Adkins[170]. I cannot attach any physical significance to this $\beta_{ES}$ value, but it appears to be system-dependent[27].

Considering our inability to determine the Mott characteristic temperature with much accuracy, our results still seem quite consistent with the experimental findings of Zhang *et al.*[168] on the relationship, $T_{ES} \propto (T_M)^{2/3}$. This is shown in Fig. 8-6.

### 8.2.6 Coulomb gap and the crossover temperature

In this section we discuss the importance of the Coulomb gap in our system and its size in the light of our experimental results.

The size of a Coulomb gap $\Delta_{Cg}$ has been determined independently by several authors[38, 174, 199] to be

$$\Delta_{Cg} = \frac{e^3}{\epsilon^{3/2}} N(E_F)^{1/2} = k_B \left( \frac{T_{ES}^3}{T_M} \right)^{1/2} \quad . \tag{8.20}$$

A number of equations leading to the calculation of the size of a Cg are presented below using the existing VRH expressions. From the $T_{Cg}$ expressions (Eqs. (8.18) and (8.19)), we can write $\Delta_{Cg}$ as

$$\Delta_{Cg} \simeq k_B T_{Cg} = k_B \left( \frac{T_M}{801} \right) \tag{8.21}$$

and

$$\Delta_{Cg} = k_B \left( \frac{T_{ES}}{\beta_{ES} (4\pi)^{1/2}} \right) \quad . \tag{8.22}$$

The electrical conductivity crossover, from the non-electron interaction Mott VRH regime into a strong long-range electron-electron correlation regime of ES, is expected to occur when the mean hopping energies, $\overline{\Delta}_{hop,M}$ and $\overline{\Delta}_{hop,ES}$, are of comparable magnitude. Combining Eq. (8.11) and Eq. (8.13) defines the crossover temperature as[104, 174]

$$T_{cr} = 16 \left( \frac{T_{ES}^2}{T_M} \right) \quad . \tag{8.23}$$

Using Eq.(8.23), we can then express $\Delta_{Cg}$ as

| Sample | Dose | Symbol | $T_{Cg} = \Delta_{Cg}/k_B$ (K) | $T_{Cg} = \Delta_{Cg}/k_B$ | $T_{Cg} = \Delta_{Cg}/k_B$ | $T_{Cg} = \Delta_{Cg}$ |
|---|---|---|---|---|---|---|
| Name | ($\times 10^{15}$ cm$^{-2}$) | | $\frac{T_{ES}}{(4\pi)^2\beta_{ES}}$; $\beta_{ES} = 7.27$ | $\frac{T_{ES}}{(4\pi)^2\beta_{ES}}$; $\beta_{ES} = 2.8$ | $\frac{T_{ES}}{(4\pi)^2\beta_{ES}}$; $\beta_{ES} = 0.57$ | $\frac{T_M}{801}$ |
| AB21 | 21 | □ | 244 | 634 | 3113 | 3433 |
| AB24 | 24 | ○ | 279 | 724 | 3555 | 3995 |
| AB27 | 27 | △ | 87 | 226 | 1108 | 612 |
| AB30 | 30 | ◇ | 67 | 175 | 860 | 812 |
| AB33 | 33 | * | 78 | 204 | 1000 | 16 |
| AB36 | 36 | + | 41 | 105 | 516 | 13.1 |
| AB39 | 39 | × | 40 | 103 | 505 | 12.9 |
| AB42 | 42 | ■ | 7.2 | 18.6 | 92 | 11.5 |
| AB45 | 45 | • | 10.2 | 26.4 | 130 | 104 |
| AB48 | 48 | ▲ | 3.96 | 10.3 | 51 | 25.6 |

| Sample | Dose | Symbol | $T_M$ (K) $\times 10^4$ | $T_M$ (K) $\times 10^4$ | $T_M$ (K) $\times 10^4$ | $T_M$ (K) $\times 10^4$ |
|---|---|---|---|---|---|---|
| Name | ($\times 10^{15}$ cm$^{-2}$) | | (Experimental) | $\beta_{ES} = 7.27$ | $\beta_{ES} = 2.8$ | $\beta_{ES} = 0.57$ |
| AB21 | 21 | □ | 275 | 20 | 51 | 284 |
| AB24 | 24 | ○ | 320 | 22 | 58 | 325 |
| AB27 | 27 | △ | 49 | 6.9 | 18 | 101 |
| AB30 | 30 | ◇ | 65 | 5.39 | 14 | 79 |
| AB33 | 33 | * | 1.28 | 6.26 | 16 | 91 |
| AB36 | 36 | + | 10.5 | 3.23 | 8.5 | 47 |
| AB39 | 39 | × | 1.03 | 3.16 | 8.3 | 46 |
| AB42 | 42 | ■ | 0.92 | 0.57 | 1.5 | 84 |
| AB45 | 45 | • | 8.34 | 0.81 | 2.1 | 12 |
| AB48 | 48 | ▲ | 2.05 | 0.32 | 0.83 | 4.6 |

Table 8.2: Values for quantities associated with the conductivity theory are listed in this table. Error estimates associated with the characteristic temperatures have been given in table 7.1. The non-consistency in the $T_{Cg} = \Delta_{Cg}/k_B$ (K) values seems to cast some doubts on the reliability of the VRH model over the temperature ranges that we have investigated.

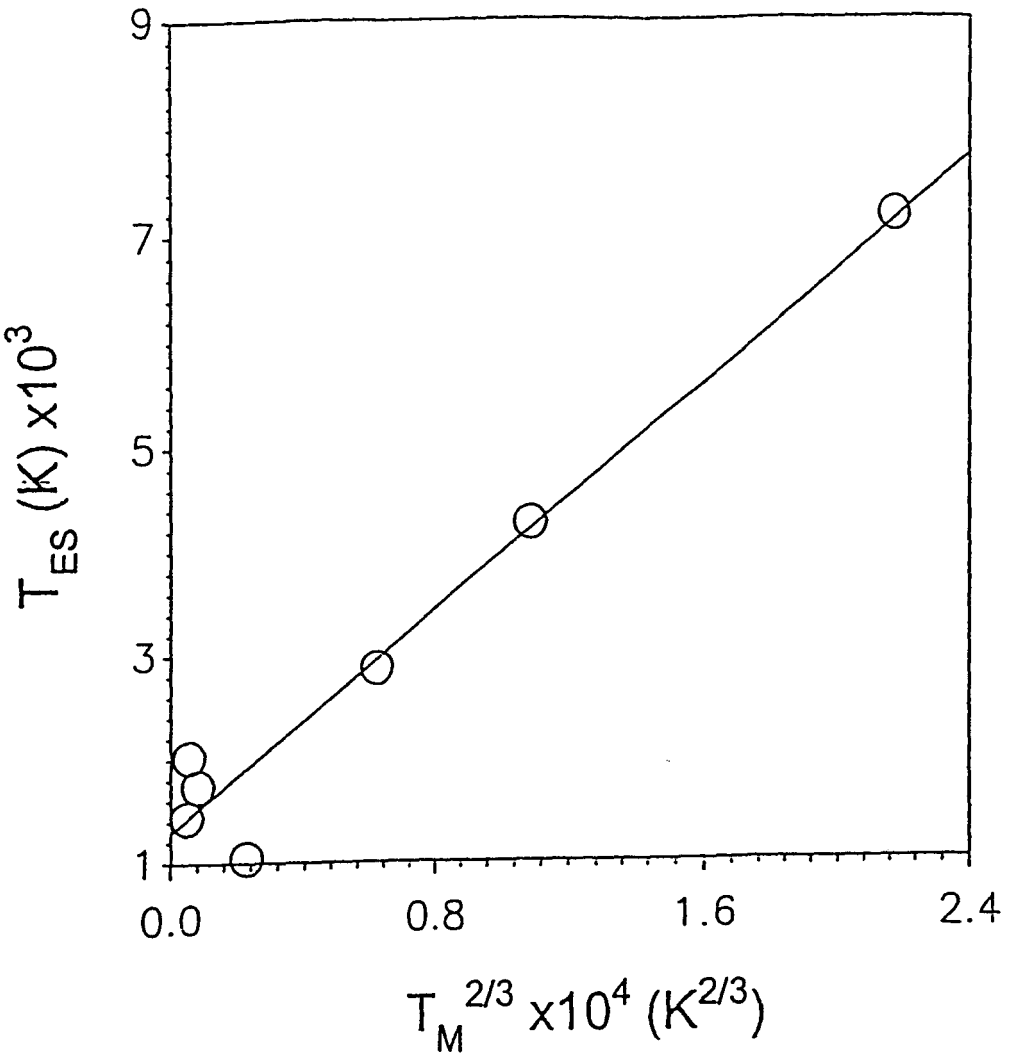


Figure 8-6: This plot demonstrates the relationship between the Mott and ES characteristic temperatures in the VRH regime.

$$\Delta_{Cg} = \frac{1}{4} k_B \left(T_{cr}\, T_{ES}\right)^{1/2} . \tag{8.24}$$

Four expressions for $\Delta_{Cg}$ have been written down, and I have checked them for consistency. Entries are recorded in table 8.2. All expressions of $\Delta_{Cg}$ are related proportionally to $T_{ES}$ ($T_M$ can be written in terms of $T_{ES}$ via Eq. (8.17)).

The size of the Cg is expected to decrease when the M-I transition is approached from below $n_c$, since $T_{ES} \rightarrow 0$. The progressive narrowing (or filling up) of a Cg is reflected by a decrease of the crossover temperature as the concentration of the boron impurity atoms is increased. Similar observations were made by several authors. Among these authors are Zhang *et al.*[168] and Rosenbaum[174].

### 8.2.7 The unperturbed density of states

In this section we study the behaviour of the localized electronic density of states (DOS) near the Fermi energy. The DOS is said to be unperturbed because effects due to long-range electron-electron interactions are ignored or regarded as negligible, and that the DOS is regarded as constant or slowly varying function of energy outside the Cg.

The unperturbed DOS is given in chapter 2 (cf. Eq. (2.5) as

$$N_o(E_F) = \frac{18}{k_B \xi^3 T_M} \quad . \tag{8.25}$$

Substituting $T_M$ from Eq. (8.23) into Eq. (8.25), the DOS can be expressed in terms of $T_{ES}$ and $T_{cr}$ as

$$N_o(E_F) = \frac{9}{8} \frac{T_{cr}}{T_{ES}^2} \alpha^3 \left( \frac{1.602 \times 10^{-19} \times 10^{-6}}{k_B} \right) \quad \mathrm{eV}^{-1}\ \mathrm{cm}^{-3} \quad . \tag{8.26}$$

Using $\alpha$ in Eq. (8.15) gives

$$N_o(E_F) = 1.44 \times 10^{12} \ (T_{cr}\, T_{ES}) \qquad \left(\mathrm{eV}^{-1}\ \mathrm{cm}^{-3}\right) \quad . \tag{8.27}$$

For sample AB21, we estimate $N_o(E_F) = 2 \times 10^{18}$ eV$^{-1}$ cm$^{-3}$. Approximately the same value is obtained using $N_o(E_F) = \beta_M / (k_B \xi^3 T_M) = 1.2 \times 10^{18}$ eV$^{-1}$ cm$^{-3}$ with $T = 275 \times 10^4$ K. We expect that $N_o(E_F)$ should remain non-changing with respect to temperature as long as $\overline{\Delta}_{hop,M}(T) > \overline{\Delta}_{hop,ES}(T)$ as discussed in section 8.2.6. In this case the hopping electrons will not be affected by the presence of the Cg since $k_B T >> \overline{\Delta}_{Cg}$.

### 8.2.8 Möbius *et al.* scaling model in the VRH regime

A new type of scaling behaviour was proposed recently in amorphous semiconducting films by Möbius *et al.*[12]. These authors suggested a 'universal' scaling function of the form[12, 31],

$$\sigma(T, x, ...) = \sigma_a \varphi \left(T \ / \ T_{ES}(x), ...\right) \quad , \tag{8.28}$$

where $\sigma_a$ is a proportionality constant and $\varphi$ is a function of dimensionless quantities. This model describes transport properties only in the regime where the hopping exponent $m \sim 0.5$. By analyzing temperature-conductivity data for composite film specimens well below 50 K, and plotting ln $\sigma$ against $T^{-1/2}$, Möbius *et al.*[12, 31] found that all the interpolated straight lines intersect the ln $\sigma$ axis at almost the same point, $\sigma_1$. The point of intersection $\sigma_1$ where six of the eight plotted curves intersect was used as a scaling parameter in Eq. (8.28) replacing $\sigma_a$. The justification of this method is that only one thermally activated conduction mechanism is acting in this region. We have explored this procedure in ◇C:B system.

Fig. 8-7 shows plots of ln $\sigma$ against $T^{-1/2}$ for boron-ion implanted diamond specimens.

The range of the experimental data in which the scaling law is valid was determined using the logarithmic derivative method. Only data obeying ES VRH was selected for fitting. The experimental data can be collapsed into a single universal curve, shown by plots in Fig. 8-8. The latter figure shows plots of data corresponding to doses $3.0 - 4.2 \times 10^{16}$ $cm^{-2}$. The details for this procedure can be found in articles by Möbius *et al.*[12, 32]. It should be pointed out here that the model by Möbius *et al.*[12, 31, 32] applies only to samples that show ES VRH behaviour. The model is not applicable to systems which show a conductivity crossover.

Another interesting feature in the Möbius *et al.*[12, 32] scaling law is the behaviour of the characteristic temperature $T_o$ (K), determined by fixing $m = 1/2$, as a function of boron-ion concentration. Extrapolating the $T_o$ values obtained to the lowest measurable characteristic temperature (since the plot is in semi-log scale), we obtain $n \simeq 4.0 \times 10^{21}$ $cm^{-3}$. Fig. 8-9 shows plots of $T_{ES}$ (K) *vs.* $n$, where $T_o$ are the characteristic temperatures of Mott, ES and Möbius *et al.*[12, 32]. Incidentally, $n \simeq 4.0 \times 10^{21}$ $cm^{-3}$ has been determined using the Shlimak *et al.*[16] method to correspond to the critical boron-ion concentration. The method of Shlimak *et al.*[16] will be described later in this chapter. In Fig. 8-9 (b), we show a plot of $T_{ES}$ *vs.* $n$. It is clear that we cannot determine $n_c$ from this plot.

### 8.2.9 Aharony *et al.* scaling law in the VRH regime

A universal scaling function for samples which show electrical conductivity crossover from Mott to ES VRH behaviour, in 3D systems, has been proposed recently by Aharony *et al.*[200]. They have shown that the resistivity data of disordered insulators obey the general scaling function of the form:

$$\ln\left(\frac{R}{R_o}\right) = A\, f\left(\frac{T}{T_x}\right) \quad , \tag{8.29}$$

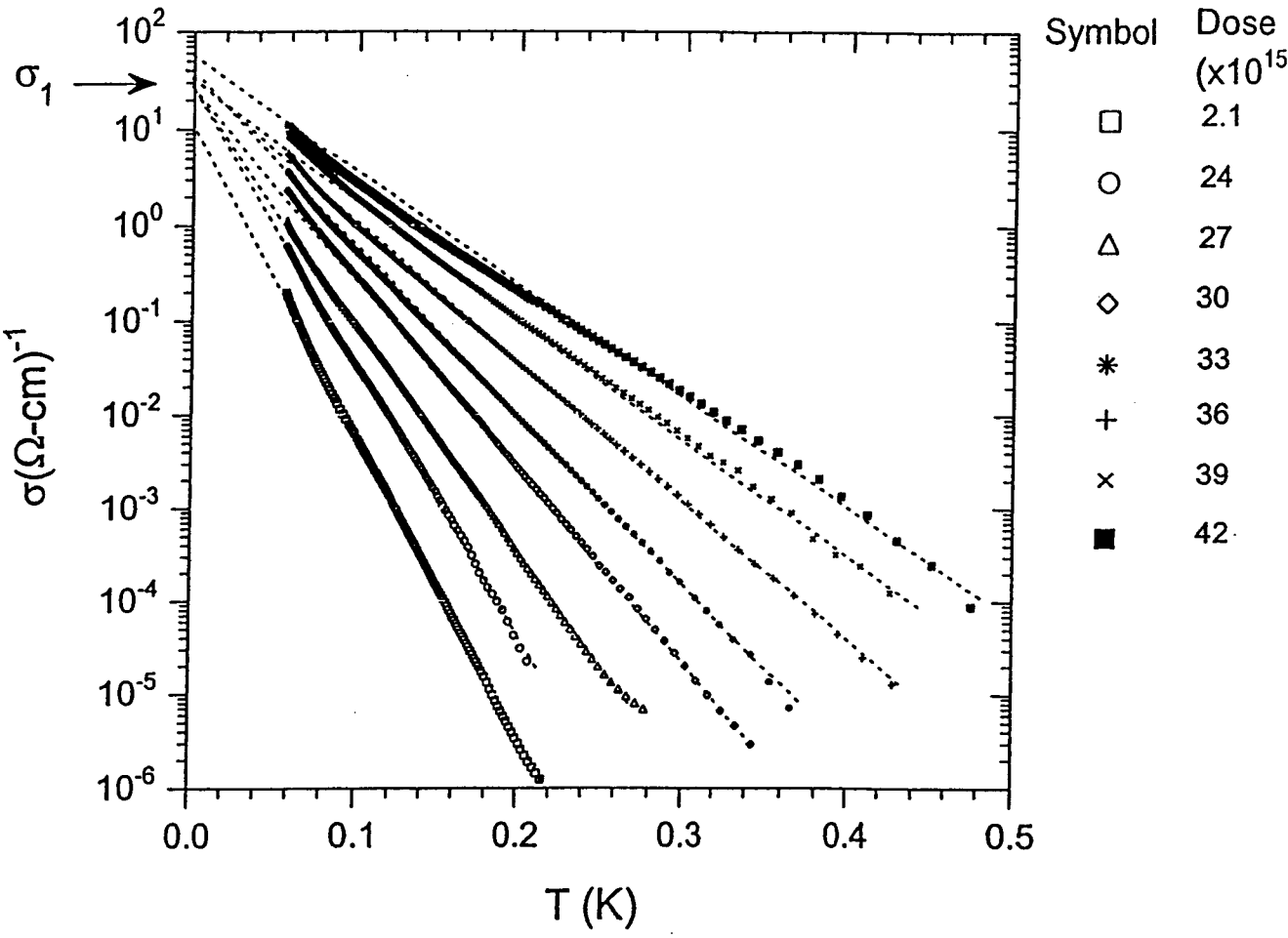


Figure 8-7: Plots of ln $\sigma$ *vs.* $T^{-1/2}$ for boron-ion implanted diamond specimens. The scaling parameter $\sigma_1$ is shown in the figure.

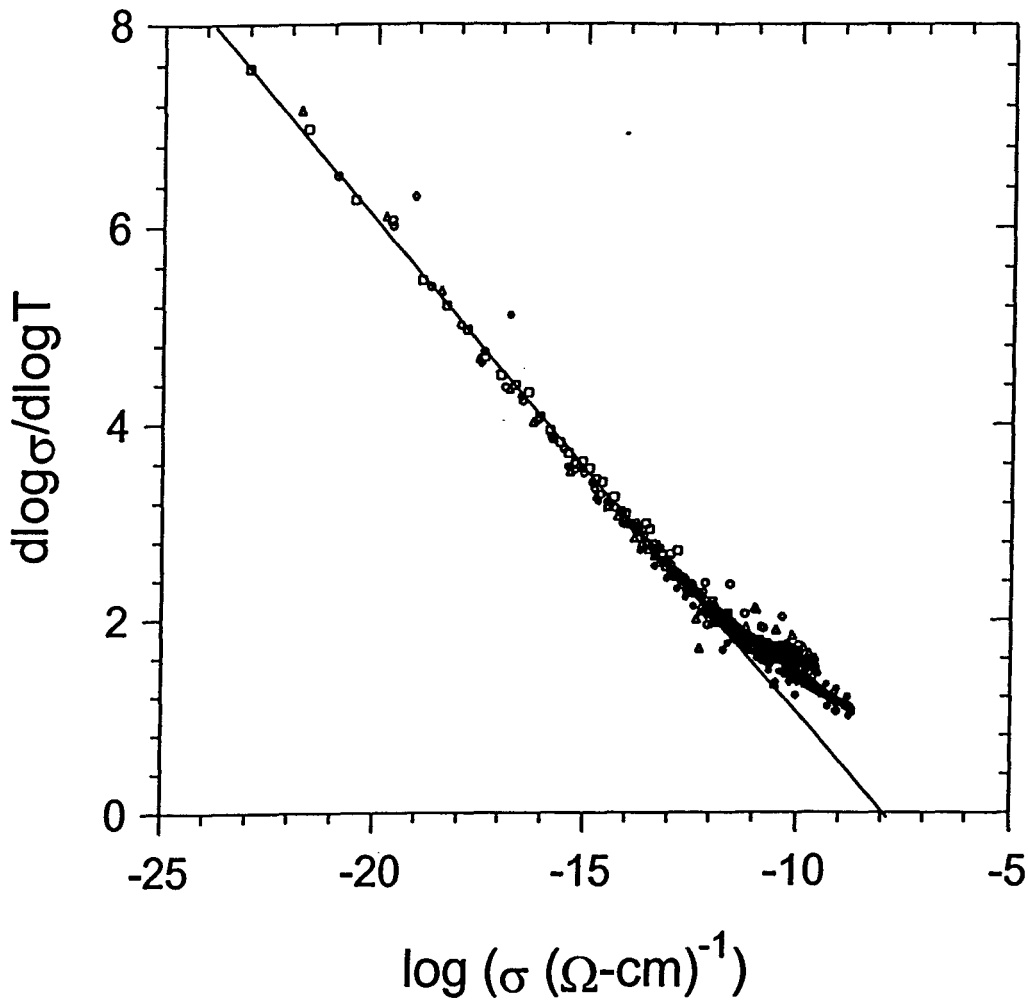


Figure 8-8: Plots shown in Fig. 8.7 can be collapsed into a single universal curve using $\sigma_1$ as the scaling parameter. We have plotted data corresponding to doses $3.0-4.2\times10^{16}$ cm$^{-2}$. Details of the method can be found in papers by Mobius *et al.*[32].

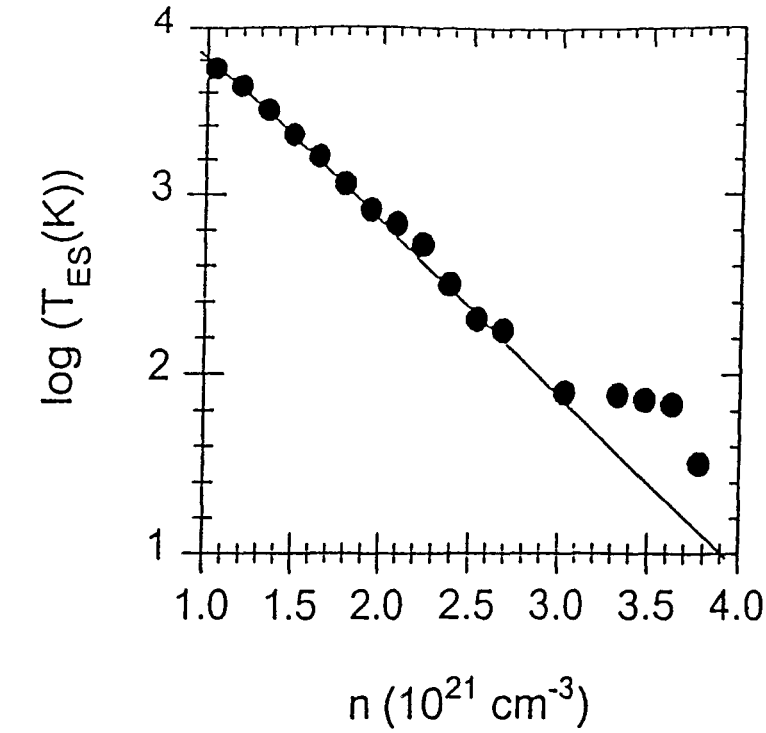


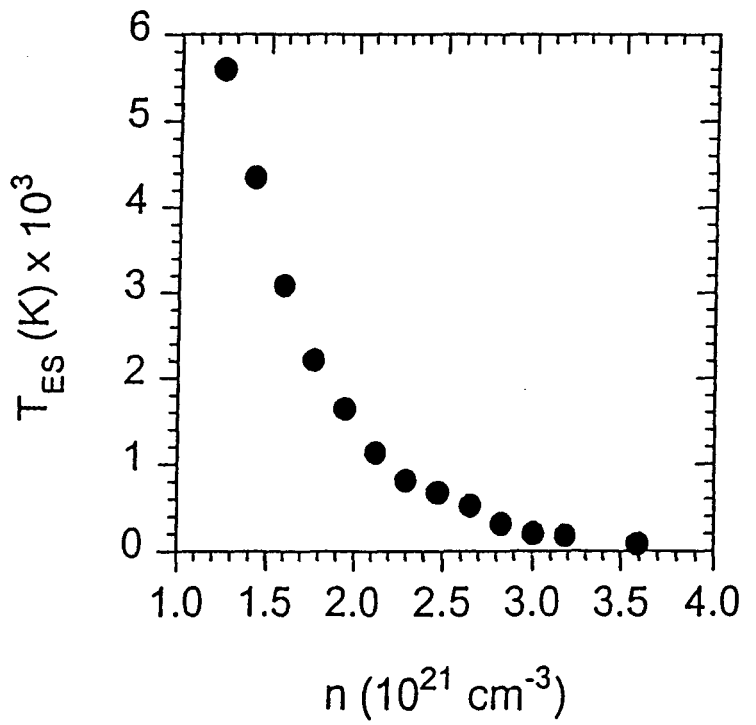


Figure 8-9: Plots of $T_{ES}$ versus $n$ in semilog and linear scales. The $T_{ES}$ values were obtained with the hopping exponent fixed to $m = 1/2$ and $\sigma_1$ read from Fig. 8.7.

where the scaling factors $A$ and $T_x$ depend on individual sample properties, but the function $f(x)$ is universal. Values of $A$, $T_x$ and $R_o$ have been deduced for each sample using non-linear least squares fitting procedure. The universal function $f(x)$, where $x = T/T_x$ , has the limiting behaviours in VRH regimes:

$$f(x) \propto \begin{cases} x^{-1/4}, & \text{for } x \gg 1 \quad \text{(Mott case)} \\ x^{-1/2}, & \text{for } x \ll 1 \quad \text{(ES case)} \end{cases} \quad . \tag{8.30}$$

Aharony *et al.* have derived expressions for both $T_M$ and $T_{Es}$ in terms of the crossover temperature, $T_x$, as

$$T_M = A^4 T_x \tag{8.31}$$

and

$$T_{ES} = \frac{9}{2} A^2 T_x \quad . \tag{8.32}$$

Combining Eqs. (8.31) and (8.32), we can eliminate the scaling temperature $T_x$, and write $A$ as

$$A = \left( \frac{9}{2} \frac{T_M}{T_{ES}} \right)^{1/2} \quad . \tag{8.33}$$

Substituting Eq. (8.31) into either Eq.(8.32) or Eq. (8.33) yields $T_x$, as

$$T_x \simeq \frac{1}{20} \left( \frac{T_{ES}^2}{T_M} \right) = \frac{1}{320} T_{cr} \quad . \tag{8.34}$$

There exists a discrepancy in the prefactor of the scaling temperature $T_x$ when compared to $T_{cr}$ given by Eq. (8.23). The assumptions made in the derivation of the Aharony *et al.*[200] method have recently been questioned by Rosenbaum *et al.*[27]. Quantities extracted using the Aharony *et al.*[200] method are summarized in table 8.3. Furthermore, we show that our data, which exhibit a smooth conductivity crossover from Mott to ES VRH, can be described by a simple heuristic function[200],

$$\ln\left(\frac{\rho}{\rho_o}\right) = Af(x) = A\left[\frac{1+\left((1+x)^{1/2}-1\right)/x}{\left((1+x)^{1/2}-1\right)^{1/2}}\right] \quad . \tag{8.35}$$

Fig. 8-10 shows plots of $1/A\ln(\rho/\rho_o)$against $\ln(T/T_x)$ for a number of insulating samples. The solid line represents the function $f(x)$ of Eq.(8.35). A percolation picture has recently been used by Meir[175] to derive a crossover function from the Mott to the ES hopping regime.

## 8.3 Conduction in the metallic regime

We use the analytical procedure of Rosenbaum *et al.*[18, 99] to determine the value of $n_c$ from our experimental data. To do this, we first obtain values of $\sigma(0)$ for metallic samples by extrapolating the low temperature measured electrical conductivity to zero temperature. In making this extrapolation, we fit the low temperature data to the fitting function,

$$\sigma(T) = \sigma(0) + CT^Z \quad . \tag{8.36}$$

(See chapter 2 as to why other higher order terms are dropped from Eq. (8.36)). This procedure has been used over the past few decades[204], and it is now referred to as the conventional method. In spite of many years of the application of the conventional method to metallic systems, there still remain a number of major theoretical and experimental challenges. In particular, the critical behaviour of the electrical conductivity at $T = 0$ K and the critical conductivity exponent are still difficult to determine to a high degree of accuracy[86, 87, 88, 106]. Fig. 8-11 shows a plot of one of the metallic samples, AB84. The solid line represents a fit to Eq. (8.36). The degree of reliability of the conventional method depends largely on the lowest temperatures that can be measured. Most reliable results are those obtained when extrapolations are made in the mK

| | | | | Experimental | | | | Theoretical |
|---|---|---|---|---|---|---|---|---|
| Sample | Dose | Symbol | $A$ | $T_x$ (K) | $R_o$ ($\Omega$) | $T_M$ (K) | $T_{ES}$ (K) | $T_x$ (K) |
| Name | ($\times 10^{15}$ cm$^{-2}$) | | | | | $\times 10^4$ | $\times 10^3$ | |
| AB21 | 21 | □ | 24.837 | 2.141 | 124.95 | 81.5 | 5.9 | 694 |
| AB24 | 24 | ○ | 15.179 | 4.637 | 225.08 | 24.6 | 4.8 | 1502 |
| AB27 | 27 | △ | 13.121 | 4.448 | 323.55 | 13.2 | 3.5 | 1442 |
| AB30 | 30 | ◇ | 11.361 | 4.240 | 327.82 | 7.1 | 2.5 | 1373 |
| AB33 | 33 | * | 14.454 | 1.928 | 218.34 | 8.4 | 1.8 | 625 |
| AB36 | 36 | + | 15.968 | 1.0471 | 208.09 | 6.8 | 1.2 | 339 |
| AB39 | 39 | × | 16.104 | 0.745 | 184.22 | 5.0 | 8.7 | 241 |

Table 8.3: Quantities extracted using the method of Aharony are summarized in this table.

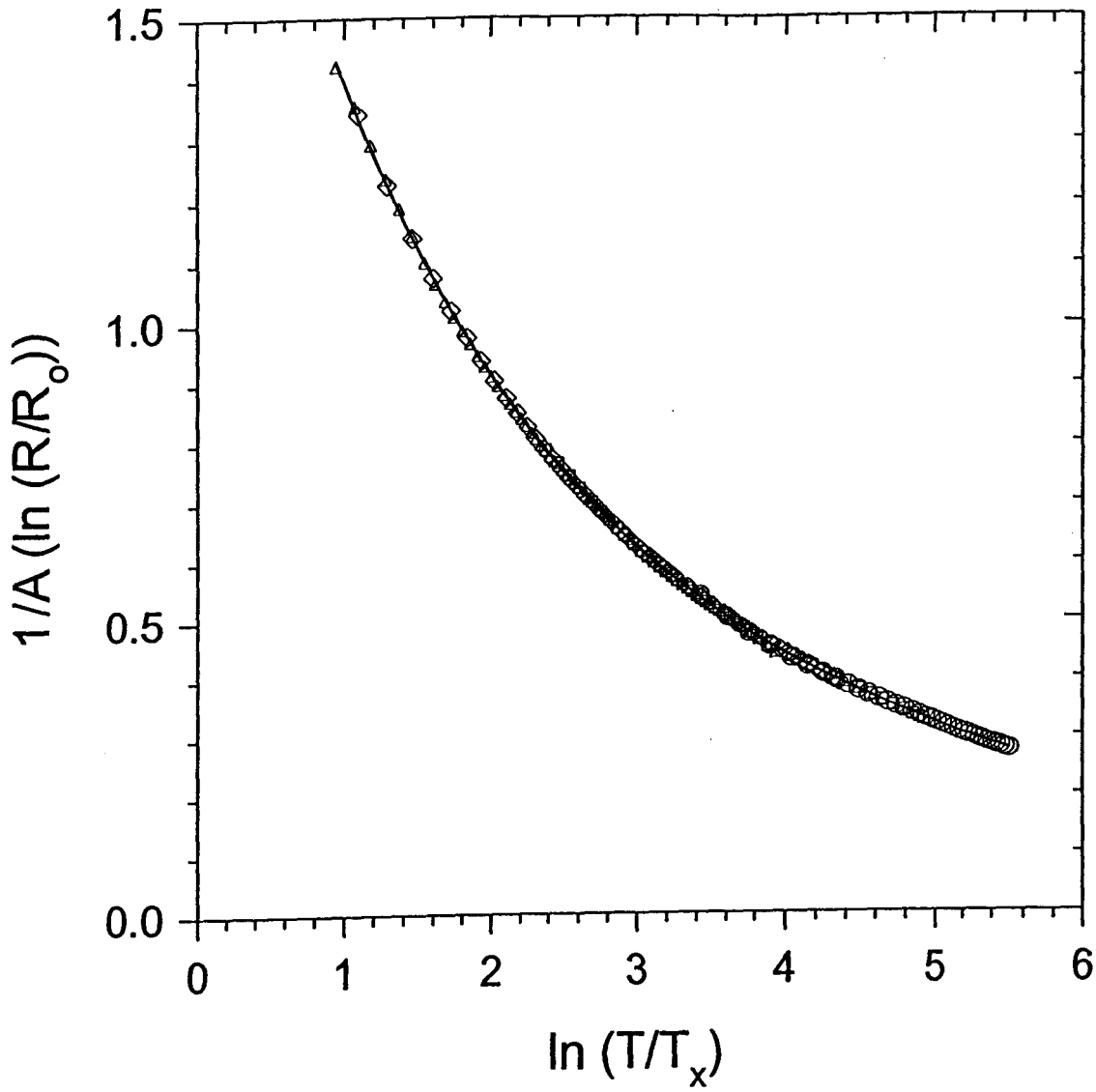


Figure 8-10: Universal scaling function crossover plot of scaled resistance versus the scaled temperature for some insulating diamond specimens. The method used to generate this plot is given by Aharony *et al.*[200].

ranges. Another important factor that governs the conventional method is the linearity of the experimental data when $\sigma(T)$ is plotted against $T^Z$ ($Z = 1/2$ or $1/3$) at low temperatures.

The conventional method has some disadvantages. Despite the uncertainty of the extrapolated results and the linearity of the conductivity with $T^{1/2}$, erroneous results can still be obtained when,

- there are strong fluctuations of the low-temperature experimental data set,
- the sample is inhomogeneous, and
- the M-I transition is too sharp[16, 34].

Fig. 8-12 shows $\sigma(0)$ as a function of boron-ion concentration, $n$, for samples AB78-AB84 annealed at 1700 °C. Entries of quantities in tables 8.1-8.3 depend on the $\sigma(T)$ regime selected for the fitting procedure. Different values for $\sigma(0)$ have been obtained as we progressively cut down on the temperature range from 1.5 $-100$ K down to 1.5-10 K. This may reflect on the unreliability of the extrapolation method when determining $\sigma(0)$ values. In some cases, values of $\sigma(0)$ change from being positive to negative. A negative value for $\sigma(0)$ implies that the sample is insulating[169]. By this method alone it would therefore be difficult to clearly distinguish and classify samples as either insulating or metallic. Clearly electrical conductivity measurements in the millikelvin range would reduce the difficulties encountered in extrapolation to $T = 0$ K.

A great deal of work to advance the argument for the use of the conventional method has been given by a number of authors, in particular the Sarachik group[17, 87, 168] and Lohneysen's group[194].

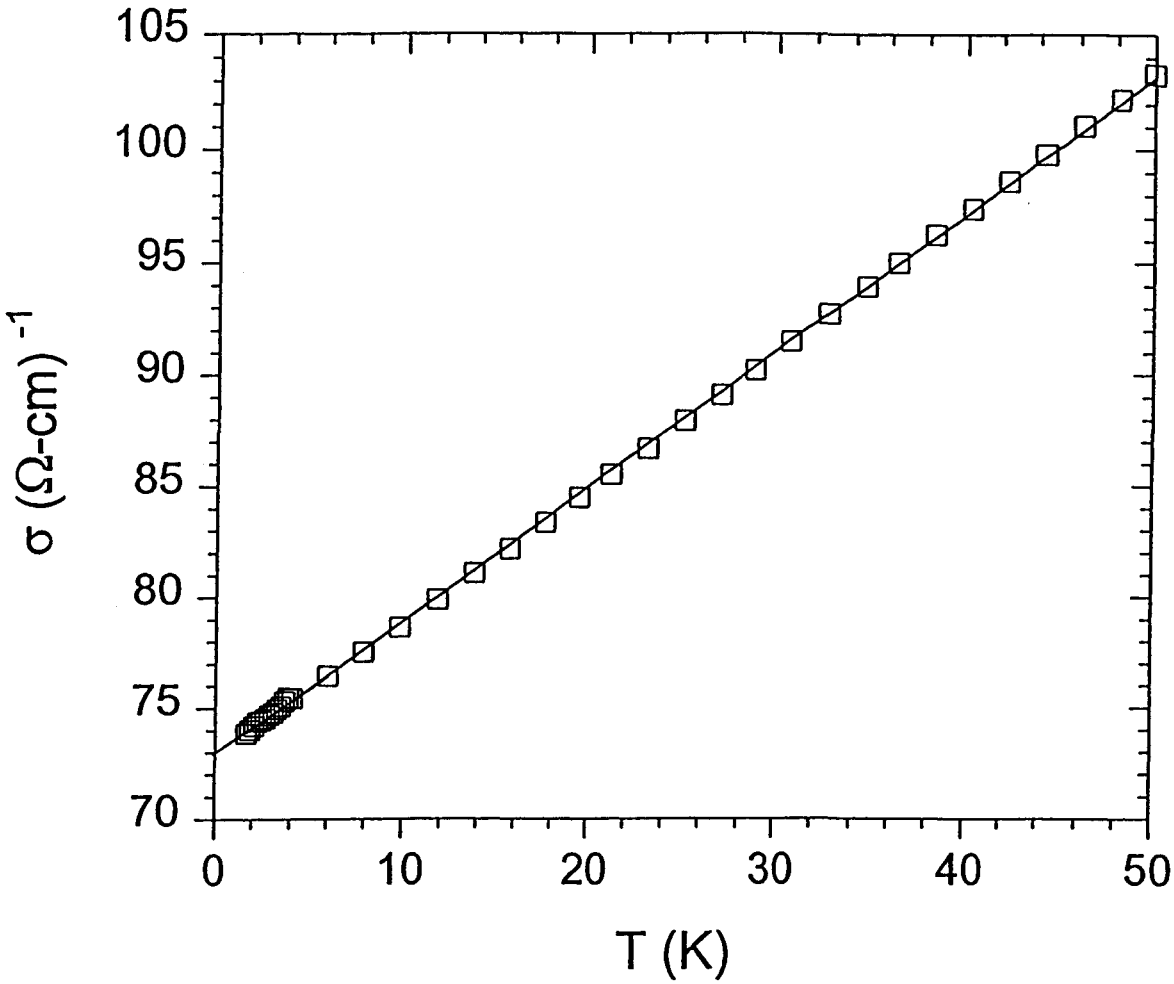


Figure 8-11: Electrical conductivity for one of the metallic samples, AB84, which has been annealed at 1700 °C.

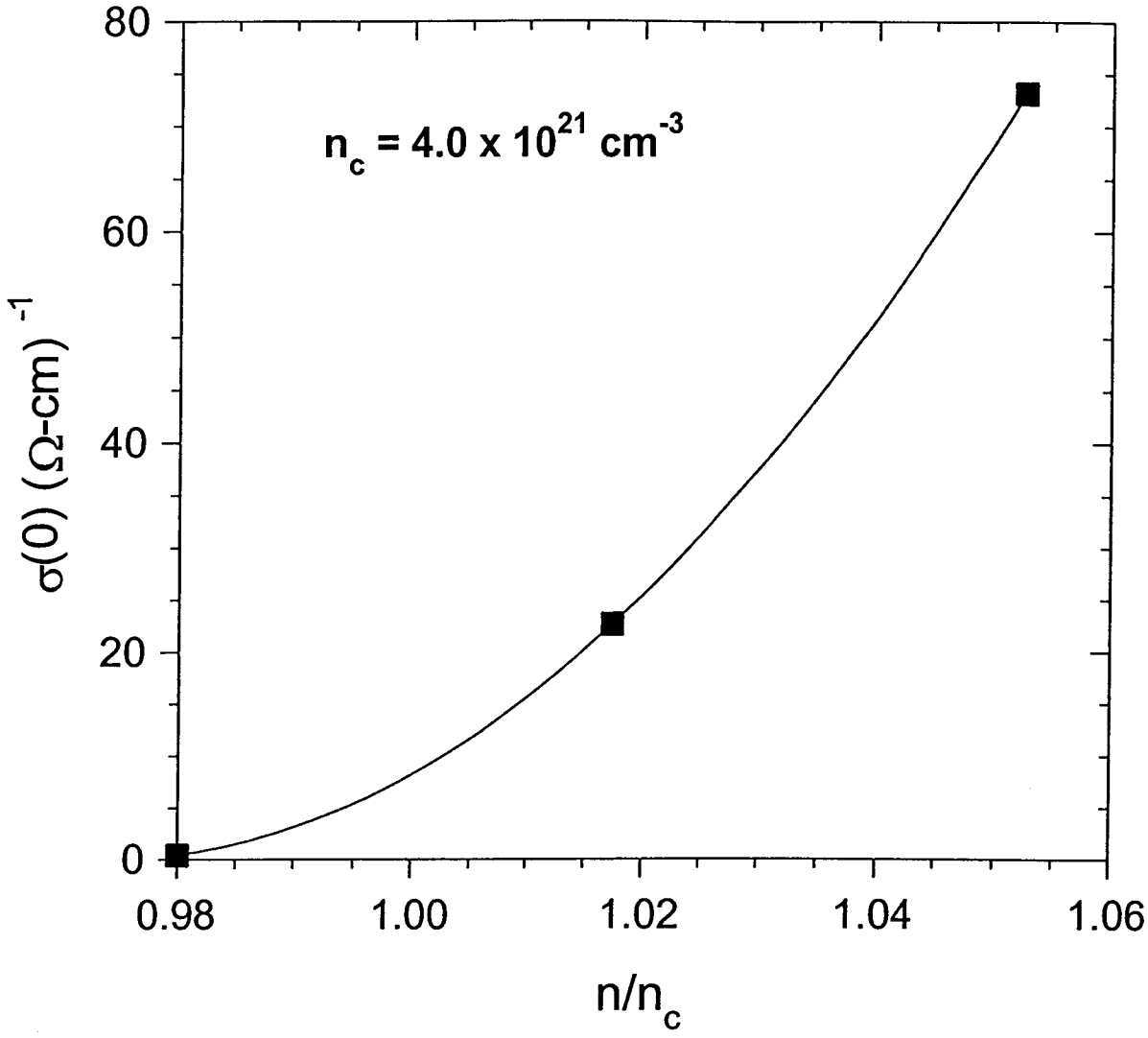


Figure 8-12: $\sigma(T)$ *vs.* $n$ for samples AB78, AB81 and AB84. These samples have been implanted close to the M-I transition. We obtained $\mu \sim 1.7$ and $\sigma_o = 9736$ $(\Omega\text{–cm})^{-1}$ from the fit of Eq. (1.1). The values of $n$ have been estimated using the SIMS technique with an error of $5 - 10$ % .

### 8.3.1 The derivative method for the metallic systems

Substituting Eq. (8.36) into Eq. (8.5) yields

$$W = \frac{ZCT^Z}{\sigma(0) + CT^Z} \equiv \frac{ZCT^Z}{\sigma(T)} \quad . \tag{8.37}$$

Two important predictions can be made, in the case of metallic samples, based on Eq. (8.37).

(i) With $\sigma(0) > 0$, $W$ should extrapolate to zero as $T \rightarrow 0$ K. This should be valid irrespective of the sign of $C$, provided only that $Z > 0$[106].

(ii) $W$ should vanish at lower temperatures, *viz*, $T < (\sigma(0)/C)^{1/Z}$, as the M-I transition is approached from above $n_c$. By making a linear regression fit to the log $(W\sigma(T))$ versus log $T$ plot one obtains the slope as $Z$ and the y-intercept as log $(ZC)$. Once the $Z$ value is known, the factor $C$ can be calculated from the expression,

$$C = \frac{10^{y-int}}{Z} \quad . \tag{8.38}$$

We can obtain $\sigma(0)$, by rearranging quantities in Eq. (8.37), as

$$\sigma(0) = CT^Z \left( \frac{Z}{W} - 1 \right) \quad . \tag{8.39}$$

$\sigma(0)$ can therefore be determined from the experimental data without extrapolating the conductivity results to zero temperature. Usually, values for $\sigma(0)$ are calculated from one conductivity data point for each different sample. These values are listed in table 8.4, and are compared to those $\sigma(0)$ values obtained using the extrapolation procedure.

As the M-I transition is approached from the insulating side, the exponential function of Eq. (8.4) would increasingly become inadequate in describing the transport phenomena, and is expected to collapse even before the transition into a metallic phase occurs. This means that some modifications to Eq. (8.4) are necessary, particular when the lowest

| | | Zabrodskii-Zinov'eva method | | | | Conventional method | |
|---|---|---|---|---|---|---|---|
| Sample | Dose | $C$ | $Z$ | $T$ (K) | $\sigma(0)$ $(\Omega\text{–cm})^{-1}$ | $\sigma(0)$ $(\Omega\text{–cm})^{-1}$ | Annealing $T$(°C) |
| | ($\times 10^{15}$ cm$^{-2}$) | | | | cf. Eq. (8.39) | cf. Eq. (8.36) | |
| AB78 | 78 | 2.43 | 0.43 | 4.91 | −0.73 | 0.44 | 1700 |
| AB81 | 81 | 0.77 | 0.64 | 5.02 | 23.65 | 22.61 | 1700 |
| AB84 | 84 | 0.52 | 1.04 | 2.46 | 71.25 | 73.12 | 1700 |

Table 8.4: Values for $\sigma(0)$ are calculated from one conductivity data point for each different sample using Eq. (8.39). These values are compared to those $\sigma(0)$ values obtained using the extrapolation procedure.

measuring temperature exceeds $T_o$. By expanding Eq. (8.4) using the Taylor expansion series, yields

$$\sigma(T) \simeq \sigma_o \left[1 - \left(\frac{T_o}{T}\right)^m + \frac{1}{2!}\left(\frac{T_o}{T}\right)^{2m} + \ldots\right]$$

$$\simeq \sigma_o - HT^{-m} \quad , \tag{8.40}$$

where $H \equiv \sigma_o T_o^{-m}$ is constant. By comparing Eq. (8.36) which describes metallic films, with Eq. (8.40), suggests that the conductivity exponent as well as the prefactor will change sign simultaneously when the M-I transition is crossed. The constant $H$ may change sign even before the transition is crossed[107].

To put some cohesion to this section, I have summarized the main points below which may serve as guides in classifying samples near the M-I transition. We have noted the following in the case of metallic samples:

- $W$ should extrapolate to zero as $T \rightarrow 0$ in spite of whether $C \lesseqgtr 0$, provided only that $Z > 0$.
- $W$ should vanish for $CT^Z < \sigma(0)$ when the M-I transition is approached from above $n_c$.
- $C$ and $Z$ must change signs simultaneously as the M-I transition is crossed[106, 186]. This claim may not necessarily be true as some evidence exits that $C$ may change sign before the M-I transition is crossed[107].

I have put these three criteria to the test, by probing samples that lie in the vicinity of the transition. Fig. 8-5 reveals sample AB78 ( $n \simeq 4.0 \times 10^{21}$ cm$^{-3}$) to be weakly insulating (*i.e.* $\sigma(T) \propto T^Z$), with $W(T) \rightarrow Q$ (where $Q$ is finite positive value) as $T \rightarrow 0$ K. Sample AB81 ($n \simeq 4.1 \times 10^{21}$ cm$^{-3}$) also show a family of curves (see Fig. 7-8) in

which $W(T) \rightarrow Q$. The smooth rise in the log $W - T$ plots, with a negative slope, has recently been addressed by Castner and Shafarman[205] by adding a correctional prefactor to the Mott VRH relation.

### 8.3.2 Classification of samples due to e-e interactions

Al'tshuler and Aronov[69] have shown that the temperature variation of the conductivity is governed mainly by electron-electron interaction, and can be written using Eq. (8.36) as

$$\Delta\,\sigma(T) \equiv \sigma(T) - \sigma(0) = CT^{1/2} \tag{8.41}$$

where $C = A/D$, and the conductivity exponent is fixed to $1/2$. Here, $A$ is a temperature-independent constant and $D$ is the diffusion constant. According to the Einstein conductivity relation,

$$\sigma = e^2 D \left(\frac{dN(E_F)}{dE}\right) \quad , \tag{8.42}$$

where $dN(E_F)/dE$ is the density of states at the Fermi energy. Combining Eq. (8.41) and Eq. (8.42), and eliminating $y = A/D$ and $D$, we obtain,

$$\sigma(T) = \sigma(0) + v\left(\frac{T}{\sigma(T)}\right)^{1/2} \tag{8.43}$$

where $v = A\,e\sqrt{dN(E_F)/dE}$. We have plotted $\sigma(T)$ *vs.* $\sqrt{(T/\sigma)}$, as shown in Fig. 8-13 and extrapolated the results to zero temperature to determine which of the samples are insulating or metallic. According to this method, sample AB78 is weakly insulating. This is consistent with the results obtained using the derivative method. An exponent of $1/3$ has been predicted for systems quite close to the metal-insulator transition[108], and observed experimentally in some doped systems[16]. The determination of an exponent

of 1/3 is presented in section 8.3.3.

### 8.3.3 Shlimak *et al.* method near the M-I transition

In a recent paper, Shlimak *et al.*[16] have proposed a new procedure to determine $n_c$ for the M-I transition and the critical conductivity exponent $\mu$ without extrapolating the temperature-dependent electrical conductivity to zero temperature. The method involves replacing $\sigma(0)$ by the difference, $\Delta\sigma(T^*) = \sigma_n(T^*) - \sigma_{n_c}(T^*)$, calculated at any low temperature $T^*$ in which the power law approximation, $\sigma(T) = \sigma(0) + CT^Z$ ($Z = 1/2$ or $1/3$), is obeyed.

Shlimak *et al.*[16] suggest that the conductivity of samples at the M-I transition should be governed by the relation, $\sigma(T) = CT^{1/3}$ (with $\sigma(0) = 0$), in accordance with the model of Al'tshuler and Aronov[67]. A new dimensionless parameter, $\alpha$, which characterizes the M-I transition in the regime where the power law is valid, is given by

$$\alpha = \frac{R(T_1)}{R(T_2)}\left(\frac{T_1}{T_2}\right)^{1/3} = \begin{cases} > 1 & \text{(metallic conductivity} \\ 1 & \text{(metal-insulator transition)} \\ < 1 & \text{(insulating)} \end{cases} , \qquad (8.44)$$

where temperatures $R(T_1)$ and $R(T_2)$ are resistances of a given sample measured at any two temperatures in a regime where the metallic conductivity expression, $\sigma(T) = \sigma(0) + CT^{1/3}$, is observed. In Fig 7-7 we showed plots of $\sigma(T)$ dependences of samples in the vicinity of the transition in the $T^{1/3}$ and $T^{1/2}$ scales. It is apparent from those plots that in the vicinity of the M-I transition, the experimental curves are better fitted by the relation $\sigma(T) \propto CT^{1/3}$, than $\sigma(T) \propto CT^{1/2}$. Two temperatures, $T = 4.2$ K and $T = 2.0$ K, have been selected to calculate the $\alpha$ values. Table 8.5 lists values of the $\alpha$ parameters for most of the samples near the M-I transition. Alongside the $\alpha$ values are

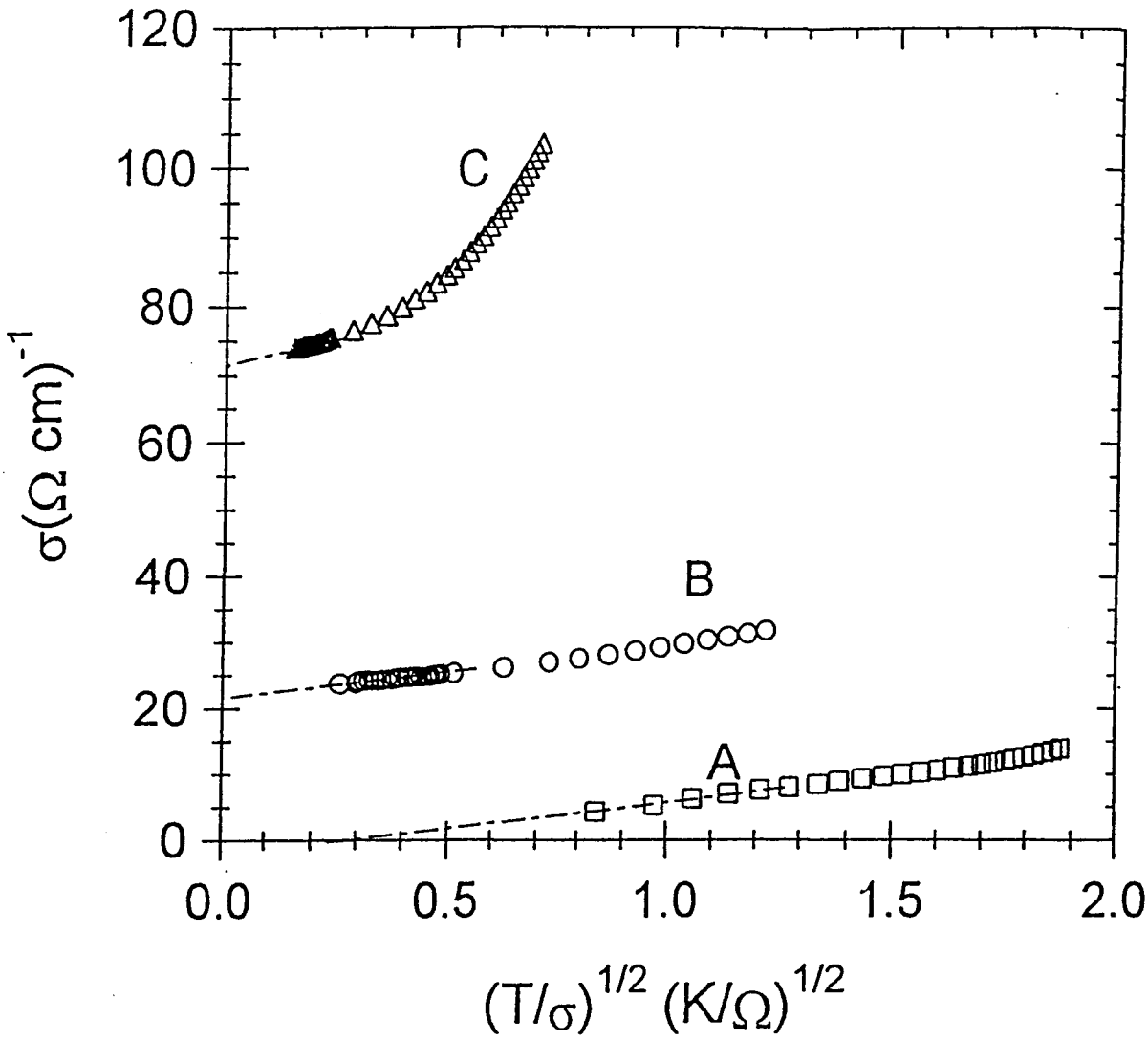


Figure 8-12: Following the work of Watanabe *et al.* [178], we can further classify sample AB78 (curve A) as insulating, but AB81 (curve B) may taken as 'weakly' metallic with a finite conductivity at $T = 0$ K. Sample AB84 is represented by curve C.

the boron-ion doses and the annealing temperatures. A value of $\alpha \simeq 1$ corresponds to sample AB78. The critical boron-ion concentration, according to method of Shlimak *et al.*[16], may be taken to be $\simeq 4.0 \times 10^{21}$ cm$^{-3}$. A close inspection of plots in Fig. 7-7 shows all $\sigma(T)$ curves to be almost parallel, and therefore $\Delta\sigma(T^*) \simeq \sigma(0)$. This make it possible for us to use Eq. (2.30), *viz.* $\log(\Delta\sigma(T^*)/\sigma_o) = \mu \log(n/n_c - 1)$ to calculate $\mu$. We obtained an average value of $\mu$ to be $\sim 1.7$. and $\sigma_o = 9736$ $(\Omega\text{–cm})^{-1}$ as shown in Fig. 8-14. A value of $\mu = 1$ has been reported by Shlimak *et al.* in a number of systems at low temperatures, and it is claimed to be universal. The Shlimak method has recently been questioned by Sarachik's group[17]. According to these authors, the conventional method remains the only reliable method to use in extracting quantities which describes the M-I transition. Quite recently Bogdanovich *et al.*[201] have obtained an exponent of $Z = 1/2$ in Si:B system located in the critical regime. The system was tuned at the M-I transition using uniaxial stress. The controversy that surrounds the critical conductivity exponent in systems which are in the critical regime still remains unresolved [47, 92, 194, 201].

## 8.4 Conduction at the M-I transition

### 8.4.1 Mott Criterion and the minimum metallic conductivity

Mott has shown that systems which undergo the M-I transitions can be described by the criterion[8]

$$n_c^{1/3} a_H^* \simeq 0.26 \quad , \tag{8.45}$$

where $a_H^*$ is the Bohr radius of the impurity centre, which in my case can be taken to be the mean free path between the scattering boron impurity centres. The Mott criterion has been confirmed by experimental data for systems with $n_c$ varying over 9 orders of

| Dose | Annealing $T$ | $T_1$ | $T_2$ | $R_1$ | $R_2$ | $\alpha$ |
|---|---|---|---|---|---|---|
| ($\times 10^{15}$ cm$^{-2}$) | (°C) | (K) | (K) | ($\Omega$) | ($\Omega$) | |
| 78 | 1200 | 5.03 | 3.11 | 24714 | 34294 | 0.85 |
| 78 | 1700 | 4.91 | 2.96 | 14118 | 17559 | 0.95 |
| | | | | | | |
| 81 | 500 | 4.06 | 2.41 | 14880 | 19812 | 0.89 |
| 81 | 500 | 4.01 | 2.40 | 16162 | 21312 | 0.90 |
| 81 | 1300 | 4.12 | 2.00 | 7549 | 10651 | 0.91 |
| 81 | 1400 | 4.27 | 2.04 | 7556 | 9636 | 0.98 |
| 81 | 1500 | 4.32 | 2.10 | 5654 | 6833 | 1.05 |
| 81 | 1600 | 3.99 | 2.09 | 2127 | 2412 | 1.09 |
| 81 | 1700 | 4.20 | 2.09 | 650 | 675 | 1.22 |
| | | | | | | |
| 84 | 1700 | 5.88 | 4.84 | 415 | 421 | 1.05 |

Table 8.5: The $\alpha$ values, shown in the last column, have been calculated using Eq. (8.44) for some samples located close to the metal-insulator transition. The $\alpha$ values were found to increase as annealing temperatures were increased. This is an indication that samples may be driven into the metalic phase by annealing them at high temperatures.

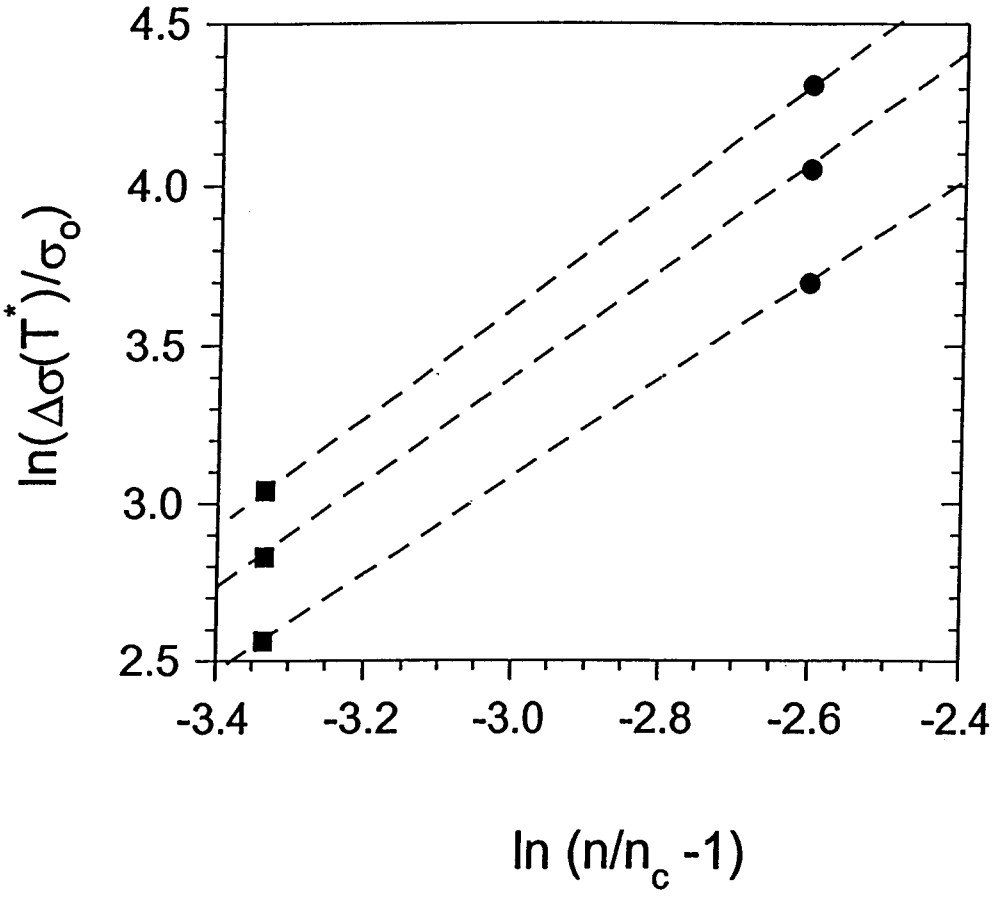


Figure 8-13: Shlimak *et al.*[16] method to determine the critical conductivity exponent $\mu$. We have calculated the $\mu$ value to be $\sim 1.7$. The procedure for the calculation of $\mu$ is outlined in the text.

magnitude. A summary of the results obtained for a large number of systems is given by Edwards and Sienko[79], and is captured in Fig. 8-15. For $n_c \simeq 4.0 \times 10^{21}$ cm$^{-3}$, the Mott criterion gives $a_H^* \simeq 0.17$ nm. By using $n_c \simeq 4.1 \times 10^{21}$ cm$^{-3}$, we obtain $a_H^* \simeq 0.16$ nm. It is noted that the $a_H^*$ value is approximately equal to that of diamond lattice spacing, *viz.* 0.154 nm. It is of interest to compare our present results with those for Si:B, which has been comprehensively studied for many years. Table 8.6 shows a comparison of these systems together with the M-I transition results.

We have added our calculated $n_c$ to Fig. 8-15 in order to compare with other doped semiconductors. Our $n_c$ value seems to be in good agreement with the prediction of Mott[8].

The minimum metallic conductivity, discussed in chapter 2, is given by

$$\sigma_{\min} = C_1 \frac{e^2}{\hbar l} = \frac{C_1}{l} \left(2.4 \times 10^{-4}\right) \ \Omega^{-1} \tag{8.46}$$

where $C$ is a numerical constant in the range 0.025 to 0.1. If we assume $l \simeq a_H^* \simeq 0.16$ nm obtained from the Mott criterion, we then obtain $\sigma_{\min} = 424 - 450$ $(\Omega\text{–cm})^{-1}$. A value of $\sigma_{\min} = 240$ $(\Omega\text{–cm})^{-1}$ has been estimated following the use of $l \equiv a_H^* = 0.3$ nm. When the latter $a_H^*$ value is used in Eq. (8.45), we obtain $n_c = 6.05 \times 10^{20}$ cm$^{-3}$ which clearly corresponds to one of the insulating samples. The fact that $\sigma(0)$ for sample AB84 is lower than $\sigma_{\min} = 450$ $(\Omega\text{–cm})^{-1}$ may be a signature for a continuous transition. Values of $\sigma(0)$ lower than $\sigma_{\min}$ are now commonplace[86, 106].

### 8.4.2 The derivative method for systems at the M-I transition

Consider Eq. (8.37). Setting $\sigma(0) = 0$, gives $W = Z$. This means that samples at the transition should exhibit temperature-independent values of $w$. But, by letting $\sigma(0) = 0$,

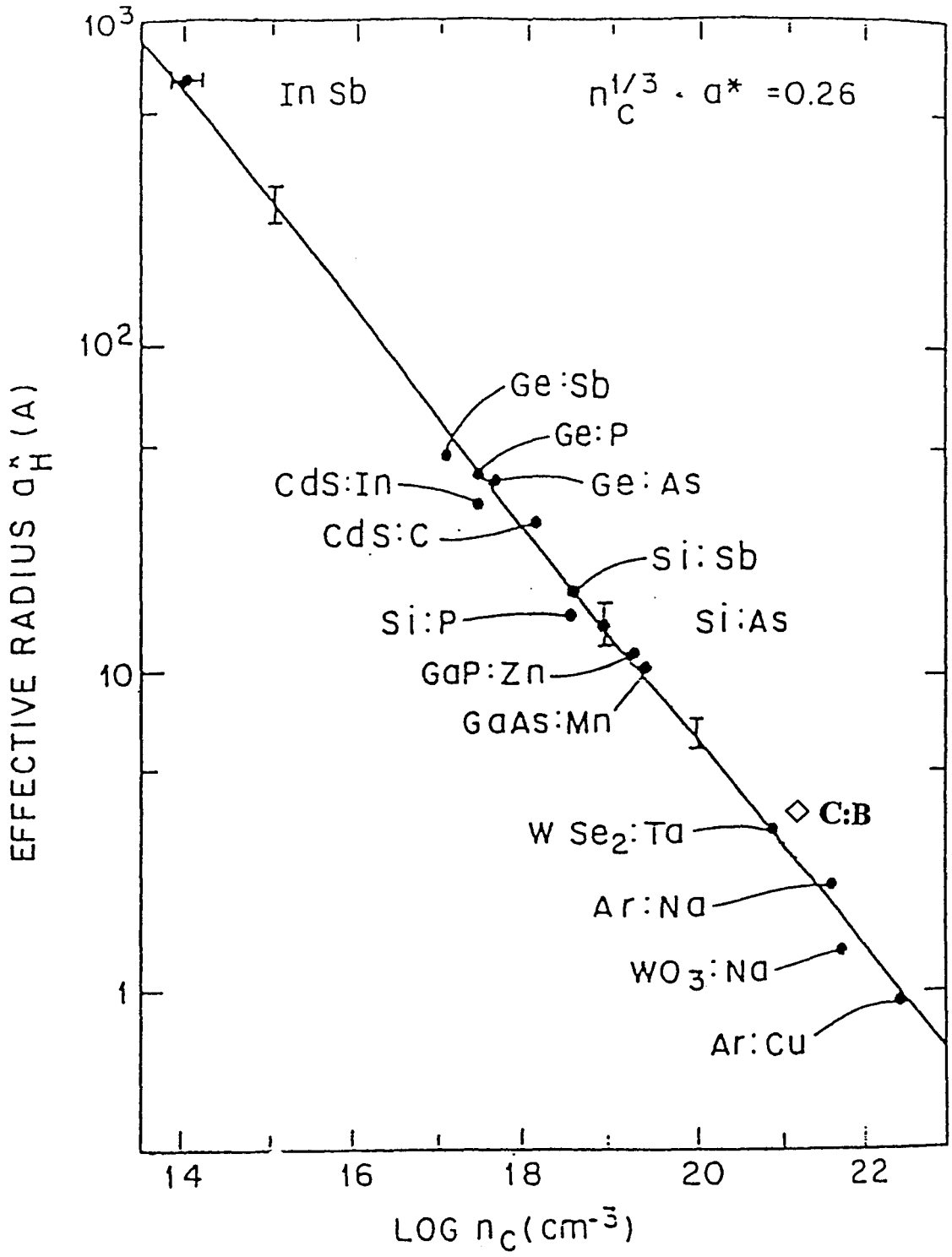


Figure 8-15: Edwards-Sienko plot [79] demonstrating the Mott criterion. The ◇C:B sample that we have studied is shown against other doped semiconductors in this figure.

| | Energy gap $E_g$ (eV) | Spin-orbit energy $\Delta E_{so}$ (eV) | Acceptor-activation energy $E_a$ (eV) | Dielectric constant $\varepsilon$ | Lattice spacing $a$(nm) | Hydrogenic radius $a^*_H$(nm) | $n_c$ ($\times 10^{18}$ cm$^{-3}$) | $\mu$ |
|---|---|---|---|---|---|---|---|---|
| **Si:B** | 1.08 | 0.04 | 0.045 | 11.7 | 0.235 | 1.6 | 4 | 1.0 |
| **◊C:B** | 5.5 | 0.006 | 0.37 | 5.7 | 0.154 | 0.16 | 4000 | 1.7 |

Table 8.6: A comparison of values of parameters obtained from ◇C:B and those of the Si:B semiconductor system.

the conductivity data can be described by an expression

$$\sigma(T) = BT^Z \quad , \tag{8.47}$$

with $C$ and $Z = w$ being the two fitting parameters. Eq. (8.47) is used to describe the weakly insulating materials, since $\sigma(T) \rightarrow 0$ as $T \rightarrow 0$ K[206]. The general VRH law cannot be fitted successfully to weakly insulating samples. According to the scaling theory of electron localization, setting of $\sigma(0) = 0$ should correspond to a continuous M-I transition. This behaviour has only been observed, to my knowledge, by Zabrodskii[207] on p-and n-type germanium doped systems, and is still to be reported in other doped semiconductor systems. By allowing $\sigma(0)$ to be non-zero, one may obtain some plausible results, as was recently demonstrated by Rosenbaum *et al.*[27] and Möbius *et al.*[13, 14]. We wish to point out that there is still some controversy surrounding this procedure and one needs to be cautious in analyzing results using this method. The widely used method involves the extrapolation of $\sigma(T)$ to $T = 0$ K[99].

Finite $W(T \rightarrow 0)$ values reflect a vanishing $\sigma(T \rightarrow 0)$ in accordance with the exponential and power laws shown in Eq. (8.48) below. Metallic conduction is indicated by $W(T \rightarrow 0) = 0$. Möbius *et al.*[13, 14] proposed an equation of the general empirical form, in the case of a discontinuous transition at $T = 0$ K,

$$\sigma(T, x) = \begin{cases} A\left(\sigma(0, x \rightarrow x_c) + T^m \exp\left[-\left(\frac{T_{ES}}{T}\right)^m\right]\right) \\ \sigma(0, x \rightarrow x_c) + BT^Z \end{cases} \quad , \tag{8.48}$$

where $\sigma(0, x \rightarrow x_c) = 1$ and $T_{ES} = 0$. By considering the effects of electron-electron interactions, the exponents $m$ and $Z$ are set to $1/2$. The $W(T)$ curves corresponding to this function were shown in Fig. 7-8. For the highest annealing temperature (1700 °C), with the data fitted with a solid line, $W(T)$ may tend to zero, which may be taken as indicative of a continuous transition at $T = 0$ K. We found that by annealing samples at high temperatures can drive them towards the M-I transition. Details of Möbius *et al.*'s

method have been given elsewhere[14].

## 8.5 Compensation of boron-ion impurity centres

It should be noted that some of the boron-ion atoms implanted into diamond get compensated by deep-lying donor centres. The values for the boron-ion concentrations that we have consistently used above could be less than reported. We need to carry out Hall-effect measurements to determine the carrier concentrations in this system. Our efforts on Hall measurements proved fruitless. The Hall-effect measurements were tried at the University of Pretoria and Simon Frazer University in Canada at 4 K and 77 K. In both cases, the concentration of the activated boron-ion centres was lower than expected. The values of $n$ quote above have been estimated from the SIMS measurements. Instead of dividing the implanted boron-ion dose with the estimated depth, to determine the concentrations, we used the following method. To work out $n$ of say sample AB84, we followed this relation: $n$(AB84)= $D$(AB84)$\times n$(AB73)/$D$(AB73). Recall that SIMS profiles were carried out on samples AB73 and AB12. In the case of insulating samples, we used this relation with results of sample AB12. For those samples which lie in between AB12 and AB73, an average of these two-values were used to calculate their concentrations.

# Chapter 9

# Conclusions

A summary of the principal results, presented in chapters 5 to 8 on type IIa diamond specimens which were implanted with boron ions and carbon ions using the CIRA (cold-implantation-rapid-annealing) process, is given in this chapter. I have used the following notations ◇C:B to refer to boron-ion implanted diamond specimens and ◇C:C to refer to carbon-implanted diamond specimens. These notations will be used hence-forth. Suggestions regarding future research work on these systems are made.

**Analysis of the ◇C:B results.**

## 9.1 Insulating samples

On the insulating side of the metal-insulator transition, our experimental results can be described using phonon-assisted VRH relations. The experimental data follow the Mott VRH behaviour at high-temperatures ($\sim 100 - 300$ K) with the hopping exponent close to $m = 1/4$. In the temperature range $\sim 1.5 - 100$ K, the ES VRH conduction mechanism, with $m \simeq 1/2$, dominates electronic transport processes in the ◇C:B system.

The exponent $m = 1/2$ is usually associated with the appearance of a Coulomb gap in the density of states near the Fermi energy. Our experimental results demonstrate the existence of the conductivity crossover from Mott VRH to ES VRH behaviour as the temperature is lowered. We have noticed a decrease in the crossover temperature when the boron-ion concentration is progressively increased. This phenomenon, which has been investigated over a wide range of doped semiconductors but only observed in a few cases, may be related to a decrease of the size of the Coulomb gap[168].

The experimental data, on the insulating side of the transition and in the vicinity of the metal-insulator transition, may be fitted to various scaling functions which were proposed recently by Aharony *et al.*[200] and Möbius *et al.*[13].

## 9.2 Conduction near the metal-insulator transition

Using the scaling theory of localization described by Eq. (1.1), *viz*,

$$\sigma(0) \propto \left(1 - \frac{n}{n_c}\right)^{\mu} \quad , \tag{9.1}$$

we determined the critical conductivity exponent to be $\mu \sim 1.7$. The critical boron-ion concentration for the metal-insulator transition, $n_c$, was calculated using the Shlimak *et al.*[16] method to be $n_c \simeq 4.0 \times 10^{21}$ cm$^{-3}$. According to the method of Shlimak *et al.*[16], $n_c$ can be determined without extrapolating $\sigma(T)$ to $T = 0$ K although as pointed out by Sarachik and Bogdanovich[17] extrapolation of $\sigma(T)$ to $T = 0$ K is preferable.

## 9.3 Conduction in the metallic regime

The temperature dependence of our low-temperature conductivity data follows the conventional expression given by Eq. (2.11), which is

$$\sigma(T) = \sigma(0) + CT^Z \quad (Z = 1/2 \text{ or } 1/3) \ . \tag{9.2}$$

Higher order terms associated with weak inelastic scattering have been dropped in Eq. (9.2) due to their insignificant contribution in our system. We found the conductivity exponent of $Z = 1/3$ gives a better fit to our low temperature experimental data than $Z = 1/2$ sample at $n_c$. In the case of samples $n > n_c$, $Z = 1/3$ gives a better fit to the data than $Z = 1/2$.

## 9.4 High-temperature annealing

The resistance (or conductivity) showed a remarkable improvement when samples were annealed at temperatures above 1200 °C. The drop in resistivity has been associated with two phenomena: (i) the diminishing of the compensating centres with high-temperature annealing cycles and/or (ii) the reduction in the lattice disorder in ◇C:B system. The origin and the nature of the vacancy-related compensating centres are still not well understood.

**Analysis of the ◇C:C results.**

## 9.5 Percolation transition

Our experimental results seem not to follow a sharp percolation model suggested by Kalish *et al.*[143], indicating that the transformation of diamond from a highly insulating state into a highly conducting phase may be less precipitate than suggested by a simple percolation model[219].

On the insulating side the transition, our experimental data show VRH type behaviour, with an apparent conductivity crossover as the temperature is lowered.

## 9.6 Future Directions

A variety of options in the implantation-annealing routine need to be tested in ◇C:B and ◇C:C systems. Only the CIRA Technique was pursued in this study. Various authors have characterized their diamond specimens using various implantation-annealing procedures[116, 145]. Annealing of samples beyond 1700 °C proved unsuccessful, owing to a milky-colour that developed on the implanted surface. Alternative ways of annealing at high temperature need to be explored.

Electrical conductivity measurements need to be extended to the millikelvin range in order to extract reliable exponent and other information from the $\sigma(T)$ plots. Effects due to weak-localization may also be examined in this system.

The actual boron-ion concentrations, participating in the conduction processes, were

not known precisely in our system. The net concentration of the boron concentration was measured using SIMS analysis. The latter technique has disadvantages. Besides being destructive to the very surface it intends to probe, the SIMS spectroscopy cannot resolve the precise location of the trace element as to whether it resides in a substitutional or interstitial lattice site. This means that Hall-effect measurements are needed on these samples to determine the density of the activated boron atoms.

Magnetoresistance measurements should also be made in this system. We made measurements in ◇C:B samples in the presence of a 1 T field, and the results proved inconclusive.

## 9.7 Published papers

The work carried out in this research project culminated into a number of presentations in local and international conferences. The following articles have been published:

M. J. R. Hoch, T. Tshepe, and J. F. Prins, Ann. Phys. (Leipzig) **8**, (1999) in print.

T. Tshepe, J. F. Prins and M. J. R. Hoch, Diamond and Related Materials **8**, 1508 (1999).

T. Tshepe, J. F. Prins and M. J. R. Hoch, Czech. J. Phys. **46**, 2439 (1996), Suppl. S5.

T. Tshepe, J. F. Prins and M. J. R. Hoch, Czech. J. Phys. **46**, 2441 (1996), Suppl. S5.

In preparation:

T. Tshepe and M. J. R. Hoch, to be submitted to Phys. Rev. B.

J. Wu, T. Tshepe and M. J. R. Hoch, J. E. Butler, to be submitted to Phys. Rev. B.

# Bibliography


[1] D. R. MacKenzie, D. A. Muller, E. Kravtchinskaia, D. Segal, D. J. H. Crockayne, G. Amaratunga and R. Silva, Thin Solid Films **206**, 198 (1991).

[2] S. Tolansky, *The History and Use of Diamond* (The Shenval Press, London, 1962); R. C. Eden, Diamond and Relat. Mater. **2**, 1051 (1993).

[3] J. E. Field, *The Properties of Natural and Synthetic Diamond,* edited by J. E. Field (Academic Press, London,1992).

[4] J. F. Prins, in *Int. School of Phys. "Enrico Fermi" Course CXXXV-The Physics of Diamond*, edited by A. Paoletti and A. Tucciarone (IOS Press, Amsterdam, 1997) p. 411.

[5] M. S. Dresselhaus and R. Kalish, *Ion Implantation in Diamond, Graphite and Related Materials* (Springer Series in Materials Science **22**, Springer-Verlag, Berlin,1992).

[6] J. F. Prins, Phys. Rev. B **38**, 5576 (1988).

[7] J. F. Prins, Nuclear Instrum. and Methods B **35**, 484 (1988); Nuclear Instrum. and Methods in Phys. Research B, in press.

[8] N. F. Mott, *Metal-Insulator Transitions* (Taylor and Francis, London, 1990).

[9] P. W. Anderson, Phys. Rev. **109**, 1492 (1958).

[10] A. F. Ioffe and A. R. Regel, Proc. Semicond. **4**, 237 (1960).

[11] E. Abrahams, P. W. Anderson, D. C. Licciardello and T. V. Ramakrishnan, Phys. Rev. Lett. **42**, 693 (1979).

[12] A. Möbius, D. Elefant, A. Heinrich, R. Muller, J. Schumann, H. Vinzelberg and G. Zies, J. Phys. C: Solid State Phys. **16**, 6497 (1983).

[13] A. Möbius, C. Frenzel, R. Thielsch, R. Rosenbaum, C. J. Adkins, M. Schreiber, H.-D, Bauer, R. Grotzschel, V. Hoffmann, T. Krieg, N. Matz, H. Vinzelberg and M. Witcomb, Proc. $24^{th}$ Int. Conf. Phys. of Semicond. Jerusalem, Israel, 1998.

[14] A. Möbius and C. J. Adkins, Current Opinion in Sold State and Mater. Sci. **4**, 303 (1999).

[15] G. A. Thomas, Phil. Magazine B **52**, 479 (1985).

[16] I. Shlimak, M. Kaveh, R. Ussyshkin, V. Ginodman and L. Resnick, Phys. Rev. Lett. **77**, 1103 (1996).

[17] M P. Sarachik and S. Bogdanovich, Phys. Rev. Lett. **78**, 3977 (1997).

[18] T. F. Rosenbaum, K. Andries, G. A. Thomas and R. N. Bhatt, Phys. Rev. Lett. **45**, 1723 (1980).

[19] M. J. Hirsch, U. Thomanschefsky and D. F. Holcomb, Phys. Rev. B **37**, 8257 (1988).

[20] A. T. Collins, in ref. [4]; M. A. Omar, *Elementary Solid State Physics* (Addison-Wesley Publishing Company, 1975).

[21] A. T. Collins, in *Properties and Growth of Diamond*, edited by Gordon Davies (Published by INSPEC, the Institution of Electrical Engineers, London, United Kingdon, 1994), chapt. 9, p. 261.

[22] M. Werner and R. Locher, Rep. Prog. Phys. **61**, 1665 (1998).

[23] B. I. Shklovskii and A. L. Efros, *Electronic Properties of Doped Semiconductors* (Springer Series in Solid State Science **45,** Springer-Verlag, Berlin, 1984).

[24] H. Böttger and V. V. Bryksin, *Hopping Conduction in Solids* (VCH Publishers, Academie-Verlag, Berlin, 1985).

[25] D. Belitz and T. R. Kirkpatrick, Rev. Modern Phys. **66**, 261 (1994).

[26] Uwe Hans Thomanschefsky, PhD Thesis (Cornell University, Ithaca, New York, 1990), Chapt. 2, p. 10.

[27] R. Rosenbaum, N. V. Lien, M. R. Graham and M. Witcomb, J. Phys. Condens. Matter **9**, 6247 (1997).

[28] R. Rosenbaum, A. Heines, M. Karpovskii, M. Pilosof and M. Witcomb, J. Phys. Condens. Matter **9**, 5413 (1997).

[29] R. Rosenbaum, A. Heines, A. Palevskii, M. Karpovskii, A. Gladkikh, M. Pilosof, A. J. Daneshvar, M. R. Graham, T. Wright, J. T. Nicholls, C. J. Adkins, M. Witcomb, V. Prozesky, W. Przybylowicz and R. Pretorius, J. Phys. Condens. Matter **9**, 5395 (1997).

[30] R. L. Rosenbaum, N. V. Lien, M. R. Graham and M. Witcomb, Phys. sol. (b) **205**, 41 (1998).

[31] A. Möbius, H. Vinzelberg, D. Elefant, J. Schumann and G. Zies, J. Phys. C **18**, 3337 (1985).

[32] A. Möbius, J. Phys. C **18**, 4639 (1985).

[33] A. Möbius, J. Phys. C **19**, L147 (1986).

[34] A. Möbius, Non Cryst. Solids **97+98**, 483 (1987).

[35] A. Möbius, Phys. Rev. B **40**, 4194 (1989).

[36] A. M. Finkel'shtein, Sov. Phys. JETP **57**, 97 (1983).

[37] A. L. Efros and B. I. Shklovskii, J. Phys. C **8**, L49 (1975).

[38] M. Pollak, Discuss. Faraday Soc. **50**, 13 (1970).

[39] G. Srinivasan, Phys. Rev. B **4**, 2581 (1971); R. Chocon, M. Ortuno and M. Pollak, Phys. Rev. B **37**, 10520 (1988).

[40] T. Kurosawa and K. Sugimoto, Prog. Theor. Phys. Suppl. **57**, 217 (1975).

[41] A. Perez-Garrido, M. Ortuno, E. Cuevas, J. Ruiz and M. Pollak, Phys. Rev. B **55**, 8630 (1997).

[42] A. L. Efros and B. I. Shklovskii, J. Phys. C **8**, 249 (1975).

[43] M. Pollak, Phil. Magazine B **65**, 657 (1992).

[44] M. Pollak and M. Ortuno in *Electron-Electron Interactions in Disordered Systems*, edited by M. Pollak and A. L. Efros (North-Holland, Amsterdam, 1985) chapt. 4, p. 287. The reader is referred also to a chapter by A.L. Efros and B. I. Shklovskii in this book.

[45] Masatoshi Imada, Atsuhi Fujimori and Yoshunori Tokura, Rev. Modern Phys. **70**, 1039 (1998).

[46] J. G. Massey and Mark Lee, Phys. Rev. Lett. **75**, 4266 (1995).

[47] Conf. Proc. *Hopping and Related Phenomena*, published in Phys. sol. (b) **205**, (1998).

[48] Phil. Trans. R. Soc. London A **356**, (1998).

[49] N. F. Mott, J. Non-Cryst. Solids **1**, 1 (1968).

[50] Vinay Ambegaokar, B. I. Halperin and J. S. Langer, Phys. Rev. B **4**, 2612 (1971).

[51] N. F. Mott and E. A. Davis, *Electronic Processes in Non-Crystalline Materials* (Claredon, Oxford, 1979).

[52] E. M. Hamilton, Phil. Magazine **26**, 1043 (1972).

[53] Ju-Jin Kim and Hu Jong Lee, Phys. Rev. Lett. **70,** 2798 (1993).

[54] E. Cuevas, M. Ortuno and M. Pollak, Phys. Rev. B **45**, 11542 (1992).

[55] J. Ruiz, M. Ortuno and E. Cuevas, Phys. Rev. B **48**, 10777 (1993).

[56] M. Pollak and M. L. Knotek, Solid State Commun. **21**, 183 (1977).

[57] V. L. Nguyen and B. I. Shklovskii, Sov. Phys. Semicond.**13**, 1281 (1979).

[58] M. L. Knotek and M. Pollak, Phys. Rev. B **9**, 664 (1974).

[59] K. Tenelsen and M. Schreiber, Phys. Rev. B **49**, 12662 (1994).

[60] R. Chicon, M. Ortuno and M. Pollak, Phys. Rev. B **37**, 10520 (1988).

[61] S. D. Baranovskii, B. I. Shklovskii and A. L. Efros, Sov. Phys. JETP **51**, 199 (1980).

[62] J. H. Davies, Phil. Magazine B **52**, 511 (1985).

[63] K. Tenelsen and M. Schreiber, Phil. Magazine **65**, 695 (1992).

[64] K. Tenelsen and M. Schreiber, Phys. Rev. B **52**, 13287 (1995).

[65] A. N. Ionov, M. J. Lea and R. Rentzsch, JETP Lett. **54**, 473 (1991).

[66] I. Terry, T. Penny, S. von Molnar and P. Besla, Phys. Rev Lett. **69**, 1800 (1992).

[67] B. L. Al'tshuler and A. G. Aronov, Solid State Commun. **30**, 115 (1979); Sov. Phys. JETP **50**, 960 (1979); Sov. Phys. JETP Lett. **30**, 482 (1979).

[68] G. A. Thomas, A. Kawabata, Y. Ootuka, S. Katsumoto, S. Kobayashi and W. Sasaki, Phys. Rev. B **26**, 2113 (1982).

[69] B. L. Al'tshuler and A. G. Aronov, JETP Lett. **37**, 410 (1983).

[70] P. A. Lee and T. V. Ramakrishnan, Rev. Modern Phys. **57**, 287 (1985).

[71] C. Castellani, C. DiCastro, H. Fukuyama, P. A. Lee and M. Ma, Phys. Rev. B **33**, 7277 (1986).

[72] Albert Schmid, Z. Physik, **271**, 251 (1974).

[73] D. Belitz and K. I. Wysokinski, Phys. Rev. B **36**, 9333 (1987).

[74] R. M. Hill, Phys. Stat. Sol. A **35**, K29, (1976); *ibid.* **34**, 601 (1976).

[75] R. Hill and Jonscher, J. Non-Cryst. Solids **32**, 53 (1979).

[76] A. G. Zabrodskii and K. N. Zinov'eva, Soviet Phys. JETP **59**, 425 (1984).

[77] J. Hubbard, Proceeding of Royal Soc. A (London) **276**, 238 (1963).

[78] N. F. Mott, *Conduction in Non Crystalline Materials* (Oxford, London, 1993).

[79] P. P. Edwards and M. J. Sienko, Phys. Rev. B **17**, 2575 (1978).

[80] J. Hubbard, Proceeding of Royal Soc. A (London) **277**, 237 (1964); *ibid.* **281**, 401 (1964).

[81] D. J. Thouless, Phys. Reports C **13**, 93 (1974).

[82] F. J. Wegner, Z. Physik B **25**, 327 (1976).

[83] G. J. Dolan and D. D. Osheroff, Phys. Rev. Lett. **43**, 721 (1979).

[84] N. Giordano, Phys. Rev. Lett. B **22**, 5635 (1980).

[85] T. F. Rosenbaum, G. A. Thomas and M. A. Paalanen, Phys. Rev. Lett. **72**, 2121 (1994).

[86] H. Stupp, M. Hornung, M. Lakner, O. Madel and H. v. Lohneysen, Phys. Rev. Lett. **71**, 2634 (1993).

[87] P. Dai, Y. Zhang and M. P. Sarachik, Phys. Rev. Lett. **67**, 136 (1991).

[88] P. Dai, Y. Zhang and M. P. Sarachik, Phys. Rev. Lett. **66**, 1914 (1991); Phys. Rev. B **45**, 3984 (1992).

[89] P. Dai, Y. Zhang and M. P. Sarachik, Phys. Rev. B **49**, 14039 (1994); Phys. Rev. Lett. **70**, 1968 (1993)

[90] A. P. Long and M. Pepper, J. Phys. C **17**, L425 (1984).

[91] D. Belitz and T. R. Kirkpatrick, Phys. Rev. B **52**, 1392 (1995).

[92] T. G. Castner, Phys. Rev. Lett. **88**, 1539 (2000); *ibid.* **84** 2905 (2000).

[93] C. Castallani, G. Kotliar and P. A. Lee, Phys. Rev. Lett. **59**, 323 (1987).

[94] C. Castallani, C. DiCastro, P. A. Lee and M. Ma, Phys. Rev. B **30**, 527 (1984).

[95] S. Hikami, Phys. Rev. B **24**, 2671 (1981).

[96] W. Sasaki, in *Z Localization,* edited by T. Ando and H. Fukuyama (Springer-Verlag, Berlin, 1988) p. 11.

[97] W. L. McMillan and J. Mochel, Phys. Rev. Lett. **46**, 556 (1981).

[98] G. Hertel, D. J. Bishop, E. G. Spencer, J. M. Rowell and R. C. Dynes, Phys. Rev. Lett. **50**, 743 (1983).

[99] G. A. Thomas, Y. Ootuka, S. Katsumoto, S. Kobayashi and W. Sasaki, Phys. Rev. B **25**, 4288 (1982).

[100] U. Thomanschefsky and D. F. Holcomb, Phys. Rev. B **45**, 13356 (1992).

[101] P. Dai, Y. Zhang, S. Bogdanovich and M. P. Sarachik, Phys. Rev. B **48**, 4941 (1993).

[102] P. F. Newman and D. F. Holcomb, Phys. Rev. Lett. **51**, 2144 (1983).

[103] D. W. Koon and T. G. Castner, Phys. Rev. Lett. **60**, 1755 (1988).

[104] T. G. Castner, in *Hopping Transport in Solids,* edited by M. Pollak and B. I. Shklovskii (Elsevier / North-Holland, Amsterdam, 1991), p. 1; Phys. Rev. B **52**, 12434 (1995).

[105] K. M. Itoh, E. E. Haller, J. W. Beeman, W. L. Hansen, J. Emes, L. A. Reichertz, E. Kreysa, T. Shutt, A. Cummings, W. Stockwell, B. Sadoulet, J. Muto, J. W. Farmer, V. I. Ozhogin, Phys. Rev. Lett. **77**, 4058 (1996).

[106] R. Rosenbaum, M. Slutzky, A. Möbius and D. S. McLachlan, J. Phys. Condens. Matter **6**, 7797 (1994).

[107] *Private communication with Prof. M. J. R. Hoch following his discussions with Prof. T. G. Castner and Prof. D. Holcomb* (1999).

[108] M. C. Maliepaard, M. Pepper, R. Newbury and G. Hill, Phys. Rev. Lett. **61**, 369 (1988).

[109] N. F. Mott, Phil. Magazine **26**, 1015 (1972).

[110] G. A. Thomas, M. Paalanen and T. F. Rosenbaum, Phys. Rev. B **27**, 3897 (1983); T. F. Rosenbaum, K. Andries, G. A. Thomas and R. N. Bhatt, Phys. Rev. Lett. **45**, 1723 (1980); M. Paalanen, T. F. Rosenbaum, G. A. Thomas and R. N. Bhatt, Phys. Rev. Lett. **48**, 284 (1982).

[111] J. S. Langer and T. Neal, Phys. Rev. Lett. **16**, 984 (1966).

[112] T. Neal, Phys. Rev. **169**, 508 (1968).

[113] Gerd Bergmann, Phys. Reports **107**, 1 (1984).

[114] A. Kawabata, Solid State Commun. **34**, 431 (1980); J. Phys. Soc. Japan **49**, 628 (1980).

[115] B. I. Al'tshuler and A. G. Aronov, in *Electron-Electron Interactions in Disordered Systems*, edited by M. Pollak and A. L. Efros (North-Holland, Amterdam, 1985) chapt. 1, p. 1.

[116] V. S. Vavilov, M. I. Guseva, E. A. Konorova, V. V. Krasnopevtsev, V. F. Sergienko and V. V. Tutov, Sov. Phys. Solid State **8**, 1560 (1966).

[117] J. F. Prins, Diam. and Relat. Mater. **5**, 907 (1996).

[118] J. F. Prins Mater. Sc. Rep. **7**, 271 (1992).

[119] J. F. Prins, Phys. Rev. B **31**, 2472 (1985).

[120] J. F. Prins, Phys. Rev. B **44**, 2470 (1991).

[121] J. Koike, D. M. Parkin and T. E. Mitchell, Appl. Phys. Lett. **60**, 1450 (1992).

[122] J. F. Prins, Thin Solid Films **212**, 11 (1992).

[123] J. F. Prins, Physica B **185**, 132 (1993).

[124] J. F. Prins, Nuclear Instrum. and Methods Phys. Res. B **80/81**, 1433 (1993).

[125] J. F. Prins, Nuclear Instrum. and Methods B **35**, 484 (1993); J. F. Prins, Nuclear. Instrum. and Methods Phys. Res. B **80/81**, 1433 (1993).

[126] J. F. Prins, Nuclear. Instrum. and Methods B **59/60**, 1387 (1991).

[127] J. F. Prins, Diam. and Relat. Mater. **9**, 1835 (2000).

[128] J. J. Hauser and J. R. Patel, Solid State Commun. **18**, 789 (1976).

[129] S. Prawer and R. Kalish, Phys. Rev. B **51**, 15711 (1995).

[130] R. S. Nelson, J. A. Hudson and D. J. Mazey, British Patent no. 1599668 (1981).

[131] R. A. Spitz, T. E. Derry, J. F. Prins and J. P. F. Sellschop, Nuclear Instrum. and Methods B **51**, 1366 (1990).

[132] R. Zeidler, C. A. Hewett and R. G. Wilson, Phys. Rev. B **47**, 2065 (1993).

[133] J. F. Prins, Phys. Rev. B **39**, 3764 (1989).

[134] H. B. Dyer and F. Ferdinando Br. J. Appl. Phys. **17**, 419 (1996).

[135] E. W. Maby, C. W. Magee and J. H. Morewood, Appl. Phys. Lett. **39**, 157 (1981).

[136] J. F. Prins, T. E. Derry and J. P. F. Sellschop, Phys. Rev. B **34**, 8870 (1986).

[137] J. F. Prins, T. E. Derry and J. P. F. Sellschop, Nuclear. Instrum. and Methods Phys. Res. B **18**, 261 (1987).

[138] J. F. Ziegler, J. P. Biersack and U. Littmark, *The Stopping and Range of Ions in Solids* (Pergamon Press, New York, 1985).

[139] J. F. Prins, Nucl. Instrum. Methods B **59/60**, 1387 (1991).

[140] Robert C. Richardson and Eric. N. Smith, *Experimental Techniques in Condensed Matter Physics at Low Temperatures* (Addison-Wesley Publishing Company, New York, 1988).

[141] D. S. Betts, *Refrigeration and Thermometry Below One Kelvin* (Sussex University Press, 1976).

[142] Anthony Kent, *Experimental Low Temperature Physics* (MacMillan Physical Sciences Series, The MacMillan Press, Ltd., Kent, Great Britain, 1993).

[143] R. Kalish, T. Bernstein, B. Shapiro and A. Talmi, Radiation Effects **52**, 153, (1980).

[144] J. J. Hauser, J. R. Patel and J. N. Rogers, Appl. Phys. Lett. **30**, 129 (1977).

[145] R. Kalish, in *Int. School of Phys. "Enrico Fermi" Course CXXXV-The Physics of Diamond*, edited by A. Paoletti and A. Tucciarone (IOS Press Amsterdam, 1997).

[146] R. Kalish, Diam. and Relat. Mater. **2**, 621 (1993).

[147] R. Kalish, in *Properties and Growth of Diamond* (Published by INSPEC, the Institution of Electrical Engineers, London, United Kingdom, 1994) chapt. 6, p. 189.

[148] A. Hoffman, S. Prawer and R. Kalish, Phys. Rev. B **45**, 12736 (1992).

[149] J. F. Prins, Diam. and Relat. Mater. **3**, 922 (1994).

[150] J. F. Prins, Appl. Phys. Lett. **76**, (2000) in press.

[151] S. R. Broadbent and J. M. Hammersley, Proc. Cambridge, Phil. Soc. **53**, 629 (1957).

[152] V. K. S. Shante and S. Kirkpatrick, Adv. Phys. **20**, 325 (1971).

[153] S. Kirkpatrick, Rev. Modern Phys. **45**, 574 (1973).

[154] J. W. Essam, Rep. Prog. Phys. **43**, 833 (1980).

[155] D. J. Bergman and D. Stroud, in *Solid State Physics*, edited by H. Ehrenneich and D. Turnbull (Academic Press, San Diego, 1992).

[156] D. S. Stauffer and A. Aharony, *Introduction to Percolation Theory*, 2nd Edition, (Taylor and Francis, 1994). The reader is referred also to a paper by P. Smilauer, Contemporary Physics **32**, 89 (1992).

[157] R. P. Kusy, J. Appl. Phys. **48**, 5301 (1977).

[158] C. Domb, E. Stoll and T. Schneider, Comtemporary Physics **21**, 577 (1980).

[159] J. M. Hammersley and D. J. A. Welsh, Contemporary Physics **21**, 593 (1980).

[160] I. Balberg, Phil. Magazine B **56**, 991 (1987).

[161] Z. Ball, H. M. Phillips, D. L. Callahan and R. Sauerbrey, Phys. Rev. Lett. **73**, 2099 (1994).

[162] A. Y. Dovzhenko and P. V. Zhirkov, Phys. Lett. A **204**, 247 (1995).

[163] D. S. Stauffer, *Introduction to Percolation Theory*, (Taylor and Francis, 1985).

[164] A. Carl, G. Dumpich and E. F. Wassermann, Thin Solid Films **174**, 225 (1989).

[165] Ce-Wen Nan, Prog. Mater. Science **37**, 1 (1993).

[166] M. B. Heaney, Phys. Rev. B **52**, 12477 (1995); G. Deutscher, A. Kapituinik and M. Rappaport, in *Percolation Structures and Processes*, edited by G. Deutscher, R. Zallen and J. Adler (Annals of the Israel Phys. Soc. **5**, 1983), chapt. 10, p. 207.

[167] S. Prawer, A. Hoffman, M. Petravic and R. Kalish, J. Appl. Phys. **73**, 3841 (1993).

[168] Y. Zhang, P. Dai, M. Levy and M. P. Sarachik, Phys. Rev. Lett. **64**, 2687 (1990).

[169] M. Paalanen, T. F. Rosenbaum, G. A. Thomas and R. N. Bhatt, Phys. Rev. Lett. **48**, 284 (1982).

[170] C. J. Adkins, J. Phys. Condens. Matter **1**, 1253 (1989).

[171] C. J. Adkins, J. Phys. Condens. Matter **1**, 123 (1990).

[172] C. J. Adkins, in *Hopping and Related Phenomena,* edited by H. Fritzche and M. Pollak (World Scientific Publishing, 1990) p. 93.

[173] J. C. Dawson and C. J. Adkins, J. Phys. Condens. Matter **7**, 6297 (1995); T. Frauenheim, U. Stephanu, K. Beuriloga, F. Jungnickel, P. Blaudeck and E. Fromm, Thin Solid Films **182**, 63 (1989).

[174] R. Rosenbaum, Phys. Rev. B **44**, 3599 (1991).

[175] Y. Meir, Phys. Rev. Lett. **77**, 5265 (1996).

[176] C. H. Olk, S. M. Yalisove, J. P. Heremans and G. L. Doll, Phys. Rev. B **52**, 4643 (1995).

[177] *Private Communication with Prof. Boris A. Aronzon (*1998).

[178] M. Watanabe, Y. Ootuka, K. M. Itoh and E. E. Haller, Phys. Rev. B **58,** 9851 (1998).

[179] E. A. Davis and W. D. Compton, Phys. Rev. **140**, A2183 (1965).

[180] W. Sasaki and Y. Yamanouchi, J. Non Cryst. Solids **4**, 183 (1970).

[181] F. R. Allen and C. J. Adkins, Phil. Magazine **26**, 1027 (1972).

[182] P. T. Wedepohl, Proc. Phys. Soc. B **70**, 177 (1957); C. J. Rauch, Phys. Rev. Lett. **7**, 83 (1961).

[183] J. F. Prins, Phys. Rev. B **61**, 1 (2000).

[184] M. I. Buraschi, G. U. Pignatel and S. Sanguinetti, J. Phys.: Condens. Matter **2**, 10011 (1990).

[185] *Private communications with Dr. Anoulf Möbius and Prof. Ralph Rosenbaum* at the $24^{th}$ International Conference on the Physics of Semiconductors (ICPS24) held in Jerusalem, Israel (1998). See also ref.[221].

[186] J. Shoshany, V. Goldner, R. Rosenbaum, M. Witcomb and D. S. McLachlan, J. Phys. Condens. Matter **8**, 1729 (1996).

[187] H. White and D. S. McLachlan, J. Phys. C: Solid State Phys. **19**, 5415 (1986).

[188] R. A. Davies, M. Pepper and M. Kaveh, J. Phys. C: Solid State Phys. **16**, L285.

[189] H. Akima, J. of A.C. M. **17**, 589 (1970).

[190] B. Kramer and A. Mackinnon, Rep. Progress in Physics **56**, 1469 (1993).

[191] S. J. Lee, J. B. Ketterson and N. Trivedi, Phys. Rev. B **46**, 12695 (1992).

[192] N. V. Lien and R. Rosenbaum, Phys. Rev. B **56**, 14960 (1997); N. V. Lien, Phys. Lett. **207**, 379 (1995).

[193] J. G. Massey and M. Lee, Phys. Rev. Lett. **75**, 4266 (1996).

[194] M. Hornung and H. v. Löhneysen, Czech. J. Phys. **46**, 2437 (1996), Suppl. S5.

[195] N. F. Mott, in [8], p50.

[196] N. F. Mott, in [78], p32.

[197] A. S. Skal and B. I. Shklovskii, Sov. Phys.: Solid State **16**, 1190 (1974).

[198] M. Ortuno and M. Pollak, J. Non Crystalline Solids **59+60**, 53 (1983).

[199] A. L. Efros and B. I. Shklovskii, J. Phys. C **8**, L49 (1975).

[200] A. Aharony, Y. Zhang and M. P. Sarachik, Phys. Rev. Lett. **68**, 3900 (1992).

[201] S. Bogdanovich, M. P. Sarachik, R. N. Bhatt, Phys. Rev. Lett. **82**, 137 (1999).

[202] S. Bogdanovich, D. Simonian, S. V. Kravchenko, M. P. Sarachik, R. N. Bhatt, Phys. Rev. B **60**, 2286 (1999).

[203] S. Bogdanovich, M. P. Sarachik, R. N. Bhatt, Phys. Rev. B **60**, 2292 (1999).

[204] P. A. Lee and T. V. Ramakrishnan, Rev. Modern Phys. **57**, 287 (1985).

[205] T. G. Castner and W. N. Shafarman, preprint, to be submitted for publication (2000).

[206] J. R. Friedman, Y. Zhang, P. Dai and M. P. Sarachik, Phys. Rev. B **53**, 9528 (1996).

[207] A. G. Zabrosdkii, Sov. Phys. Semicond. **14,** 670 (1980); *ibid* **14**, 781 (1980).

[208] M. B. Isichenko, Rev. Modern Phys. **64**, 961 (1992).

[209] H. Ryssel and I. Ruge, *Ion Implantation* (Wiley, New York, 1986).

[210] V. S. Vavilov, M. I. Guseva, E. A. Konorova, V. V. Krasnopevtsev, V. F. Sergienko and V. V. Tutov, Soviet Phys. Semicond. **4**, 6 (1970) ; *ibid* 12; L. A. Davidson, S. Chou, J. F. Gibbons and W. S. Johnson, Radiation Effect **7**, 35 (1971).

[211] C. Uzan-Saguy, C. Cytermann, R. Brener, V. Ritcher, M. Shaanan and R. Kalish, Appl. Phys. Lett. **67**, 1194 (1995).

[212] A. G. Zabrodskii and K. N. Zinov'eva, Soviet Phys. JETP **59**, 425 (1984).

[213] S. Prawer, A. Hoffman and R. Kalish, Appl. Phys. Lett. **57**, 2187 (1990).

[214] B. I. Shklovskii and A. L. Efros, in [23] p206 and p240.

[215] G. Davies, Nature **269**, 494 (1977).

[216] *Private communication with Prof. J. F. Prins* (1998).

[217] See the remarks made by A. Möbius to Dr. G. Kotliar in Phil. Trans. R. Soc. London A **356**, 73 (1998); see also, P. P. Edwards, R. L. Johnston, C. N. R. Rao, D. P. Tunstall and F. Hensel, Phil. Trans. R. Soc. London A **356**, 3 (1998).

[218] *Private communication with Prof. Ralph Rosenbaum* (1996).

[219] T. Tshepe, J. F. Prins and M. J. R. Hoch, Czech. J. Phys. **46**, 2441 (1996), Suppl. S5.

[220] A. T. Collins and E. C. Lightowlers, in *The Properties of Natural and Synthetic Diamond,* edited by J. E. Field (Academic Press, London,1979) p. 79; J. F. H. Custers, Physica **18**, 489 (1952).

[221] P. P. Edwards, R. L. Johnston, C. N. R. Rao, D. P. Tunstall and F. Hensel, Phil. Trans. R. Soc. London A **356**, 3 (1998); Note the remarks made by Dr. A. Möbius to Dr. G. Kotliar on page 73 of the same Journal.

[222] J. C. Bourgoin and J. Walker, Industrial Diamond Review 362 (1976).